

Automated surface wave dispersion measurements and surface wave tomography of central and northern Europe



Dissertation

zur Erlangung des Doktorgrades
der Mathematisch-Naturwissenschaftlichen Fakultät
der Christian-Albrechts-Universität zu Kiel

vorgelegt von
Riaz Ahmed Soomro

Kiel, 2015
Institut für Geowissenschaften
Abteilung Geophysik

First Referee:

Prof. Dr. Thomas Meier

Second Referee:

Prof. Dr. Wolfgang Rabbel

Day of oral examination:

16. 10. 2015

Approved for publication:

XX. XX. 2015

Signed Prof. Dr. Wolfgang J. Duschl, Dekan

Erklärung

Hiermit versichere ich an Eides statt, dass ich diese Dissertation selbstständig und nur mit Hilfe der angegebenen Quellen und Hilfsmittel erstellt habe. Ferner versichere ich, dass der Inhalt dieses Dokuments weder in dieser, noch in veränderter Form einer weiteren Prüfungsbehörde vorliegt. Die Arbeit ist unter Einhaltung der Regeln guter wissenschaftlicher Praxis der Deutschen Forschungsgemeinschaft entstanden.

(Ort) (Datum) (Riaz Ahmed Soomro)

Abstract

Very broad band phase velocity dispersion measurements from earthquake recordings within the period range from 8 s to more than 250 s yield information about the middle to lower crust, the mantle lithosphere as well as the asthenosphere. Therefore these measurements provide complimentary information to noise interferometry as the latter is limited to short periods. Here an algorithm for the automatic determination of the phase velocity dispersion curves is presented. Waveforms recorded at two stations are cross correlated and frequency dependent windows are applied to the cross correlation function. The dispersion curves are calculated from the weighted cross correlation function. The smooth parts of the phase velocity dispersion curves are selected and all the measurements for each inter-station path are averaged in order to obtain average dispersion curve. Off all individual dispersion curves measured for a given station pair, some percentage of outlier measurements are removed and standard deviation and standard error calculated at each frequency. By comparing measurements in opposite propagation direction we can identify and remove/correct erroneous measurements due to off-path propagation, polarity, timing errors, and instrument response issues. In that respect, the method is also helpful in identifying stations with quality issues such that timing, response, polarity problems.

The previous implementation of the classical inter-station method was limited to small regions due to substantial burden in manual picking of the smooth parts of the phase velocity dispersion curve. We have exploited and expanded the benefits of the inter-station method, which has an advantage over the source based methods as the former diminishes influences of errors in the source parameters and the propagation from the source to the receiver region.

By applying this method to a large dataset of 1.37 million waveforms from seismic stations across central and northern Europe, we have obtained a highly consistent phase velocity data set of 63000 Rayleigh and 27500 Love wave inter station dispersion curves in the period range from 8 s to more than 250 s. These unique set of dispersion curves were subsequently tomographically inverted for high resolution isotropic and azimuthally anisotropic phase velocity maps for central and northern Europe.

Synthetic reconstruction tests reveal that the regions with dense path coverage possess a lateral resolution of about 100 km to 150 km.

Large-scale low velocity anomalies in the crust are attributed to the Central European Basin System (CEBS) and Alpine Carpathian region at lower period phase velocity maps. The mantle lithosphere in central Europe appears to be rather homogeneous, with no imprint of the Variscan sutures. The low velocities at 60-80 s periods are due to shallow asthenosphere

in central Europe as well as in the Pannonian basin. In central Europe the location of the shallow asthenosphere matches well with the Cenozoic volcanic fields in the area. The high velocities in the Bohemian massif are due to its thicker lithosphere as compared to the surrounding region. In the western Alpine region the European slab starts to become visible in our phase velocity maps at about 60 s. In central Europe azimuthal anisotropy is parallel to the Variscan sutures in the mantle lithosphere and follows the Alpine front in the south.

A remarkable feature in our long period phase velocity maps is that the TESZ (Trans European suture zone) marks as a clear and distinct boundary between thick Precambrian EEC (East European Craton) and younger and complex Phanerozoic central Europe. The TTZ (Tornquist- Teisseyre Zone) as part of the TESZ is accompanied with a strong lateral contrast in the lithospheric thickness whereas a gradual transition across STZ (Sorgenfrei-Tornquist Zone) is observed. Southeast of the EEC, azimuthal anisotropy parallel to the TTZ is found in the mantle lithosphere and asthenosphere.

In spite of the fact that the depth sensitivity of Love waves are less focused as compared to Rayleigh waves, the main features resolved in Rayleigh wave phased velocity maps are also present in our Love wave phased velocity maps e.g. low velocities at lower period phase velocity maps, a homogeneous mantle lithosphere.

Zusammenfassung

Breitbandige Dispersionsmessungen der Phasengeschwindigkeit von erdbebengenerierten Oberflächenwellen im Periodenbereich von 8 bis mehr als 250 s liefern Informationen über die Struktur der Erdkruste, der Mantellithosphäre und der Asthenosphäre. Solche Messungen sind daher komplementär zur Interferometrie von seismischem Rauschen, von welchem kürzere Periodenbereiche extrahiert werden können. In der vorgelegten Arbeit wird ein Algorithmus für die automatische Bestimmung der Phasengeschwindigkeits-Dispersionskurven vorgestellt. Die Wellenformen an zwei seismischen Stationen werden kreuzkorreliert, frequenzabhängige Fenster auf die Kreuzkorrelationsfunktion angewendet und die Dispersionskurve aus der so gewichteten Kreuzkorrelationsfunktion berechnet. Um durchschnittliche Dispersionskurven für jedes Stationspaar zu erhalten, werden glatte Segmente der Dispersionskurven ausgewählt und alle Messungen für jedes Stationspaar gemittelt.

Aus allen Einzelmessungen für ein Stationspaar werden Ausreisser entfernt und anschliessend die Standardabweichung und der Standardfehler der mittleren Dispersionskurve frequenzabhängig bestimmt. Durch den Vergleich von Messungen in entgegengesetzter Ausbreitungsrichtung können fehlerhafte Messungen durch strukturbedingte Ausbreitungseffekte, aber auch durch Zeitfehler oder Probleme der Polarität oder der Instrumentenantwort identifiziert und entfernt werden. In dieser Hinsicht ist das Verfahren auch hilfreich bei der Identifizierung von Stationen mit Qualitäts- oder technischen Problemen.

Die bisherige, manuelle Umsetzung der klassischen Zwei-Stations-Methode war aufgrund des erheblichen Prozessierungsaufwandes auf kleine Datensätze beschränkt. Durch die vorgelegte Automatisierung können die Vorteile der Zwei-Stations-Methode nun auch auf grösseren Datensätzen Anwendung finden. Dazu gehören vor allem die Unabhängigkeit von Quellparametern (und deren Unsicherheiten) und von der Wellenausbreitung von der Quelle zur Empfängerregion.

Das Verfahren wurde auf einen großen Datensatz von 1,37 Mio. Wellenformen von seismischen Stationen in Mittel- und Nordeuropa angewendet und wir erhielten einen sehr konsistenten Datensatz von 63000 und 27500 Rayleigh und Love-Wellen- Dispersionskurven im Periodenbereich von 8 bis über 250 s. Dieser einzigartige Datensatz wurde anschließend tomographisch in isotrope und azimuthal anisotrope Phasengeschwindigkeitskarten für Mittel- und Nordeuropa invertiert.

Synthetische Rekonstruktionstests zeigen, dass die Regionen mit dichter Pfadüberdeckung eine Auflösung von bis zu 100 - 150 km aufweisen.

Ausgedehnte Bereiche erniedrigter Geschwindigkeit finden sich in der Kruste vor allem im Bereich des zentraleuropäischen Beckensystems (CEBS) und der Alpen- und Karpatenregion bei den kürzerperiodischen Phasengeschwindigkeitskarten. Die Mantellithosphäre in Mitteleuropa, sichtbar bei Perioden um 60-80s, erscheint eher homogen ohne deutlichen Ausdruck der variszischen Suturen. Erniedrigte Geschwindigkeiten in diesem Periodenbereich deuten auf eine flache Asthenosphäre in Zentraleuropa sowie im Pannonischen Becken hin. In Mitteleuropa stimmt die Lage der flachen Asthenosphäre gut mit den Känozoischen Vulkanfeldern überein, während die erhöhten Geschwindigkeiten im Böhmisches Massiv auf eine, im Vergleich zur Umgebung, dickere Lithosphäre hindeuten. Im westlichen Alpenraum beginnt die subduzierte Europäischen Platte bei etwa 60s in unseren Phasengeschwindigkeit Karten sichtbar zu werden. Azimuthale Anisotropie zeigt sich in der Mantellithosphäre Mitteleuropas im Allgemeinen parallel zu den variszischen Suturen und parallel zur alpinen Front im Süden.

Bemerkenswert in unseren langperiodischen Phasengeschwindigkeitskarten ist, dass die TESZ (Trans European Suture Zone) als klare und deutliche Grenze zwischen dem dicken, präkambrischen osteuropäischen Kraton (EEC) und dem jüngeren und komplexeren phanerozoischen Mitteleuropa abgebildet ist. Die TTZ (Tornquist- Teisseyre Zone) als Teil des TESZ ist mit einem starken lateralen Kontrast in der Lithosphärendicke ausgeprägt, während weiter nordwestlich ein weniger scharfer Übergang im Bereich der STZ (Sorgenfrei-Tornquist Zone) zu beobachten ist. Südöstlich des EEC zeigt die azimuthale Anisotropie parallel zur TTZ, sowohl in der Mantellithosphäre, als auch in der Asthenosphäre.

Obwohl die Tiefensensibilität von Love-Wellen im Vergleich zu Rayleigh-Wellen weniger fokussiert ist, sind die wichtigsten Merkmale der Rayleigh-Wellen-Karten auch in unseren Love-Wellen-Geschwindigkeitskarten zu erkennen, u.a. die niedrigen Geschwindigkeiten bei kürzeren Perioden oder die tendenziell homogene Mantellithosphäre.

Acknowledgements

Few words are not enough to acknowledge all the people who supported my work and continually encouraged me throughout the writing of this dissertation. Without their time, attention, encouragement, thoughtful feedback and patience, I would not have been able to achieve this endeavor. However, I will try my best to extend great appreciation to every one who helped me scientifically and emotionally during the whole PhD period.

Above all I would like to express my special appreciation and thanks to my supervisor Prof. Dr. Thomas Meier, He has been a tremendous mentor for me. I always remain thankful to him that he provided me the opportunity to do my PhD under your kind supervision. As I started my master education some years after my job. Therefore, if he had not provided this excellent opportunity it would not have possible to acquire the highest academic degree. Therefore, due to him my dream have become true. He always encouraged me to grow as a research scientist. Being a scientist a critical thinking is important. I understood from him the significance of 1%. For me if I achieve 99%, it is more than satisfactory but I learnt from him “why not 100%”. I learnt from him how to be perfectionist as well as realistic. He helped and supported me throughout my PhD tenure, like father some time he become little bit strict but I understand that it was required to achieve high standards. He gave tremendous amount of time, help, encouragement, without these, it would not have possible to complete my PhD and dissertation.

I would like to thank Dr. Christian Weidle. I was very lucky to have a room partner like him I was able to obtain immediate help and support in my PhD work. It was very easy to discuss the ideas and results. I learnt a lot from his guidance. Without him it would have been difficult to achieve this task. I experienced his importance during his leave period.

I would like to thank my colleague Dr. Luigia Cristiano, we both started at same time in Kiel University. She was supportive from day one. She was the one to whom I could share my feelings. She was a source of moral support during my difficult times.

I would like to thank my colleague Dr. Martin Thorwart who helped me to solve some problems related to generic mapping tools (GMT) software. I would like to thank Dr. Carsten Griewatsch I learnt some basics about Linux operating system. He and his team was always ready to help within no times. They made my life easy, without them it would have taken enormous time to solve software and hardware issues. I would like to thank all the group members of Prof. Dr. Thomas Meier for their support during my PhD time and I also would like to thank all members of Institute of Geosciences who provided support on one way or other in successful completion of PhD work.

This dissertation would not have been possible without funding from the German research foundation – DFG (Deutsche Forschungsgemeinschaft), therefore, I am thankful for their generous support which helped me to carry out my PhD studies.

I especially thank prof. Dr. Sergei Lebedev for his support during my entire PhD tenure, though he was not reachable personally but he always replied promptly when ever I need help. Without his codes and help I would not be able to obtain high resolution phase velocity maps.

I would again like to thank my colleague Dr. Christian Weidle for his valuable suggestions which proved to be very helpful in reshaping the manuscript greatly. He also helped in translation of the summary to German language.

My special thanks goes to my colleagues Mr. Iftikhar Shaheen Mirza and Mr. Ejaz Ashraf Tanoli for their support in official matters. They encouraged and provided moral support during my PhD period.

I would again like to thank Mr. Iftikhar Shaheen Mirza for his thorough review of the thesis.

The present shape of the manuscript is due to valuable suggestions of my senior colleague Dr. Muhammad Ali Shah who provided valuable suggestions, I thank and appreciate him for his precious time he spent and efforts he made.

There are no proper words to say thanks to my wife Saira Riaz without her continuous support and help I would not be in position to accomplish this.

I thank to my lovely daughters Mahrukh Riaz Soomro and Maheen Riaz Soomro who are the pride and joy of my life. I love them more than anything and I appreciate all their patience and support during my PhD studies. I would like to thank to my family members including my sisters who suffered me a lot during my absence, my brothers who supported and helped me to pursue my goal. I would also like to thank my father-in-law, mother-in-law sister-in-law and brother in laws for their continuous support and encouragement.

Finally, I am thankful to almighty Allah: without his will I would have never found a right path. His mercy is with me throughout my life. I also offer my humblest thanks from the deepest core of my heart to the Holy prophet MUHAMMAD (peace be upon him) who is forever a torch of guidance and knowledge for humanity as a whole.

I would like to dedicate my thesis to my mother and my late father. It is all due to their prayers and constant and untiring support to achieve my goals without their prayers and support in life I am nothing.

Table of contents

Abstract	vi
Zusammenfassung	viii
Acknowledgements	x
List of figures	iii
List of tables	vii
1 Introduction	1
2 Introduction to surface waves	7
2.1 Seismic wave types	7
2.1.1 Body waves	7
2.1.2 Surface waves	7
2.2 Surface wave methods	12
2.2.1 Single station method	12
2.2.2 Inter-station method	13
2.2.3 Array based methods	14
2.2.4 Noise tomography	15
2.2.5 Waveform fitting methods	17
2.2.6 Methods based upon Surface wave portion of the waveform . . .	17
2.3 Previous surface wave studies	20
2.3.1 Global surface wave studies	20
2.3.2 European surface wave studies	21
2.4 Motivation	26
3 Phase velocities of Rayleigh and Love waves	31
3.1 summary	31
3.2 Introduction	32
3.3 Method	36
3.3.1 Cross-correlation measurement of phase velocities	36
3.3.2 Automated selection of individual phase velocity curves	41

3.3.3	Automatic averaging of inter-station phase velocities	46
3.3.4	Loose vs. conservative parameter settings	47
3.4	Application to central and northern Europe	49
3.4.1	Quality Control	49
3.4.2	Phase velocities	54
3.5	Conclusions	56
3.6	acknowledgments	60
References		61
4	Response and timing issues at broadband stations	69
4.1	summary	69
4.2	Automated data analysis	70
4.3	Method and synthetic example	71
4.4	Data examples	73
4.5	Discussion	74
4.6	acknowledgements	76
References		77
5	Rayleigh and Love wave phase velocity tomography	79
5.1	Data	79
5.1.1	Data sampling	80
5.2	Tomographic Inversion	80
5.2.1	Effect of regularization	90
5.2.2	Finding optimal damping parameters	91
5.2.3	Resolution tests	93
5.3	Reliability test for Rayleigh wave 2Ψ Anisotropy	96
5.3.1	Removal of unresolved node	96
5.4	Reliability test for Love wave 4Ψ Anisotropy	104
5.4.1	Removal of unresolved node	104
5.5	Rayleigh and Love wave phase velocity maps	105
5.5.1	East European Craton	111
5.5.2	Central and north–western Europe	112
5.5.3	Trans–European Suture Zone	113
5.5.4	Alps and Carpathians	114
6	Conclusions and future outlook	121
6.1	Conclusions	121
6.2	Future outlook	123
References		125

List of figures

1.1	A tectonic map of the study region	2
2.1	Explanation of the ambient noise tomography.	16
2.2	Map view of shear wave velocity model by Legendre et al. (2012) at 110 km depth	22
2.3	Vertical cross sections from the shear wave velocity model by Legendre et al. (2012). (sections from A to D)	27
2.4	Vertical cross sections from the shear wave velocity model by Legendre et al. (2012). (sections from E to H)	28
3.1	Seismic station coverage in Europe.	37
3.2	Example of an inter-station, phase-velocity measurement for the station pair BFO (Black Forest Observatory, Germany) and CLL (Collmberg, Germany)	42
3.3	An example of a noisy inter-station measurement of phase velocity for the station pair MOX (Moxa, Germany) and CLL (Collmberg, Germany) 43	
3.4	Application of the selection criteria for automated dispersion measurements.	44
	a Phase-velocity difference from the background model prediction.	44
	b Smoothness and length criteria.	44
3.5	Automatic averaging of individual dispersion measurements for station path BFO-CLL	48
3.6	Overview of processed data and retrieved measurements.	50
	a No. of analysed waveforms per station.	50
	b No. of processed events per path.	50
	c No. of phase velocity measurements per path.	50
	d No. of avg. phase velocity curves per station.	50
3.7	Histograms showing differences in phase-velocity measurements for the entire data-set	53
	a Rayleigh waves	53
	b Love waves	53
3.8	Difference in average inter-station phase velocities between "loose" and "conservative" parameter sets as function of distance.	53
	a Rayleigh waves	53

b	Love waves	53
3.9	Average standard deviation (a) and difference between two propagation directions (b) per station, averaged over all frequencies.	53
a	Standard deviation	53
b	Difference between two propagation directions	53
3.10	2-D histograms of all automatically measured phase velocity curves of the entire data-set	55
a	Rayleigh waves	55
b	Love waves	55
3.11	Standard deviations (a, c) and standard errors (b, d) as a function of inter-station distance for all measurements in the entire data-set for Rayleigh (a, b) and Love (c, d) waves.	55
a	Standard deviation as a function of inter-station distance for entire data-set (Rayleigh waves)	55
b	Standard error as a function of inter-station distance for entire data-set (Rayleigh waves)	55
c	Standard deviation as a function of inter-station distance for entire data-set (Love waves)	55
d	standard error as a function of inter-station distance for entire data-set (Love waves)	55
3.12	Isotropic checkerboard tests with anomalies of approximately 100 km (a) and 150 km (b)	57
a	Checkerboard test for Rayleigh waves	57
b	Checkerboard test for Love waves	57
3.13	Isotropic phase velocity maps for selected periods (12s,30s, 60s).	58
4.1	Simulation of potential data errors in the inter-station phase velocity measurement.	71
4.2	Automated phase velocity measurements between station NC602 in southern Norway and VSU in Estonia.	72
4.3	Automated phase velocity measurements between station FUR and ASSE in southern and northern Germany, respectively.	73
4.4	Automated phase velocity measurements between station FLT1 in northern Germany and OKC in the eastern Czech Republic.	74
4.5	Averaged deviations of measured dispersion curves in the period range 25–100 s.	75
5.1	Inter-station paths obtained from more than 1000 permanent and temporary stations	81
a	Rayleigh wave	81
b	Love wave	81
5.2	Histogram shows no. of paths as function of period for Rayleigh and Love wave.	82
5.3	Path coverage for Rayleigh waves.	83

5.4	Path coverage for Love waves	84
5.5	Assessment of optimal regularization parameters: Left and right half circles show data variance and model norm, respectively.	85
	a 60 s	85
	b 125 s	85
5.6	Effect of varying isotropic damping on Rayleigh wave phase velocity maps. Rayleigh wave isotropic and anisotropic 2Ψ component is plotted	86
5.7	Effect of varying isotropic damping on Rayleigh wave phase velocity maps. Isotropic and Rayleigh wave 4Ψ component is plotted here . . .	86
5.8	Effect of varying anisotropic damping on Rayleigh wave phase velocity maps.	87
5.9	Effect of varying isotropic damping on Love wave phase velocity maps. Here Love wave isotropic and anisotropic 4Ψ component is plotted. . .	87
5.10	Effect of varying anisotropic damping parameters for Love wave phase velocity maps. Here Love wave isotropic and anisotropic 4Ψ component is plotted.	88
5.11	Effect of smoothing on phase velocity maps. Smoothing values of 0.1, 0.4, 0.6 (our preferred value), 1.0 are plotted here.	91
5.12	Rayleigh wave isotropic checker-board tests with anomalies of approximately 100 km (left) and 150 km (right).	94
5.13	Love wave isotropic checker-board tests with anomalies of approximately 100 km (left) and 150 km (right).	95
5.14	Various anisotropic direction thresholds ($\sigma\theta_{rot}$) are tested to see the effect of these threshold values for Rayleigh waves. On the left column the inversion result is plotted in yellow and the shifted result is plotted in white and the nodes where the anisotropy is resolved is plotted in green color. On the right column the result of the resolution test is plotted. Here yellow colored bars are input to resolution test, output of the resolution test is plotted in white, and the green colored nodes are accepted ones after applying the amplitude and direction criteria. . . .	99
	a $\sigma\theta_{rot} = 90^\circ$	99
	b $\sigma\theta_{rot} = 50^\circ$	99
	c $\sigma\theta_{rot} = 0^\circ$	99
5.15	Different thresholds to test the recovery of amplitude of the anisotropy for Rayleigh waves. On the left column the inversion result is plotted in yellow and the shifted result is plotted in white and the nodes where the anisotropy is resolved is plotted in green color. On the right column the result of the resolution test is plotted. Here yellow colored bars are input to resolution test, and output of the resolution test is plotted in white and the green colored nodes are accepted ones after applying the amplitude and direction criteria.	100
	a $\sigma a_{rot} = 100\%$	100
	b $\sigma a_{rot} = 50\%$	100

c	$\sigma_{a_{rot}} = 0\%$	100
5.16	Different thresholds to test the recovery of amplitude of the anisotropy for Love waves.	101
a	$\sigma_{\theta_{rot}} = 45^\circ$	101
b	$\sigma_{\theta_{rot}} = 30^\circ$	101
c	$\sigma_{\theta_{rot}} = 0^\circ$	101
5.17	Effect of changing anisotropic amplitude threshold for Love waves.	102
a	$\sigma_{a_{rot}} = 100\%$	102
b	$\sigma_{a_{rot}} = 50\%$	102
c	$\sigma_{a_{rot}} = 0\%$	102
5.18	The resulting Rayleigh wave phase velocity maps after finalizing the threshold parameter for anisotropic amplitude and direction	103
5.19	The resulting Love wave phase velocity maps after finalizing the threshold parameter for anisotropic amplitude and direction	104
5.20	8 s (a) and 12 s (b) isotropic phase velocity maps.	106
a	8 s isotropic phase velocity maps.	106
b	12 s isotropic phase velocity maps.	106
5.21	30 s (a) and 60 s (b) isotropic phase velocity maps.	107
a	30 s isotropic phase velocity maps.	107
b	60 s isotropic phase velocity maps.	107
5.22	60 s phase velocity maps	108
a	Cenozoic alkaline volcanism in central Europe.	108
b	Rotliegend (Permian) volcanics	108
5.23	60 and 80 s isotropic phase velocity maps	109
a	60 s phase velocity maps with Mesozoic volcanism.	109
b	80 s isotropic phase velocity map	109
5.24	Rayleigh wave isotropic and azimuthally anisotropic phase velocity maps	116
5.25	Comparison of the Rayleigh wave phase velocity maps with Fry et al. (2010)	117
5.26	Comparison of the result with SKS splitting result of Vecsey et al. (2014).	118
5.27	Love wave isotropic and azimuthally anisotropic phase velocity maps	119

List of tables

3.1	Statistical parameters of the distribution shown in Fig. 3.7a (Rayleigh waves).	52
3.2	Statistical parameters of distribution shown in Fig. 3.7b (Love waves).	52
5.1	Damping parameters used to obtain Rayleigh and Love wave phase velocity maps	93

Chapter 1

Introduction

There is a rapid increase in the number of seismic stations in recent years, resulting in large data volumes. These large data volumes pose challenge to seismologists in all data processing aspects. Manual operations are complemented or partly replaced by automatic processing (e.g. Hanka et al., 2010; Olivieri & Clinton, 2012; Withers, 1999). The retrieval of seismological observables used for the imaging of Earth structure - including arrival time picking, polarization or dispersion analysis - is, however, still often conducted manually. This is possible and feasible for spatially restricted study regions and relatively small data sets. In order to process the very large amount of all of now available broadband data, automated processing techniques are needed. Automated routines have been proposed for the picking of body-wave arrival times (e.g. Allen, 1978; Baer & Kradolfer, 1987; Küperkoch et al., 2010), locations of seismic events (e.g. Hanka et al., 2010; Olivieri & Clinton, 2012; Withers, 1999), waveform inversions (e.g. Lebedev et al., 2005; Lee & Chen, 2013; Legendre et al., 2012; Maggi et al., 2009; Yoshizawa & Ekström, 2010), receiver function processing (e.g. Crotwell & Owens, 2005), and SKS splitting studies (Evans et al., 2006; Walther et al., 2014). Here we discuss the automated determination of phase velocities of fundamental mode surface waves, measured between two single seismic stations. Various surface wave methods and their advantages as well as shortcomings are discussed comprehensively in Chapter 2. The use of phase velocity measurements in tomographic inversion is explained in Chapter 5.

The Europe is an excellent place to study various tectonic processes. The present day configuration of the Europe is a result of various successive tectonic events. The Europe continent comprises Precambrian Baltic shield of Fennoscandia, which is bordering to Caledonides. The central Europe is characterized by Veriscan realm, and the Alpine Mediterranean is most youngest one with the age 230 Ma to present (Blundell et al., 1992). The Europe continent has a 4.5 y tectonic history (Grad & Tiira, 2009).

The Trans-European Suture Zone (TESZ) is the major and most prominent boundary that separates Precambrian EEC (East European Craton) and Caledonides and Veriscid(es in Western Europe (Artemieva & Thybo, 2013). It separates the thick

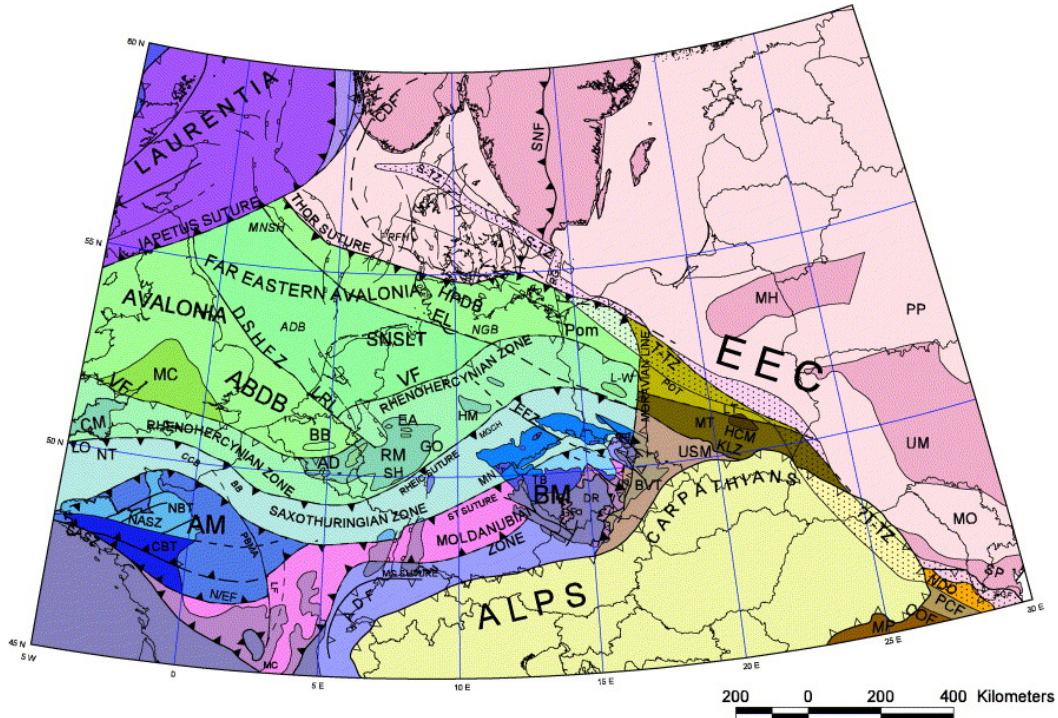


Fig. 1.1: A tectonic map of the study region (modified after Banka et al., 2002). Some notable tectonic features include: EEC, East European Craton; TTZ, Tornquist-Teisseyre Zone; STZ, Sorgenfrei-Tornquist Zone; EL, Elbe Line; VF, Variscan Front and so on.

Precambrian EEC from that of younger Phanerozoic Europe. The surface of this suture is hidden due to repeated past tectonic events (Knappmeyer-Endrun et al., 2013a). TESZ comprises two linear segments: STZ (Sorgenfrei–Tornquist Zone) on north western side, including areas of Sweden, Denmark, Germany, and TTZ (Tornquist–Teisseyre Zone) on south–eastern side starting from north sea in north west towards black sea in south–east (Bogdanova et al., 2008; Thybo, 2000). The central western Europe is result of various orogenic events; in result various continental fragments rifted off the northern margin of the Gondwana and accreted towards SW Baltica (Banka et al., 2002; Janutyte et al., 2014; Nolet & Zielhuis, 1994; Pharaoh, 1999; Winchester, 2002). The present day configuration of the areas around TESZ is due to various tectonic events namely, (1) Caledonian orogeny and Caledonian collision tectonics, (2) Variscian orogeny, (3) Mesozoic rifting, and (4) Alpine orogenic events (Bogdanova et al., 2008; Thybo, 2000). The structure on the western and central Europe is complex as compared to EEC (Babuška & Plomerová, 2001; Dadlez et al., 2005; Knappmeyer-Endrun et al., 2013c). The crust on the north eastern side of TESZ is thick with a thickness of around 50 km while it is 40 km along TESZ. An international project started in year 2006 for the duration of two years (Wilde-Piórko et al., 2008). The project’s aim was to study the structure of the crust and mantle lithosphere around this long suture zone known as TESZ (Trans-European Suture Zone) extending from north-western Europe

in the region of STZ (Sorgenfrei-Tornquist Zone) towards south-eastern Europe across TTZ (Tornquist-Teisseyre Zone). The Trans-European Suture Zone acts as a boundary between Phanerozoic central Europe and Precambrian East European Craton.

Therefore, this dissertation is based on PASSEQ 2006-2008 (PASSive Seismic Experiment around TESZ) project. Various methods have been applied to the PASSEQ data i.e. body wave travel time tomography (Janutyte2014), P wave residuals (Wilde-Piórko et al., 2010), SKS splitting (Vecsey et al., 2014), receiver functions (Knapmeyer-Endrun et al., 2013a) etc. We have used surface wave data to study the lithospheric structure of this boundary and surrounding regions. As the duration of the project was limited to only two years, therefore, in addition to PASSEQ data, we have used all the available data in European region from permanent as well as temporary stations in the period from January 1990 to October 2013. Here, we present the automated procedure to determine phase velocities of fundamental mode surface waves, measured between two single seismic stations, and we assess the station quality issues and use these automatically obtained path average phase velocity dispersion measurements for both Rayleigh and Love waves in tomographic inversion for the isotropic and azimuthally anisotropic structure of the central and northern Europe. Details of the method to automatically obtain path average dispersion curves are provided in Chapter 3. Details about main findings of our study are discussed in chapter 5.

A brief overview of the chapters is provided below.

Overview of the chapters

In **chapter 2** a brief introduction of seismic wave types and various methods to measure surface waves has been made. After that, briefly discussed are previous surface wave studies in Europe and around the Globe. Surface waves can be produced by natural or man-made sources (ballistic sources) or through noise sources, therefore, a glimpse of noise tomography is given as well. In the end the manual inter-station method and the motivation to automate the inter-station method, to handle large data sets has been discussed.

Chapter 3 provides a methodological base of this work. In the beginning of the chapter, the theory behind cross-correlation of inter-station phase velocities is elaborated, while the criteria for automatic selection of individual phase velocity curves are also discussed, and a method to obtain a smooth path average dispersion curve from all the individual smooth measurements for any inter-station pair is discussed as well. Then, the effect of loose and conservative setting on phase velocities curves is discussed. Moreover, a brief description of station quality issues is given as well in this chapter and more detailed discussion about potential problems in instrumentation has been made in Chapter 4. Finally, the application of inter-station method to a data-set covering entire Europe is presented. Here statistical analysis is provided and in addition to that, the isotropic Rayleigh and Love wave phase velocity maps for central Europe are provided for three

periods (12 s, 30 s, and 60 s), the resolution of the tomographic inversion is accessed through checker-board tests and a brief interpretation about the results is also provided. This chapter is submitted as a paper to Geophysical Journal International (GJI) with title “Phase velocities of Rayleigh and Love waves in central and northern Europe from automated, broadband, inter-station measurements”. My contribution in this paper was focused on development of the procedure to automatically select the smooth parts of the phase velocity curves, rigorous testing of the method with range of values of various parameters, finding optimal threshold values of these parameters, defining and applying the procedure to obtain path average phase velocity curves, statistical evaluation of the automatically obtained phase velocity measurements. Performing tomographic inversion based upon Deschamps et al. (2008). I accessed the isotropic and anisotropic resolution with the help of checker board and rotation test (Deschamps et al., 2008).

Chapter 4 discusses various station quality issues. While applying averaging and quality control procedure to entire data set, we observed systematic deviations at certain stations which cannot be related to wave propagation effects. Therefore, this chapter explains the statistical analysis procedure to identify problematic stations with polarity, timing, and response problems. This chapter is published as a paper in *Advances in Geosciences* with title “Identification of response and timing issues at permanent European broadband stations from automated data analysis”. In this chapter, I contributed in obtaining average phase velocity dispersion curves, and pointed out the anomalous dispersion curves, then developed a procedure to estimate following quantities at each station.

1. Overall standard deviation at each station
2. Difference between both propagation directions
3. Difference to the background model

I obtained above-mentioned quantities for entire period range as well as at three periods i.e. higher periods, intermediate periods, and lower periods, in order to assess the effects at these period ranges. The procedure, I developed, helped in detecting polarity, timing, and response problems at some stations in central Europe.

In **chapter 5** the details about the tomographic inversion of average phase velocity curves are provided. The basic formulation for tomographic inverse problem is provided. The effect of regularization on the tomographic maps is checked by testing range of damping values and optimal damping parameters for this data set are suggested with the help of “L” curve test and by visual inspection of the phase velocity maps with different damping values. The isotropic and anisotropic resolution tests are performed. The resolution for isotropic phase velocities with the help of quasi checkerboard with various anomaly sizes is evaluated, for anisotropy a rotation test is applied to the fast directions of Rayleigh and Love wave phase velocity maps, and an automated procedure to remove the unresolved nodes in order to ensure the anisotropic resolution

is applied. In the end, different features of the isotropic and anisotropic phase velocity maps are discussed.

The **Chapter 6** concludes and highlights the main results and outcome of the study. It also discusses future outlook.

Chapter 2

Introduction to surface waves

2.1 Seismic wave types

Ground shaking caused by natural or man-made sources produce vibrations. These vibrations carry energy from the source and propagate outward in all directions. These vibrations produce seismic waves. Mainly there are two types of waves in seismology: body waves which travel in to the body of the earth and surface waves which travel along the earth surface.

2.1.1 Body waves

Body waves can be classified into two types 1) longitudinal waves, 2) transverse waves. Longitudinal waves are also called P (primary), dilatational, irrotational, or compressional waves. P waves shake the ground in the direction they travel. These waves travel faster as compared to other types of waves, with the speed in between 4–8 km/sec. Therefore, they arrive first on the seismogram, followed by other wave types. When a P wave travels it oscillates around its equilibrium position. This causes a volume change. These waves are similar to sound waves. The other body wave types are transverse waves, which are also called shear or S waves. These waves displace ground in transverse direction. They can travel in solid medium only. These waves travel slowly with a usual speed in between 2.5–4 km/sec. These waves cause no volume change.

2.1.2 Surface waves

The solution of wave equation for body waves exists in whole space (Shearer, 2009, Ch. 8, p. 215). With the presence of free space, other solutions also exist, and they are named as surface waves. They travel along the earth surface. Surface waves are

generated by the interaction of body waves with the free surface. Due to geometrical spreading the energy carried by surface waves spread in 2-D and their energy decays with $\sim \frac{1}{r}$ where 'r' is the distance, which is in contrast to body waves which spread in 3-D and their energy decays with $\sim \frac{1}{r^2}$. Owing to this reason surface waves are recorded with larger amplitudes also at longer distances. The shallow earthquakes generate strong surface waves. These waves travel slowly as compared to body waves, therefore these waves are recorded after the body wave arrival. Surface waves are dominant waves on seismograms, and for large earthquakes they can circle the globe many times. At noisy stations, surface waves are the main source to obtain source parameters. Surface waves can be classified into two types, i.e Rayleigh waves and Love waves.

Rayleigh waves

Rayleigh waves are coupled P-SV waves. They produce elliptical retrograde or prograde particle motion, recorded on vertical or radial components.

In order to derive the equation for Rayleigh and Love wave, we mainly follow Shearer (2009)

The wave equation of a plane P-wave, propagating in +x direction is given by

$$u = Ae^{-i\omega(t-ps-\eta z)}, \quad (2.1)$$

where p is the horizontal slowness, $\eta = \sqrt{1/c^2 - p^2}$ is the vertical slowness and c is the P-wave velocity.

The wave equation can also be written in the form of potentials, where ϕ is the scalar potential, which represents a P wave and ψ is the vector potential for S wave.

$$u = \nabla\phi + \nabla \times \psi, \quad \nabla \cdot \psi = 0, \quad (2.2)$$

The ψ_y is the only part of ψ that produces SV motion. The solutions for plane wave for ϕ and ψ_y are given by.

$$\phi = Ae^{-i\omega(t-px-\eta_\alpha z)}, \quad (2.3)$$

$$\psi_y = Be^{-i\omega(t-px-\eta_\beta z)}, \quad (2.4)$$

A and B are the amplitudes for P and S wave, respectively. The vertical slowness η for P and SV wave can be written as

$$\eta_\alpha = (1/\alpha^2 - p^2)^{1/2}, \quad (2.5)$$

$$\eta_\beta = (1/\beta^2 - p^2)^{1/2}, \quad (2.6)$$

It is assumed that both P and SV wave have same horizontal slowness, therefore, the ray parameter p is constant and y component of the displacement and its partial derivatives are zero for P/SV plane wave. Therefore, the displacement of x and z component can be written as follows

$$u_x^P = \partial_x \phi = pAi\omega Ae^{-i\omega(t-px-\eta_\alpha z)}, \quad (2.7)$$

$$u_z^P = \partial_z \phi = \eta_\alpha Ai\omega Ae^{-i\omega(t-px-\eta_\alpha z)}, \quad (2.8)$$

The SV displacement can be defined as,

$$u_x^S = -\partial_z \psi_y = -\eta_\beta Bi\omega e^{-i\omega(t-px-\eta_\beta z)}, \quad (2.9)$$

$$u_z^S = \partial_x \psi_y = pBi\omega e^{-i\omega(t-px-\eta_\beta z)}, \quad (2.10)$$

The boundary condition at a free surface ($z = 0$), the normal and shear traction must vanish.

Therefore, $\tau_{xz} = \tau_{zz} = 0$.

$$\tau_{xz} = \mu(\partial_z u_x + \partial_x u_z), \quad (2.11)$$

solving the above equation yields,

$$\tau_{xz}^P = -A(2\mu p \eta_\alpha) \omega^2 e^{-i\omega(t-px-\eta_\beta z)}, \quad (2.12)$$

$$\tau_{zz} = \lambda(\partial_x u_x + \partial_z u_z) + 2\mu \partial_z u_z, \quad (2.13)$$

and solving the above equation yields

$$\tau_{zz}^P = -A[(\lambda + 2\mu)\eta_\alpha^2 + \lambda p^2] \omega^2 e^{-i\omega(t-px-\eta_\alpha z)}, \quad (2.14)$$

$$\tau_{xz}^S = -B\mu(p^2 - \eta_\beta^2) \omega^2 e^{-i\omega(t-px-\eta_\beta z)}, \quad (2.15)$$

$$\tau_{zz}^S = -B(2\mu\eta_\beta p) \omega^2 e^{-i\omega(t-px-\eta_\beta z)}, \quad (2.16)$$

the condition for free surface is,

$$\tau_{xz} = \tau_{xz}^P + \tau_{xz}^S = 0, \quad (2.17)$$

$$\tau_{zz} = \tau_{zz}^P + \tau_{zz}^S = 0, \quad (2.18)$$

by substituting equation 2.3 and 2.4 into 2.7 we get

$$A(2p\eta_\alpha) + B(pr - \eta_\beta^2) = 0, \quad (2.19)$$

by substituting equation 2.5 and 2.6 into 2.8 we get

$$A\left[\alpha^2(\eta_\alpha^2) + p^2\right] - 2\beta^2 p^2 + B[2\beta^2 \eta_\beta p] = 0, \quad (2.20)$$

these two equations describe $P - SV$ boundary condition at free surface, where p is horizontal slowness.

The vertical slowness is given by following set of equations:

$$\eta_\alpha = (1/\alpha^2 - p^2)^{1/2} \text{ and } \eta_\beta = (1/\beta^2 - p^2)^{1/2},$$

where $p > \beta^{-1} > \alpha^{-1}$, and η_α and η_β are imaginary.

From equation 2.10

$$u = Ae^{i\omega\eta z} e^{-i\omega(t-ps)}, \quad (2.21)$$

It can be seen that, if η is imaginary, it will lead to positive values in exponent. This will result in evanescent waves. Evanescent are inhomogeneous waves and their amplitude decay or grow with depth. For homogeneous waves, the vertical slowness has real values. In this case, there is no dispersion. The non-trivial solution can be obtained only when the determinant of the coefficient matrix is zero.

The equations 2.19 and 2.20 can be written in matrix form

$$\begin{bmatrix} (2p\eta_\alpha) & (pr - \eta_\beta^2) \\ \alpha^2(\eta_\alpha^2) + p^2 - 2\beta^2 p^2 & B[2\beta^2 \eta_\beta p] \end{bmatrix} \begin{bmatrix} A \\ B \end{bmatrix} = 0,$$

solving the determinant yields,

$$(p^2 - \eta_\beta^2) \left[\alpha^2(\eta_\alpha^2) + p^2 - 2\beta^2 p^2 \right] - 4\beta^2 p^2 \eta_\alpha \eta_\beta = 0, \quad (2.22)$$

by substituting the values of η_β , η_α , the above equation can be written in terms of ray parameter p , P , and S velocities.

$$\left(2p^2 - \frac{1}{\beta^2}\right)^2 + 4p^2 \left(\frac{1}{\alpha^2} - p^2\right)^{1/2} \left(\frac{1}{\beta^2} - p^2\right)^{1/2} = 0, \quad (2.23)$$

further simplifying by taking β^2 common and for the imaginary values of η_α η_β ($p > \beta^{-1} > \alpha^{-1}$)

$$\left(2p^2 - \frac{1}{\beta^2}\right)^2 - 4p^2 \left(p^2 - \frac{1}{\alpha^2}\right)^{1/2} \left(p^2 - \frac{1}{\beta^2}\right)^{1/2} = 0. \quad (2.24)$$

This equation is the Rayleigh equation. Lord Rayleigh obtained this result around 100 years ago. This has dependence upon P – wave velocity, α , and S – wave velocity β . The roots of the equation give Rayleigh wave velocity, which propagates over an isotropic and elastic surface defined on the half surface ($y \geq 0$). The phase velocity

is $c = 1/p$, and its value is slightly less than β . The value of $c = .092\beta$ for poison solid.

Love waves

Rayleigh wave can propagate in the presence of a free space, but Love wave cannot. The condition for Love wave to propagate is the presence of a layer over half space. Love wave can travel in case only when the velocity structure keep turning energy. Therefore, if the shear wave velocity increases with the depth, it forms a wave guide, where SH waves are trapped. The dispersion equation for Love waves (Lay & Wallace, 1995b, chapter 4) can be written as

$$\tan(\omega\eta_{\beta_1}H) = \frac{\mu_2\eta_{\beta_2}}{i\mu_1\eta_{\beta_1}} = \frac{\mu_2\hat{\eta}_{\beta_2}}{\mu_1\eta_{\beta_1}}, \quad (2.25)$$

It is assumed here, that a post critical situation where $c = 1/p < \beta_2$ will yield $\eta_{\beta_2} = i\hat{\eta}_{\beta_2}$ and $\hat{\eta}_{\beta_2}$ is real. The above equation gives a condition related to ω and c which must be satisfied. The wave velocity depends upon ω and c . Rewriting above equation yields,

$$\tan(H\omega\sqrt{1/\beta_1^2 - 1/c^2}) = \frac{\mu_2\sqrt{1/c^2 - 1/\beta_2^2}}{\mu_1\sqrt{1/\beta_1^2 - 1/c^2}}. \quad (2.26)$$

The condition to ensure that all the terms are real is, $\beta_1 < c < \beta_2$. This equation is the dispersion equation for Love waves, c is the phase velocity and ω is angular frequency.

Dispersion characteristics of surface waves

The variation in velocity with respect to frequency is called dispersion. Due to dispersion, the wave-train is deformed. The high frequency waves have short wavelength as compared to low frequency waves. Due to their long wavelength, they sample deeper structures. In a homogeneous isotropic half space, the surface waves are non-dispersive. The simplest case in which, Love waves can travel is homogeneous isotropic layer over a homogeneous half space. In this case both Rayleigh and Love waves are dispersive. The presence of Love wave proves that, the earth is inhomogeneous, rather it is layered. Therefore, in real case the Rayleigh waves are dispersive. Different spectral component of a wave travels at different velocity called a phase velocity.

To understand the phenomenon of the dispersion, we consider the sum of two harmonic waves with slightly different frequency and wave number.

$$u(x,t) = \cos(\omega_1t - k_1x) + \cos(\omega_2t - k_2x), \quad (2.27)$$

ω is angular frequency and k is wave number.

$$\omega_1 = \omega - \delta\omega, \quad k_1 = k - \delta k, \quad (2.28)$$

$$\omega_2 = \omega + \delta\omega, \quad k_2 = k + \delta k, \quad (2.29)$$

by substituting equations 2.28 2.29 in equation (2.1) we get

$$\begin{aligned} u(x, t) &= \cos(\omega t - \delta\omega t - kx + \delta kx) + \cos(\omega t + \delta\omega t - kx - \delta kx) \\ &= \cos[(\omega t - kx) - (\delta\omega t - \delta kx)] + \cos[(\omega t - kx) + (\delta\omega t - \delta kx)] \\ &= 2 \cos(\omega t - kx) \cos(\delta kx - \delta\omega t), \end{aligned} \quad (2.30)$$

to solve equation 2.30 we used the trigonometric identity $\cos(A + B) + \cos(A - B) = 2\cos A \cos B$.

Here the short period wave travels at ω/k and long period envelope travels at the speed of $\delta\omega/\delta k$. The short period wave is phase velocity and long period wave is group velocity. The group velocity (U) is written as,

$$U = d\omega/dk, \quad (2.31)$$

as $\omega = ck$, therefore, group velocity can also be written as,

$$U = \frac{d\omega}{dk} = \frac{dck}{dk} = c + k \frac{dc}{dk} = \left(1 - k \frac{dc}{d\omega}\right)^{-1}, \quad (2.32)$$

The phase velocity of both Rayleigh and Love waves increases with period. From this equation, it can be seen that, group velocity is dependent upon phase velocity. As $dc/d\omega$ is negative in equation 2.32, this shows that group velocity is less than phase velocity ($U < c$) (Shearer, 2009, Ch. 8, p. 225). If change in phase velocity is zero, in this case, the group and phase velocities are the same. Generally the phase velocity is increasing with period, and decreasing with frequency.

2.2 Surface wave methods

2.2.1 Single station method

We can write a surface wave seismogram as

$$u(x, t) = \frac{1}{\pi} \int_0^\infty \hat{u}(\omega, x) \times \cos\left(\omega t - \frac{\omega}{c(\omega)}x + \phi_0(\omega)\right) d\omega, \quad (2.33)$$

The $\phi(\omega) = \phi_0(\omega) - [\omega x/c(\omega)] + 2\pi N + \omega t$ is phase, whereas ϕ_0 is initial phase. $2\pi N$ is periodicity. $\hat{u}(\omega, x)$ is the amplitude term.

From the above equation the phase at each frequency can be obtained as

$$\phi_1(\omega) = \omega t_1 + \phi_0(\omega) - \frac{\omega x_1}{c(\omega)} + 2\pi N, \quad (2.34)$$

where ϕ_0 is initial phase, $2\pi N$ represents the periodicity, $\phi_1(\omega)$ is the phase at a station, t_1 is the arrival time of the phase and x_1 is the source–receiver distance, whereas $c(\omega)$ is the phase velocity. It can be seen from the equation 2.34 that, there is need of initial phase information in order to compute the phase velocity.

The earlier group velocity single station measurements were carried out by Gutenberg (1924) and Ewing & Press (1950). They measured group travel time from source to station in time domain. Landisman et al. (1969) introduced time frequency analysis for single station method. This method was improved by (e.g. Levshin et al., 1989; Ritzwoller & Levshin, 1998; Vdovin et al., 1999).

The most recent use of the single station method is by Foster et al. (2014), where they extended the method by introducing a correction of the propagation direction with the help of dense mini arrays.

The measurement of phase or group velocity with single station is affected by the errors due to incorrect source mechanisms and source locations. These effects are pointed out by (e.g. Levshin et al., 1999; Muzyert & Snieder, 1996), and may introduce some errors.

2.2.2 Inter-station method

To overcome the errors caused by erroneous source locations and source mechanisms Brilliant & Ewing (1954) measured Rayleigh wave phase difference between two stations in time domain, by eliminating the phase shifts due to the source and the propagation of the fundamental modes from the source to the first station. The equation for inter-station phase velocity (by following Lay & Wallace, 1995a, Ch. 4, p. 146) can be written as

$$\phi_1(\omega) = \omega t_1 + \phi_0(\omega) - \frac{\omega x_1}{c(\omega)} + 2\pi N, \quad (2.35)$$

$$\phi_2(\omega) = \omega t_2 + \phi_0(\omega) - \frac{\omega x_2}{c(\omega)} + 2\pi N, \quad (2.36)$$

subtracting 2.35 and 2.36 yields

$$\phi_1(\omega) - \phi_2(\omega) = \omega(t_1 - t_2) - \frac{\omega}{c(\omega)}(x_1 - x_2) + 2\pi N, \quad (2.37)$$

The above equation (2.37) can be solved for phase velocity $c(\omega)$ by using the fact $T = 2\pi/\omega$

$$c(\omega) = \frac{x_1 - x_2}{(t_1 - t_2) + T[N - (\frac{1}{2\pi})(\phi_1(\omega) - \phi_2(\omega))]}, \quad (2.38)$$

again t_1, t_2 is the arrival time of the phase at station 1 and station 2, respectively, and x_1, x_2 is source receiver distance at station 1 and station 2, respectively. It can be seen from this equation (2.38) that, the source phase term is canceled out, but the 2π ambiguity is still there. Therefore, correct N is required, for which a background model is helpful to identify the N . Toksöz & Ben-Menahem (1963) measured phase velocities from a single station by successive passages of the same wave, by making a slight modification in the above equation.

$$C(T) = \frac{\Delta_0}{\delta t + T(\delta\phi + N + \frac{1}{2})}, \quad (2.39)$$

here Δ_0 is the length of the great circle, $\delta t = t_{n+2} - t_n$, $\delta\phi = \phi_{n+2} - \phi_n$, and $\frac{1}{2}$ is the circle phase shift due to two extra polar passages, with a $\pi/2$ phase shift per polar passage (Brune et al., 1961). The application of the two-station method in frequency domain was carried out by McEvelly (1964). He measured phase velocities for both Rayleigh and Love waves and he observed Love–Rayleigh discrepancy i.e. the difference in velocities of horizontally (SH) and vertically (SV) polarized shear waves. The inter-station method was widely used during last decade, with the help of broadband arrays and regional networks (e.g. Adam & Lebedev, 2012; Beghein et al., 2010; Darbyshire & Lebedev, 2009; Deschamps et al., 2008; Endrun et al., 2004, 2008, 2011; Lebedev & Van Der Hilst, 2008; Lebedev et al., 2006, 2009, 2013; Meier et al., 2004; Prindle & Tanimoto, 2006; Yao et al., 2006; Yoshizawa & Ekström, 2010).

2.2.3 Array based methods

Lateral heterogeneities in the local structure may lead to erroneous phase velocity measurements (e.g. Forsyth & Li, 2005; Friederich et al., 1994; Maupin, 2011; Pedersen et al., 2013, 2006; Wielandt, 1993). The Ray theory is based upon high frequency approximation, and it works if the length scale of the perturbations is larger than the wavelength and Fresnel zone width. Problems may arise if the heterogeneities are comparable to wavelength or even smaller. In that case, the simplified ray theory based methods may fail (Passier & Snieder, 1995). Press (1956) suggested a method to correct the propagation direction caused by the lateral heterogeneities in the local structure.

To account the deviations in propagation direction of a plane wave, various algorithms have been suggested by several authors for single event array analysis based upon f-k analysis with the plane wave assumption (e.g., Capon, 1970; Maupin, 2011; Sun & Helmberger, 2011). Friederich et al. (1994) measured local phase velocities with the use of phase as well as amplitude measurements using the Helmholtz equations by allowing curved wave-fronts. Prindle & Tanimoto (2006) used spectral analysis technique to confirm the validity of the great circle path approximation. They found that small correction is required in order to adjust the off great circle path effects.

Forsyth & Li (2005) used a different approach in order to account for the scattering and multipathing problems. They call their method as two plane wave method. In this method, the assumption is that, one plane wave arrive from a direct path and other from the scattered path. To represent the structure by considering a finite width of the response of the plane wave, a Gaussian sensitivity function was utilized. The interference of two plane waves can be helpful to model the non-plane wave behavior due to scattering and multipathing. Tanimoto & Prindle (2007) used beam-forming approach to study the surface waves. He measured phase velocities by accounting the deviations from the great circle path. These deviations are significant at high frequencies. Dense arrays are helpful to identify these great circle deviations. Foster et al. (2014) used the single station method by calculating the arrival angle in order to correct the off great circle deviation. The array based methods provide fine-scale structure of the earth interior but are limited to the studies in regional scale (Rost & Weber, 2002), whereas the classical inter-station method can be used in local, regional, as well as global studies.

2.2.4 Noise tomography

Normal traditional seismology require identifiable impulsive sources, there are two kinds of these sources, earthquake or human made sources such as explosions, also called ballistic sources. These sources are energetic one. The ever present amount of energy called ambient noise is traditionally removed from the analysis, due to its non-impulsive nature, and lack of available methods to extract the useful information present in the noise.

A new method has been developed to extract usable signal even from the noise. This method can be used to extract valuable information about the sub surface and helpful to study the areas which are seismically quiescent. Therefore, the ambient noise interferometry can be used to study the surface waves generated by ambient noise sources, these noise sources can be wind, ocean waves, rock fracturing, and anthropogenic activity. As these sources travel similar to impulsive sources, therefore, they also carry information about the sub surface. The early theoretical studies related to ambient noise were carried out by (e.g. Derode et al., 2003; Larose et al., 2005; Snieder, 2004; Wapenaar, 2004; Weaver & Lobkis, 2001, 2004). Campillo & Paul (2003); Paul et al. (2005) used coda waves and with multiple scattering of waves by small scale heterogeneities, Sabra et al. (2005); Shapiro & Campillo (2004) used ambient noise of surface waves. Roux et al. (2005) used crustal body waves. The earlier practical applications based upon ambient noise, were developed and improved by (e.g. Campillo & Paul, 2003; Wapenaar, 2004).

After the construction of the Green's function, traditional tomographic imaging methods can be used to investigate the structure of the crust and upper mantle. The Green's function between two seismic stations can be constructed by cross correlating long time record, recorded at the two stations, where one station can be understood as source

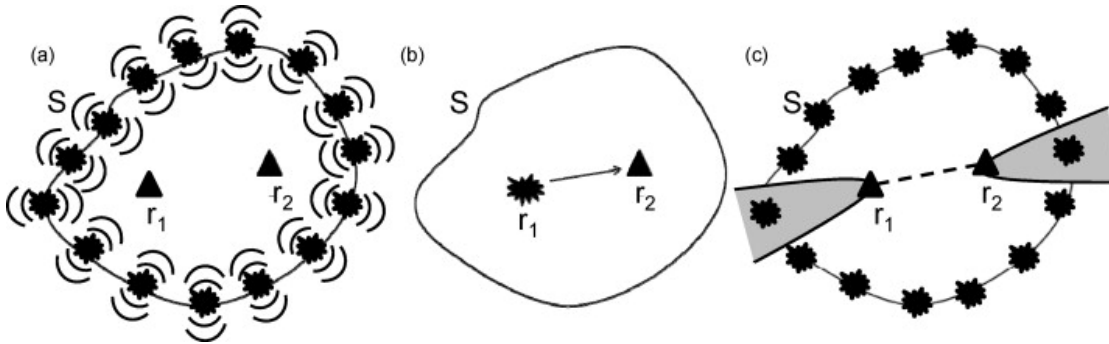


Fig. 2.1: Explanation of the ambient noise tomography. r_1 , r_2 are the receiver 1 and 2, respectively. "S" are the sources surrounded by these two receivers, each of which transmits energy to the other. The sources in grey regions are contributing their energy at the receivers r_1 and r_2 , energy generated by the other sources is canceled out due to destructive interference (modified after Nicolson et al., 2012).

and the other as receiver. The Green's function is the seismogram recorded at one station due to instantaneous or impulsive energy at the other. The Green's function tells how the energy travels from one point to the other. Claerbout (1968) proved the possibility to construct a Green's function from the source starting from one station and traveling through sub surface and arrive back at the same station. The Green's function describes how energy travels through sub surface from one source and reflect back at the same point.

To illustrate the problem, consider that, two seismometers are surrounded by a source of energy (see fig. 2.1). The wave-field due to these sources propagates in the medium. The energy recorded by these arbitrary sources, recorded at these two stations is cross correlated and all these cross correlations from all sources are stacked. Due to this stacking process, the constructive energy is added and destructive energy is canceled out. The constructive energy is one, which is traveled by the sources located at the extensions of the inter-receiver path.

Snieder (2004) showed that energy generated by the sources located along the extension of the two receivers contributes most (fig. 2.1 c). Cross correlation of the ambient noise provide more homogeneous sampling as compared to the earthquake based imaging techniques. In a traditional way the seismologists analyze earthquakes and artificial source that travels through the earth.

The period ranges of traditional inter-station based tomography (5–10 s to 400 s, in regional to global applications) and ambient noise tomography (about 5 s to 50 s, in regional applications) overlap each other. Therefore, the phase velocities obtained through ambient noise and earthquake data yield complimentary information, whereas the earthquake based tomography has added advantage of broader bandwidth.

2.2.5 Waveform fitting methods

The waveform based methods can be classified into two main categories i.e. 1) surface wave portion of the waveform, 2) full waveform methods.

2.2.6 Methods based upon Surface wave portion of the waveform

In the approach used by Nolet (1990), synthetic seismograms are fitted with the data. Synthetic seismograms are computed by summing surface wave modes. 1-D average velocity structure is determined along each wave path. In the second step, all the individual linear equations obtained in first step, are combined to obtain the 3-D structure.

The simple way to write a synthetic seismogram based upon JWKB approximation is,

$$s(\omega) = \sum A_m(\omega) \exp[i\omega\Delta / (C_m^0(\omega) + \overline{\delta C_m(\omega)})], \quad (2.40)$$

and the phase velocity perturbations as a function of averaged shear (S) wave perturbations are written as,

$$\overline{\delta C_m(\omega)} = \int_0^a \frac{\partial(C_m^0(\omega))}{\partial\beta(r)} \overline{\delta\beta(r)} dr, \quad (2.41)$$

subscript m is mode number. The summation is taken over all modes, Δ is source receiver distance, a is earth radius. $C_m^0(\omega)$ is reference phase velocity and $\frac{\partial(C_m^0(\omega))}{\partial\beta(r)}$ are the Fréchet derivatives and are related to perturbation in path average phase velocities. The real data $d(t)$ is fitted with the synthetics $s(t)$ with the help of the least square minimization.

$$F(\overline{\delta\beta(r)}) = \left| \mathbf{R}d - \mathbf{R}s(t, \overline{\delta\beta(r)}) \right|^2 dt. \quad (2.42)$$

The perturbations obtained in above equation are used to obtain a 3-D shear wave structure. Due to small scale heterogeneities, there may be a change in the wave-speed. Scattering can result due to these heterogeneities. If the scattering is large, then the JWKB approximation may become invalid. These effects should be accounted while calculating the synthetic seismograms.

As it is known that surface wave portion of the seismogram is highly non-linear. Nolet (1990) used a non-linear optimization technique in fitting the synthetic with real data. Cara & Lévêque (1987) solved the non-linearity problem with the help of secondary observables, their approach is similar to isolation filter technique of Gee & Jordan (1992). Debayle (1999) automated the Cara & Lévêque (1987) technique. They used similar two step procedure discussed above, but with different algorithms. In the first step they obtained path averaged 1-D models and, in the second step, they inverted them to obtain 3-D structure. Debayle & Sambridge (2004) used waveform method to extract

surface wave information and obtained global SV wave and azimuthal tomographic model. Lebedev et al. (2005) developed AMI which was based upon two step procedure of Nolet (1990). They fit the observed seismograms with synthetic seismogram based upon JWKB approximation. They automatically identify the time frequency windows which contain the signal and accurately model with JWKB approximation. Their optimal procedure eliminates chance fits and cycle skipping problem. AMI splits the large scale tomographic problem into traceable inversions of the seismograms individually.

These waveform fitting methods are source based, therefore, they provide information about the upper mantle and deeper structure. For these methods accurate source information is required in order to remove these source effects and obtain structural information. Lebedev et al. (2006) combined inter-station and source based single station method and obtained very broad band dispersion measurements from 10 s to more 350 s, the low period information was obtained from inter-station method whereas high period information was obtained from source based single station method using AMI (Lebedev et al., 2005).

Full waveform methods

Full waveform methods include finite difference method, boundary element method, spectral or pseudo spectral methods, spectral element method etc. Finite difference method is grid point method where computational domain is covered by a space-time grid. The placement of space and time grids affects the accuracy. The information is unknown in between the grid points. A derivative of the function at these grid points is taken with the use of finite difference formula by using the values at grid points. Finite difference method can be applied both in time domain and in frequency domain, but in seismology the time domain FD method is more common. The finite difference method is easy to implement but has some limitations. Some limitations include,

1. unable to calculate accurate surface waves
2. unable to account for the deformed geometries for example topography at free surface
3. difficulty in adaptive grid size with respect to wavelength

Therefore, finite difference methods are unable to tackle the challenges of global seismology. Chaljub & Tarantola (1997); Igel & Weber (1995, 1996) applied the finite difference method on some simplified geometries. Some improvements in the finite difference method are made by (e.g. Zingg, 2000; Zingg et al., 1996). Peter et al. (2007) used finite difference method and obtained global model. They modeled surface wave propagation by assuming smoothly heterogeneous earth. They implemented the wave equations numerically on a spherical membrane with zero thickness. Method developed by Peter et al. (2007) is less accurate compared to full 3-D numerical solutions but is faster.

The other full waveform technique is boundary element method which is based upon integral representation theorems. In this method, the Green's functions are calculated with discrete wave number expansion in order to incorporate the realistic surface and interface topography (Bouchon & Sanchez-Sesma, 2007). There is a limitation of finite number of homogeneous layers, which can lead to large ill conditioned linear matrix systems in 3-D cases. In general the finite difference methods are superior to ray based methods.

Spectral and pseudo spectral methods offer some improvements over finite difference methods (FDM), as they require small number of grid points, with these methods body waves can be modeled more accurately as compared to surface waves (e.g., Carcione, 1994). These methods are also restricted to smooth media, because of the global nature of polynomial basis functions. The classical FEM (finite element methods) methods are well suited to handle complex geometries, but due to their high computation costs their use is rare. Spectral element method (SEM) is highly accurate, but computationally very expensive. In this method irregular meshes are used which yield accurate structure. Spectral element method accurately solves elastic wave equation by computing synthetic seismograms in strongly heterogeneous 3-D media (Rickers et al., 2013). This method is suitable for the simulations of the global seismic wave propagation with unmatched accuracy. As compared to other full waveform methods, this method overcomes the problems of local topography and sharp gradients.

The adjoint based tomographic methods use spectral element method in the computation of the synthetic seismogram. In the global wave-field simulations, the spectral element method can be used for the periods 20 s and higher (Komatitsch & Tromp, 2002). Komatitsch & Tromp (2002) used the spectral element method to perform 3-D simulations. Finite difference (FD) based full waveform methods may fail in the presence of surface topography or discontinuities. The SEM is computationally expensive as the computing time increases with propagation distance. The advantage of SEM over other global methods lie in the case that both methods are similar except the small scale structure near the source and receiver are not well resolved in the mode summation technique because of the far field approximation. Rickers et al. (2013) used full waveform modeling on body as well as surface waveforms in a non-linear way. They applied the method to Iceland and highlighted some new insights on the structure of the region. Tape et al. (2010) used the SEM based adjoint method to study the California crust. Fichtner et al. (2009) used the method to study the upper-mantle structure in the Australasian region. Zhu et al. (2012) studied the European upper mantle structure with the use of adjoint methods. The adjoint method is time domain convolution of two fields i.e. the source field and adjoint field. The source wave-field is generated by an earthquake hypocenter and adjoint wavefield is generated by the adjoint source at receiver. Adjoint based techniques are near field approximation whereas for example mode summation technique and other ray based techniques are far field approximation. Fichtner et al. (2010) used full waveform tomography based upon SEM and adjoint tomography to obtain a radially anisotropic structure of Australia. They have obtained a first continental-scale full waveform tomographic model for Australia. Zhou et al.

(2011) compared mode summation with adjoint based SEM. In global studies the adjoint based methods are computationally expensive. Zhou et al. (2011) also showed that 1D model is adequate enough in case of Rayleigh waves.

The full waveform methods are highly accurate and account for finite frequency effects but are computationally very expensive. In global applications these methods perform well at periods 20 s and higher (Komatitsch & Tromp, 2002) in this case they lack crustal information, therefore, crustal corrections are required to infer information about upper mantle and deeper structures.

2.3 Previous surface wave studies

In order to have some insight information about the previous work based upon surface waves, I have discussed some global surface wave studies, as well as European surface wave studies.

2.3.1 Global surface wave studies

The initial surface wave studies were done independently by Love (1911) and Golitzin (1912). Some earlier surface wave studies were done by (e.g. Byerly, 1930; Gutenberg, 1924, 1926; Gutenberg & Richter, 1936; Jeffreys, 1928, 1935; Stoneley, 1926, 1928, and others).

The ground breaking work done by Dziewonski et al. (1977); Masters et al. (1982) played a significant role in development of earlier models and provided earliest picture of the 3-D earth (Ritzwoller et al., 1995). Below is the short description of some global models which used surface waves.

Nataf et al. (1986); Woodhouse & Dziewonski (1984) did a pioneering work in developing upper mantle models. Woodhouse & Dziewonski (1984) developed upper mantle model using waveform inversion of very long period seismogram which are mainly dominated by fundamental mode surface waves. Masters et al. (1996) computed absolute and differential delay times by using surface wave phase velocity measurements and with normal mode data. Su et al. (1994) and Liu & Dziewonski (1994, 1998) used absolute and differential time measurements by using body, and surface waveform data with the use of surface wave formalism. Li & Romanowicz (1996) used hand-picked SH waveforms to derive a model and formulated forward and inverse problems which is valid for both body and surface wave data. Mégnin & Romanowicz (2000) developed a 3-D V_{SH} shear wave velocity model for whole mantle obtained by hand-picking of body, surface and higher mode waveforms. Kustowski et al. (2008) presented a radially anisotropic model (S362ANI) which is based upon surface and body wave phase and travel time anomalies and has an approximate resolution of 1000 km. Ekström (2011) developed an anisotropic global model (GDM52) for Rayleigh and Love waves in the

period range of 25–250 s. The Love wave model is isotropic only, whereas anisotropy is also considered in their Rayleigh wave model. Ritsema et al. (2011) developed a model using Rayleigh wave phase velocities, body wave travel times, and normal mode splitting measurements. Lekic & Romanowicz (2011) used SEM to construct upper mantle model. Debayle & Ricard (2012) presented a new SV model with the use of fundamental and higher order Rayleigh wave mode measurements. They used waveform modeling technique to extract fundamental and higher order Rayleigh wave modes. Schaeffer & Lebedev (2013) presented a vertically polarized shear wave model (SL2013sv) for the upper mantle with the help of automated multi-mode inversion of surface and S-wave forms. French & Romanowicz (2014) presented a first radially anisotropic shear wave velocity model (SEMUCB-WM1) of the entire mantle derived from Spectral Element based forward modeling approach. The resolution of the previous models is limited to around 1000 kilometers, whereas French & Romanowicz (2014) claims 800 km resolution. Some other whole-mantle models (e.g. Houser et al., 2008; Panning & Romanowicz, 2006; Simmons et al., 2006, 2010).

The limiting factor in the resolution of global models is due to the fact that most of the earthquakes occur at plate boundaries and receivers are located mostly on the continents, which makes only one third of total earth hence two third area remains un-instrumented, therefore, there is uneven distribution of sources and receivers, particularly in southern hemisphere (Bodin et al., 2015). Recently Meschede & Romanowicz (2015) compared various features of some representative global and regional models. All the global models mentioned above confirm long wavelength features present in these global models. Due to long wave length nature and large source station distance they lack short period information. Therefore, all of these models discuss upper mantle and deeper structures, and crustal corrections are required in these models. These global models possess some common features as well e.g. Pannonian basin in central Europe is only one example which is common in all the global models and there may be similarities in other regions as well, and there are considerable discrepancies among these models in terms of small scale (<2500km) features (Becker & Boschi, 2002; Dziewonski, 2005) and in terms of anisotropy (e.g. Becker et al., 2008).

2.3.2 European surface wave studies

There are numerous surface wave studies in Europe, some earlier surface wave studies include, (e.g. Calcagnile & Panza, 1978, 1979, 1980, 1990; Calcagnile et al., 1985; Dost, 1990; Lomax & Snieder, 1995; Mantovani et al., 1985; Mindevalli & Mitchell, 1989; Mueller & Sprecher, 1978; Pedersen et al., 1994; Snieder, 1988; Stange & Friederich, 1993; Vaccari & Panza, 1993; Yanovskaya & Ditmar, 1990).

The above studies were based upon earlier implementation of either two station method of (e.g. Brune & Dorman, 1963; Knopoff et al., 1966), MFA (multiple filter analysis) technique of Dziewonski et al. (1969), or tacking of fundamental and higher order

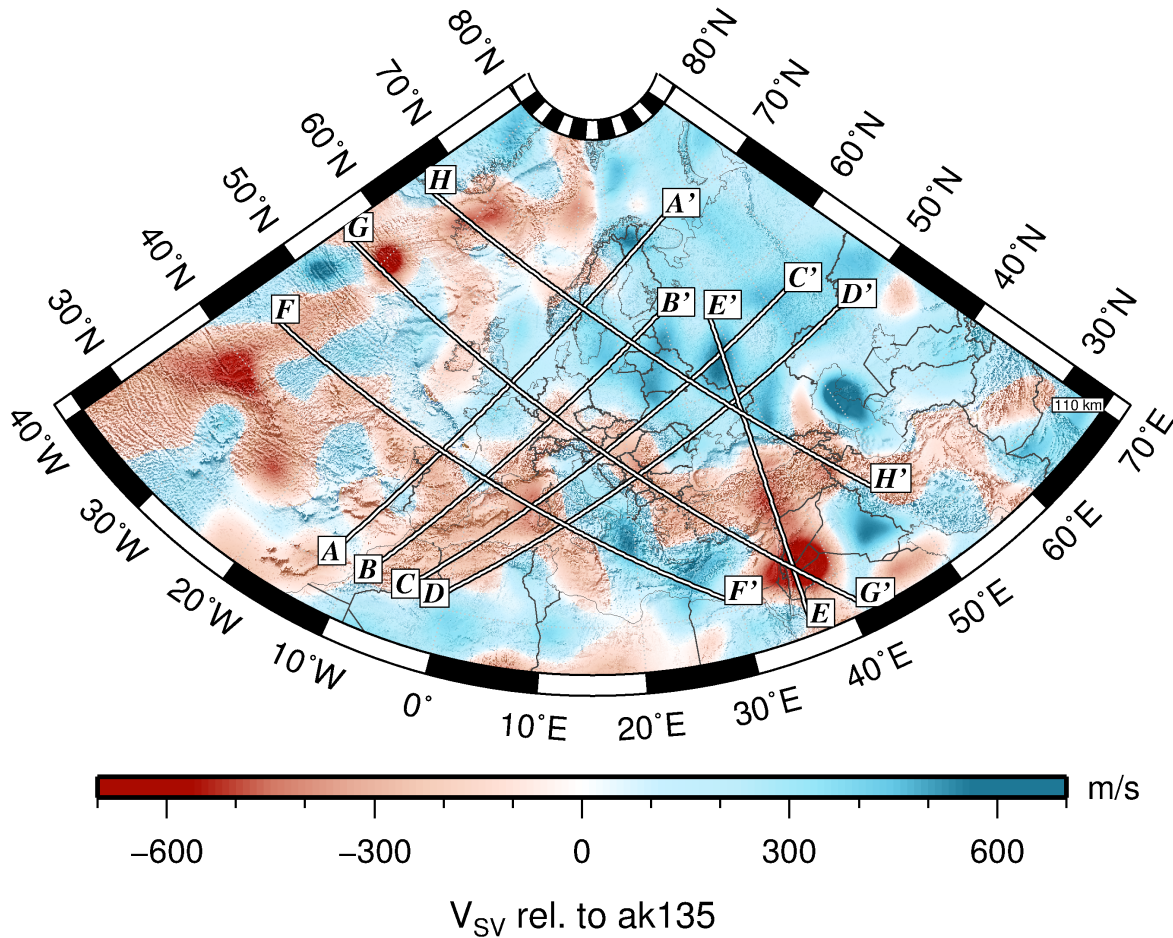


Fig. 2.2: map view of shear wave velocity model by Legendre et al. (2012) at 110 km depth. Lines A to H are the cross sections. The cross sections from A to H are plotted in figures 2.3 and 2.4, respectively.

modes (Dost, 1990) etc. These studies were limited to smaller regions due to substantial burden of manual processing.

Here I present some notable recent tomographic studies based upon surface waves.

Pilidou et al. (2005) presented a 3-D SV wave velocity isotropic and azimuthally anisotropic upper mantle model for the North Atlantic and surrounding regions derived from multi-mode Rayleigh wave seismograms. The resolution of their model is up to 400 kilometers. Fry et al. (2008) obtained a European Mediterranean tomographic phase velocity model with phase velocity measurements from various experiments e.g. MidSEA (van der Lee et al., 2001), SDSNet (Baer et al., 2000), TomoCH (Fry et al., 2005), and GRSN (Henger et al., 2002). Schivardi & Morelli (2009) presented a Rayleigh and Love wave model in the period range from 35 s to 150 s for European Mediterranean region using group velocities. Boschi et al. (2009) compiled a new shear wave velocity model of the upper mantle based upon surface wave measurements

obtained through the technique developed by Ekström et al. (1997). Schaefer et al. (2011) applied a grid search approach to surface wave tomography and obtained a new 3-D anisotropic European upper mantle model (FMADVOXEU), which is obtained from a joint inversion of various phases. Schaefer et al. (2011) used the data-set of Fry et al. (2008) as well as global data-set of Ekström et al. (1997). The data-set used by Boschi et al. (2009) is also the same as Schaefer et al. (2011) and there are similarities between these two models but latter offer increased resolution e.g. the Trans-European suture zone is clearly imaged in the models by Boschi et al. (2009); Pilidou et al. (2005). The model presented by Schaefer et al. (2011) able to detect more local structures e.g. narrow Cratonic keel underneath southern Finland Sandoval et al. (2004). Sandoval et al. (2004) found very deep lithosphere–asthenosphere boundary in southern Finland using body wave studies, this boundary was vague in the study by Pilidou et al. (2004). Legendre et al. (2012) contributed a shear wave velocity model of the European upper mantle with the help of automated inversion of seismic shear and surface wave waveforms. Their model is based upon AMI (Lebedev et al., 2005). In their model the parts of the waveforms that are in accordance with JWKB approximation (Dahlen & Tromp, 1998) are inverted with the help of sensitivity kernels. Zhu et al. (2012) presented a new European crustal and upper mantle model EU_{30} with the use of simultaneous wave form fitting of body and surface waves, In this way their technique is free from crustal corrections and claims higher resolution than the previous models. In addition to small scale features e.g. slabs, upwellings and delaminations which are present in most of the models some additional features are also present in the model by Zhu et al. (2012) e.g. fast seismic wave speeds beneath the Dinarides Mountains, which they interpret as a signature of subduction of Adria plate in north eastward direction. The low velocities in northern part of Rhine Graben act as a reservoir connected to Eifel hotspot. The lithosphere in the Scandinavia is delaminating and breaking away. Zhu & Tromp (2013) presented an isotropic shear wave and azimuthally anisotropic model EU_{60} for the Europe and north Atlantic ocean based upon adjoint seismic tomography. Palomeras et al. (2014) developed a 3-D shear wave model of the crust and upper mantle for western Mediterranean by using finite frequency Rayleigh wave tomography. Phase velocity measurements are performed with the help of two plane wave method developed by Forsyth & Li (2005). With the use of dense network in the study region with station spacing of ≤ 60 km, they claim higher resolution as compared to Legendre et al. (2012) and Zhu et al. (2012).

Due to higher resolution of the regional models as compared to global ones some features appear only in regional models e.g. Massif Central in France (Meschede & Romanowicz, 2015). There are similarities between these European models; these models are able to distinguish small features remarkably. Even in the lowest resolution models the east European Craton and North Atlantic ridge is well resolved. These features are present in global models as well. The small scale features in Europe e.g. Pannonian basin is overall similar as global models. The model presented by (Zhu & Tromp, 2013) possess very high resolution and small scale features are distinguished in

their models. The starting period of their maps is from 50 s. Therefore, all the above mentioned models discuss features related to upper mantle and deeper structure.

In order to obtain insight information about the distinct tectonic features of these European models, we took European shear wave velocity model by Legendre et al. (2012) which has very high resolution in upper 200 km beneath western and central Europe and the circum-Mediterranean. The resolution in Mediterranean region is very good but resolution of slab segments is poor as compared to local studies in the region (e.g. Giacomuzzi et al., 2012; Totaro et al., 2014). The shear wave velocity variation across the Europe at the depth of 110 km is shown in figure 2.2. We have plotted various cross sections based upon this model, which depicts interesting features in the region.

If we look at the map view shown in figure 2.2, the north and central Atlantic region is characterized by low velocities. These low velocity anomalies beneath the Mid-ocean ridge are reported by various tomographic studies (e.g. Helmberger et al., 1998; Mocquet et al., 1989; Pilidou et al., 2005; Shen et al., 1996, 2002; Silveira & Stutzmann, 2002). In order to see the details about the structure in this region we have made three cross sections (marked as F, G, H) covering south, central, and north Atlantic region, respectively.

The other profiles (A, B, C, D, E) runs from SW–S towards NW–NE. In the southern part they cover the regions of Iberia, the western Mediterranean, north Africa and EEC on northern side.

In the profile H–H' the low velocities in the Iceland area are due to Iceland plume. Legendre et al. (2012) concluded that the low velocities in the northwestern margin of EEC are due to erosion of the Cratonic mantle lithosphere by the hot asthenosphere in the region beneath the Scandes. The high velocities in the middle and eastern side of this profile (H–H') are due to thick Cratonic lithosphere. Along the eastern side of the profile H–H', the Turkish-Iranian plateau is located in the south of Zagros mountains, the low velocity anomaly in this region is due to shallow mantle lithosphere. These low velocity anomalies are also detected with surface wave tomography (Maggi & Priestley, 2005; Piromallo, 2003; Zor, 2008). The gravity studies in this region also suggest thin lithosphere (Ates et al., 1999; Barazangi et al., 2006). The high velocities at the depths greater than 200 km may be due to the detached Tethys slab from the Arabian plate (Zor, 2008).

On the profile G–G' mid oceanic ridge is characterized by low velocities indicating a shallow asthenosphere. The low velocities beneath Ireland makes this region distinct from the Western Europe. This region is considered as a part of North Atlantic Volcanic province (Arrowsmith et al., 2005). The WECML (Western European Continental mantle lithosphere) is characterized by high velocities; the lithosphere is thin in central Europe. There is the relation between thin lithosphere and Cenozoic volcanism pointed out by (e.g. Hoernle et al., 1995). Legendre et al. (2012) compiled the locations of Cenozoic anorogenic alkaline volcanism in central and Western Europe and the

circum-Mediterranean. They found that low velocities correlate well with Cenozoic volcanism in the area. The lower velocities in central Europe at deeper level (at the depth of around 300 km) are due to possible west European Plume.

The low velocities in the Pannonian basin may be due to upwelling of the asthenosphere (Horváth, 1993; Horváth et al., 2006). The high velocities at the depth around 300 km are due to deeper continuation of alpine slab (Dando et al., 2011). Further to the east of the profile G-G', the low velocities are due to shallow Anatolian asthenosphere. The Dynarides slab is visible at the depth of 150 km. The Cyprus region is characterized by high velocities as compared to neighboring regions. The Cyprus slab is imaged by the tomographic images by Bakırcı et al. (2012) as well.

On the profile F-F' the Pyrenees slab is visible in Pyrenees area located in southwest Europe bordering between Spain and France, The high velocity anomaly in the Pyrenees may be obduction related (Souriau et al., 2008), further east along the profile H-H' the low velocities are due to shallow western Mediterranean asthenosphere.

On the southern side of the profile E-E' the Middle East asthenosphere is characterized by low velocities. The Harrat lawa volcanic fields are the result of rifting and upwelling in Red Sea (Pallister et al., 2010). This region is considered as an area of widespread Cenozoic volcanism (Koulakov et al., 2015). Eastern Anatolian plateau is formed due to collision of Arabian and Eurasian plates. The east Anatolian plateau comprises widespread magmatic area with 2 km high topography. The crust is ~ 45 km (Zor, 2003). They argue that the plateau is not supported by thick crust but rather by the hot mantle. Very thin lithosphere is reported by Al-Lazki et al. (2004) as well. They found very slow mantle lid velocities (7.6–7.8 km/s), Gök (2003) observed S_n wave blockage and Maggi & Priestley (2005) found low S wave velocities. All these studies suggest the detached subducting Neo-Tethys oceanic lithosphere and hence the asthenosphere came direct into the contact with the bottom of the crust. Therefore, the high velocities at the depth greater than 250 km are due to this detached Neo-Tethys slab. Along the northern side of the profile the high velocities show thicker lithosphere of the east European Craton.

The low velocities along the profile A-A' are related to shallow oceanic lithosphere in central Atlantic. The lithosphere is shallow in the Iberian region (located in extreme south west of the Europe). The high velocity anomaly at the depth greater than 80 km is interpreted as Alboran slab. The delaminated lithosphere is detected by the P wave tomography model by Bartol & Govers (2014). The high velocities along the north of the profile are due to thick Cratonic lithosphere of EEC.

Along the profile B-B', the asthenosphere is shallow in the Iberia region. The high velocities at the depth around 80 km near Andorra region are interpreted as Pyrenees slab. Souriau et al. (2008) also found high velocities in this region. The asthenosphere is shallow in the central Europe and high velocities on northern side are due to thick lithosphere of EEC. The low velocities in the Western Europe are due to west European plume. The high velocities at the greater depth at the edge of east European Craton are

interpreted as cool downwellings caused by small scale convection (Knapmeyer-Endrun et al., 2013b).

Along C-C' profile the low velocities in western Mediterranean region are due to shallow asthenosphere. Chang et al. (2010); Dando et al. (2011) also reported low velocities in the eastern Pannonian and western Carpathian region. Tari et al. (1999) interpreted these low velocities as high heat flow associated with rifting process.

We observe a high velocity anomaly in mantle transition zone. Piromallo (2003); Wortel & Spakman (2000) also reported high velocities and interpreted as remnant oceanic slab subducted along the Carpathian arc. The high velocities on north of the profile C-C' are due to thick Cratonic structure of EEC.

On the profile D-D' the North Africa is characterized by low shear wave velocities. Calabrian slab is imaged at the depth larger than 100 km near the Calabrian arc. The low shear wave velocities in Tyrrhenian basin are related to hydrous asthenosphere (Greve et al., 2014) as water content plays important role in the shear wave velocity in the Tyrrhenian Sea. The high velocities in southern Apennines are due to its thick lithosphere. The high velocity anomaly below the Tyrrhenian Sea is Apennine slab. Further north of the profile D-D' the low shear wave velocities are due to shallow asthenosphere in the Pannonian basin.

2.4 Motivation

The inter-station method is widely used in regional networks and broadband arrays, (e.g., Adam & Lebedev, 2012; Beghein et al., 2010; Darbyshire & Lebedev, 2009; Deschamps et al., 2008; Endrun et al., 2004, 2008, 2011; Lebedev & Van Der Hilst, 2008; Lebedev et al., 2006, 2009, 2013; Meier et al., 2004; Yao et al., 2006). All these studies were limited to either small regions or time span of few years only due to time consuming manual selection of smooth parts of the phase velocity dispersion measurement.

Some notable previous applications include, Baja California region, central Europe or Ireland used 4, 17, 10, and 24 stations, respectively (Endrun et al., 2004; Polat et al., 2012; Roux et al., 2011; Zhang et al., 2007). Adam & Lebedev (2012) used inter-station method over an 112 temporary and two permanent stations in south Africa and measured very broad band 5 s to 250–400 s (Rayleigh) and 5 s to 100–250 s (Love) waves.

As there is a rapid growth in the number of seismic stations in recent past around the world, especially in the Europe. For example in Europe there were around 20 seismic stations in 1990 and at present there are more than 1000 seismic stations (see fig. 2.1 in Chapter 2). Therefore, in order to handle these large data volumes automated schemes are required.

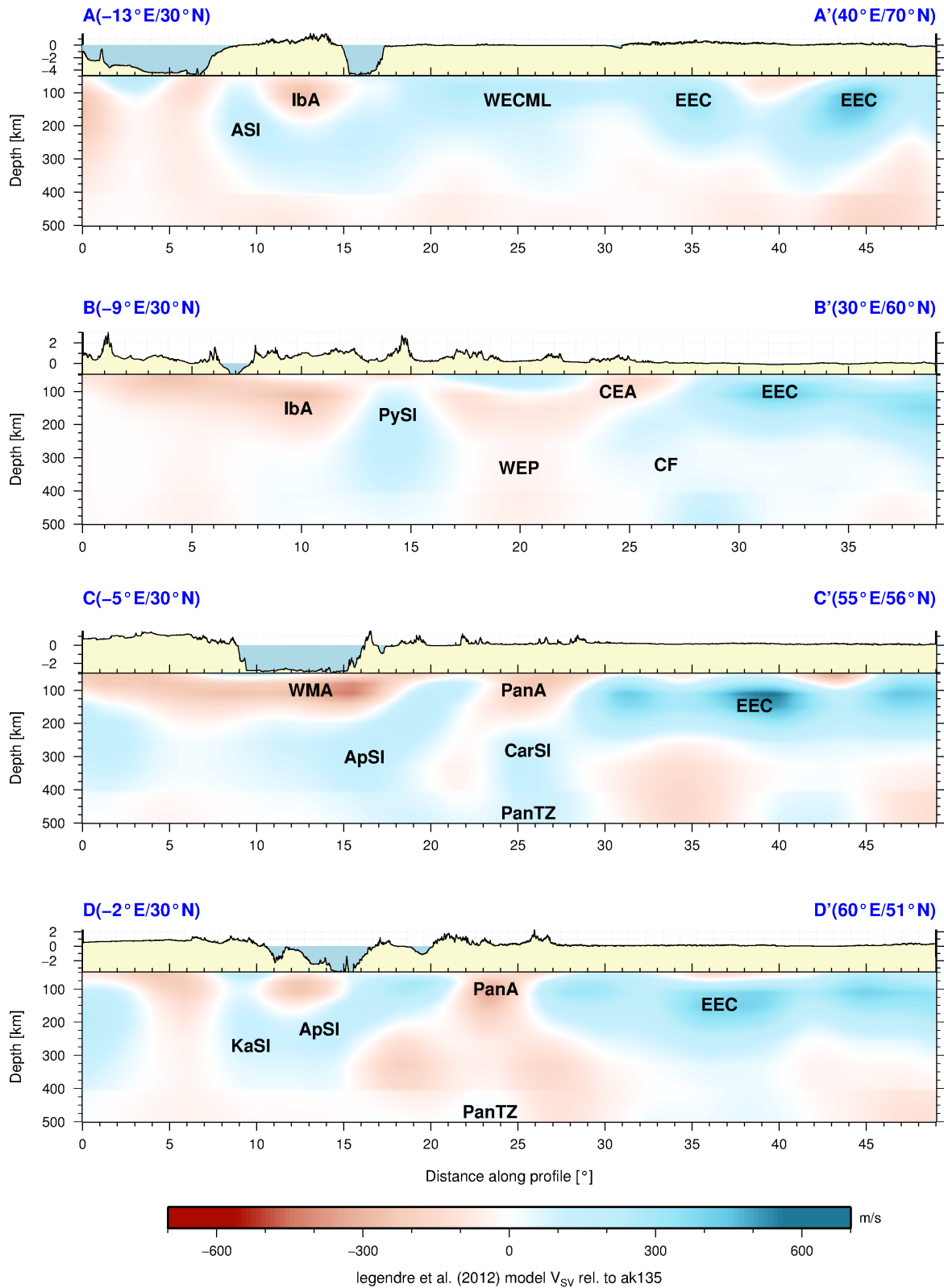


Fig. 2.3: Vertical cross sections from the shear wave velocity model by Legendre et al. (2012). Some notable tectonic features along section A to D (ApSI, Appenninic Slab; ASI, Alboran Slab; CarSI, Carpathian Slab; CEA, Central European Asthenosphere; CF, corner flow; EEC, East European Craton; KaSI, Kabylia Slab; MEP, Middle East Plume; PanA, Pannonian Asthenosphere; PanTZ, Pannonian Transition Zone; PySI, Pyrenean Slab; IbA Iberian Asthenosphere; WMA, Western Mediterranean Asthenosphere; WECML, West European Continental Mantle Lithosphere; WEP, West European Plume). The topography is plotted in yellow. (see text for the details about these tectonic features)

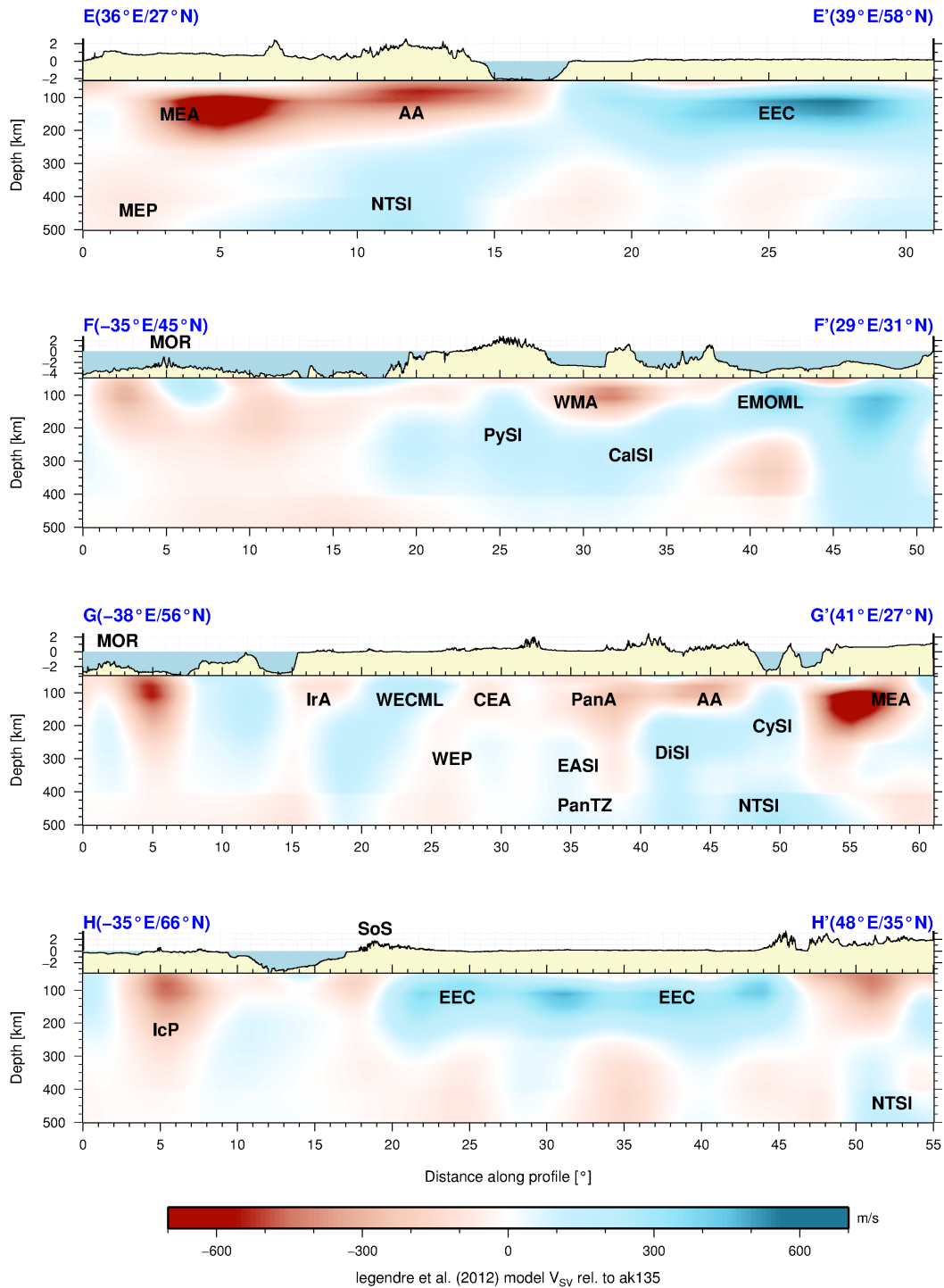


Fig. 2.4: Vertical cross sections from the shear wave velocity model by Legendre et al. (2012). Some notable tectonic features along the profile E-H (AA, Anatolian Asthenosphere; CalSl, Calabrian Slab; CEA, Central European Asthenosphere; CySl, Cyprus Slab; DiSl, Dinaridic Slab; EASl, East Alpine Slab; EEC, East European Craton; EMOML, Eastern Mediterranean Oceanic Mantle Lithosphere; IcP, Iceland Plume; IrA, Irish Asthenosphere; MEA, Middle East Asthenosphere; NTSI, Neo-Tethys Slab; PanA, Pannonian Asthenosphere; PanTZ, Pannonian Transition Zone; PySl, Pyrenaean Slab; SoS, Southern Scandes; WMA, Western Mediterranean Asthenosphere; WEP, West European Plume). The topography is plotted in yellow. (see text for the details about these tectonic features)

With the cross correlation based inter station method very broad band highly accurate phase velocity dispersion measurements for periods as low as 3 s in case of local networks (Endrun et al., 2004) to more than 250 s can be obtained. Therefore, the method provides complimentary information to ambient noise interferometry with the added advantage of long period information. These very broad band measurements are difficult to obtain with source based methods where short period information is difficult to obtain due to longer distance between source and receiver especially in the seismically quiet regions e.g. central Europe. In order to exploit the benefits and advantages of the inter-station method, an automated scheme was required. Another advantage of the automated schemes is that, the repeated measurements are possible which are difficult with time consuming manual operations. Therefore, different parameters can be tested easily. The big advantages come in the shape of consistent measurements which are difficult with manual operation. Therefore, keeping all these points in mind we have automated the inter-station method. We have applied the method to very large data-set of more than 1000 seismic stations and 1.37 million waveforms and have obtained high quality very broad band phase velocity measurements in the period range from as low as 8 s to more than 250 s for both Love and Rayleigh waves and have obtained high resolution tomographic image of the middle to lower crust, the mantle lithosphere as well as asthenosphere in central and northern Europe.

Chapter 3

This chapter is submitted to *Geophysical Journal International*

Geophys. J. Int. (0000) **000**, 1–1

Phase velocities of Rayleigh and Love waves in central and northern Europe from automated, broadband, inter-station measurements

R. A. Soomro¹, C. Weidle¹, L. Cristiano¹, S. Lebedev², T. Meier¹ and PASSEQ Working

¹ *Institute of Geosciences, Christian-Albrechts Universität Kiel, Otto-Hahn-Platz 1, 24118 Kiel, Germany,*

E-mail: soomro@geophysik.uni-kiel.de

² *Dublin Institute for Advanced Studies, School of Cosmic Physics, Geophysics Section, 5 Merrion Sq., Dublin 2, Ireland.*

³ *Member list is provided in acknowledgements.*

DRAFT version from: 3 July 2015

3.1 summary

The increasingly dense coverage of Europe with broadband seismic stations makes it possible to image its lithospheric structure in great detail, provided that structural information can be extracted effectively from the very large volumes of data. We develop an automated technique for the measurement of inter-station phase velocities of the fundamental-mode surface waves in very broad period ranges. We then apply the technique to all available broad-band data from permanent and temporary networks across Europe. In a new implementation of the classical two-station method, Rayleigh and Love dispersion curves are determined by cross-correlation of seismograms from a pair of stations. An elaborate filtering and windowing scheme is employed to enhance the target signal and makes possible a significantly broader frequency band of the measurements, compared to previous implementations of the method. In the time domain, frequency-dependent tapers are applied to cross-correlation functions of the waveforms to optimize the time-frequency resolution. The selection of acceptable phase

velocity measurements for each event is performed in the frequency domain, based on a number of fine-tuned quality criteria including a smoothness requirement. Between 5 and 3000 single-event dispersion measurements are averaged per inter-station path in order to obtain robust, broad-band dispersion curves with error estimates. In total, around 63000 Rayleigh- and 27500 Love-wave dispersion curves between 10 s and 350 s have been determined, with standard deviations lower than 2 % and standard errors lower than 0.5 %. Comparisons of phase-velocity measurements using events at opposite back-azimuths and the examination of the variance of the phase velocity curves are parts of the selection process. As a by-product of the quality control procedures, we present maps for permanent and temporary broad-band stations in Central Europe indicating possible instrumental problems at some of the stations.

The roughness often seen in the measured phase velocity curves is due to noise, interference of the fundamental and higher modes, or scattering of the fundamental modes. This can cause substantial errors, and we exclude the rough curves and curve segments systematically using smoothness criteria. Comparing the average interstation dispersion curves obtained with different degrees of smoothness enforced, we find that rough perturbations do not normally bias the average dispersion measurement systematically, especially at inter-station distances larger than about 300 km. It is concluded that rough perturbations in the dispersion measurements can be treated as random, in the sense that they do not bias phase velocities systematically towards greater values (They do need to be removed, however, in order to reduce random errors of the measurements).

Using our large new dataset, we construct phase-velocity maps for central and northern Europe. According to checkerboard tests, the lateral resolution in central Europe is ≤ 150 km. Comparison of regional surface-wave tomography with independent data on sediment thickness in North-German Basin and Polish Trough (from a compilation of deep seismic sounding (DSS) results) confirms the accuracy of the imaging using our short-period, phase-velocity measurements. At longer periods, the structure of the lithosphere and asthenosphere around the Trans-European Suture Zone (TESZ) is seen clearly. The region of the Tornquist-Teisseyre Zone (TTZ) is associated with a stronger lateral contrast in the lithospheric thickness from the East European Platform (EEP) towards the southwest compared to the region across the Sorgenfrei-Tornquist Zone (STZ). The new, broad-band, phase-velocity dataset offers abundant, valuable information on the structure of the crust and upper mantle beneath Europe.

3.2 Introduction

The rapid growth of seismic networks in western and central Europe has produced dense coverage of the entire region with broadband stations (Fig. 3.1). The improving coverage makes it possible to map the lithospheric structure of Europe with increasingly high resolution (e.g. Legendre et al., 2012; Yang et al., 2007; Zhu et al., 2012).

Phase velocities of the fundamental Rayleigh and Love surface-wave modes are essential observables for the study of the Earth's lithosphere and sub-lithospheric mantle. In the period range 5 – 300 they are sensitive to the structure of the crust, mantle lithosphere and asthenosphere (e.g. Aki & Richards, 1980; Ben-Menahem & Singh, 1981; Dahlen & Tromp, 1998; Laske et al., 2011). In order to maximize the resolution, we wish to obtain highly accurate measurements in broad period ranges and to utilize as much data as is available. Given the large data volumes, full automation of the measurements is thus highly desirable.

In this paper we present an automated technique for the measurement of phase velocities of the fundamental-mode surface waves in very broad period ranges and an application of the technique to a very large volume of data from across Europe. Phase-velocity maps computed with the new data show detailed lateral structural variations. We test the resolution of the images both with standard resolution tests and by means of comparisons with tectonic boundaries and sediment thickness data.

Phase velocities of Rayleigh waves depend primarily on the velocity of vertically polarized S-waves, but also on density and P-wave velocity. Love-wave phase velocities depend mainly on the velocity of horizontally polarized S waves and on density. The dispersive nature of surface waves (Gutenberg, 1924) is caused by the increasing sensitivity of the waves at longer periods to deeper structure within the Earth, with an additional effect from the sphericity of the Earth (Alterman et al., 1961). Main characteristics of Rayleigh-wave dispersion curves include a phase-velocity increase from about 2 km/s to 3 km/s at short periods below 10 s to about 4 km/s at intermediate periods (20 - 50 s), reflecting the velocity increase across the Moho (Fig. 3.2, bottom right). Another strong increase, to more than 5 km/s, occurs at periods longer than 100 s. The strong sensitivity of Rayleigh-wave phase velocities to the Moho depth and their weaker but measurable sensitivity to the lithosphere-asthenosphere boundary depth have been analyzed and discussed by, e.g., Bartsch et al. (2011); Lebedev et al. (2013). In these studies it was concluded that highly accurate phase velocity measurements with errors well below 1 % are needed in order to resolve the essential details of the S-wave velocity structure of the crust and upper mantle.

Love-wave phase velocities are higher than Rayleigh-wave phase velocities for periods lower than about 120 s and show a steadier increase with period (see, e.g., Section 3.2). The latter property is related to the less focussed depth sensitivity of Love compared to Rayleigh waves: for Love waves, the sensitivity at greater depths increases with increasing periods but the sensitivity to a specific depth range is less pronounced compared to Rayleigh waves (e.g. Dahlen & Tromp, 1998; Lebedev et al., 2013). At very long periods Love-wave phase velocities are normally lower than Rayleigh-wave phase velocities.

Early systematic surface-wave measurements were carried out as single-station measurements of their group velocities by Gutenberg (1924) and Ewing & Press (1950), with group traveltimes from the source to stations estimated as a function of period in the time domain. Time-frequency analysis for single-station group-traveltime measure-

ments was introduced by Landisman et al. (1969). It was improved and used extensively in the following decades (e.g. Levshin et al., 1989; Ritzwoller & Levshin, 1998; Vdovin et al., 1999). Recent examples of single-station measurements are given by Lebedev et al. (2006), based on waveform inversion, and by Foster et al. (2014). Single-station measurements yield phase or group velocities along the entire source-station paths and are affected by errors in the source location and the source mechanism, as pointed out, e.g., by Muyzert & Snieder (1996) and Levshin et al. (1999).

In order to minimize errors due to the event location and source mechanism uncertainties, Brilliant & Ewing (1954) measured, in the time domain, Rayleigh-wave phase differences between stations. This eliminated the phase shifts due to the source mechanism and due to the propagation of the fundamental modes from the source to the first of the stations. In order to diminish the influence of the source on phase velocity measurements, Toksöz & Ben-Menahem (1963) measured phase velocities in the frequency domain using successive passages of surface waves at a single station. McEvelly (1964) measured the phase difference between two stations in the frequency domain for both Love and Rayleigh waves and discovered the so called Love-Rayleigh discrepancy (caused by radial anisotropy, i.e., the difference in the velocities of horizontally and vertically polarized S-waves). With the two-station method, distant sources may be used to study the average local structure between stations in the region under consideration. The influence of the unknown (or uncertain) source parameters is minimized and the problem of the 2π ambiguity of phase velocity measurements is diminished because of the relatively small inter-station distances, compared to epicentral distances in single-station measurements.

Over the last decade, inter-station phase velocity measurements have been widely performed using stations of broadband arrays and regional networks (e.g. Adam & Lebedev, 2012; Agius & Lebedev, 2013; Beghein et al., 2010; Darbyshire & Lebedev, 2009; Deschamps et al., 2008; Endrun et al., 2004, 2008, 2011; Lebedev et al., 2006, 2009; Meier et al., 2004; Prindle & Tanimoto, 2006; Yao et al., 2006; Yoshizawa & Ekström, 2010). The inter-station dispersion measurements can yield phase-velocity curves in a very broad frequency band. For regional networks (station spacing on the order of 100 km) the period range may span from below 10 s to 200-400 s. Lebedev et al. (2006) compared the inter-station phase velocity measurements made using cross-correlation with those computed from single-station measurements. In general, the bandwidth of the dispersion curves is broader for the inter-station cross-correlation measurements, in particular at higher frequencies. Inter-station phase velocities from single-station measurements are complementary, extending the bandwidth towards lower frequencies. Using local networks with finer station spacing (on the order of 10 km), phase velocities may be obtained for periods as low as 3 s (Endrun et al., 2004).

Inter-station group or phase velocities may also be determined from cross correlation of ambient noise or of the coda of surface waves excited by earthquakes (e.g. Campillo & Paul, 2003; Shapiro & Campillo, 2004; Shapiro et al., 2005; Yang et al., 2007). An

advantage of the ambient noise cross correlation is the independence from earthquake sources of seismic waves. Inhomogeneous distributions of seismic events or ambient noise sources may introduce a bias, which can be estimated and corrected, to an extent (Paul et al., 2005; Roux et al., 2005; Yao et al., 2006). There is a considerable overlap of the period ranges investigated using the cross-correlation of ambient noise (about 5 s to 50 s, in regional-scale applications) and the cross-correlation of earthquake data (from 5-10 s to 400 s, in regional to global applications). Phase velocities calculated from cross correlations of ambient noise and of earthquake waveforms yield complementary information and may be jointly inverted for three-dimensional S-wave velocity structure (e.g. Köhler et al., 2012; Yang et al., 2008; Yao et al., 2006).

It has been shown that lateral heterogeneity may lead to considerable perturbations in single-event inter-station phase-velocity measurements (Forsyth & Li, 2005; Friederich et al., 1994; Maupin, 2011; Pedersen et al., 2013, 2006; Wielandt, 1993). In order to overcome this problem the propagation direction in the region under consideration may be measured, as has been suggested already by Press (1956). Several algorithms have been proposed for single-event array analysis, including the f-k analysis based on the assumption of a plane wave (e.g. Capon, 1970; Maupin, 2011; Sun & Helmberger, 2011), the approximation of the incoming wavefield by two interfering plane waves Forsyth & Li (2005) or the determination of local phase velocities from phase as well as amplitude measurements using the Helmholtz equation and allowing for curved wavefronts (Friederich et al., 1994). Prindle & Tanimoto (2006) measured the propagation direction from particle motion analysis in order to correct inter-station measurements and Foster et al. (2014) extended the single-station approach including a correction of the propagation direction, estimated from densely spaced mini-arrays.

An alternative approach to suppress the errors due to off-path propagation is the rejection of perturbed inter-station phase velocity measurements and the averaging of many single-event measurements. Using sensitivity kernels for two-station measurements, De Vos et al. (2013) showed that averaging of single-event measurements from events on both sides of the station pair decreases the influence of the structure off the inter-station path. However, some sensitivity to strong off-path lateral heterogeneity still remains. Because of the strong frequency dependence of the diffraction effects, they normally result in roughness of phase velocity curves. Consistent rejection of such perturbed (non-smooth) portions of phase-velocity curves and the averaging over many single-event measurements has been shown to yield smooth and reliable inter-station phase velocities, provided that (1) suitably elaborate signal-processing techniques are applied (see Section 2.1), (2) noisy and unreliable measurements are consistently rejected, and (3) measurements are averaged for many events, from both propagation directions when possible (Meier et al., 2004). Investigating sensitivity kernels for two-station measurements.

The distribution of permanent and temporary broad-band stations in Europe is highly uneven (Fig. 3.1). Furthermore, the instrumentation, the time of deployment and also the quality of the stations are heterogeneous. Array methods can only be applied

to sub-regions and limited time periods. Inter-station measurements, in contrast, are well suited to determine phase velocities of fundamental modes for the entire, very large available data volumes (Yang et al., 2007). Previous applications of broadband inter-station cross-correlation measurements of phase velocities using earthquake signals have been limited to relatively small regions, due to the substantial burden of the manual data processing. Typical applications in the Baja California region, central Europe or Ireland, for example, used 17, 10, and 24 stations, respectively (Polat et al., 2012; Roux et al., 2011; Zhang et al., 2007). Here, we present an automated processing scheme designed to obtain smooth, path-average fundamental mode dispersion curves using large data sets recorded by permanent and temporary stations. The main elements of the scheme include (1) a solution for the 2π ambiguity, (2) the automated determination of the frequency range of reliable measurements, (3) the identification of smooth segments of the dispersion curve and the rejection of rough perturbations, (4) the detection of quality problems caused by wrong response information or timing problems, and (5) the rejection of outliers.

The advantages of automated processing are the consistency in the determination of phase velocities and the option to repeat the processing with different parameter sets, for example, in order to examine the influence of rough phase-velocity perturbations on path-average dispersion curves. In this study, broad-band inter-station Rayleigh and Love phase velocities are determined for Europe. Their quality is evaluated statistically and by the analysis of the phase velocity maps computed using the new measurements. Our new measurements using the heterogeneous European data set offer new insight into the potential of surface wave tomography, in the region and beyond.

3.3 Method

3.3.1 Cross-correlation measurement of phase velocities

In inter-station measurements the phase difference of Rayleigh or Love waves propagating nearly along the great circle path between two considered stations, is measured on the vertical or transverse component, respectively. The Fourier transform of the fundamental mode waveform $u_0(t)$ may be expressed as

$$U_0(\omega) = |U_0(\omega)| \exp(i\phi_0(\omega)) \approx |U_0(\omega)| \exp(-i \int_0^\Delta k(\omega, s) ds) \quad (3.1)$$

where $\phi_0(\omega)$ is the phase spectrum of the fundamental mode, $k(\omega, s)$ is the frequency dependent wavenumber along the path and Δ the epicentral distance. An estimate of the path average wavenumber, $k(\omega)$, or the average phase velocity, $c(\omega)$, may then be obtained simply from the phase $\phi(\omega)$ of the spectral ratio between the Fourier

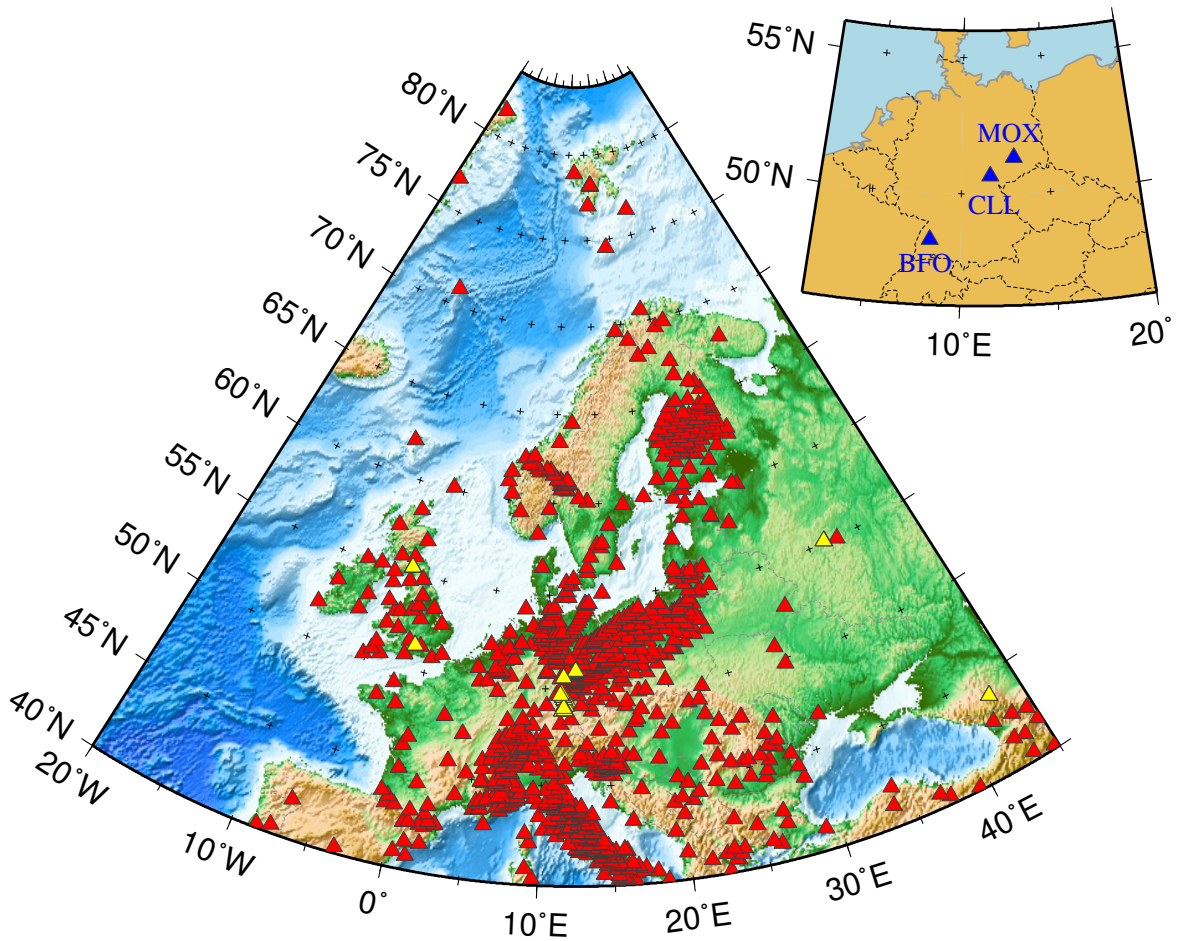


Fig. 3.1: Seismic station coverage in Europe. Triangles indicate permanent and temporary stations that provide data since before 1990 (yellow) and after 1990 (red). Top right: the stations of the German Regional Seismic Network (GRSN) used to illustrate the measurements below.

transforms of the fundamental mode waveforms recorded at the station closer to the epicenter $U_{01}(\omega)$ and the more distant station $U_{02}(\omega)$ because of

$$\frac{U_{01}(\omega)}{U_{02}(\omega)} = \frac{|U_{01}(\omega)|}{|U_{02}(\omega)|} \exp(i\phi(\omega)) \quad (3.2)$$

with

$$\phi(\omega) = \phi_{01}(\omega) - \phi_{02}(\omega) \approx k(\omega)(\Delta_2 - \Delta_1) \quad (3.3)$$

and

$$c(\omega) \approx \frac{\omega(\Delta_2 - \Delta_1)}{\phi(\omega) + 2n\pi} \quad (3.4)$$

where $\phi_{01}(\omega)$ and $\phi_{02}(\omega)$ are the phase spectra of the fundamental modes at stations 1 and 2, respectively and Δ_1 and Δ_2 are the epicentral distances for station 1 and station 2, respectively.

Because of the ambiguity in the phase, the correct n has to be determined by comparison with phase velocities for a background model at a reference frequency that is decreasing with increasing inter-station distance (here it is chosen to vary linearly between 0.02 Hz at 400 km and 0.0083 Hz at 3000 km inter-station distance).

We note that there are two sources of errors in the estimation of the phase velocity according to eq. (4). The first results from deviations of the fundamental mode propagation from a ray theoretical approximation and the second results from errors in the estimation of the phase difference between the fundamental modes. As has already been pointed out by Wielandt et al. (1987) and Prindle & Tanimoto (2006), the spectral ratio method gives poor estimates of the inter-station phase difference if it is determined from spectral ratio of the waveforms recorded at the two stations. This is because the spectrum of the waveform is also influenced by the spectra of higher modes $U_j(\omega), j > 1$, and noise $N(\omega)$:

$$U(\omega) = U_0(\omega) + \sum_j U_j(\omega) + N(\omega). \quad (3.5)$$

Therefore, Kulesh et al. (2005); Laske et al. (2011); Levshin et al. (1989) apply time-frequency analysis, the wavelet transform or a multi-taper technique, respectively in order to isolate the contribution from the fundamental mode in the time-frequency domain before calculating the spectral ratio. In the time-frequency domain, $u(\omega_n, t)$, higher modes are separated from the fundamental mode. The higher modes may therefore be downweighted in order to obtain a cleaned time-frequency representation $u_w(\omega_n, t)$ that contains only the contribution of the fundamental mode and some noise

$$u_w(\omega_n, t) \approx u_0(\omega_n, t) + n(\omega_n, t). \quad (3.6)$$

From the cleaned time-frequency representations the spectral ratio may be determined in order to estimate the phase $\phi_w(\omega_n)$:

$$\frac{U_{w1}(\omega_n)}{U_{w2}(\omega_n)} = \frac{|U_{w1}(\omega_n)|}{|U_{w2}(\omega_n)|} \exp(i\phi_w(\omega_n)). \quad (3.7)$$

This is a much better approximation of the phase difference of the fundamental modes than the spectral ratio of the unprocessed waveforms, although it may be perturbed by noise.

Alternatively to eqn. (2), the phase difference of the fundamental modes may be determined from the cross correlation of fundamental mode waveforms $\rho_0(t)$:

$$F\{\rho_0(t)\} = |U_{01}(\omega)| |U_{02}(\omega)| \exp(i\phi(\omega)). \quad (3.8)$$

where $\phi(\omega)$ is the same as in eqn. (3). The cross-correlation function (CCF) calculated from waveforms, $\rho(t)$, is not affected by uncorrelated noise and the contribution of the fundamental mode to the CCF is enhanced because of the product of the amplitude spectra and the large amplitudes of the fundamental mode. Time-frequency analysis may be performed after the cross correlation in order to obtain $\rho(\omega_n, t)$. Again, windowing is applied (Laske & Masters, 1996; Meier et al., 2004; Wielandt et al., 1987) in order to downweight cross correlations between the fundamental mode and higher modes and between higher modes. This results in $\rho_w(\omega_n, t)$. Time windows may be positioned around the maximum of the filtered cross-correlation function (Meier et al., 2004) in order to isolate the contribution of the fundamental mode. By this procedure the contribution of higher modes and uncorrelated noise is strongly reduced and the filtered and weighted cross-correlation function (CCF) of the seismograms $\rho_w(\omega_n, t)$ is approximately equal to the filtered and weighted CCF of the fundamental modes $\rho_0(\omega_n, t)$:

$$\rho_w(\omega_n, t) \approx \rho_0(\omega_n, t). \quad (3.9)$$

The phase difference between the fundamental modes may then be determined from the phase of the filtered and weighted CCF, $\phi_{\text{CCF}}(\omega_n)$, in the frequency domain: for each ω_n a Fourier transform is applied to $\rho_w(\omega_n, t)$ before measuring the phase at the frequency ω_n . The phase difference between the fundamental modes at the two stations is then determined according to:

$$\phi_{\text{CCF}}(\omega_n) \approx \phi_{02}(\omega_n) - \phi_{01}(\omega_n). \quad (3.10)$$

In our implementation, we apply Gaussian filters

$$F(\omega, \omega_n) = \exp(-\alpha_f (\frac{\omega}{\omega_n} - 1)^2) \quad (3.11)$$

with a width of the Gaussian filter that depends linearly on frequency: $\alpha_f = \gamma_f^2 \omega_n \Delta t$ in order to optimize the time-frequency resolution where the parameter γ_f is chosen

usually between 12 and 20 (here 16) and Δt is the sampling interval in the time domain. Windowing in the time domain is easy after the cross correlation because dispersion is diminished compared to the original seismogram, narrower windows may be applied, and the window is easier to position. We apply Gaussian windows $w(t)$ in the time domain according to:

$$w(t) = \exp(-\omega_n^2(t - t_{\max})^2 / (4\alpha_w)) \quad (3.12)$$

where t_{\max} is the time of the maximum amplitude of the CCF after filtering and the width of the Gaussian window is again a linear function of frequency: $\alpha_w = \gamma_w^2 \omega_n \Delta t$. Because the dispersion is stronger for longer inter-station paths the parameter γ_w varies linearly so that it is 20 for 400 km inter-station distance and 50 for 3000 km inter-station distance. It has been pointed out by Laske & Masters (1996); Meier et al. (2004) that a careful selection of the frequency range in which the phase velocity measurement is accepted has to be performed. This becomes obvious by comparing the two examples in Figs. 3.2 and 3.3. The left panel in Fig. 3.2 shows the time series at the two stations and the corresponding amplitude of the time-frequency representation where the group arrival of the fundamental mode Rayleigh wave clearly emerges as a ridge across the time-frequency map. Cross correlation of the two waveforms (top right) reduces the dispersion strongly. The phase $\phi(\omega_n)$ is extracted from the complex spectrum of the band-passed and weighted CCF in the frequency domain (bottom right), and we get a bundle of candidate phase velocity curves (blue lines) due to the inherent 2π ambiguity of the phase measurement. In manual processing, the analyst would have to pick the correct branch, in this example easily identified by the proximity of one branch to a background model, and select a frequency band in which the measurement is acceptable (red segment).

The strength of the cross correlation technique becomes evident when looking at the higher frequencies in this example. Both waveforms are strongly scattered at frequencies above ca. 60 mHz, a typical observation reflecting heterogeneities in crustal structure along the wave-propagation path. However, the CCF shows that these scattered waves are highly correlated between the two stations, implying that scattering must have primarily occurred outside of the inter station path at distant heterogeneity. The scattered wavefields propagate still approximately on the same great circle path as the direct wave-front. It is thus possible, despite scattered signals, to determine a consistent phase velocity well above 60 mHz.

In contrast, the waveforms in Fig. 3.3 are less consistent. As the wavefield at both stations is already quite disturbed, with no clear group arrival in the time-frequency map, it is not possible to determine a smooth dispersion curve from the phase of the CCF. Although one branch falls close to our background model, it is rather bumpy and shows rough perturbations around the expected, smooth dispersion curve. This is indicative of an inconsistent phase of the CCF across the frequency range of the measurement. Obviously, this may occur due to strong noise, interference of different modes or when scattered wavefields are not as well correlated as in Fig. 3.2, leading to

strong variations in spectral amplitude across frequencies and larger uncertainties in the phase determination.

As illustrated by these examples, an automated procedure for the selection of phase velocity curves must be able to identify the correct branch (the correct n) and select smooth segments of the curve that are in an acceptable distance to a background model. The automated procedure allows us then to process and measure large datasets not only consistently but also repeatedly with varying selection constraints, in order to assess the influence of rough perturbations on path-average phase velocity curves.

3.3.2 Automated selection of individual phase velocity curves

Due to the broad depth span of the fundamental mode depth sensitivity kernels (the Fréchet derivatives of phase velocity with respect to shear wave speed as a function of depth) and due to the gradual changes of these kernels with frequency (e.g. Dahlen & Tromp, 1998), smooth dispersion curves are expected for any realistic one-dimensional (1-D) Earth models. In an automated inter-station method, we thus wish to select the smooth parts of an observed dispersion curve while rejecting those parts that exceed a certain level of roughness.

We introduce a set of criteria to automatically select smooth parts of the phase velocity dispersion curves which are illustrated in Fig. 3.4 and formulated as follows:

1. *Background model criterion*

In the first step, we need to select the correct 2π branch on which the measurement should be performed. As can be seen in the examples in Figs. 3.2 and 3.3, the branches are strongly diverging with decreasing frequency and identification of the desired 2π branch is thus straightforward by comparing the branches at intermediate to lower frequencies to a reference dispersion curve. However, as phase jumps may occur across the frequency band, we also test neighboring curves as they may fulfill the criterion at higher frequencies and in case of segments overlapping with respect to frequency the segment close to the reference model is considered. After identification of the desired 2π branch, we apply our first selection criterion, which is defined by the difference of the measured curve from a path-specific background model:

$$\left| \frac{c(\omega_i) - c_o(\omega_i)}{c_o(\omega_i)} \right| \times 100\% < th_{\Delta C}, \quad (3.13)$$

where $th_{\Delta C}$ is the maximum deviation from the background model in percent, $c_o(\omega_i)$ is the phase velocity for the background model, and $c(\omega_i)$ is the measured phase velocity at every sample ω_i in the frequency domain.

Segments of the curve that exceed the defined threshold are rejected (blue segment in Fig. 3.4). Note that we reject also a number of frequency samples before and

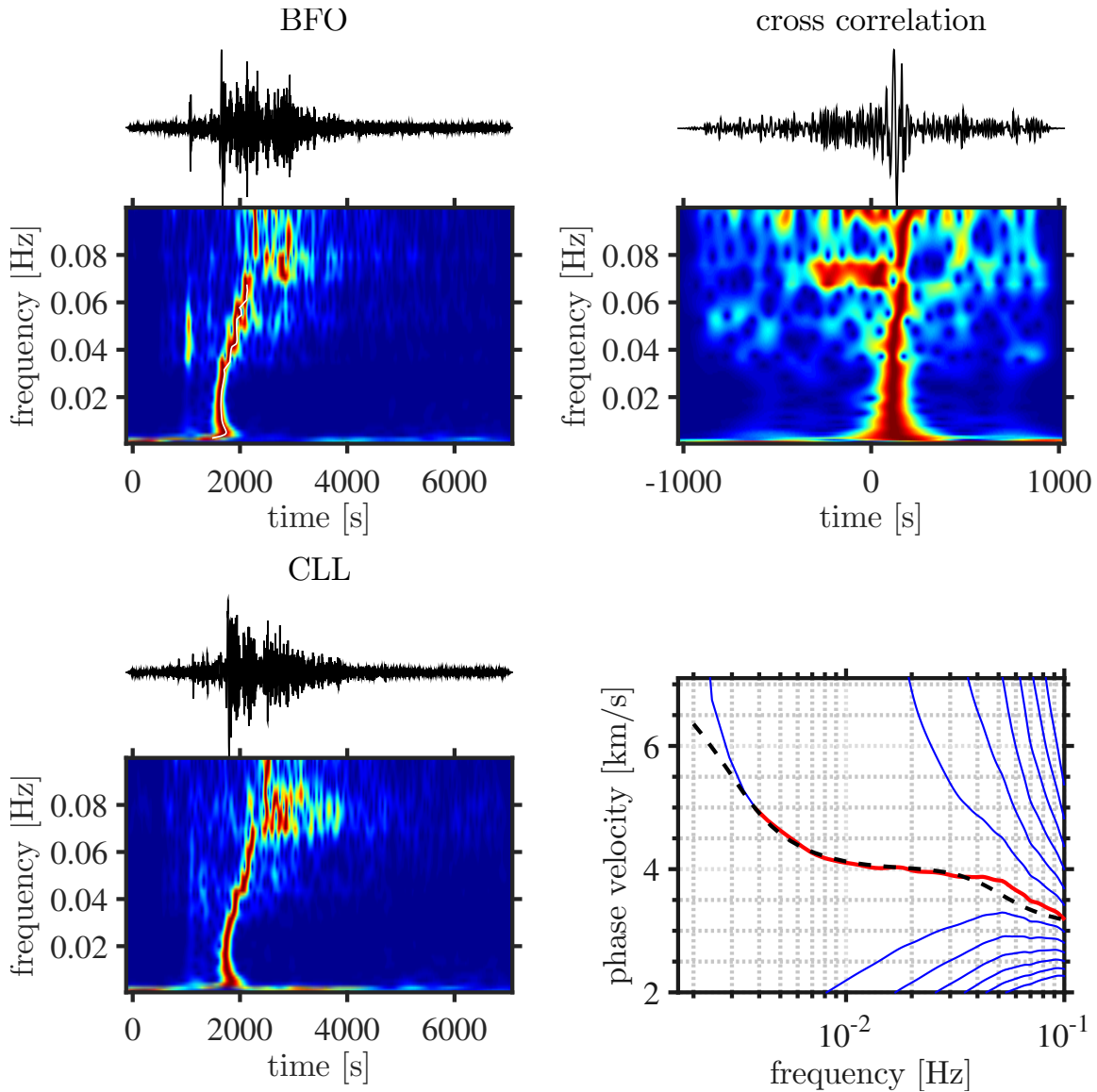


Fig. 3.2: Example of an inter-station, phase-velocity measurement for the station pair BFO (Black Forest Observatory, Germany) and CLL (Collmberg, Germany) (see Fig. 3.1 for station locations.). The 2-hour long seismograms and the time-frequency representations of their waveforms are shown in the left panels. Top right: the cross correlation function and its time-frequency representation. Bottom right: the 2π ambiguous phase velocity curves (blue lines), plotted together with the reference model (black dashed); red line: the manually selected portion of the curve that is accepted as the dispersion measurement.

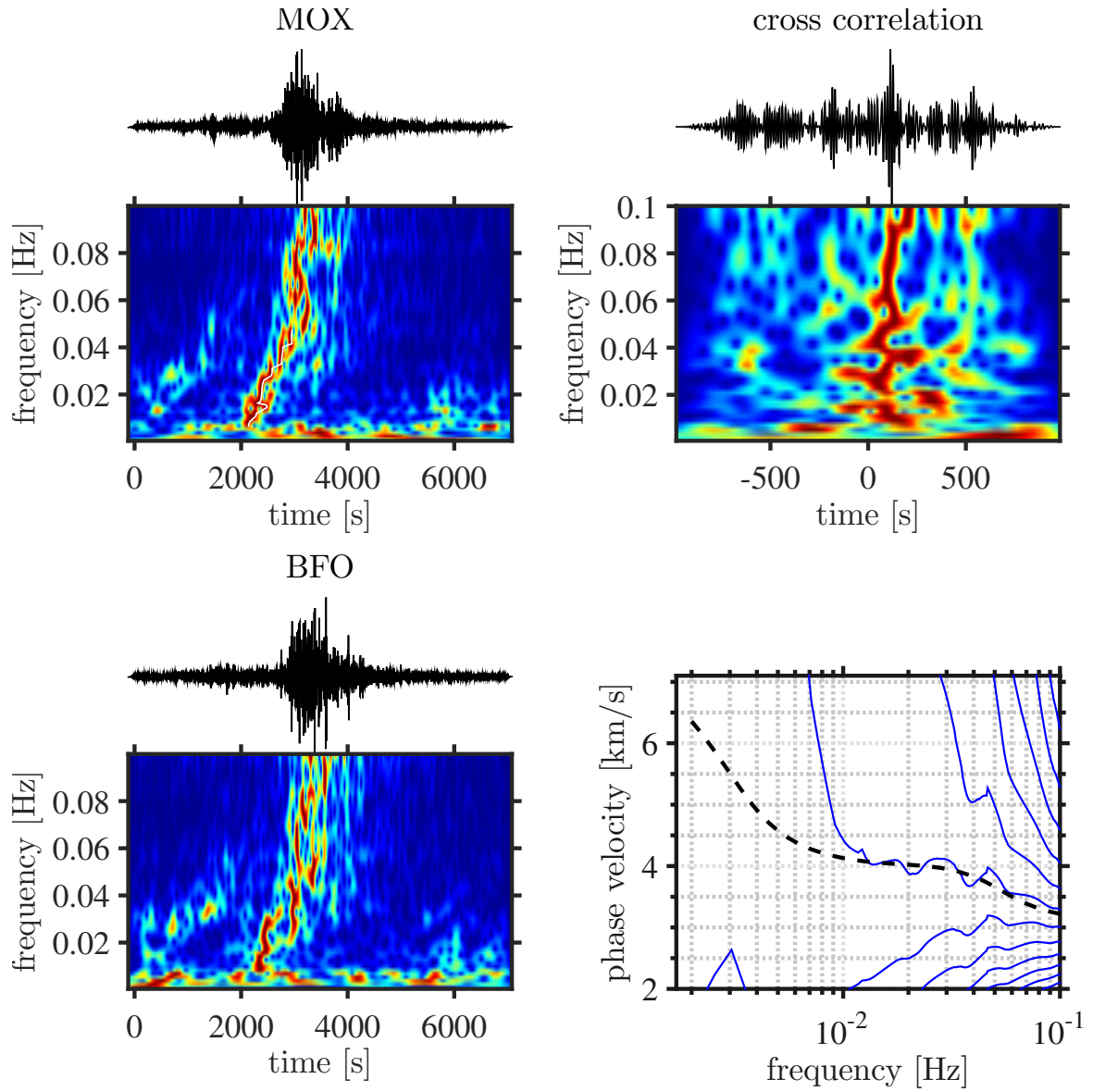
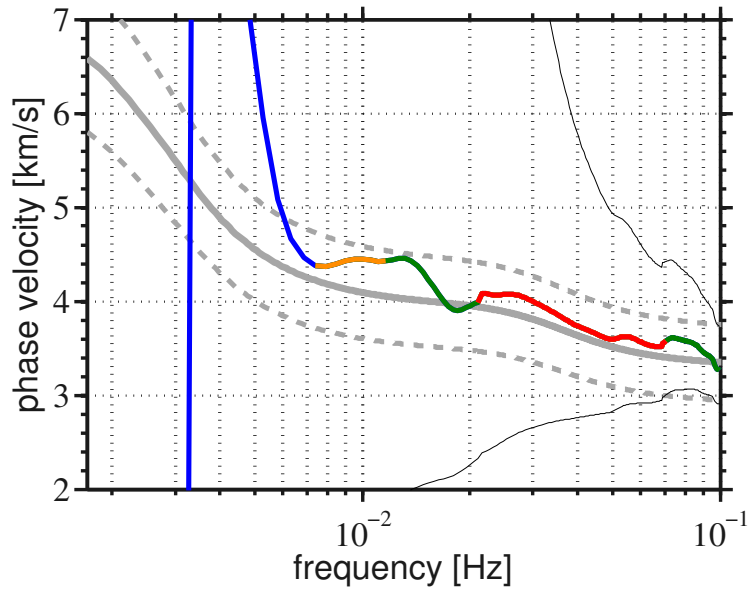
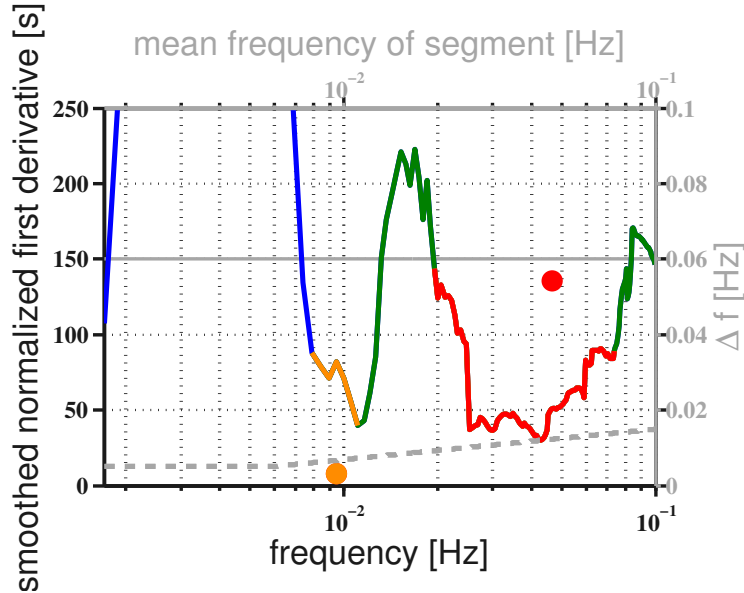


Fig. 3.3: An example of a noisy inter-station measurement of phase velocity for the station pair MOX (Moxa, Germany) and CLL (Collmberg, Germany) (Locations in Fig. 3.1). Plotting conventions are as in Fig. 3.2.



(a) Phase-velocity difference from the background model prediction. Grey lines show the dispersion curve computed for a background model (solid) and the maximum deviation thresholds (dashed), thin black lines are 2π ambiguous curves that are not processed and the multi-coloured curve is the processed phase-velocity curve.



(b) Smoothness and length criteria. Grey lines indicate the thresholds given by the smoothness (solid, left y-axis) and length (dashed, right y-axis) criteria. The multi-coloured curve is the "smoothness curve" (eqn. 3.14). The large dots show the measures of the length of the same-colored curve segments, computed for the application of the length criterion, plotted at the mean frequency of the segment.

Fig. 3.4: Application of the selection criteria for automated dispersion measurements.

after a violating segment, to account for the finite resolution of the measurements in the frequency domain.

Although a global 1-D model would be sufficient for branch identification, we apply path-specific reference models, which we calculate - for each station pair - as path averages through a 3-D model composed of CRUST2.0 (Bassin et al., 2000) and PREM (Dziewonski & Anderson, 1981). These models take into account the first order structural variations to which surface wave dispersion are strongly sensitive, primarily Moho depth or the presence of sedimentary basins along the inter-station path. These path-averaged models proved to be sufficient to define one globally valid parameter set in our routines.

The choice of the threshold parameter influences many of the individual measurements, and we shall discuss the parameter choice and the sensitivity of the automated measurements to it in detail in section 3.4.1. In general, we prefer to keep this parameter as "loose" as possible, so as to account for sufficient variation from our reference models and to avoid a bias of the measurements towards them.

2. *Smoothness criterion*

While criterion (i) is designed to be relatively loose, we introduce a stricter second criterion to enforce a desired degree of smoothness on the accepted measurements. We quantify the roughness of the curve by calculating the first derivative of phase velocity with respect to frequency $c'(\omega)$, and compare it with the corresponding value of the background model, $c'_o(\omega)$:

$$S(\omega_i) = \sum_{\omega_j=\omega_i-d(\omega_i)}^{\omega_i+d(\omega_i)} \left| \frac{c'(\omega_j) - c'_o(\omega_j)}{c_o(\omega_j)} \right| < th_S, \quad (3.14)$$

where th_S is, again, a constant threshold. A typical value of this threshold is 150 s for both Love and Rayleigh waves.

We perform a summation of the first derivative deviation from the reference model over a moving window in the frequency domain. The absolute value is taken so that positive as well as negative deviations are treated equally. The frequency range of the summation, $2d(\omega_i)$, is increasing linearly with frequency, to account for the stronger variability of the phase velocities at lower frequencies. Therefore, a frequency independent threshold can be applied. We note also that this empirical criterion is sensitive to the length of the cross correlation function in the time domain as a longer time series decreases the sampling rate in the frequency domain and the summation in eqn. 3.14 is carried out over an increased number of frequency samples. The length of the cross correlation is varied linearly with inter-station distance, such that it is 1000 s for an inter-station distance of 400 km and 2000 s for an inter-station distance of 3000 km. As the sampling interval in the frequency domain decreases with increasing length of the CCF in the time domain, the summation in eqn. 3.14 is carried out over an increased

number of samples. That means the criterion becomes more sensitive for larger distances as required because the smoothness of the phase velocity curve increases with increasing inter-station distance. Therefore, the threshold is independent of frequency and inter-station distance and is easy to apply. Again, we reject a number of samples before and after a violating segment as can be seen by the green segments in Fig. 3.4.

3. *Length criterion*

The routine may select any number of smooth segments of the phase velocity curve with variable length. Very short segments, however, are of little use and are typically determined with less confidence, particularly at higher frequencies where fluctuations in the dispersion curves may be larger due to greater heterogeneities in the crust. In order to avoid segments too short, we apply the length criterion. This is frequency dependent, relaxed at lower frequencies and more strict at higher frequencies (Fig 3.4b). The length of the accepted segments has to be greater than the threshold $th_{\Delta\omega}$: where ω_m is the center frequency of the segment. Typical values are $a = 0.0088$ Hz, $b = 0.0524$ Hz, and $minthresholdvalue = 1/200$ Hz . These values have been determined empirically.

With increasing inter-station distance the ambiguity in the phase velocity due to cycle skipping is increasing. Therefore, an upper frequency limit of the phase velocity curve is chosen such that the difference between neighboring phase velocity curves is larger than a certain threshold which is large enough to overcome the problem.

In the example in Fig. 3.4 two segments have passed the first two criteria, a short segment starting at 7 mHz (orange) and a long segment starting at 20 mHz (red). While the first segment falls below the threshold of the length criterion, the second one passes the criterion and is accepted as a dispersion curve measurement between 20 and 70mHz.

3.3.3 Automatic averaging of inter-station phase velocities

After measuring all available data for a given station pair, we obtain a bundle of measurements, as in the example shown in Fig. 3.5a,b for the station pair BFO-CLL of the German Regional Seismic Network (GRSN). In this example 20 years of data, in total 476 events, were processed (Fig. 3.5a), resulting in 368 acceptable dispersion curves. Obviously, the measurements are highly mutually consistent, although with relatively greater variability at frequencies below 60 mHz. We note that the measurements for the two different propagation directions (black and red curves) are highly consistent: the red curves cover the black curves nearly fully. To obtain a robust inter-station curve from this bundle of measurements we need to average the single-event curves and assess the measurement quality statistically.

In that process we apply the following conditions and selection steps: (1) outliers are rejected (here, the 10 % outermost values are rejected), (2) at each frequency a minimum number of measurements (here, 5) is required, (3) the mean phase velocity and standard deviation are calculated separately for the two directions and if the phase velocity difference for the two directions exceeds a threshold (here, the maximum standard deviation of the two directions) the measurement is rejected at the corresponding frequency, (4) the standard deviation of all measurements should be smaller than a certain threshold (here, 3%), and (5) finally the length criterion as explained in section 3.3.2 is also applied to the resulting average curve.

Fig. 3.5c,d shows the remaining curves after the application of this secondary selection procedure. The remaining curves are highly mutually consistent and yield a final path-average phase velocity measurement with low standard deviation (Fig. 3.5f).

3.3.4 Loose vs. conservative parameter settings

Naturally, the choice of parameters and thresholds is an essential step in fine tuning the method for application to a large data set. Out of the three criteria, the smoothness criterion turns out to be the most sensitive to the measurement quality. If we relax the smoothness criterion, the bandwidth will increase, the smoothness of the curve will decrease and the standard deviation may also increase. Therefore, there is a trade-off between maximum bandwidth, least standard deviation and smoothness. The first criterion, the limit on the difference with the background model, has only a minor influence compared to the smoothness constraint. The effect of the length criterion is obvious.

We illustrate the effects of varying smoothness parameters by comparing a "loose" (250s) and "conservative" (150s) parameter setting. The effect becomes clear in Fig. 3.4b where the green segments of the curve would be accepted or rejected in the "loose" or "conservative" parameter sets. Clearly, the "loose" setting finds rougher curves acceptable.

Fig. 3.5 shows a comparison of all measurements for the station pair BFO-CLL located in Germany using both parameter settings. Although the rejection rates are not very different, the total bundle of curves (Fig. 3.5a,b) appears much broader and rougher in the "loose" setting. Fig. 3.5c,d shows the resulting curves after removing outliers, now the curve bundle is smoother as compared to Fig. 3.5a,b. The difference in average dispersion curve between "loose" and "conservative" setting is small (Fig. 3.5f) but a slightly increased standard deviation of the measurements persists in the "loose" setting, as expected. However, the final measurement, the averaged dispersion curve is almost identical in both parameter settings (3.5f) indicating that reasonable selection parameters can be determined with few tests only. A more detailed analysis of the effect of "loose" and "conservative" setting is discussed in detail in sec 3.4.1

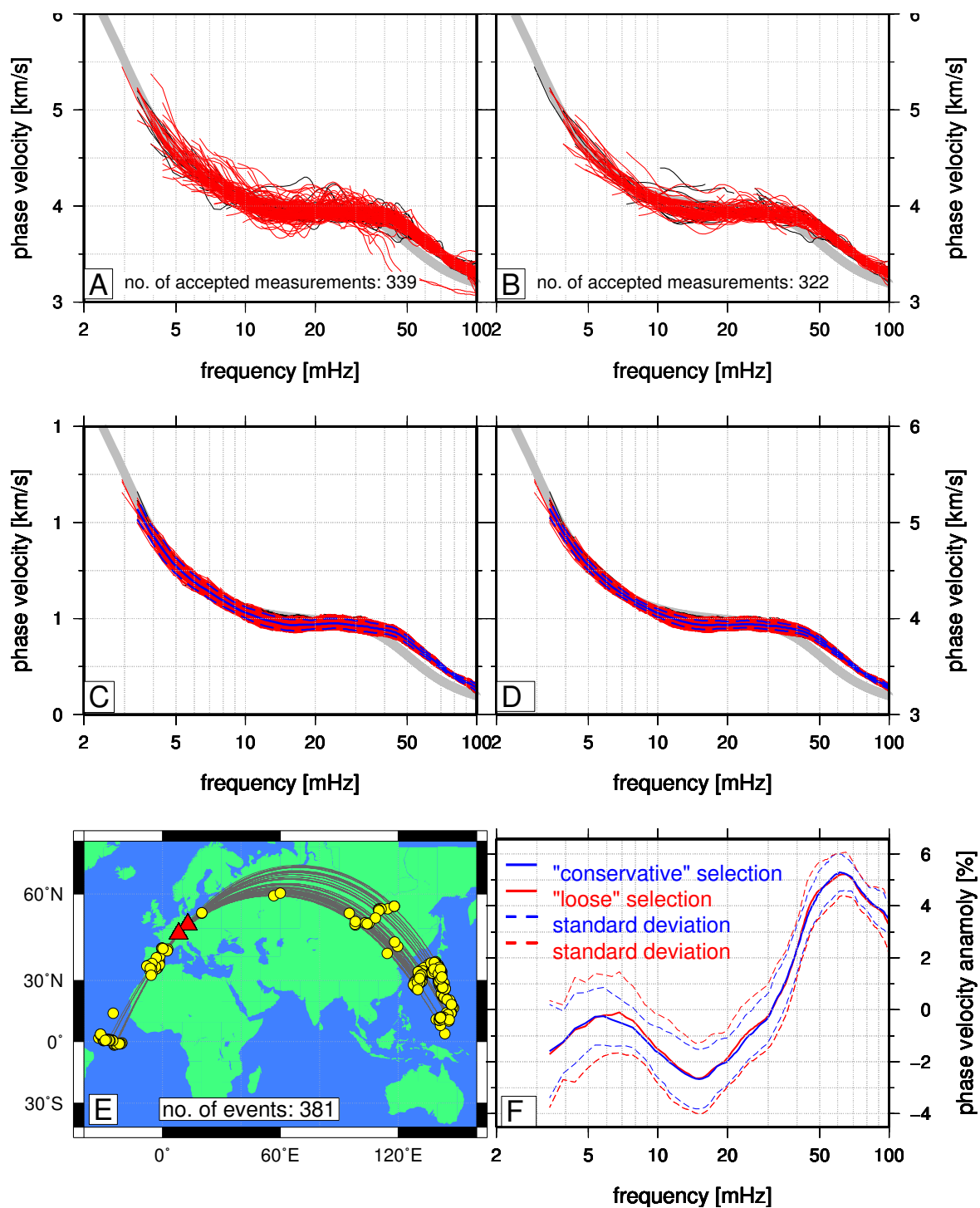


Fig. 3.5: Automatic averaging of individual dispersion measurements for station path BFO-CLL for a "loose" (a,c) and "conservative" (b,d) set of measurement parameters. (a,b) all selected individual measurements. (c,d) average dispersion curve and standard deviation after outlier rejection. (e) map of station locations (triangles) and processed events (circles) for this station pair. (f) perturbation of average curves from background model for "loose" (red) and "conservative" (blue) parameters and their standard deviations.

3.4 Application to central and northern Europe

We applied the method to a large data-set recorded by 1073 seismic stations in and around Europe (Fig. 3.1, 3.6). We used the EHB (Engdahl et al., 1998) when available and NEIC catalogues and searched for suitable events from January 1990 to October 2013. For each station pair with an inter-station distance between 1° and 30° , we conduct a search in the catalogue for all events that (1) are at a back-azimuth within 7° of the great circle defined by the station pair, (2) have an epicentral distance between 5° and 120° , and (3) have a maximum depth of 100 km. Furthermore, the minimum magnitude of the events is a linear function of epicentral distance. It varies between magnitude 4 at 5° and 6 at 120° . The maximum magnitude of 8 for the selected events has been chosen.

We retrieve waveform data through the European Integrated Data Archive (EIDA) infrastructure. An automated routine based on ObsPy (Beyreuther et al., 2010) is used to request approximately 4.6 million waveforms through the Arlink interface of WebDC (<http://www.webdc.eu>) for a total of 364.939 station pairs.

Of all requests, we retrieved around 1.37 million waveforms and performed more than 12 million inter-station measurements with acceptable measurements for 164231 station pairs for Rayleigh waves and 133736 station pairs for Love waves. As a result, we have obtained 1.6 million acceptable individual (single-event) and 63000 inter-station average phase-velocity curves for Rayleigh waves and ca. 1.3 million individual and 27500 inter-station average curves for Love waves.

The number of processed events per station pair (Fig. 3.6b) is greater for station pairs with a NE to SE azimuth, owing to the high event rates in East Asia. For paths with a more northerly azimuth, there are significantly fewer events, with moderate event rates in eastern Mediterranean and the northeastern Pacific. Another factor that is seen here is that most of the older seismic stations are located in Central Europe, covering a larger portion of the total time span of the data-set. When applying our automated dispersion measurement procedure to the data-set, on average, 1/4 of the measurements per inter-station path are accepted (Fig. 3.6c). Typically, this amounts to around 200 - 400 measurements for station pairs with older stations in continental Europe, and around 20-30 for more recently or temporarily installed stations (Fig. 3.6d).

3.4.1 Quality Control

The advantages of the automated processing are its consistency and the possibility to study the influence of different parameters on the final average phase velocity curves. To assess the effect of different parameter sets on the final measurements of our entire data-set, we compare differences between two parameter sets with a "loose" and a tighter "conservative" setting, with smoothness parameters of 250 s and 150 s, respectively. In

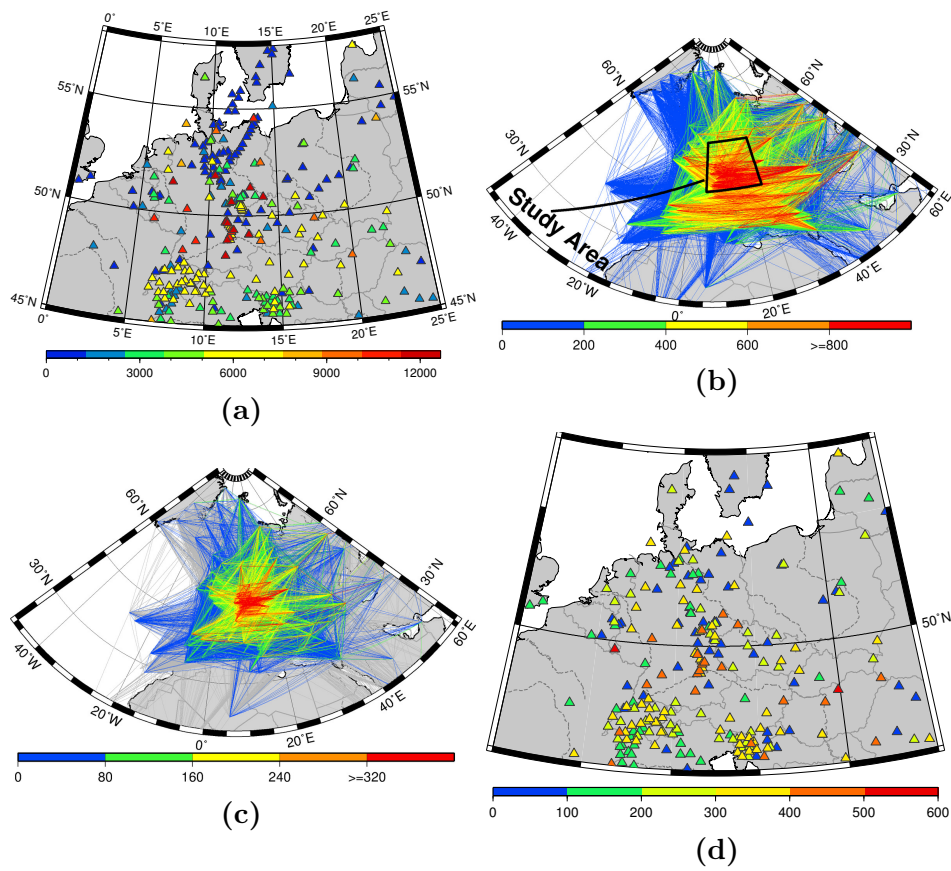


Fig. 3.6: Overview of processed data and retrieved measurements.

Fig. 3.7 we compare the difference between "loose" and "conservative" selection for all final average dispersion measurements of the entire data-set, for both Rayleigh and Love waves in three frequency bands. Tables 3.1 and 3.2 compare statistical parameters of these distributions. This comparison illustrates the influence of rough perturbations in the individual phase velocity curves on the average phase velocity curve. The influence of random noise is expected to cancel out during averaging. The influence of higher modes, however, may bias the phase velocity towards higher velocities. Also, deviations of nearly plane waves from the expected propagation directions may cause a positive bias of the average phase velocity. Large deviations of surface-wave rays from the predicted great-circle direction—around 20° —are observed (e.g. Weidle et al., 2010), but these phenomena affect only a specific frequency range, for example around 20-40 s when the wave-front is deflected by strong variations in the crustal structure or the Moho depth. Such effects are reflected by distinct "bumps" in the individual phase velocity measurements that are usually rejected by our selection criteria. By comparing wave-fronts propagating in both directions between stations of a given station pair, strong wave-front deviations are easily detectable, because the waves propagate through different tectonic settings between the sources and the stations.

Furthermore, the approximation of the wave-front by a plane wave may be insufficient (e.g. Bodin & Maupin, 2008; Cotte et al., 2000; Forsyth & Li, 2005; Friederich et al., 2000; Pedersen et al., 2006; Wielandt, 1993) leading to frequency dependent perturbation in the phase velocities that may bias the phase velocities towards larger or smaller values. Since most of these different perturbations are expected to cause rough perturbations in the phase velocity, the proposed automated processing is well suited to test if they bias the results towards higher velocities.

Therefore, we expect that the "loose" setting might lead to "faster" measurements, as more deflected and scattered waves pass our measurement acceptance criteria. In a statistical sense, when we compare distributions of velocity differences "loose" – "conservative", the distributions should thus tend to positive values, both in the mean and the skewness. Figure 3.7 shows this comparison and the statistical parameters are summarized in Tables 3.1, 3.2. To assess potential effects at different frequency ranges, we calculate the distributions in three frequency bands. Most importantly, from Fig. 3.7 and Tables 3.1, 3.2, it becomes obvious that the average value as well as the most likely value do not change significantly between the two selections.

For Rayleigh waves the mean difference is slightly but insignificantly positive with a maximum velocity deviation of 0.05%. Only for the intermediate period Love waves the mean is slightly higher (0.091%). Standard deviations are overall on the order of 0.5%, slightly elevated for long-period Love waves where number of data and measurement quality is poorest. The skewness values tend to slightly positive values, implying more positive outliers in the velocity differences. The kurtosis of all distributions is positive and > 3 . A kurtosis of 3 is expected for a normal distribution. The large values of the kurtosis reflect the overall peak-like character of the distributions and imply rather few larger outliers beyond the standard deviation. The difference in kurtosis between 10-25s

Table 3.1: statistical parameters of the distribution shown in Fig. 3.7a (Rayleigh waves).

<i>period</i>	<i>mean</i>	<i>std</i>	<i>var</i>	<i>skewness</i>	<i>kurtosis</i>
100-200s	0.048	0.49	0.24	1.86	53.47
25-100s	0.044	0.28	0.08	2.24	46.63
10-25s	0.049	0.52	0.27	-0.08	4.86

Table 3.2: statistical parameters of distribution shown in Fig. 3.7b (Love waves).

<i>period</i>	<i>mean</i>	<i>std</i>	<i>var</i>	<i>skewness</i>	<i>kurtosis</i>
100-200s	0.008	1.10	1.21	2.72	38.26
25-100s	0.091	0.63	0.40	5.34	98.98
10-25s	-0.007	0.58	0.34	-0.06	9.36

and 25-100s Love waves - where the distributions in Fig. 3.7 are rather similar - is explained by larger outliers in the 25-100s period range. The distribution for 100-200s Love waves is significantly different as only approximately half the number of data are available as compared to the lower period bands (ca. 3500 vs. ca. 7000). The distribution of the difference between the "loose" and "conservative" selection implies thus in conclusion that the variability we measure is due to data noise and rather random perturbations in the phase velocities caused by complicated wavefields.

When we compare a potential bias in the phase velocity measurements as a function of inter-station distance (Fig. 3.8) we note that the bias is, as seen before, very small particularly at inter-station distances larger than approx. 300 km. At short distances, a bias may be present but on average not larger than around 0.5% for both Rayleigh and Love waves. We may conclude that the bias due to rough perturbations is smaller than expected. But it is necessary to reject rough perturbations as they can introduce significant positive or negative errors in the average phase velocity curves. The consistent selection and averaging of individual phase velocities is an efficient tool to obtain reliable phase velocity measurements. We note that numerical modeling is needed to quantify a possible bias of the average phase velocity curve by smooth perturbations in the individual curves that are similar for both propagation directions. Such perturbations are possible but not likely as they require strong but smooth lateral heterogeneity that varies only slightly with depth. We thus prefer the 'conservative' setting (smoothness parameter 150 s) which results in an overall improved standard deviation.

The data quality is not only affected by noise and complexities in the wavefield, but also by (1) incorrect response information, (2) timing problems, and (3) wrong polarities (polarity switch). The automated evaluation of the average deviation from the background model and the comparison of average phase velocities for both directions, allow us to detect stations with such data quality problems (Weidle et al., 2013).

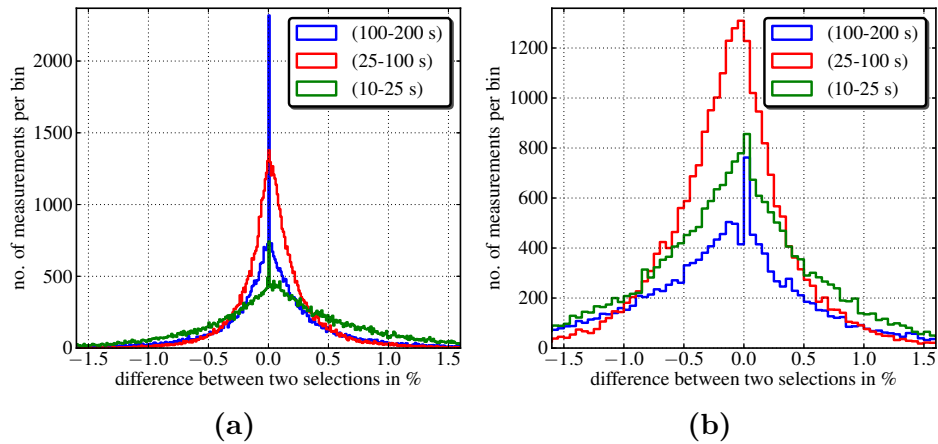


Fig. 3.7: Differences in phase-velocity measurements for the entire data-set obtained with a "loose" (250 s) and a "conservative" (150 s) roughness threshold used in data selection.

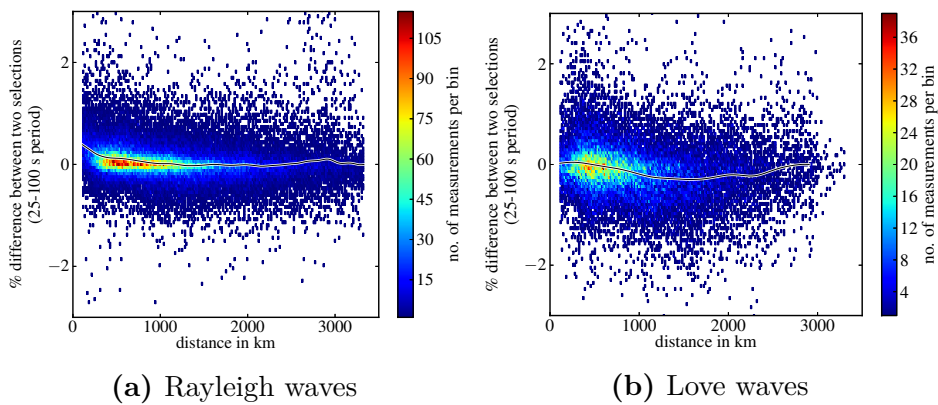


Fig. 3.8: Difference in average inter-station phase velocities between "loose" and "conservative" parameter sets as function of distance.

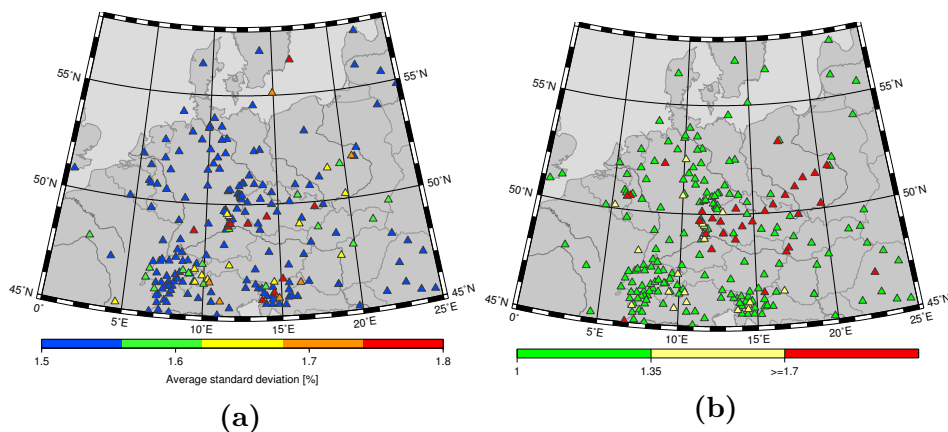


Fig. 3.9: Average standard deviation (a) and difference between two propagation directions (b) per station, averaged over all frequencies.

This is illustrated in Fig. 3.9 where we show the average standard deviation of all measurements per station and the frequency-averaged difference of velocity measurements in two directions. Large values in either of these maps are mere indicators of potential data quality problems, e.g. a difference in the velocities measured in two propagation directions can be related to an incorrect station response information (see Weidle et al., 2013, for details).

3.4.2 Phase velocities

When we compare all measurements processed in the entire data set it becomes clear that, overall, Rayleigh wave dispersion curves may be automatically measured using cross-correlation down to frequencies of around 3 mHz, while for the Love waves most measurements have a low frequency bound at around 8-10 mHz (Fig. 3.10) close to the cross-over frequency of Love and Rayleigh phase velocities. We get most measurements in the frequencies between around 10-60 mHz, with fewer acceptable data at higher frequencies due to stronger scattering from crustal heterogeneities. It is also notable that for Love waves the spread of the measured curves at high frequencies increases, while for Rayleigh waves the width of the curve bundle is more constant over the entire frequency range. Some of the reasons for these findings are: (1) the measurements may be perturbed by interference of higher order Love modes with the fundamental one at about 12.5-16.6 mHz (60-80 seconds). (2) At this frequency, the transverse component is also influenced by Rayleigh waves in case of lateral heterogeneity and anisotropy. Perturbations of the measured Love-wave phase velocity at this frequency are therefore likely and the number of Love wave phase velocities at periods larger than about 60 to 80 s is strongly reduced. (3) In addition, the noise on the horizontal components is generally higher in amplitude than on the verticals. In total, the amount of Love wave measurements is only about 1/5 of the number of Rayleigh wave measurements.

In Fig. 3.11 we show the 2-D histograms of the standard deviation and standard error of all the measurements in the data-set as a function of inter-station distance. For the standard deviation they show the expected decrease of the standard deviation with inter-station distance. This is readily explained because according to eqn. (4) a small error in the phase measurement ϵ will result in a phase-velocity error ϵ_c that amounts to $\epsilon_c = \frac{\omega(\Delta_1 - \Delta_2)}{\zeta(\omega)} \cdot \frac{-\epsilon}{\zeta(\omega) + \epsilon}$, where $\zeta(\omega)$ is the unwrapped (absolute) phase and thus much larger than ϵ . As the unwrapped phase increases with increasing inter-station distance, i.e. more 2π cycles are added to the phase, the second term and hence the phase velocity error, decreases.

In general, we find standard deviations of $< 2\%$ for inter-station distances of and below a few hundred kilometers, decreasing to $< 1\%$ for paths longer than about 1000 km, both for Rayleigh and Love waves. Given the large number of measurements, the standard error (the standard deviation of the mean) is much lower, indicating an overall uncertainty in the estimated mean phase velocities of $< 0.3\%$ and $< 0.5\%$ for Rayleigh and Love waves, respectively.

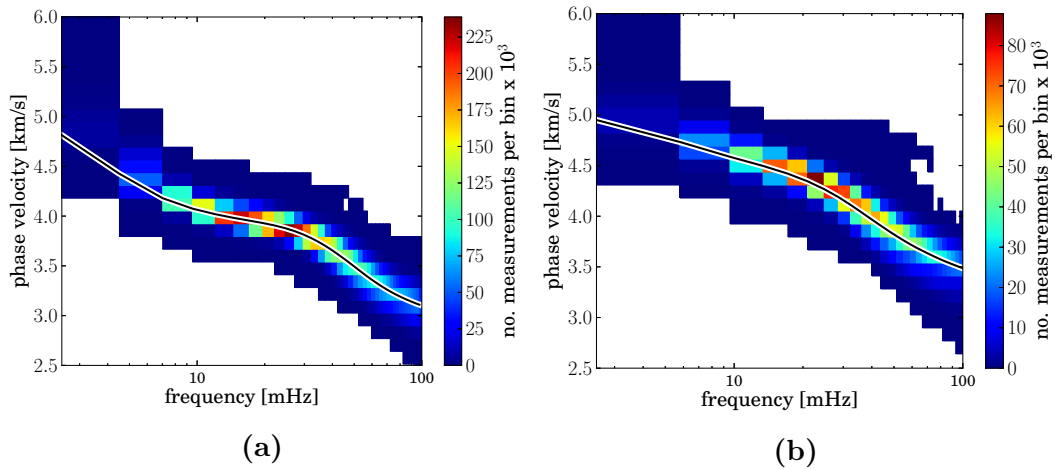


Fig. 3.10: 2-D histograms of all automatically measured phase velocity curves of the entire data-set for Rayleigh (a) and Love (b) waves. Shown are all individual curves after outlier rejection in the averaging step.

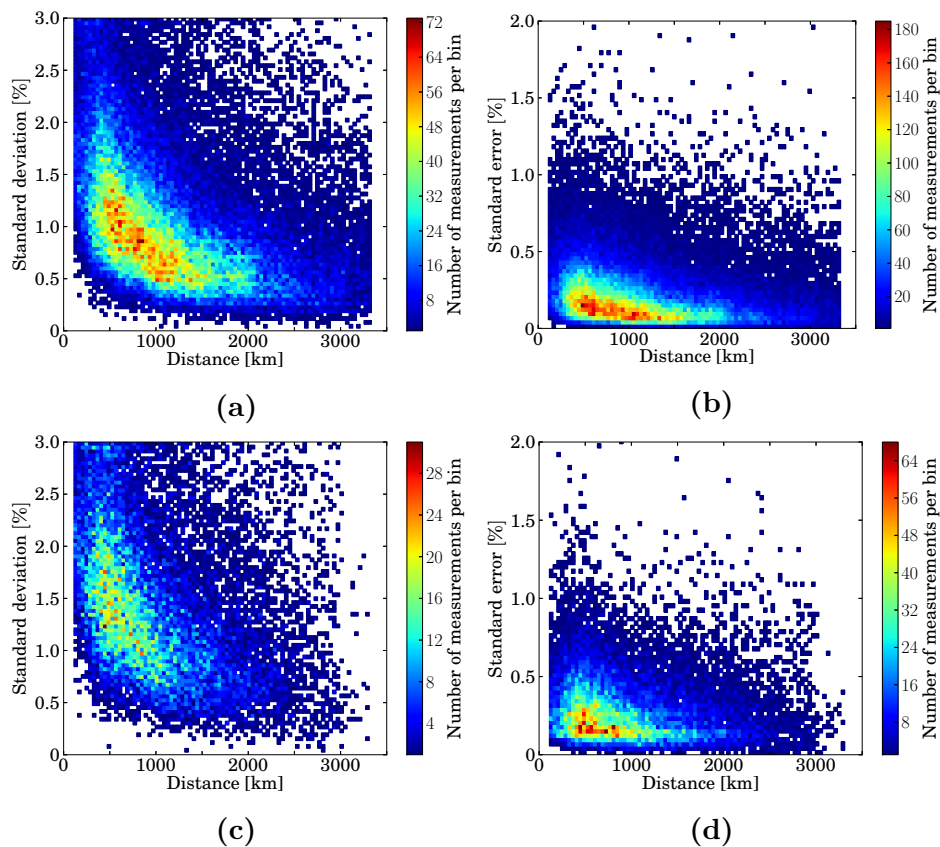


Fig. 3.11: Standard deviations (a, c) and standard errors (b, d) as a function of inter-station distance for all measurements in the entire data-set for Rayleigh (a, b) and Love (c, d) waves.

In order to test the consistency of the phase velocity measurements, phase-velocity maps and synthetic checkerboard tests were calculated for up to 54022 station-pairs for Rayleigh and 23852 station pairs for Love waves following the procedure of Darbyshire & Lebedev (2009). In Fig. 3.13 examples are plotted for Rayleigh and Love waves at 12, 30, and 60s period. In the central and southern parts of our study area the anomalies are well recovered in terms of amplitude and shape as compared to the north, south east, and south west. Slight lateral smearing is visible towards the east. These checker-board tests (Fig. 3.12) indicate therefore that the lateral resolution reaches 100 km for periods $< \sim 30$ s Rayleigh waves in regions with high path coverage (see Fig. 3.6) and about 150 km otherwise.

At short periods of 12s, both Rayleigh and Love waves are strongly sensitive to thick sedimentary cover, as in the North German Basin and in the Polish Trough. The thickness of sediments, as outlined from the model EUCRUST07 (Tesauro et al., 2008) shows that our regional surface wave tomography is consistent with compilations of results by Deep Seismic Sounding and confirms the high resolution for the 3D crustal structure. At longer periods, the properties of the lithosphere-asthenosphere system in the TESZ and in Central Europe are clearly imaged. Northeast of the TESZ high velocities indicate the thick cratonic mantle lithosphere of the East European Craton and the Baltic Shield. It is interesting to note the lateral differences in the lithosphere-asthenosphere system between the Sorgenfrei-Tornquist-Zone (STZ) in the northern part of the TESZ and the Tornquist-Teysseire-Zone (TTZ). The region of the Tornquist-Teisseyre Zone (TTZ) is associated with a stronger lateral decrease in the lithospheric thickness from the East European Platform (EEP) towards the southwest than the region of the Sorgenfrei-Tornquist Zone (STZ). Furthermore, the shallow asthenosphere in Central Europe in the region of the Cenozoic volcanic centers like Eifel or Vogelsberg and in the Pannonian Basin is clearly visible. It is also remarkable that the Eurasian slab in the western Alps is imaged clearly, thanks to the high station density in this region. The Love-wave phase velocities at 60 s are mainly sensitive to the mantle lithosphere, as indicated by high velocities in central to northern Europe, and to the shallow asthenosphere, as in the Pannonian Basin where Love-wave phase velocities are low. Love waves also indicate a shallow asthenosphere in the Eifel region. Altogether, these results confirm the high quality and rich information content of the large, new set of Rayleigh and Love phase-velocity measurements. A more detailed discussion of our tomography results and its geodynamic implications would be beyond the scope of this paper.

3.5 Conclusions

An automated processing scheme for the determination of broadband, Rayleigh and Love wave phase velocities is suggested, based on the cross-correlation of earthquake data. Robust dispersion curves are computed as averages over numerous curves and curve segments determined from data from different earthquakes and the same station

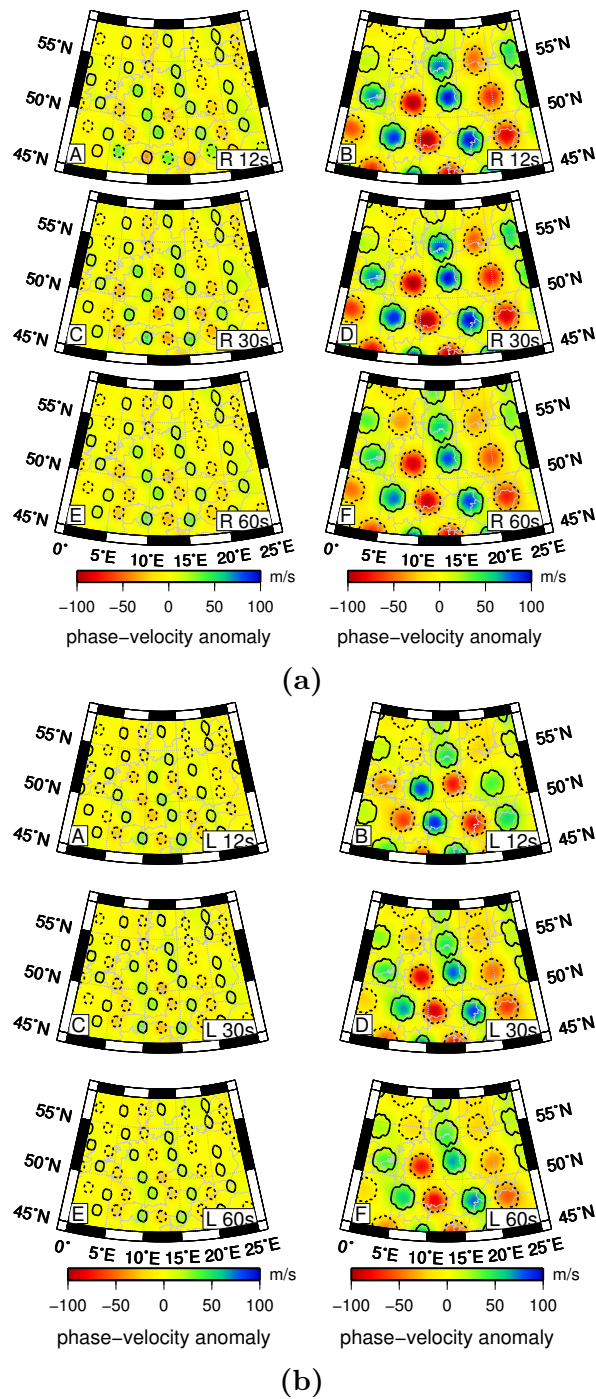


Fig. 3.12: Isotropic checkerboard tests with anomalies of approximately 100 km (a) and 150 km (b) size and 100m/s input amplitude. Solid and dashed outlines mark positive and negative input anomalies, respectively.

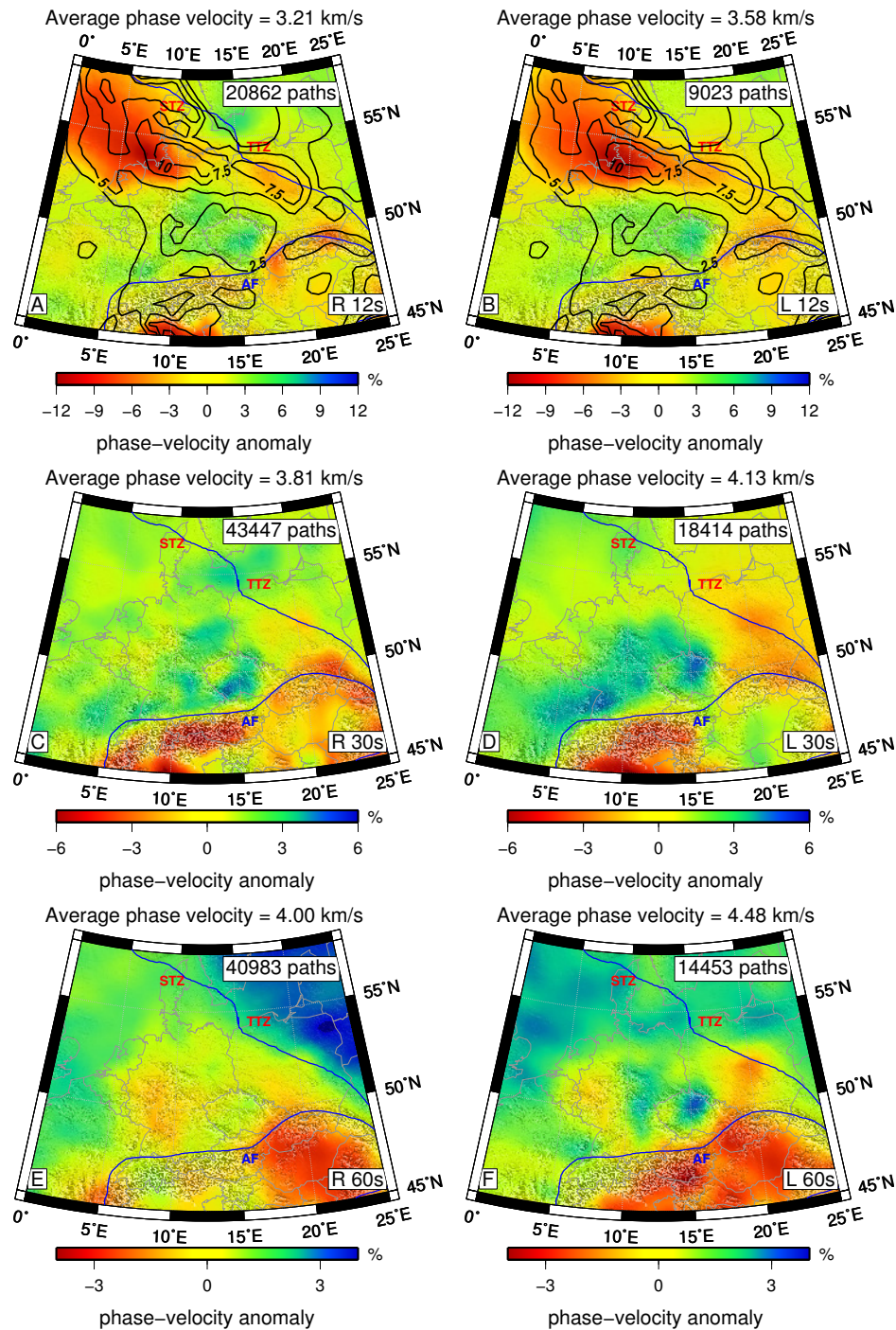


Fig. 3.13: Selected isotropic phase velocity maps. Some major tectonic lines are given for orientation (TTZ: Tornquist-Teisseyre Zone, STZ: Sorgenfrei-Tornquist-Zone, AF: Alpine Front). (a,c,e) Rayleigh and (b,d,f) Love wave phase velocity maps are shown for (a,b) 12s, (c,d) 30s and (e,f) 60s period. The 12s maps (a,b) are overlain by sedimentary thickness from EUCrust07 (Tesauro et al., 2008) (black).

pair. In our algorithm for the automated determination of inter-station, fundamental mode phase velocities, segments of the phase-velocity curves are selected based on the following criteria. The individual phase velocity measurements should be close to phase velocities for a path-dependent background model. They must be smooth. Furthermore, the accepted segments should have a sufficient length: their band width should exceed a frequency dependent threshold. The thresholds have to be fine-tuned to the data set under consideration. The comparison of phase velocity measurements for both propagation directions is essential in order to make sure that there are no systematic deviations between the two, indicative of errors.

A side product of the procedure is that stations with erroneous response information or timing problems may be detected.

Thanks to the automated processing, large data sets can be processed and the influence of rough perturbations on the phase velocity curves can be quantified by comparing results from two runs with different selection parameters. Rough perturbations (rough curve segments) can have a strong influence on the average dispersion curves and should be rejected. Interestingly, our tests suggest that the deviations can be both positive and negative, with the overall bias due to rough perturbations relatively small and detectable only for distances smaller than about 300 km. Averaging of many individual (single event) phase velocity measurements combined with the rejection of outliers is necessary to obtain reliable fundamental mode dispersion curves.

The automated procedure has been applied to all available data from 1073 permanent stations in central and northern Europe, including more than 1.3 million waveforms. The application of the procedure resulted in a set of high-quality inter-station fundamental mode dispersion curves in the period range between about 10 s and 350 s for both Rayleigh and Love waves. For most of the dispersion curves, the value of standard deviation was below 2%, and the value of standard error below 0.5%. The low values of the standard deviation and standard error show that the proposed criteria are well suited to select acceptable individual phase velocities measurements.

The new automated procedure makes the processing of large data sets feasible and enables consistent determination of inter-station phase velocity curves. The method is applicable both to permanent stations and networks and to temporary networks, where the smaller amount of data may require loosening of the selection parameters and the available events may not provide sufficient observations in both directions along each path.

According to checker board tests the lateral resolution of phase-velocity maps constrained by our data set varies in Central Europe between about 100 km and 150 km and is the highest for intermediate period Rayleigh waves. This represents an increase in the lateral resolution compared to previous tomographic studies of the lithosphere-asthenosphere system in Central Europe. The obtained data set is complementary to dispersion measurements from ambient noise as the considered frequency range overlaps considerably at short periods but is extended towards longer periods. and

may serve as input for high-resolution surface-wave tomography at local to regional and continental scales.

3.6 acknowledgments

This work was funded by German Science Foundation grant ME 1320/4-1. SL acknowledges funding from Science Foundation Ireland grant 09/RFP/GEO2550 and 13/CDA/2192. Waveform data were obtained through webdc (<http://www.webdc.eu/>). We are grateful to network operators that provide data to the EIDA archives. Furthermore, the usage of data of a number of temporary experiments like TOR, SVEKO-LAPKO, EGELADOS, and PASSEQ is acknowledged. This work was a part of the PASSEQ 2006 – 2008 project (Wilde-Piórko et al., 2008), station equipment for the PASSEQ experiment were provided by GIPP. Generic Mapping Tools (Wessel & Smith, 1998) were used to make some of the figures.

PASSEQ working Group: M. Wilde-Piórko, W. H. Geissler, J. Plomerová, M. Grad, V. Babuška, E. Brückl, J. Čyžienė, W. Czuba, R. England and E. Gaczyński and R. Gazdova and S. Gregersen, A. Guterch, W. Hanka, E. Hegedűs, B. Heuer, P. Jedlička, J. Lazauskiene, G. Randy Keller, R. Kind, K. Klinge, P. Kolinsky, K. Komminaho and E. Kozlovskaya, F. Krüger, T. Larsen, M. Majdański, J. Málek, G. Motuza, O. Novotný, R. Pietrasiak, Th. Plenefisch, B. Růžek, S. Sliupa, P. Środa, M. Świczak, T. Tiira, P. Voss, P. Wiejacz.

References

- Adam, J. M.-C. & Lebedev, S., 2012. Azimuthal anisotropy beneath southern Africa from very broad-band surface-wave dispersion measurements, *Geophysical Journal International*, **191**(1), 155–174.
- Agius, M. R. & Lebedev, S., 2013. Tibetan and Indian lithospheres in the upper mantle beneath Tibet: Evidence from broadband surface-wave dispersion, *Geochemistry, Geophysics, Geosystems*, **14**(10), 4260–4281.
- Aki, K. & Richards, P., 1980. *Quantitative Seismology*, W.H. Freeman and Company, San Francisco, U.S.
- Alterman, Z., Jarosch, H., & Pekeris, C. L., 1961. Propagation of Rayleigh Waves in the Earth, *Geophysical Journal of the Royal Astronomical Society*, **4**, 219–241.
- Bartzsch, S., Lebedev, S., & Meier, T., 2011. Resolving the lithosphere-asthenosphere boundary with seismic Rayleigh waves, *Geophysical Journal International*, **186**(3), 1152–1164.
- Bassin, C., Laske, G., & Masters, G., 2000. The Current Limits of Resolution for Surface Wave Tomography in North America, in *EOS Trans AGU*, vol. 81 (48), p. F897.
- Beghein, C., Snoke, J. A., & Fouch, M. J., 2010. Depth constraints on azimuthal anisotropy in the Great Basin from Rayleigh-wave phase velocity maps, *Earth and Planetary Science Letters*, **289**(3–4), 467 – 478.
- Ben-Menahem, A. & Singh, A., 1981. *Seismic Waves and Sources*, Springer, New York.
- Beyreuther, M., Barsch, R., Krischer, L., Megies, T., Behr, Y., & Wassermann, J., 2010. ObsPy: A Python Toolbox for Seismology, *Seismological Research Letters*, **81**(3), 530–533.
- Bodin, T. & Maupin, V., 2008. Resolution potential of surface wave phase velocity measurements at small arrays, *Geophys. J. Int.*, **172**(2), 698–706.
- Brilliant, R. & Ewing, M., 1954. Dispersion of Rayleigh waves across the U.S., *Bulletin of the Seismological Society of America.*, **44**, 149–158.

- Campillo, M. & Paul, A., 2003. Long-Range Correlations in the Diffuse Seismic Coda, *Science*, **299**(5606), 547–549.
- Capon, J., 1970. Analysis of Rayleigh-wave multipath propagation at LASA, *Bulletin of the Seismological Society of America*, **60**(5), 1701–1731.
- Cotte, N., Pedersen, H. A., Campillo, M., Farra, V., & Cansi, Y., 2000. Off-great-circle propagation of intermediate-period surface waves observed on a dense array in the French Alps, *Geophysical Journal International*, **142**(3), 825–840.
- Dahlen, F. & Tromp, J., 1998. *Theoretical Global Seismology*, Princeton University Press, Princeton, NJ.
- Darbyshire, F. A. & Lebedev, S., 2009. Rayleigh wave phase-velocity heterogeneity and multilayered azimuthal anisotropy of the Superior Craton, Ontario, *Geophysical Journal International*, **176**(1), 215–234.
- De Vos, D., Paulssen, H., & Fichtner, A., 2013. Finite-frequency sensitivity kernels for two-station surface wave measurements, *Geophysical Journal International*, **194**(2), 1042–1049.
- Deschamps, F., Lebedev, S., Meier, T., & Trampert, J., 2008. Azimuthal anisotropy of Rayleigh-wave phase velocities in the east-central United States, *Geophysical Journal International*, **173**(3), 827–843.
- Dziewonski, A. & Anderson, D., 1981. Preliminary reference earth model, *Physics of the Earth and Planetary Interiors*, **25**, 297–356.
- Endrun, B., Meier, T., Bischoff, M., & Harjes, H.-P., 2004. Lithospheric structure in the area of Crete constrained by receiver functions and dispersion analysis of Rayleigh phase velocities, *Geophysical Journal International*, **158**(2), 592–608.
- Endrun, B., Meier, T., Lebedev, S., Bohnhoff, M., Stavrakakis, G., & Harjes, H.-P., 2008. S velocity structure and radial anisotropy in the Aegean region from surface wave dispersion, *Geophysical Journal International*, **174**(2), 593–616.
- Endrun, B., Lebedev, S., Meier, T., Tirel, C., & Friederich, W., 2011. Complex layered deformation within the Aegean crust and mantle revealed by seismic anisotropy, *Nature Geosci*, **4**(3), 203–207.
- Engdahl, E., van der Hilst, R., & Buland, R., 1998. Global Teleseismic Earthquake Relocation with Improved Travel Times and Procedures for Depth Determination, *Bulletin Of The Seismological Society Of America*, **88**, 722–743.
- Ewing, M. & Press, F., 1950. Crustal structure and surface-wave dispersion, *Bulletin of the Seismological Society of America*, **40**(4), 271–280.

- Forsyth, D. W. & Li, A., 2005. Array-analysis of two-dimensional variations in surface wave phase velocity and azimuthal anisotropy in the presence of multi-pathing interference, in *Seismic Earth: Array Analysis of Broadband Seismograms*, vol. 157, pp. 81–98, eds Levander, A. & Nolet, G., Geophysical Monograph Series, AGU Washington D.C., ISBN 0-87590-422-X.
- Foster, A., Ekström, G., & Nettles, M., 2014. Surface wave phase velocities of the Western United States from a two-station method, *Geophysical Journal International*, **196**(2), 1189–1206.
- Friederich, W., Wielandt, E., & Stange, S., 1994. Non-Plane Geometries of Seismic Surface Wavefields and Their Implications For Regional Surface-Wave Tomography, *Geophys. J. Int.*, **119**(3), 931–948.
- Friederich, W., Hunzinger, S., & Wielandt, E., 2000. A note on the interpretation of seismic surface waves over three-dimensional structures, *Geophys. J. Int.*, **143**(2), 335–339.
- Gutenberg, B., 1924. Dispersion und Extinktion von seismischen Oberflächenwellen und der Aufbau der obersten Erdschichten, *Physikalische Zeitschrift*, **XXV**, 377–381.
- Köhler, A., Weidle, C., & Maupin, V., 2012. Crustal and uppermost mantle structure of southern Norway: results from surface wave analysis of ambient seismic noise and earthquake data, *Geophysical Journal International*, **191**(3), 1441–1456.
- Kulesh, M., Diallo, M., & Holschneider, M., 2005. Wavelet analysis of ellipticity, dispersion, and dissipation properties of Rayleigh waves, *Acoustical Physics*, **51**(4), 425–434.
- Landisman, M., Dziewonski, A., & Sato, Y., 1969. Recent Improvements in the Analysis of Surface Wave Observations, *Geophysical Journal of the Royal Astronomical Society*, **17**(4), 369–403.
- Laske, G. & Masters, G., 1996. Constraints on global phase velocity maps from long-period polarization data, *J. Geophys. Res.*, **101**(B7), 16059–16075.
- Laske, G., Markee, A., Orcutt, J. A., Wolfe, C. J., Collins, J. A., Solomon, S. C., Detrick, R. S., Bercovici, D., & Hauri, E. H., 2011. Asymmetric shallow mantle structure beneath the Hawaiian Swell—evidence from Rayleigh waves recorded by the PLUME network, *Geophysical Journal International*, **187**(3), 1725–1742.
- Lebedev, S., Meier, T., & van der Hilst, R. D., 2006. Asthenospheric flow and origin of volcanism in the Baikal Rift area, *Earth and Planetary Science Letters*, **249**(3/4), 415 – 424.
- Lebedev, S., Boonen, J., & Trampert, J., 2009. Seismic structure of Precambrian lithosphere: New constraints from broad-band surface-wave dispersion, *Lithos*, **109**(1-2), 96–111.

- Lebedev, S., Adam, J. M.-C., & Meier, T., 2013. Mapping the Moho with seismic surface waves: A review, resolution analysis, and recommended inversion strategies, *Tectonophysics*, **609**, 377–394.
- Legendre, C. P., Meier, T., Lebedev, S., Friederich, W., & Viereck-Götte, L., 2012. A shear wave velocity model of the European upper mantle from automated inversion of seismic shear and surface waveforms, *Geophysical Journal International*, **191**, 282–304.
- Levshin, A., Yanovskaya, T., Lander, A., Bukchin, B., Barmin, M., Ratnikova, L., & Its, E., 1989. *Seismic Surface Waves in a Laterally Inhomogeneous Earth*, Kluwer Academic Publishers, Dordrecht Netherlands.
- Levshin, A. L., Ritzwoller, M. H., & Resovsky, J. S., 1999. Source effects on surface wave group travel times and group velocity maps, *Phys. Earth Plan. Int.*, **115**(3-4), 293–312.
- Maupin, V., 2011. Upper-mantle structure in southern Norway from beamforming of Rayleigh wave data presenting multipathing, *Geophysical Journal International*, **185**(2), 985–1002.
- McEvelly, T. V., 1964. Central U.S. Crust-Upper mantle structure from Love and Rayleigh wave phase velocity inversion, *Bulletin of the Seismological Society of America*, **54**(6A), 1997–2015.
- Meier, T., Dietrich, K., Stöckhert, B., & Harjes, H.-P., 2004. One-dimensional models of shear wave velocity for the eastern Mediterranean obtained from the inversion of Rayleigh wave phase velocities and tectonic implications, *Geophys. J. Int.*, **156**(1), 45–58.
- Muyzert, E. & Snieder, R., 1996. The Influence of Errors in the Source Parameters on Phase Velocity Measurements of Surface Waves, *Bull. Seismol. Soc. Am.*, **86**, 1863–1872.
- Paul, A., Campillo, M., Margerin, L., Larose, E., & Derode, A., 2005. Empirical synthesis of time-asymmetrical Green functions from the correlation of coda waves, *Journal of Geophysical Research: Solid Earth*, **110**(B8).
- Pedersen, H., Debayle, E., & Maupin, V., 2013. Strong lateral variations of lithospheric mantle beneath cratons – Example from the Baltic Shield, *Earth and Planetary Science Letters*, **383**(0), 164 – 172.
- Pedersen, H. A., Bruneton, M., & Maupin, V., 2006. Lithospheric and sublithospheric anisotropy beneath the Baltic shield from surface-wave array analysis, *Earth Plan. Sc. Let.*, **244**(3-4), 590–605.

- Polat, G., Lebedev, S., Readman, P. W., O'Reilly, B. M., & Hauser, F., 2012. Anisotropic Rayleigh-wave tomography of Ireland's crust: Implications for crustal accretion and evolution within the Caledonian Orogen, *Geophysical Research Letters*, **39**(4).
- Press, F., 1956. Determination Of Crustal Structure From Phase Velocity Of Rayleigh Waves Part I: Southern California, *Geological Society of America Bulletin*, **67**(12), 1647–1658.
- Prindle, K. & Tanimoto, T., 2006. Teleseismic surface wave study for S-wave velocity structure under an array: Southern California, *Geophysical Journal International*, **166**(2), 601–621.
- Ritzwoller, M. H. & Levshin, A. L., 1998. Eurasian surface wave tomography: Group velocities, *J. Geophys. Res.*, **103**(B3), 4839–4878.
- Roux, E., Moorkamp, M., Jones, A. G., Bischoff, M., Endrun, B., Lebedev, S., & Meier, T., 2011. Joint inversion of long-period magnetotelluric data and surface-wave dispersion curves for anisotropic structure: Application to data from Central Germany, *Geophysical Research Letters*, **38**(5).
- Roux, P., Sabra, K. G., Kuperman, W. A., & Roux, A., 2005. Ambient noise cross correlation in free space: Theoretical approach, *The Journal of the Acoustical Society of America*, **117**(1), 79–84.
- Shapiro, N. & Campillo, M., 2004. Emergence of broadband Rayleigh waves from correlations of the ambient seismic noise, *J. Geophys. Res.*, **31**, L07614.
- Shapiro, N. M., Campillo, M., Stehly, L., & Ritzwoller, M. H., 2005. High-Resolution Surface-Wave Tomography from Ambient Seismic Noise, *Science*, **307**(5715), 1615–1618.
- Sun, D. & Helmberger, D., 2011. Upper-mantle structures beneath USArray derived from waveform complexity, *Geophysical Journal International*, **184**(1), 416–438.
- Tesauro, M., Kaban, M., & Cloetingh, S., 2008. EuCRUST-07: A new reference model for the European crust, *Geophysical Research Letters*, **35**, L05313.
- Toksöz, M. N. & Ben-Menahem, A., 1963. Velocities of mantle Love and Rayleigh waves over multiple paths, *Bulletin of the Seismological Society of America*, **53**(4), 741–764.
- Vdovin, O., Rial, J. A., Levshin, A. L., & Ritzwoller, M. H., 1999. Group-velocity tomography of South America and the surrounding oceans, *Geophysical Journal International*, **136**(2), 324–340.

- Weidle, C., Maupin, V., Ritter, J., Kvaerna, T., Schweitzer, J., Balling, N., Thybo, H., Faleide, J. I., & Wenzel, F., 2010. MAGNUS – A Seismological Broadband Experiment to Resolve Crustal and Upper Mantle Structure beneath the Southern Scandes Mountains in Norway, *Seism. Res. Lett.*, **81**(1), 76–84.
- Weidle, C., Soomro, R., Cristiano, L., & Meier, T., 2013. Identification of response and timing issues at permanent European broadband stations from automated data analysis, *Advances in Geosciences*, **36**, 21–25.
- Wessel, P. & Smith, W. H., 1998. New, improved version of the Generic Mapping Tools released, *EOS Trans. AGU*, **79**, 579.
- Wielandt, E., 1993. Propagation and Structural Interpretation of Non-Plane Waves, *Geophys. J. Int.*, **113**(1), 45–53.
- Wielandt, E., Sigg, A., Plešinger, A., Horálek, J., & Pěč, K., 1987. Deep structure of the bohemian massif from phase velocities of Rayleigh and Love waves, *Studia Geophysica et Geodaetica*, **31**(1), 1–7.
- Wilde-Piórko, M., Geissler, W., Plomerová, J., Grad, M., Babuška, V., Brückl, E., Čyžienė, J., Czuba, W., England, R., Gaczyński, E., Gazdova, R., Gregersen, S., Guterch, A., Hanka, W., Hegedús, E., Heuer, B., Jedlička, P., Lazauskiene, J., Keller, G., Kind, R., Klinge, K., Kolinsky, P., Komminaho, K., Kozlovskaya, E., Krüger, F., Larsen, T., Majdański, M., Málek, J., Motuza, G., Novotný, O., Pietrasiak, R., Plenefisch, T., Růžek, B., Sliupa, S., Šroda, P., Świczak, M., Tiira, T., Voss, P., & Wiejacz, P., 2008. PASSEQ 2006–2008: Passive seismic experiment in Trans-European Suture Zone, *Studia Geophysica et Geodaetica*, **52**(3), 439–448.
- Yang, Y., Ritzwoller, M. H., Levshin, A. L., & Shapiro, N. M., 2007. Ambient noise Rayleigh wave tomography across Europe, *Geophys. J. Int.*, **168**(1), 259–274.
- Yang, Y., Ritzwoller, M. H., Lin, F.-C., Moschetti, M. P., & Shapiro, N. M., 2008. Structure of the crust and uppermost mantle beneath the western United States revealed by ambient noise and earthquake tomography, *J. Geophys. Res.*, **113**(B12), B12310.
- Yao, H., van der Hilst, R. D., & de Hoop, M. V., 2006. Surface-wave array tomography in SE Tibet from ambient seismic noise and two-station analysis- I. Phase velocity maps, *Geophysical Journal International*, **166**(2), 732–744.
- Yoshizawa, K. & Ekström, G., 2010. Automated multimode phase speed measurements for high-resolution regional-scale tomography: application to North America, *Geophysical Journal International*, **183**(3), 1538–1558.
- Zhang, X., Paulssen, H., Lebedev, S., & Meier, T., 2007. Surface wave tomography of the Gulf of California, *Geophys. Res. Lett.*, **34**(15), L15305–.

-
- Zhu, H., Bozdag, E., Peter, D., & Tromp, J., 2012. Structure of the European upper mantle revealed by adjoint tomography, *Nature Geosci*, **5**(7), 493–498.

Chapter 4

This chapter is published in *Advances in Geosciences (ADGEO)*

Manuscript prepared for Adv. Geosci.
with version 5.0 of the L^AT_EX class copernicus.cls.
Date: 3 July 2015

Identification of response and timing issues at permanent European broadband stations from automated data analysis

C. Weidle, R. A. Soomro, L. Cristiano, and T. Meier

Institute of Geosciences, Kiel University, Otto-Hahn-Platz 1, 24118 Kiel, Germany

Correspondence to: C. Weidle (cweidle@geophysik.uni-kiel.de)

4.1 summary

We apply automated two-station broadband phase velocity dispersion measurements to all available broadband data from permanent seismic stations in Europe, as available through the European Integrated Data Archive (EIDA, <http://www.orfeus-eu.org/eida/>) infrastructure. As part of our quality control we detect several typical patterns in our measurements that can be related to technical problems, incorrect metadata information or uncover inconsistencies in data processing routines. These effects include timing and various response issues, most prominently erroneous response information. Our procedure is thus able to identify potentially problematic (meta)data from a large set of seismic data and offers an applicable way to increase data quality at data centers.

4.2 Automated data analysis

To tackle the ever increasing amount of available broadband seismic data from European seismic stations for routine analysis, manual data processing and retrieval of observables needs to be replaced by automated processing tools. Furthermore, rapid response in case of seismic events requires automated data processing. While signal processing for detecting and locating seismicity is routinely done on an automated basis, seismogram analysis for structural interpretations often still requires manual screening. As locations of earthquakes as well as studies of the Earth's structure depend heavily on the quality of the data, automated routines are required for data quality control as well. While power spectral density estimates of the incoming data are well suited to detect data gaps, large errors in the gain information or noisy stations, the detection of response and timing problems is less evident to be detected automatically and few works have addressed this problem in the past.

Gibbons (2006) identified and documented a temporary timing problem of < 20 s at a single station using repeatedly occurring mining events. Identification of the issue was, however, rather accidental as the timing problem occurred at the time of a particular event of interest and was rather large (~ 8 s). Although the author points out that there exist “most likely [sources of repeating seismic signals] in the vicinity of many seismic stations”, a systematic implementation of his routine to all available seismic data in Europe would require a massive effort of the European seismological community.

We developed an automated routine to measure inter-station phase velocity curves of fundamental mode surface waves, including automated quality checks of the raw data (Soomro et al., 2013). The measurements are done by pairwise cross-correlating instrument corrected velocity seismograms and rely on path-specific reference models. The method is applied to all available data from permanent stations in Europe since 1990, as provided by EIDA, the European Integrated Data Archive (<http://www.orefeus-eu.org/eida/>). We use an automated routine based on ObsPy (Beyreuther et al., 2010) to download this massive dataset. Besides an unprecedented amount of regional scale two-station dispersion measurements, which is to be exploited by surface wave tomography, we observe in our dataset as part of our quality control a variety of phenomena that are indicative of technical issues related to the data, metadata and/or processing. In the following we will discuss in Sect. 2 potential expectable issues by simulating them in synthetic examples. In Sect. 3 we present some data examples of these phenomena and preliminary details on few stations which either have technical issues or where the provided station metadata is incorrect. To identify stations with odd behaviour in our automated measurements we finally present a map of stations that are suspicious in the dispersion measurements and require a manual check to exclude or identify errors in data or metadata information.

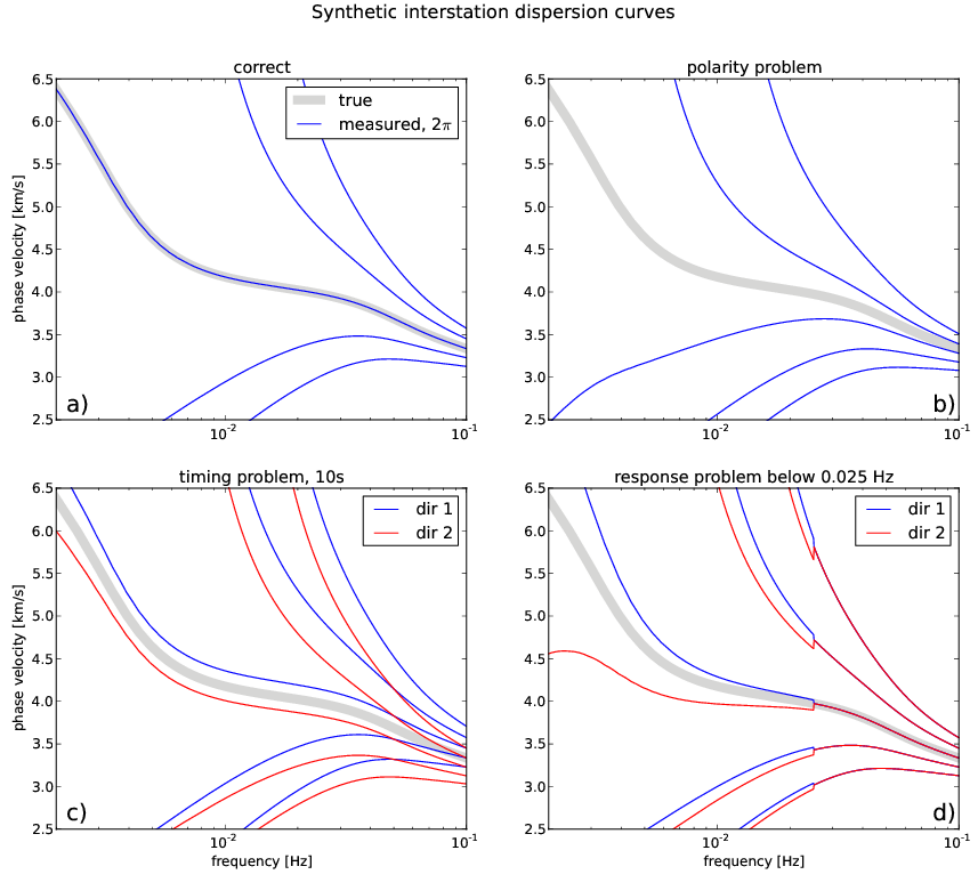


Fig. 4.1: Simulation of potential data errors in the inter-station phase velocity measurement. Synthetic waveforms are simulated in PREM (Dziewonski & Anderson, 1981) for epicentral distances of 5000 and 6000 km. For description see text.

4.3 Method and synthetic example

Very broad-band dispersion curves of fundamental modes may be measured by cross-correlation of recordings at two stations. Frequency dependent time windows are applied to the cross-correlation function before determination of phase velocity from the phase of the cross-correlation function in order to optimize resolution in the time-frequency plane. The correct 2π phase shift is identified by comparing interstation phase velocities to path-specific reference models based on CRUST2.0 and PREM (Bassin et al., 2000; Dziewonski & Anderson, 1981). Furthermore, the smoothness of the dispersion curves is carefully checked and results for both propagation directions are averaged and compared. A detailed account of the measurement procedure is given by Soomro et al. (2013). The procedure may be applied to earthquake data as well as ambient noise.

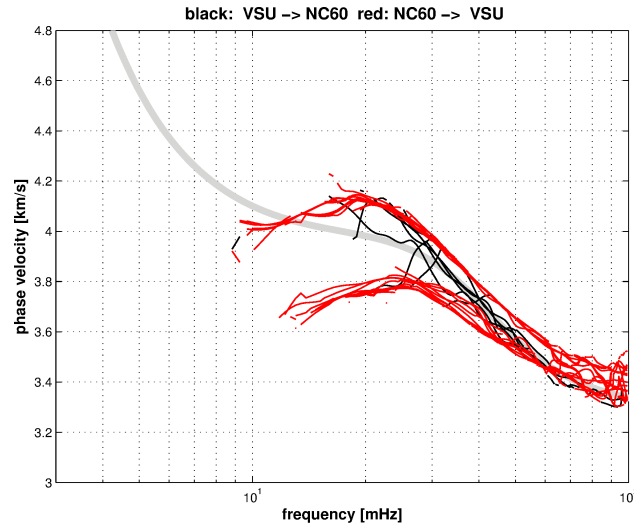


Fig. 4.2: Automated phase velocity measurements between station NC602 in southern Norway and VSU in Estonia. Curves show signature of a polarity issue with π offset from the expected reference curve.

To understand how potential data and metadata errors affect our two-station waveform analysis, we calculate synthetic waveforms at 5000 and 6000 km epicentral distance in PREM (Dziewonski & Anderson, 1981) and simulate three potential issues (Fig. 4.1):

- If data and metadata information are correct – the standard case – one 2π branch will fall close to the reference model and will be selected to determine the acceptable bandwidth of the measurement. Other 2π branches are neglected.
- If one of the stations has wrong polarity, an additional π -phase shift is introduced, and the resulting measurements are symmetrically offset from the expected reference model. Our measurements may thus fall above and/or below and have a rather large deviation from the reference model.
- If one of the stations has a timing problem, there will be an approximately constant offset from the expected reference curve. As we measure propagation in both directions, velocities will differ for the two propagation directions.
- If one of the stations has a response problem, simulated here by a $\pi/8$ error for periods above 40 s, the measurements will branch off the expected curve for low frequencies, again with differing sign for the two propagation directions. The same pattern, however, may similarly reflect differing bandwidths of the two instruments involved.

A commonly debated issue in the context of two-station measurements is deviation of the wavefront propagation direction from the greatcircle by diffraction/scattering at large scale heterogeneities (e.g. Moho topographic variations, oceans, cratons). These effects are indeed observed but are limited to certain frequency bands. We observe

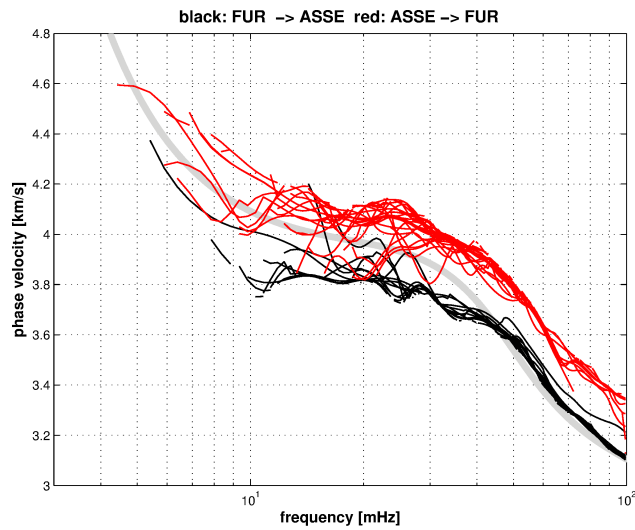


Fig. 4.3: Automated phase velocity measurements between station FUR and ASSE in southern and northern Germany, respectively. Curves show signature of a timing issue with close to constant offset of measured curves for the two propagation directions.

such deviations as “bumps” in the dispersion curve around 20–30 s if strong variations in Moho depth are encountered, or as systematic deviations between ca.50–80 s if contrasts in lithospheric thickness lead to deflection of the wavefield from greatcircle propagation. These structural effect will, however, always be visible as regional patterns at nearby stations and can thus be easily distinguished from technical issues as discussed here.

4.4 Data examples

We present some data examples with indications of polarity, timing and response issues at selected station pairs in Fig. 2.

- a. Station NO.NC602 appears in our analysis as having a polarity problem (Fig. 4.2). In fact, however, it turned out to be a problem with the response information and our application of it in the instrument correction. In the SEED convention (Ahern et al., 2012), the normalization factor A_0 is defined as: $A_0 = 1/|H(s)|$, where $H(s)$ is the transfer function of the instrument as a function of complex frequency s . A_0 is thus, per definition, a positive number and a positive normalization factor is provided by ORFEUS. At station NO.NC602, a Güralp CMG-3T sensor was installed in 2000, with poles and zeros for displacement that have a negative transfer function. Applying a positive normalization constant introduces thus a polarity flip in the instrument corrected data.

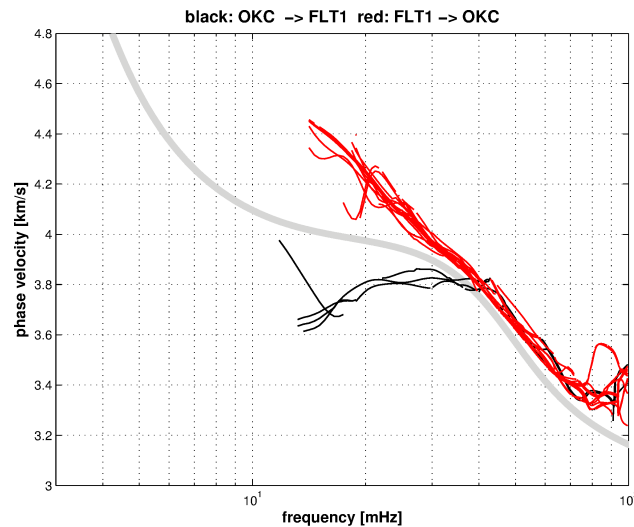


Fig. 4.4: Automated phase velocity measurements between station FLT1 in northern Germany and OKC in the eastern Czech Republic. Curves show signature of a response issue with branching offset of measured curves for the two propagation directions. This may reflect differing instrument types but could also point to wrong instrument response.

The issue was recognized by Guralp in 2006 (Guralp, 2013), however, responses for NO.NC602 provided through ORFEUS have a new, positive transfer function only for data since June 2011.

- b. A timing issue could be suspected at station ASSE in northern Germany. Based on the offset of the measurements for the two directions we estimated the timing error to be on the order of 3 s (see Discussion). Manual data inspection revealed, however, an inconsistency in our data processing where a data decimation routine within ObsPy lead to a phase shift of the data at station ASSE of 3–4 s. This highlights the usefulness of this approach as part of our quality control and the important fact that not every suspiciously behaving station has a (meta)data inconsistency.
- c. A response issue may reflect differing bandwidths of the two instruments involved but also indicate potentially erroneous responses. Here, responses supplied by ORFEUS for CZ.OKC and GE.FLT1 indicate both a STS2 seismometer, while in fact, CZ.OKC is a Guralp CMG-3ESP (Czech Regional Seismic Network, 2013).

4.5 Discussion

To systematically check our measurements for potential station issues we average deviations from the reference model and between the two directions over frequency. These stationwise averages might reflect regional structural variations where our reference

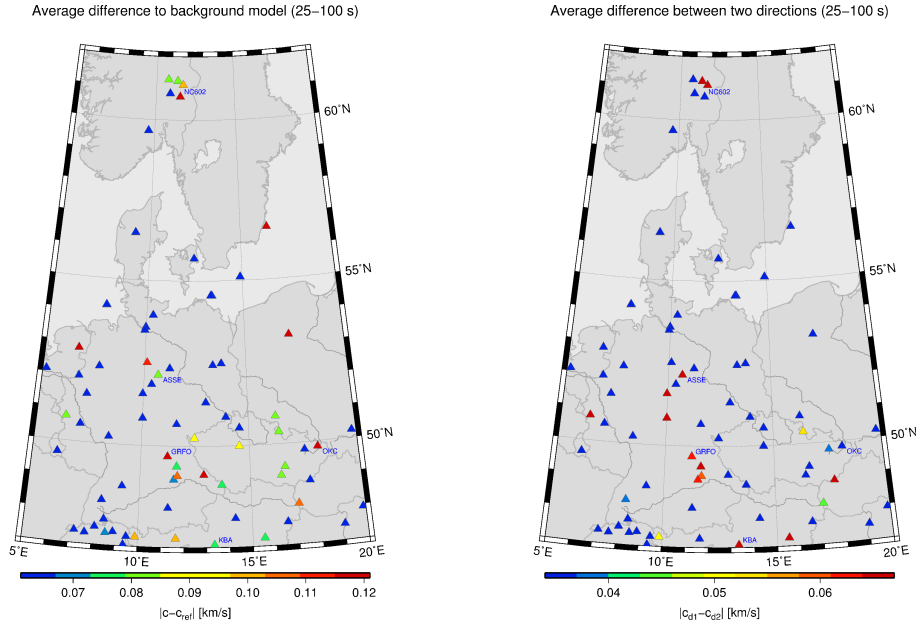


Fig. 4.5: Averaged deviations of measured dispersion curves in the period range 25–100 s (left) from the reference model and (right) between the two propagation directions. Stations with large standard deviations point to data inconsistencies which need to be manually checked. Stations with insignificant number of measurements are omitted.

models are not accurate enough but in general highlight potentially(!) problematic data. These data require then a detailed manual inspection to identify the issue that causes large deviations of our measurements from the expected reference model. It is important to stress that this procedure is designed for quality control and an anomalous station in Fig. 4.5 has not necessarily a technical issue. Besides the example (b) for station ASSE above, we have found at station GRFO, for example, an inconsistency in the applied instrument correction which had a comparable signature in the measurements as a timing or response error (Fig. 4.3, 4.4).

In principle it is straightforward to estimate the amplitude of a timing or response/phase error. The timing/phase error is related to the offset of the measured curves for two directions by $c_{1,2}(\omega) = \frac{\delta\Delta}{t(\omega) \pm \epsilon_t} = \frac{\omega\delta\Delta}{\Phi(\omega) \pm \epsilon_\Phi(\omega)}$, where $c_{1,2}(\omega)$ is phase velocity in the two directions as function of frequency ω , $\delta\Delta$ the inter-station distance, $t(\omega)$, ϵ_t the inter-station traveltime and timing error ($\epsilon_t \ll t(\omega)$), respectively and $\Phi(\omega)$, $\epsilon_\Phi(\omega)$ the phase and phase error, respectively.

As t increases with $\delta\Delta$, the offset $|c_1 - c_2|$ is strongly distance dependent with larger offsets for shorter inter-station distance. Critical for the determination of ϵ_t is the detectability of a consistent offset between curves in two directions, which we may approximate by the standard deviation of our measurements. Soomro et al. (2013) show that the measurements have an overall standard deviation of $< 2\%$ at shorter

inter-station distance. In the main frequency band of our observation (10–50 mHz), the phase velocity c is approx. 4.0 km s^{-1} , hence for an inter-station distance of 500 km a timing error of ca. 2.5 s and larger would be detectable. This value is on the same order of magnitude as suggested by Gibbons (2006) to potentially go unnoticed, as timing errors below ~ 2 s may be within the range of phase identification and picking uncertainties in local to regional seismic event location.

Phase and timing errors are linked through $\Phi = \omega t$, thus the same line of arguments can be applied to phase errors. Through $\epsilon_\Phi = \omega \epsilon_t$ the traveltime error ϵ_t resulting from a given phase error increases with decreasing frequency. Therefore, the detectability of a phase error is easier at lower frequencies as the curve offset for two directions $|c_1 - c_2|$ increases with decreasing frequency (Fig. 4.1d). Since identification of the origin of anomalous dispersion curve behaviour is still ongoing work we refrain from discussing other stations explicitly. However, based on the examples outlined in the previous section we point out that – as part of quality control in our automated dispersion measurement routine – we are able to easily identify stations with potentially technical issues or incorrect metadata information within a large dataset. Though a systematic analysis of all anomalous stations in our dataset, which comprises basically all currently available data in Europe through EIDA nodes, will be timeconsuming, it might be a viable way to uncover data and metadata inconsistencies in the databases.

4.6 acknowledgements

Johannes Schweitzer (NORSAR) kindly provided waveform and instrument metadata from NC602 and pointed out the issue of negative normalization factor. He and an anonymous reviewer are also thanked for thoughtful and constructive reviews. Waveform data were retrieved through the Arlink interface of WebDC using ObsPy (Beyreuther et al., 2010). All network operators who share their data through any EIDA partner are gratefully acknowledged. R. A. Soomro and L. Cristiano are supported by Deutsche Forschungsgemeinschaft through projects ME 1320/4-1 and ME 1320/2-1, respectively.

References

- Ahern, T., Casey, R., Barnes, D., Benson, R., and Knight, T.: SEED Reference Manual – Standard for the Exchange of Earthquake Data, International Federation of Digital Seismograph Networks Incorporated Research Institutions for Seismology United States Geological Survey, version 2.4 edn., http://www.iris.edu/manuals/SEED_chpt1.htm, 2012.
- Bassin, C., Laske, G., and Masters, G.: The Current Limits of Resolution for Surface Wave Tomography in North America, in: EOS Trans AGU, vol. 81 (48), p. F897, <http://mahi.ucsd.edu/Gabi>, 2000.
- Beyreuther, M., Barsch, R., Krischer, L., Megies, T., Behr, Y., and Wassermann, J.: ObsPy: A Python Toolbox for Seismology, *Seismol. Res. Lett.*, 81, 530–533, doi:10.1785/gssrl.81.3.530, 2010.
- Czech Regional Seismic Network: website, <http://www.ig.cas.cz/en/structure/observatories/czech-regional-seismological-network/okc/>, 2013.
- Dziewonski, A. and Anderson, D.: Preliminary reference earth model, *Physics of the Earth and Planetary Interiors*, 25, 297–356, doi:10.1016/0031-9201(81)90046-7, 1981.
- Gibbons, S. J.: On the Identification and Documentation of Timing Errors: An Example at the KBS Station, Spitsbergen, *Seismol. Res. Lett.*, 77, 559–571, doi:10.1785/gssrl.77.5.559, 2006.
- Guralp Systems Ltd.: website, <http://www.guralp.com/poles-and-zeroes-with-positive-normalization-factors/>, 2013.
- Soomro, R., Weidle, C., and Meier, T.: Automated fundamental mode surface wave phase velocity measurements and its application to central Europe, in preparation, 2013.

Chapter 5

Isotropic and Azimuthally anisotropic Rayleigh and Love wave phase velocity tomography for central Europe

5.1 Data Set

In recent years, there is unprecedented growth in number of seismic stations and more and more stations are being added continuously. There is very dense coverage of seismic stations nowadays, especially in Europe. Automatic routines are mandatory to exploit these huge data sets. In order to utilize these large data volumes Soomro et al. (2015) automated the inter-station method of Meier et al. (2004). This resulted in high quality very broad band highly consistent data set of Rayleigh waves (see fig. 5.1 a) and Love waves (see fig. 5.1 b) with inter-station paths covering almost entire Europe.

Automated schemes are useful to process large data-sets, this yields consistent measurements, and sensitivity to various parameters can be checked easily. By using events from both propagation directions and variable inter-event distances, the effect of great circle deviations and non-planar waves can be minimized. Soomro et al. (2015) downloaded data in the time period ranging from January 1990 to October 2013, made available by European Integrated Data Archive (EIDA) infrastructure. They downloaded all the available events through ObSpy (Beyreuther et al., 2010) based automated routine with a distance dependent minimum magnitude threshold of 4–6, and a maximum magnitude of 8. The choice of distance dependent magnitude is made due to low signal to noise ratio for the smaller magnitude events at larger distances, which make surface waves difficult to extract. In total they downloaded 1.38 million events with the help of Arlink interface of WebDC (<http://www.webdc.eu>). They obtained 164231 inter-station paths and performed around 12 million cross correlations,

in result they obtained ~ 63000 and ~ 27500 smooth average dispersion measurements for Rayleigh and Love waves, respectively.

5.1.1 Data sampling

Due to automated processing of the surface wave data, we are able to obtain smooth phase velocity dispersion curves in broad period range (8–350 s for Rayleigh waves) (8–250 s and Love waves). The path density is period dependent, at shorter and longer periods we have fewer phase velocity data (around \sim ten thousand) as compared to the intermediate periods. This is due to the fact that, at short periods there is interference of scattered waves with direct waves, and at larger inter-station distances it is difficult to measure high frequency waves due to short wavelength and sensitivity to shallower structure, and at long periods (>50 s) the fundamental mode interferes with S and multiple S- wave arrivals (Adam & Lebedev, 2012) makes difficult to obtain smooth measurements. Soomro et al. (2015) used crust 2.0 (Bassin et al., 2000) as a reference model. The average dispersion curve obtained through inter-station method has a moderate dependence upon the background model used, Soomro et al. (2015) allowed 12 % deviation from the background model.

In Fig. 5.3 we showed the path density for some selected periods (8 s, 15 s, 50 s, 250 s). In this figure (5.3) it can be seen that, we have more than 9000 inter-station paths at 8 s period, and this no. is gradually increasing and has a peak at around ~ 45 seconds (see fig. 5.2), here we have more than 40000 smooth phase velocity measurements, and at 250 s we have around ~ 7000 measurements (see fig. 5.2).

For Love wave we have approximately one-third of Rayleigh wave measurements. Similar trend is visible here as well (see Fig. 5.4), at 8 s period we have more than 2000 phase velocity measurements, and a peak at around 30 s with more than 15000 measurements (see 5.2). This is first time that, Love wave phase velocity measurements are performed in such a broad period range (8–200 s).

Soomro et al., 2015 processed huge amount of data covering almost entire Europe (see fig. 5.1). The path coverage for Rayleigh wave phase velocities for broader region is shown in fig. 5.3. We have very dense coverage in entire Europe, especially at intermediate periods, where it is easy to obtain smooth curves as compared to short and very long periods. The denser ray coverage is helpful to obtain high resolution image of the region.

5.2 Tomographic Inversion

In order to estimate the effects of isotropic and anisotropic contributions to the Love and Rayleigh wave phase velocity anomalies, we performed tomographic inversion of the

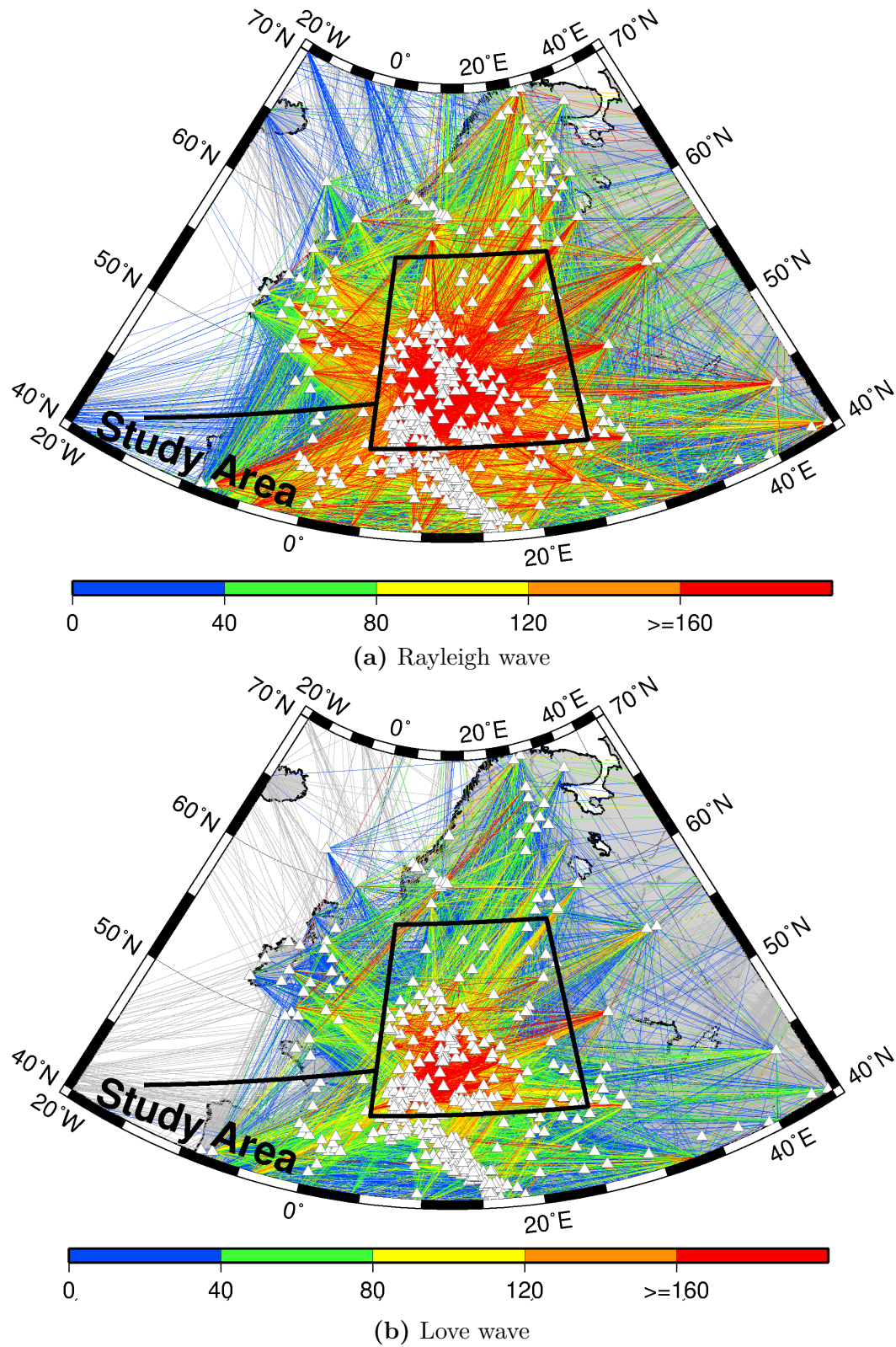


Fig. 5.1: Data from more than 1000 permanent and temporary stations is processed for more than 50000 inter-station paths for Rayleigh (a) and ~ 23000 for Love wave (b). Red color indicate ~ 160 accepted smooth curves in one inter-station path. Gray colored paths did not produce any smooth curves.

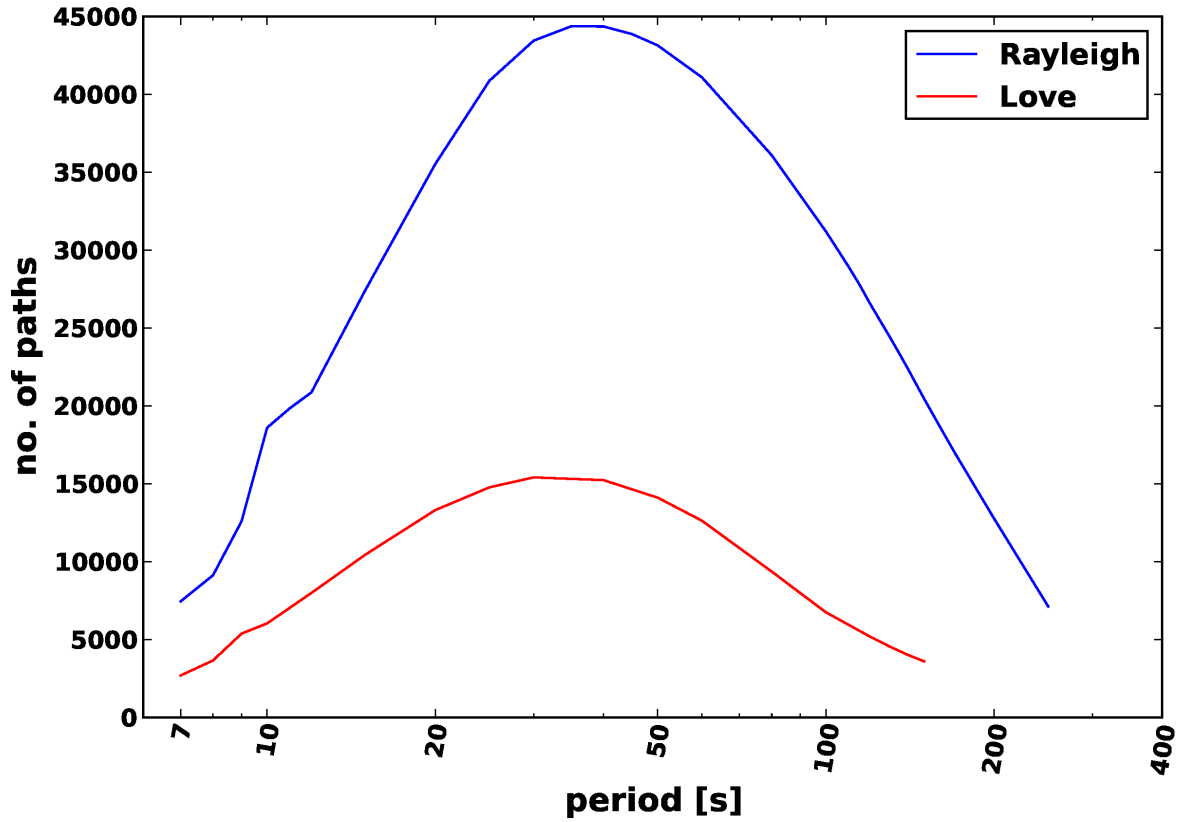


Fig. 5.2: Histogram shows no. of paths as function of period for Rayleigh and Love wave. There is a peak around ~ 40 s with more than 40000 measurements for Rayleigh waves and 15000 measurements for Love waves.

automatically obtained average phase velocity dispersion measurements by following Deschamps et al. (2008).

In each average inter-station dispersion curve $C_i(\omega)$ represents the structure in the vicinity of the two stations. The inversion for each period is carried out separately.

The phase velocity anomaly is given by

$$\delta C(\phi, \theta) = \delta C_{iso}(\phi, \theta) + \delta C_{2\Psi}(\phi, \theta) + \delta C_{4\Psi}(\phi, \theta), \quad (5.1)$$

The isotropic anomalies are represented by δC_{iso} and anisotropic anomalies in terms of 2Ψ and 4Ψ are represented by $\delta C_{2\Psi}$ and $\delta C_{4\Psi}$, respectively. Where

$$\delta C_{2\Psi} = A_{2\Psi} \cos(2\Psi) + B_{2\Psi} \sin(2\Psi), \quad (5.2)$$

and

$$\delta C_{4\Psi} = A_{4\Psi} \cos(4\Psi) + B_{4\Psi} \sin(4\Psi), \quad (5.3)$$

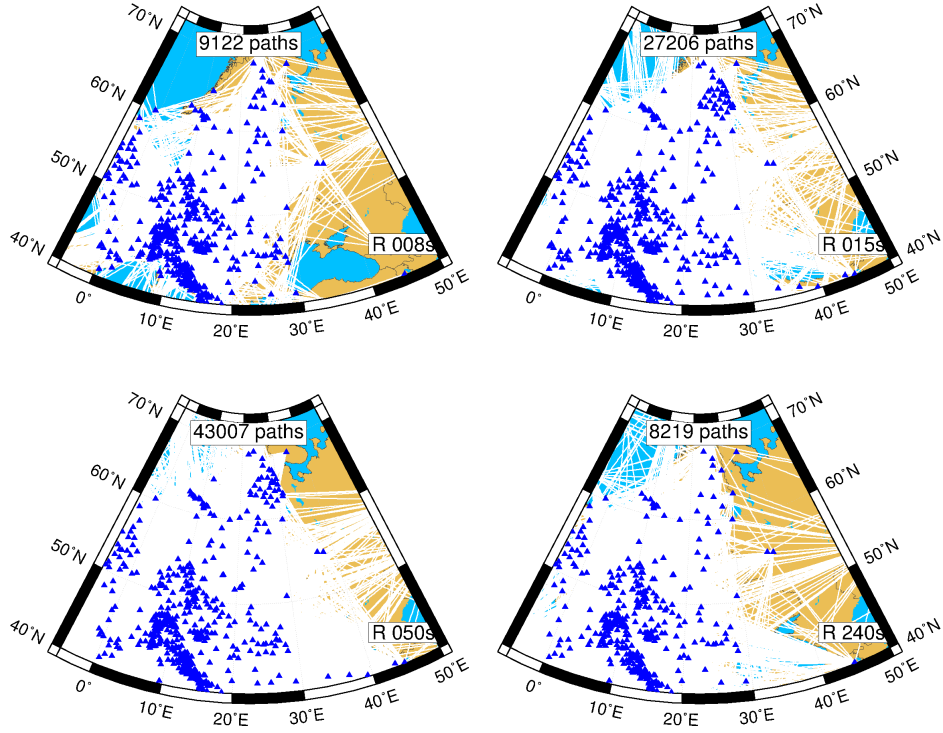


Fig. 5.3: Path coverage for Rayleigh waves is shown for some selected periods. Data from more than 1000 permanent and temporary stations in the period range from January 1990 to October 2013 has been processed.

where, Ψ is local ray azimuth. The $A_{2\Psi}$, $B_{2\Psi}$, $A_{4\Psi}$, and $B_{4\Psi}$ are four anisotropic coefficients, which are defined for each latitude θ and longitude ϕ .

The amplitude Λ and angle θ of the anomalies are given by

$$\Lambda_{2\Psi} = \sqrt{A_{2\Psi}^2 + B_{2\Psi}^2}, \quad (5.4)$$

$$\theta_{2\Psi} = \frac{1}{2} \arctan\left(\frac{B_{2\Psi}}{A_{2\Psi}}\right), \quad (5.5)$$

$$\Lambda_{4\Psi} = \sqrt{A_{4\Psi}^2 + B_{4\Psi}^2}, \quad (5.6)$$

$$\theta_{4\Psi} = \frac{1}{4} \arctan\left(\frac{B_{4\Psi}}{A_{4\Psi}}\right), \quad (5.7)$$

therefore, the phase velocity curves are inverted for five parameters. We have used triangular grid (Wang & Dahlen, 1995).

The average phase velocity along the path i is

$$\overline{\delta C_i} = \int_{\phi} \int_{\theta} K_i(\phi, \theta) \delta C(\phi, \theta) d\theta d\phi. \quad (5.8)$$

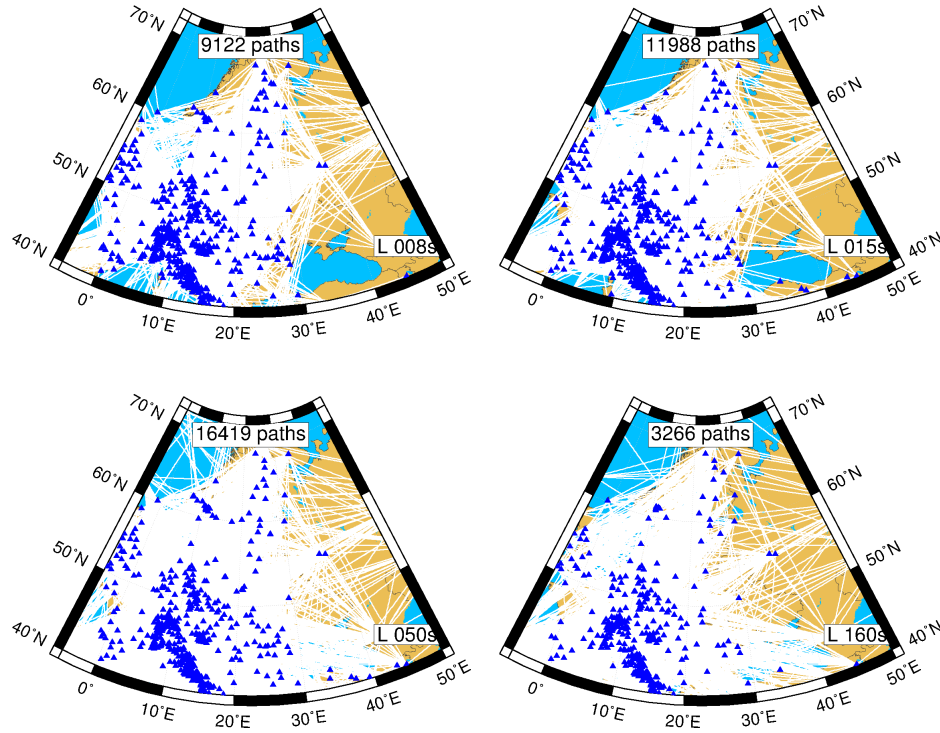


Fig. 5.4: same figure 5.3 for Love waves. The no. of paths are roughly 1/3 of Rayleigh wave paths.

Eqn. 5.1 gives local anomalies $\delta C(\phi, \theta)$ at longitude ϕ and latitude θ . $K_i(\phi, \theta)$ are the sensitivity kernels which contain weights of each knot at particular path (Lebedev & Van Der Hilst, 2008).

The sensitivity areas of the inter-station measurements are complex (Chevrot & Zhao, 2007). The sensitivity can be improved if all the possible inter-station combinations are used, hence dense station coverage is helpful in improving the sensitivity to intermediate and long wavelength structures, due to this fact, smoothing of the sensitivity areas gives robust phase velocity measurements.

We have evaluated the sensitivity areas $K(\theta, \phi)$ as Lebedev & Van Der Hilst (2008) at knots of dense triangular integration grid. This grid with equal inter-knot spacing is computed as by Wang & Dahlen (1995). We have chosen knot spacing of 30 km in the integration grid. This value is sufficiently small. The grid points surrounded by any particular point make the hexagon shape. The area of these hexagons around each knot is calculated, and $K(\theta, \phi)$ is calculated at each grid knot and multiplied with the hexagon area. This gives the weight of the knot in the sensitivity area. The model grid is also triangular but with larger knot spacing (here 70 km). This value is chosen due to denser station coverage. Similarly, as integration grid, $K(\theta, \phi)$ is computed by integrating the area surrounded by neighboring grid points.

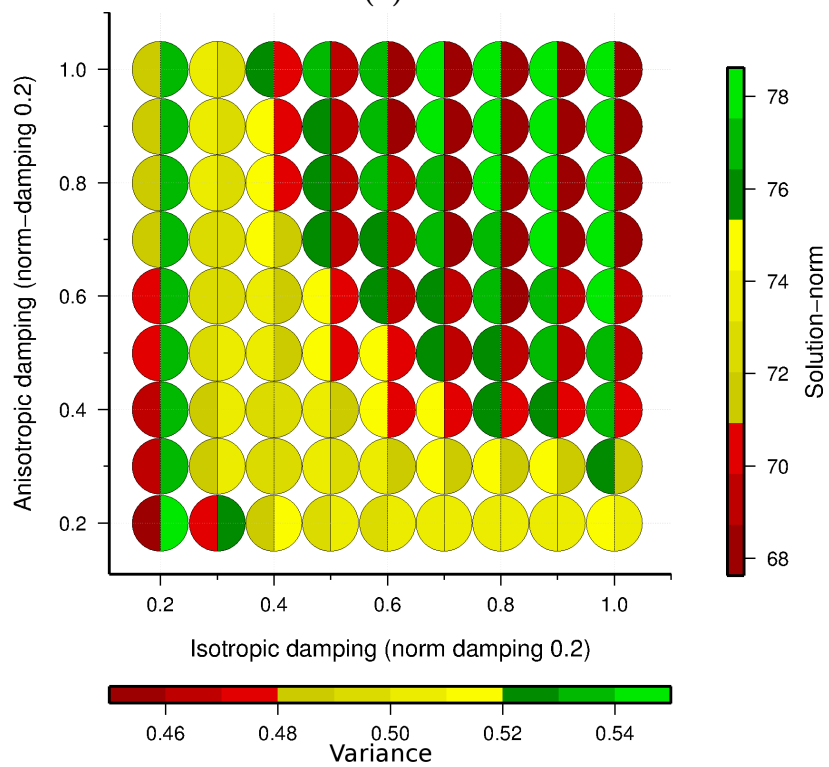
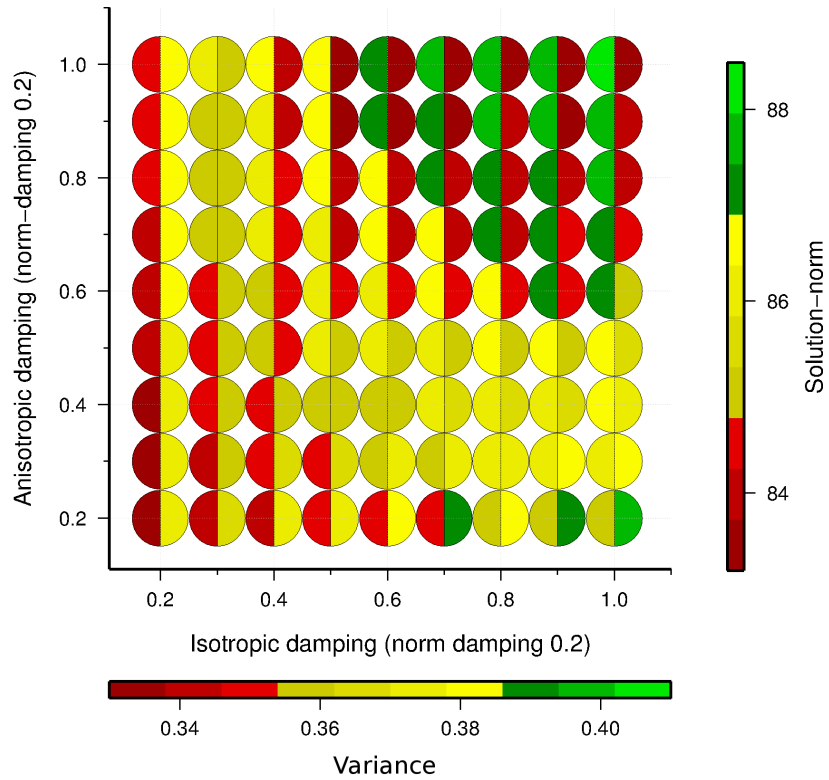


Fig. 5.5: Assessment of optimal regularization parameters: Left and right half circles show data variance and model norm, respectively, for various combinations of isotropic and anisotropic damping parameters for 60 s (a) and 125 s (b). Chosen parameter combinations are 0.4/0.5 and 0.6/0.7 for iso-/anisotropic damping at 60 s (a) and 125 s (b), respectively.

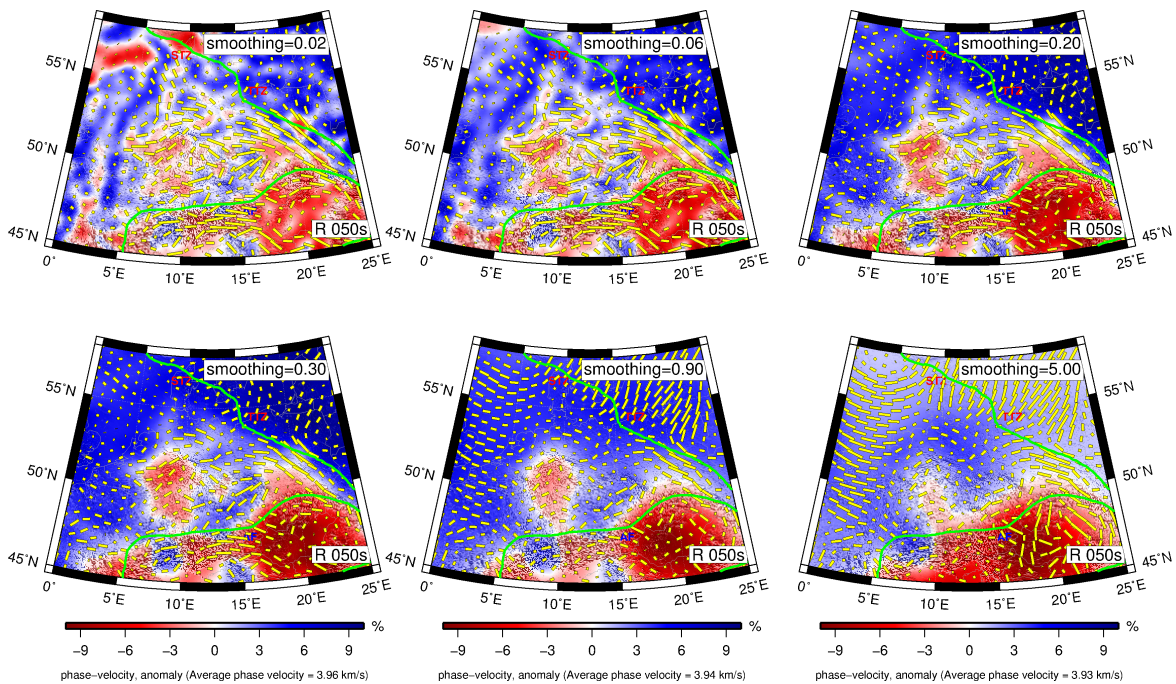


Fig. 5.6: Effect of varying isotropic damping on Rayleigh wave phase velocity maps. Anisotropic 2Ψ and 4Ψ damping values are fixed (here Rayleigh wave isotropic and anisotropic 2Ψ component is plotted).

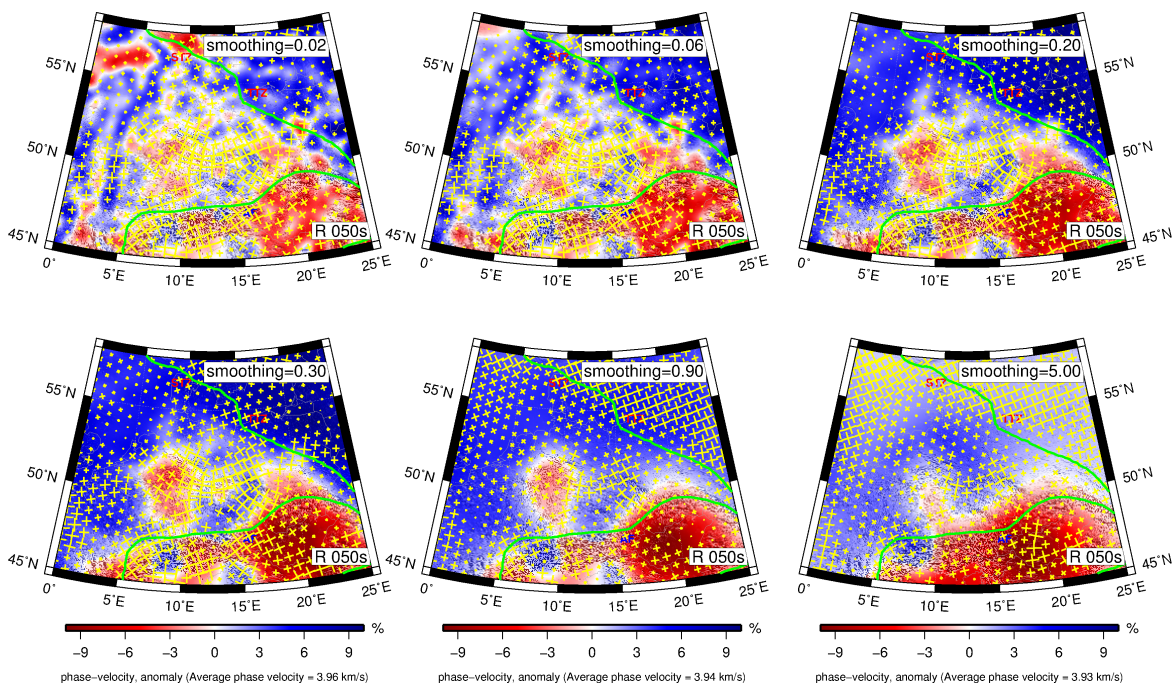


Fig. 5.7: Same as fig. 5.6. Isotropic and Rayleigh wave 4Ψ component is plotted here.

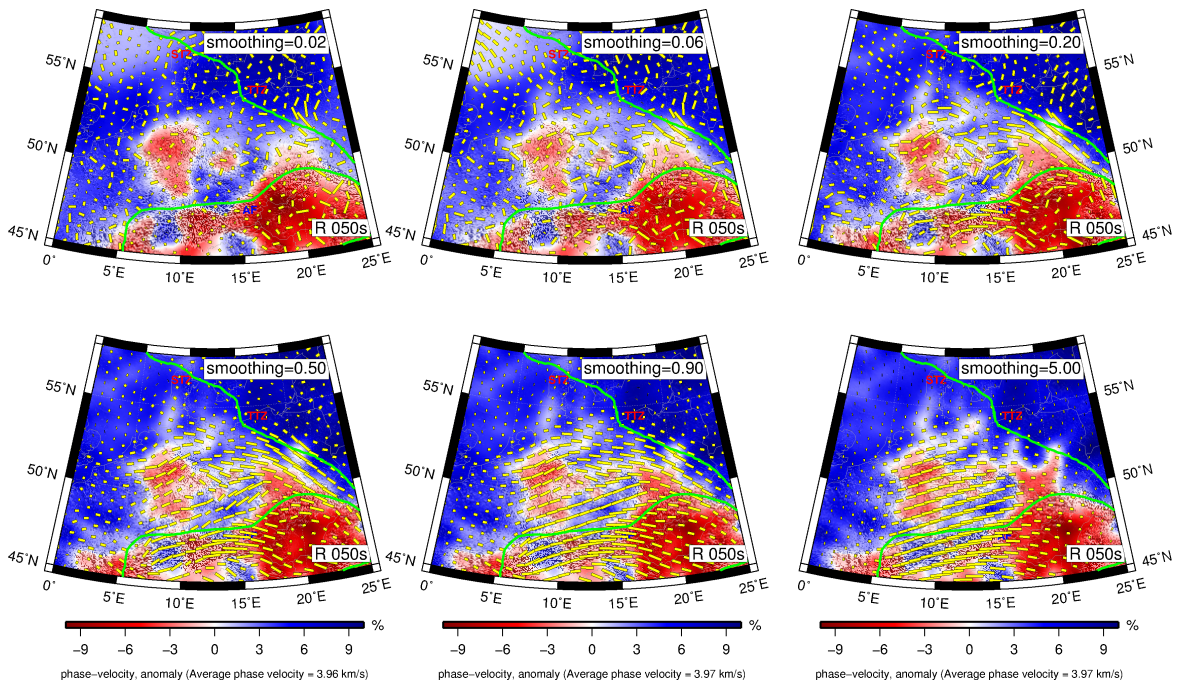


Fig. 5.8: Effect of varying anisotropic damping on Rayleigh wave phase velocity maps. Isotropic and 4Ψ damping is fixed (here Rayleigh wave isotropic and anisotropic 2Ψ component is plotted).

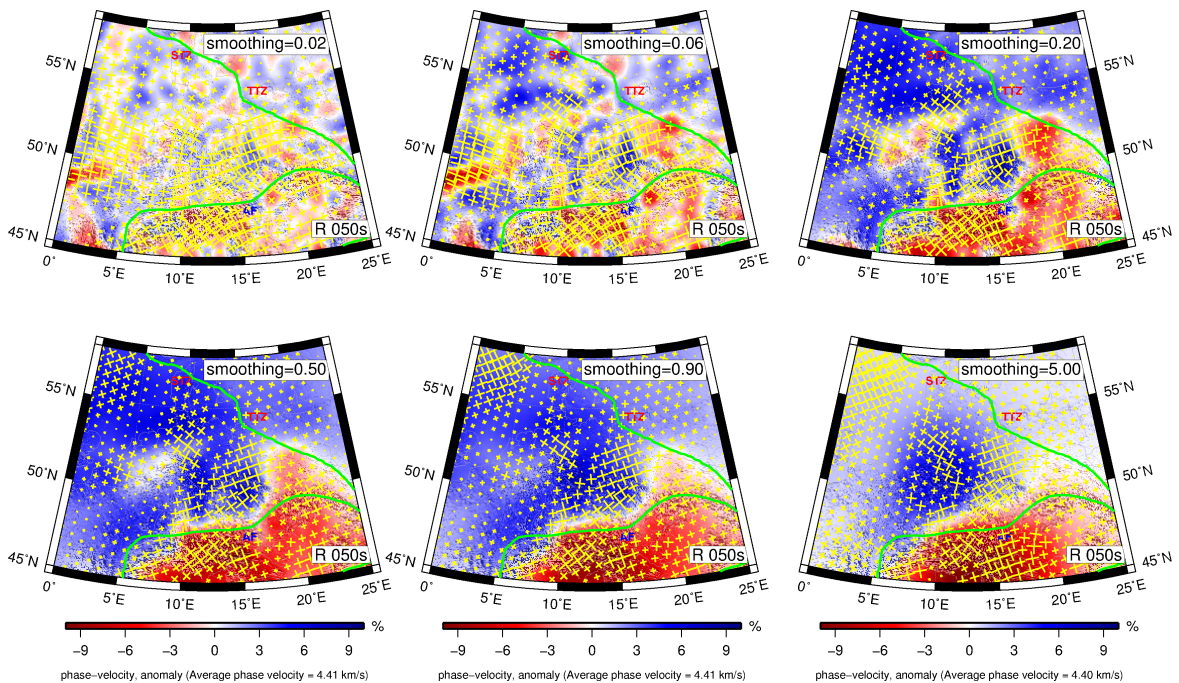


Fig. 5.9: Effect of varying isotropic damping on Love wave phase velocity maps. Love wave 2Ψ and 4Ψ components are fixed (here Love wave isotropic and anisotropic 4Ψ component is plotted).

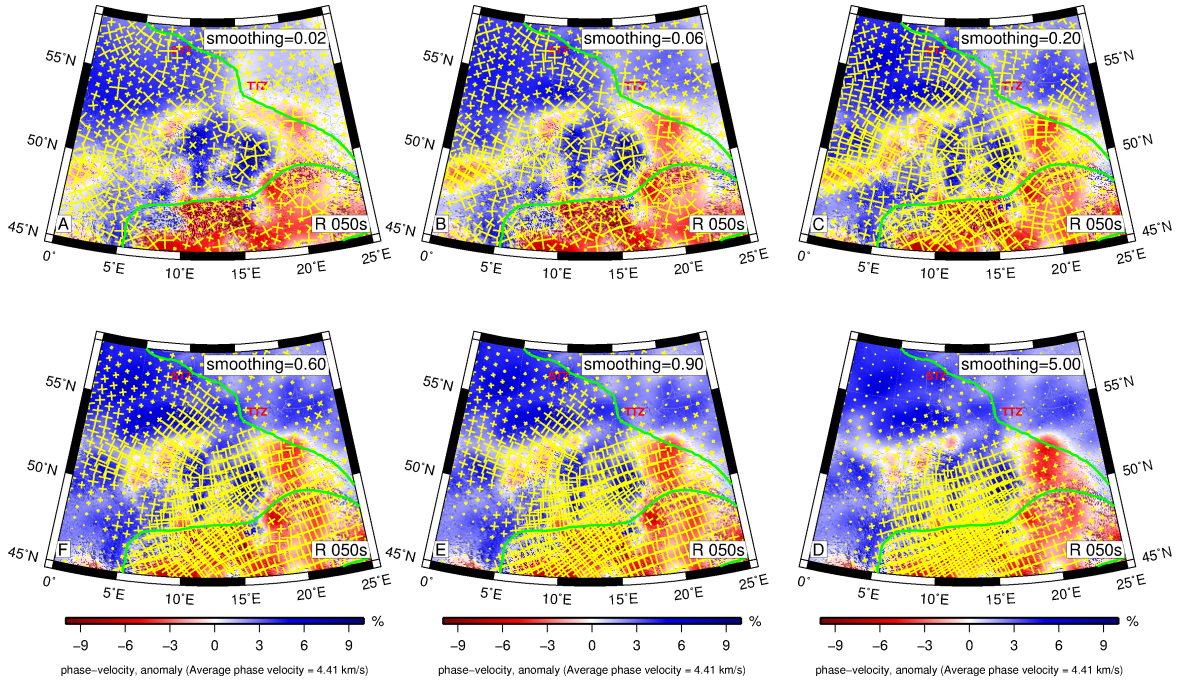


Fig. 5.10: Effect of varying anisotropic damping parameters for Love wave phase velocity maps. Isotropic and 2Ψ components are fixed. (here Love wave isotropic and anisotropic 4Ψ component is plotted).

To solve the system of linear equations in a discrete way, I follow Deschamps et al. (2008). To determine the lateral isotropic and anisotropic anomalies, it is noted that,

$$d = Gm,$$

Here d is data vector which contains the path average phase anomalies for Rayleigh and Love waves obtained from the dispersion curves at each period.

m is the model vector which contain 5 terms (one for isotropic part and two each for 2Ψ and 4Ψ anisotropy at each grid knot (see equations 5.1, 5.2, 5.3).

Suppose N is the number of paths at each period and M is the number of knots, we can write the transposed data and model vectors in the following way:

$$d^T = (\overline{\delta C_1} \dots \overline{\delta C_N}),$$

and

$$m^T = (\delta C_{iso,1} \dots \delta C_{iso,M} A_{2\Psi,1} \dots A_{2\Psi,M} B_{2\Psi,M} A_{4\Psi,1} \dots A_{4\Psi,M} B_{4\Psi,M}), \quad (5.9)$$

We can construct the G matrix with the help of sub matrices, each for isotropic, 2Ψ , and 4Ψ terms.

These sub matrices can be constructed as follows

$$G = (G_{iso} \quad G_{C2\Psi} \quad G_{S2\Psi} \quad G_{C4\Psi} \quad G_{S4\Psi}), \quad (5.10)$$

$$G_{iso} = \begin{pmatrix} K_{11} & \dots & K_{1M} \\ \dots & \dots & \dots \\ K_{N1} & \dots & K_{NM} \end{pmatrix},$$

$$G_{C2\Psi} = \begin{pmatrix} a_1 K_{11} & \dots & a_1 K_{1M} \\ \dots & \dots & \dots \\ a_N K_{N1} & \dots & a_N K_{NM} \end{pmatrix}, \quad G_{S2\Psi} = \begin{pmatrix} b_1 K_{11} & \dots & b_1 K_{1M} \\ \dots & \dots & \dots \\ b_N K_{N1} & \dots & b_N K_{NM} \end{pmatrix},$$

$$G_{C4\Psi} = \begin{pmatrix} c_1 K_{11} & \dots & c_1 K_{1M} \\ \dots & \dots & \dots \\ c_N K_{N1} & \dots & c_N K_{NM} \end{pmatrix}, \quad G_{S4\Psi} = \begin{pmatrix} d_1 K_{11} & \dots & d_1 K_{1M} \\ \dots & \dots & \dots \\ d_N K_{N1} & \dots & d_N K_{NM} \end{pmatrix}.$$

Here K_{ij} are the weights of the individual path i and knot j .

Due to automated approach we have achieved very high path density in central Europe (see fig. 5.3).

The amount of damping affects the tomographic inversion results. Normally two types of damping is used i.e. smoothing and gradient damping. The proper choice of these damping parameters affects overall shape of the tomographic maps. Over-smoothing penalizes the phase velocity maps with decreased resolution, whereas under-smoothing may introduce some artifacts due to noise or data errors (Darbyshire & Lebedev, 2009).

The first type of damping ("smoothing") penalizes the second lateral derivative of the phase velocity distribution (Deschamps et al., 2008). It is calculated by minimizing the difference at each knot with the average value of the nearest neighbors. This type of damping is suitable to retrieve regular gradients, the small scale local anomalies are averaged out.

In the second type of damping ("gradient damping"), the difference between two adjacent knots is penalized (Darbyshire & Lebedev, 2009). This type of damping is similar to taking the first derivative of the anomaly distribution.

It is subjective to quantify the amount of regularization; this depends upon the data and area under investigation. Therefore, in order to find optimal values of the regularization, extensive tests are needed to obtain meaningful results, which are not artifacts.

5.2.1 Effect of regularization

In order to find the optimal regularization, we conducted series of tests. We performed inversions by varying the lateral damping and smoothing by keeping the norm damping small (a fixed value of 0.2). We varied the isotropic and anisotropic damping values from 0.1 to 1.0, respectively. For each isotropic damping value we varied anisotropic damping from 0.1 to 1, and similarly for each anisotropic damping value we varied isotropic damping from 0.1 to 1. This forms a matrix of 81 elements with 9 rows and 9 columns, each row of the matrix represents different isotropic damping values at particular anisotropic damping, and similarly every column represents different values of anisotropic damping at particular isotropic damping.

For each damping value we have plotted a pie wedge plot (see fig. 5.5), the left half circle tells us the value of the data variance and right half circle shows model norm values. It can be observed in figure 5.5 that, in the lower left part of the plot the value of data variance is low and solution value is high, similarly in the upper right part of plot, the data variance is high but the solution norm has low value. This shows that, these damping values are unacceptable and may give some artifacts in the results. The portion with yellowish color forms a kind of "L" shape; these values of the damping are the preferred ones. This type of test is very helpful in finding the range of damping parameters for both isotropic and anisotropic damping by narrowing down the models to be viewed. We carefully looked at all the models, and our visual inspection also confirms that, very low and very high damping parameters give unfavorable results. When we apply small regularization, we get smaller anomalies. These small scale anomalies do not explain the model efficiently, and very high values of damping reduce the resolution. Therefore, with the help of this test we may come to agreeable values of the damping parameters.

The effect of high and low damping is visible in the figure 5.5. High values of the damping converge solution readily, with a low value of the solution. Similarly, the low damping values make the inversion difficult to be converged, here the value of variance is low and the value of solution is high. Therefore, it makes sense that the intermediate values of the damping parameters provide reasonable result, which is not over-damped and does not contain any possible artifacts. In figure 5.11 we have plotted phase velocity maps with a range of smoothing values. It is observed that, by increasing the isotropic and anisotropic smoothing the resolution decreases. When we introduced high isotropic damping, we observed that, isotropic signal leaked to anisotropic part (see fig. 5.6), similar effect of leakage in isotropic part is observed as well when we over damped the anisotropic part (see fig. 5.8). With low value of damping parameters, errors in dispersion measurements may dominate the resulting phase velocity maps. High damping parameters in one hand decrease the resolution and in other hand they provide a dominant feature of the particular region. With this extensive testing of different values of the damping parameters helped us in finding the optimal values.

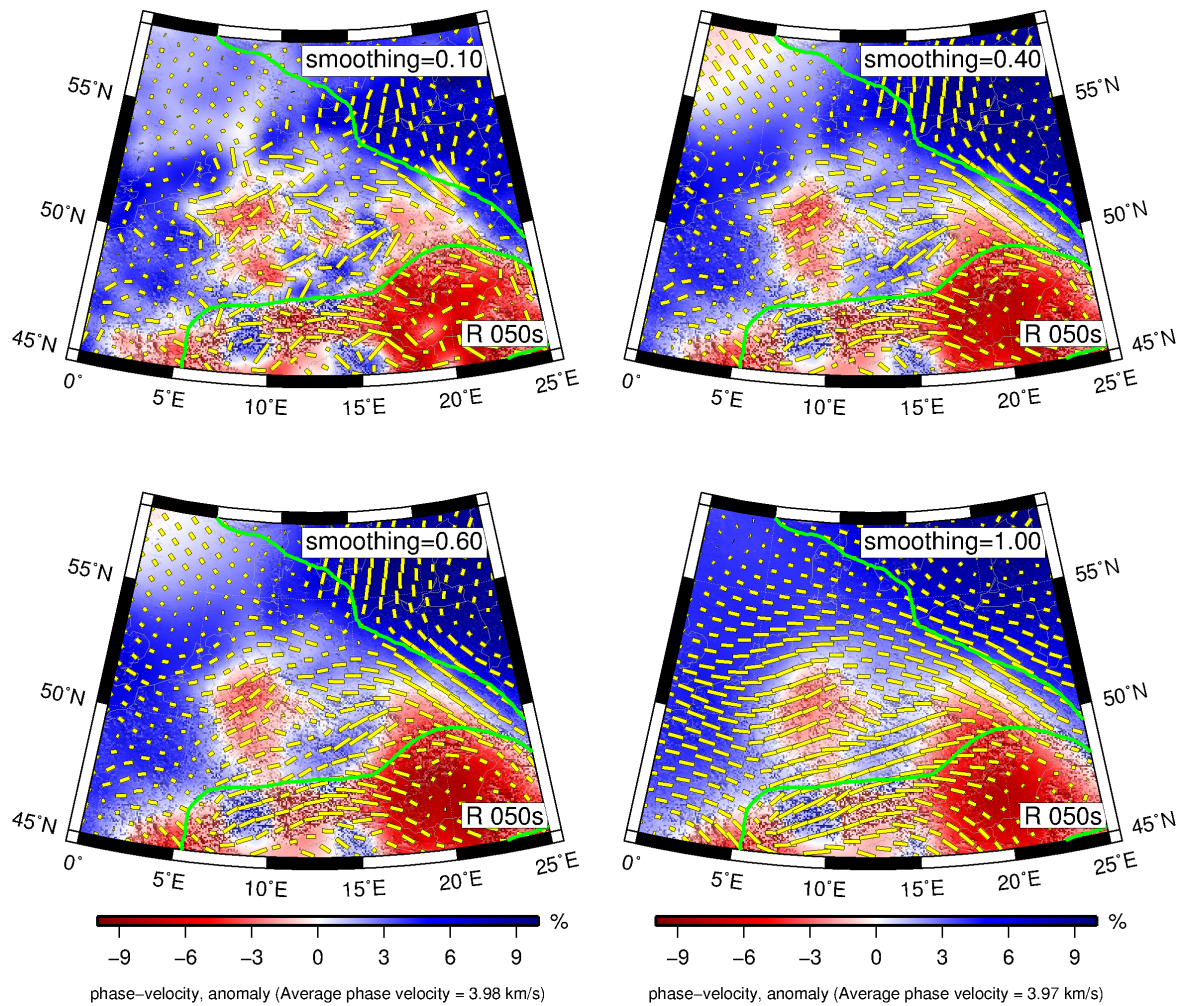


Fig. 5.11: Effect of smoothing on phase velocity maps. Smoothing values of 0.1, 0.4, 0.6 (our preferred value), 1.0 are plotted here.

5.2.2 Finding optimal damping parameters

The result of the L curve test (see fig. 5.5) helps to reduce the no. of models to be looked visually in order to find the optimal parameters.

Rayleigh wave optimal damping parameters

In order to find the optimal isotropic and anisotropic damping parameters, first we fixed anisotropic damping and varied isotropic damping in a range from 0.02 to 5. The result of this test is shown in figure 5.6. In Fig. 5.6 (top left) the small scale anomalies are visible. These small scale anomalies are difficult to explain. High isotropic damping may appear in the shape of increased amplitude of anisotropic terms. This effect can be noticed in Fig. 5.6 (bottom right) where the isotropic amplitude is strongly reduced

and appear in the form of leakage in anisotropy. The similar leakage effect is observed in 4Ψ anisotropic component as well (see fig. 5.7 bottom right) where the 4Ψ amplitude is increased significantly.

From this test we can conclude that the optimal isotropic damping value for 50 s phase velocity map is 0.3.

In order to finalize the optimal damping values for 2Ψ anisotropic components (see fig. 5.8) we first fixed the damping values of isotropic component and anisotropic 4Ψ component and varied the 2Ψ anisotropy from a damping value of 0.02 to 5. With low 2Ψ damping value, the anisotropy is not well constrained and have irregular directions of the anisotropy (see 5.8 top left). With high 2Ψ anisotropic damping the effect of leakage appears in isotropic part (see fig. 5.8 bottom right). For 50 s phase velocity maps (see fig. 5.8), we found that a damping value of 0.5 is a reasonable choice, and further increase in anisotropic damping reduce the anisotropic amplitude and appear as leakage in the isotropic part whereas the fast directions remain stable. We carried similar test at each period separately. The optimal damping parameters at each period are presented in the tabular form (see table 5.1).

The damping parameters for different periods or range of periods are chosen differently due to variable number of measurements at each period. In general the damping value for higher periods is kept high due to long wavelength nature of these long periods waves and fewer number of measurements at these periods.

Love wave optimal damping parameters

The Rayleigh wave phase velocities require both 2Ψ and 4Ψ terms but Love waves require only 4Ψ terms (Trampert & Woodhouse, 2003). We observed significant 2Ψ signal on the Love wave phase velocity maps. This may be due to the presence of Rayleigh wave energy on transverse components (Adam & Lebedev, 2012), but in general our Love wave 2Ψ signal is either lower or comparable to Love wave 4Ψ signal.

We adapted similar procedure to find optimal damping parameters for Love waves. For isotropic damping parameter we fixed the damping values of anisotropic components (2Ψ and 4Ψ) and varied isotropic damping. The result of this test is shown in Fig. 5.9, where we have plotted 50 s phase velocity maps with different damping values ranging from the damping value of 0.02 to 5. It is clear that with low damping values the small scale anomalies are visible which are difficult to explain, and with high isotropic damping the isotropic signal leaks in the anisotropy with increase in the amplitude of the anisotropy. We performed this test individually to all periods and found different damping parameters at each period (or certain period range, shown in table 5.1).

In order to finalize the Love wave anisotropic 4Ψ component, we fixed the damping value of isotropic and 2Ψ component and varied 4Ψ component. The result of this test is shown in figure 5.10. Similar effect as with Rayleigh waves is observed here as well.

Table 5.1: Damping parameters used to obtain Rayleigh and Love wave phase velocity maps

Per. range	Rayleigh		Love	
	Iso damping	Aniso damping	Iso damping	Aniso damping
10-40	0.2	0.3	0.4	0.5
50-70	0.3	0.4	0.5	0.6
80-100	0.5	0.6	0.6	0.7
110-300	0.6	0.7	0.7	0.8

If we look at the figure 5.10 (top left) we see an irregular pattern of the anisotropy, and in the figure 5.10 (bottom right), we see that anisotropic signal appears in the form of leakage in the isotropic part.

Therefore, we can conclude that for 50 s Love wave phase velocity maps a damping value of 0.6 is reasonable choice, though it is somewhat difficult to constrain the Love wave damping parameters as compared to Rayleigh wave, there are various reasons for that, the most significant is the lower signal to noise ratio at horizontal components, interference with higher order Love wave modes and with fundamental mode Rayleigh waves.

By keeping in view these factors in mind and also with the visual inspection of the phase velocity maps we have chosen slightly higher damping values both for isotropic and anisotropic ones with respect to Rayleigh waves.

The final damping parameters for Love wave isotropic and anisotropic components are listed in table 5.1.

5.2.3 Resolution tests

In order to assess the isotropic resolution of Rayleigh and Love wave phase velocity maps, we carried out checkerboard test. The checkerboard consists of diamond-shaped anomalies, the diamond shape is chosen due to triangular model and data grid. We varied the size of checkers from 100 km to 3 °. Here we plotted anomalies with two sizes i.e. 100 km and 150 km. The result of this test is shown in figure 5.12 for Rayleigh and for Love waves it is shown in figure 5.13. From figure 5.12 (left) it can be noted that the anomalies in terms of amplitude and shape at central and southern Europe are well resolved as compared to north, north-west, and north-east. Therefore, the resolution reaches 100 km in the regions of high path coverage (central Europe), it is 150 km otherwise. We performed this test for all periods. Here we show the result of checkerboard test for three representative periods, i.e 12 s, 30 s, and 60 s, which represent lower crust, upper mantle and deeper structures. The resolution at 30 s is

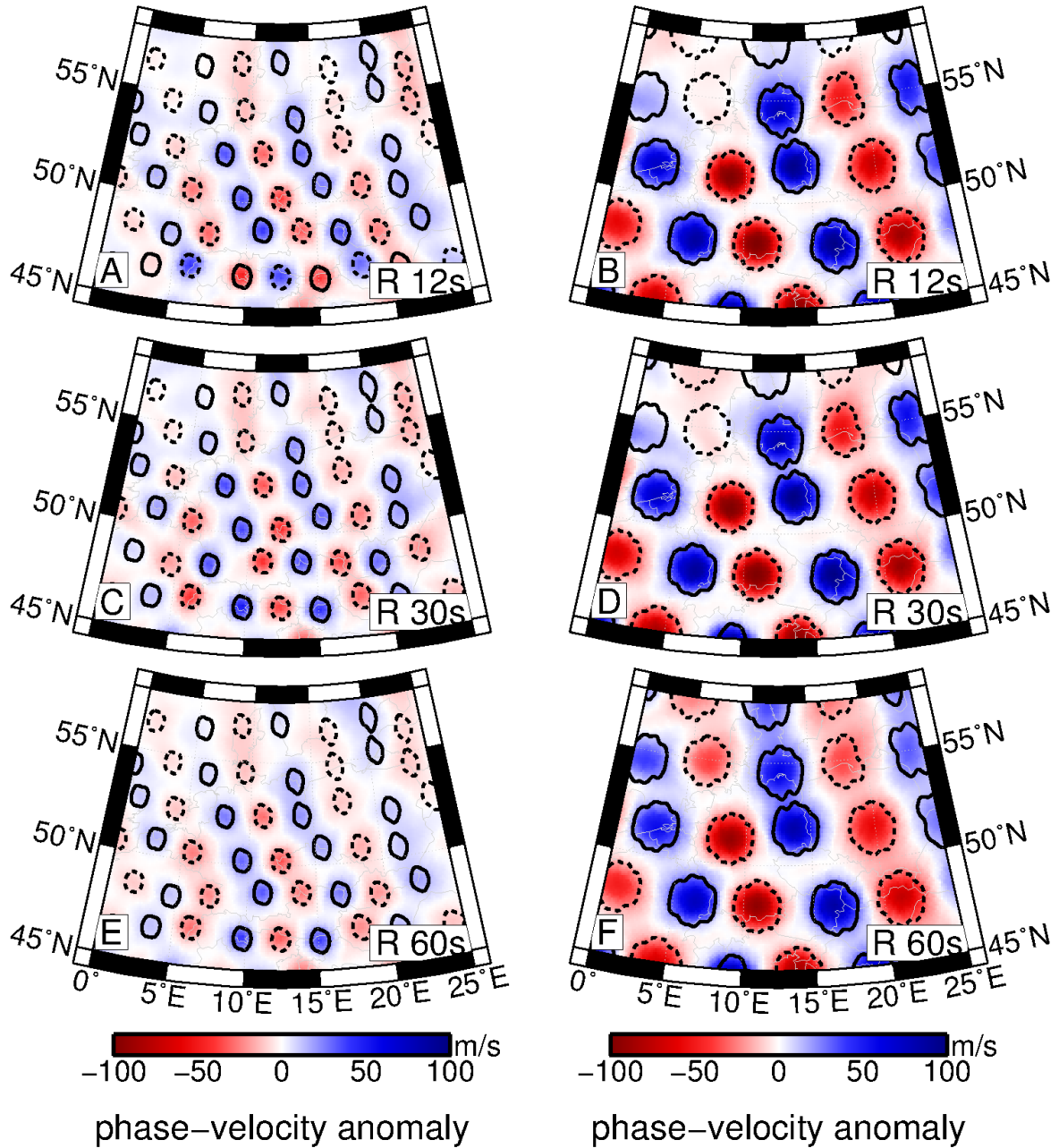


Fig. 5.12: Rayleigh wave isotropic checker-board tests with anomalies of approximately 100 km (left) and 150 km (right) size and 100 m/s input amplitude. Solid and dashed outlines mark positive and negative input anomalies, respectively.

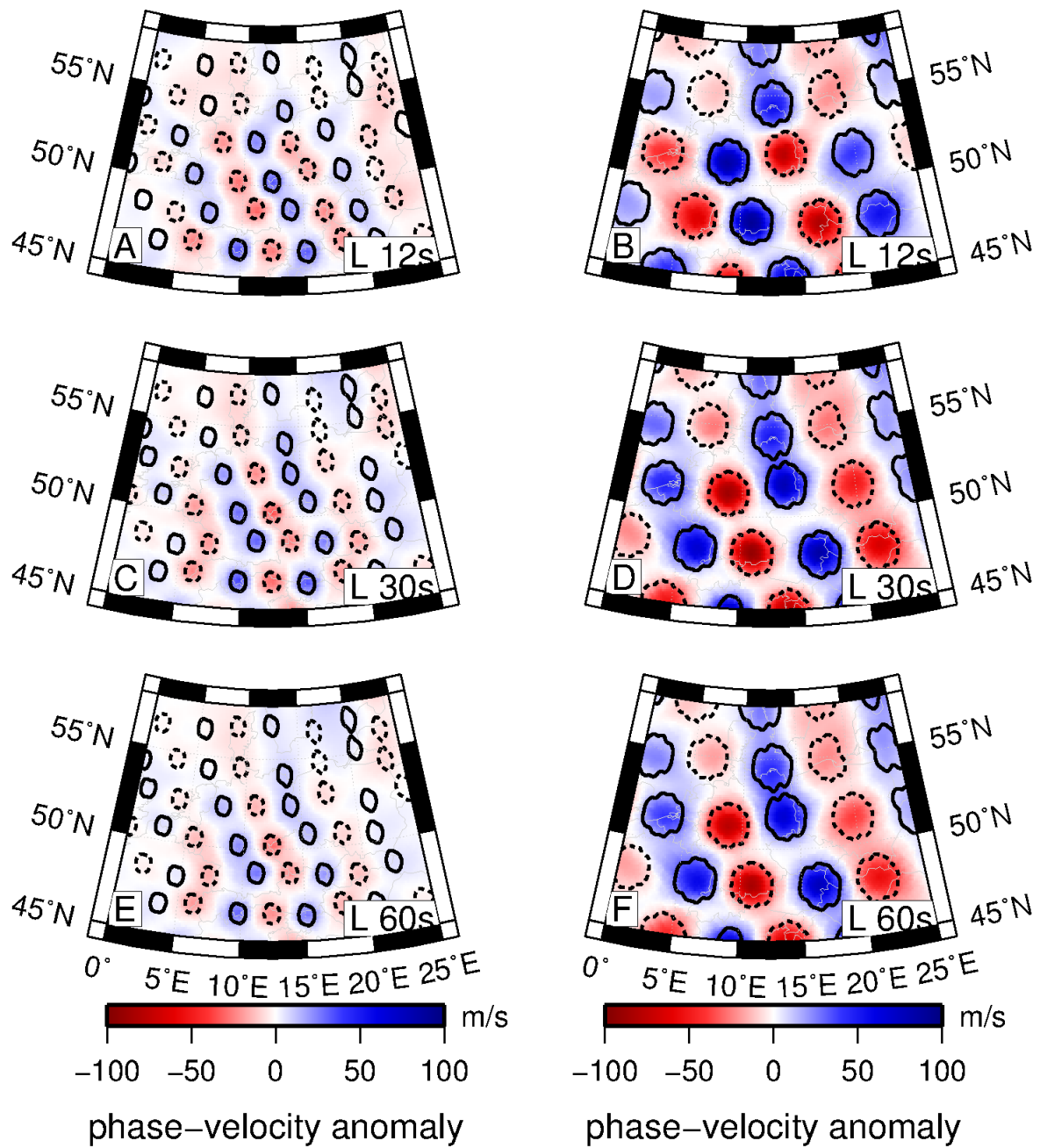


Fig. 5.13: same figure as fig. 5.12 is plotted for Love waves.

highest and slightly decreases at lower and higher periods. Overall we have resolution of 150 km at all periods (see fig. 5.12).

The number of paths for Love wave is around one third of the Rayleigh wave paths, for example, there are around 18000 inter-station paths at 30 s period for Love wave compared to 43000 paths for Rayleigh wave at same period. Therefore, we have very dense path coverage for the Love wave as well. Due to lower path coverage compared to Rayleigh wave, it is generally considered that the resolution of Love wave is poor as compared to Rayleigh wave, but if we look at the result of the checkerboard test for 30 s Love wave (see fig. 5.13), high and low anomalies are properly recovered at central Europe even with 100 km checker size.

Therefore, we can conclude that we have 100 km resolution at some parts in the central Europe, and overall we have resolution of 150 km for Love wave as well.

5.3 Reliability test for Rayleigh wave 2Ψ Anisotropy

The phase velocity maps obtained through the tomographic inversion that solves both isotropic and anisotropic parameters may contain artifacts. These artifacts arise due to leakage between isotropic and anisotropic parameters or spurious anisotropy due to path bias (Darbyshire & Lebedev, 2009). We performed a 90° rotation test as illustrated by Darbyshire & Lebedev, 2009 to the phase velocity maps obtained through tomographic inversion of the surface wave data. This test is helpful to quantify the spurious anisotropy caused by leakage between isotropic and anisotropic parameters or due to path bias.

We rotated the 2Ψ component of the phase velocity maps by 90° and computed the synthetics, and re inverted the synthetics and compared the direction and amplitude of the anisotropy between synthetic and rotated models. The significant reduction in amplitude and direction of the rotated anisotropy indicate the leakage between isotropy and anisotropy or due to path bias.

We have defined mainly two criteria, in order to remove the nodes where there is significant reduction in amplitude or shift in the direction. They are illustrated in section 5.3.1

5.3.1 Removal of unresolved node

We introduce mainly two criteria to automatically remove unresolved nodes. 1) deviation from the anisotropic direction, 2) deviation in anisotropic amplitude.

But before applying these above mentioned criteria, we first examine the nodes with small amplitudes and exclude them from testing for recovery of amplitude and direction

of the anisotropy, as it is meaningless to check nodes with smaller amplitudes. Therefore, we keep those nodes whose amplitude is smaller than certain threshold value.

The criterion to preserve smaller amplitude nodes is formulated below

$$a_{obs} > \bar{a}_{obs} \times a_{th}, \quad (5.11)$$

where a_{obs} is the amplitude of the anisotropy of the inversion result, \bar{a}_{obs} is mean amplitude, and a_{th} is the threshold value. The threshold value is chosen empirically (here it is 1/3 of the mean amplitude). We exclude the nodes which do not satisfy above criterion, and check remaining ones for anisotropic amplitude and fast direction.

1. Deviation from the anisotropic direction

In order to test recovery of anisotropic direction, we calculate the difference between synthetics (θ_{syn}) and rotated anisotropy (θ_{rot}) and compare it with certain threshold. The criterion is formulated as follows

$$\sigma\theta_{rot} = |\theta_{rot} - \theta_{syn}| < \theta_{th}, \quad (5.12)$$

where θ_{syn} is anisotropic direction of the synthetics, θ_{rot} is rotated anisotropy, and θ_{th} is the anisotropic direction threshold for removal of the anomalous nodes (see text for the description about thresholds and preferred value used). We remove those nodes that violate above criterion.

To find optimal thresholds for anisotropic direction we fixed the amplitude threshold with a relaxed value of 100%, with this threshold value we do not check anisotropic amplitude; this will help to see the effect of anisotropic direction only.

We varied the direction of anisotropy from threshold value of 0° to 90° , where 90° is loose threshold, and 0° (difference between synthetics and rotated anisotropic directions is 0°) is very strict, it is clear that, there is certain amount of leakage present in the models, and there is always a certain amount of shift in the anisotropic direction.

In order to find the optimal threshold value, we tested different values of anisotropic direction threshold from 0° to 90° with the step of 25° . 0° and 90° are two end members, we have to choose threshold value in between these two levels. The thresholds we tested are: 0° , 25° , 50° , 75° , and 90° . From this test we conclude that 50° threshold value is reasonable choice. The result of this test is shown in figure 5.14.

In order to explain the figure 5.14, first lets define some terms. The result of the inversion: M, 90° rotated (synthetic): M90, 90° inversion result: $M90_{rot}$. In figure 5.14 mainly three thresholds are plotted, which are: $\sigma\theta_{rot} = 90^\circ$ (top), $\sigma\theta_{rot} = 50^\circ$ (middle), and $\sigma\theta_{rot} = 0^\circ$ (bottom). As stated earlier that 0° and 90° are two end members.

In figure 5.14 top, the green color indicates the accepted nodes, as green color is prevalent here, this shows that, this threshold value is very loose. In middle of the figure 5.14 the threshold ($\sigma_{\theta_{rot}}$) value of 50° is tested, with this threshold we accept the nodes where the difference between synthetics ('M90') and rotated anisotropy (' $M90_{rot}$ ') is less than 50° , the violating nodes are removed automatically. The effect of applying this threshold is visible in areas where the anisotropy is unresolved which include the nodes in north–west and north–east and some nodes in south. The other threshold we tested is 0° , with this threshold value we accept the nodes (with green color) where the synthetics ('M90') and rotated anisotropy (' $M90_{rot}$ ') are at exactly 0° , it is very difficult to achieve exactly 0° difference between synthetics ('M90') and rotated anisotropy (' $M90_{rot}$ '), this is visible in the figure 5.14 bottom, that there are very few green colored nodes.

2. Deviation in amplitude

As far as the amplitude of anisotropy is concerned, there may be some reduction in the amplitude of recovered anisotropy. Therefore, the amplitude criterion will help to estimate the amount of reduction in amplitude and will remove those nodes where they are below certain threshold.

The amplitude criterion is formulated as follows.

$$\sigma_{a_{rot}} = \left| \frac{\hat{a}_{rot} - a_{syn}}{a_{rot}} \right| < a_{th}. \quad (5.13)$$

Where a_{syn} is the amplitude of the synthetics, a_{rot} is the amplitude of the rotated anisotropy, \hat{a}_{rot} is average anisotropic amplitude, and a_{th} is amplitude threshold (see text for the description about thresholds and preferred value used).

From this equation, we calculate the difference in the synthetics ('M90') and rotated (' $M90_{rot}$ ') amplitudes of the anisotropy, and compare this with a threshold value. We remove those nodes where the difference in two amplitudes (i.e. 'M90', and ' $M90_{rot}$ ') is less than a_{th} . The result of the test is shown in figure 5.15.

In order to find the optimal threshold value, we first fixed the threshold value for anisotropic direction, and made it loose enough in order to see the effect by changing different amplitude thresholds. The thresholds we tested are: 0%, 25%, 50%, 75%, and 100%, where 0% is very strict (the difference in amplitude of synthetics 'M90' and rotated anisotropy ' $M90_{rot}$ ' is zero), it is difficult to obtain 100% recovery in amplitude, this can be observed in fig. 5.15 (bottom), therefore we need to increase the threshold value. The other end member is 100%, with this threshold we accept almost all nodes (see fig. 5.15 top). Therefore, we have to choose values in between 0% and 100%, where 0% is strict and 100% is loose. From the result of this test, it is observed that a threshold value of 50% (see fig. 5.15 middle) is a reasonable choice, with this threshold value we reject those

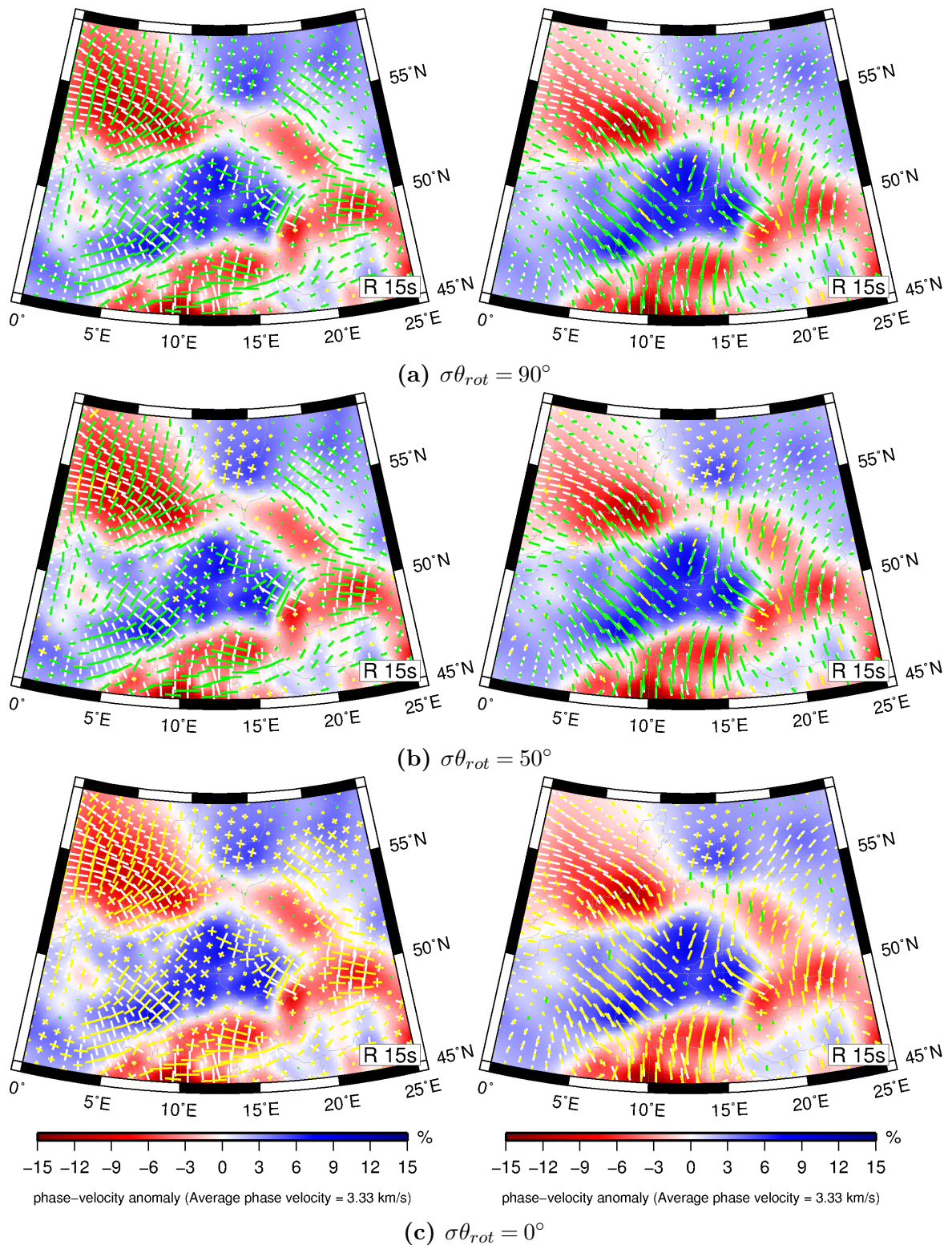


Fig. 5.14: Various anisotropic direction thresholds ($\sigma_{\theta_{rot}}$) are tested to see the effect of these threshold values for Rayleigh waves. On the left column the inversion result is plotted in yellow and the shifted result is plotted in white and the nodes where the anisotropy is resolved is plotted in green color. On the right column the result of the resolution test is plotted. Here yellow colored bars are input to resolution test, output of the resolution test is plotted in white, and the green colored nodes are accepted ones after applying the amplitude and direction criteria.

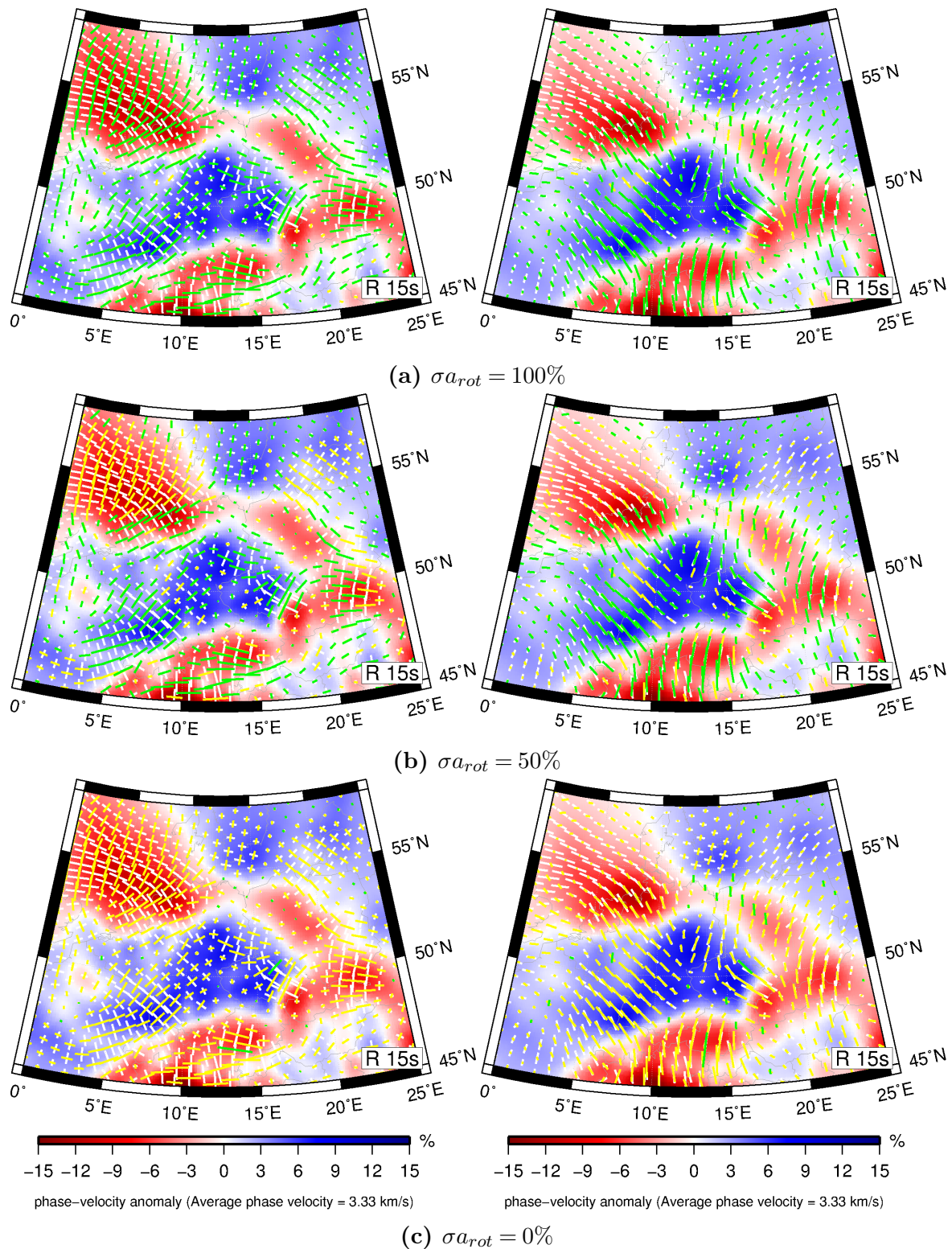


Fig. 5.15: Different thresholds to test the recovery of amplitude of the anisotropy for Rayleigh waves. On the left column the inversion result is plotted in yellow and the shifted result is plotted in white and the nodes where the anisotropy is resolved is plotted in green color. On the right column the result of the resolution test is plotted. Here yellow colored bars are input to resolution test, and output of the resolution test is plotted in white and the green colored nodes are accepted ones after applying the amplitude and direction criteria.

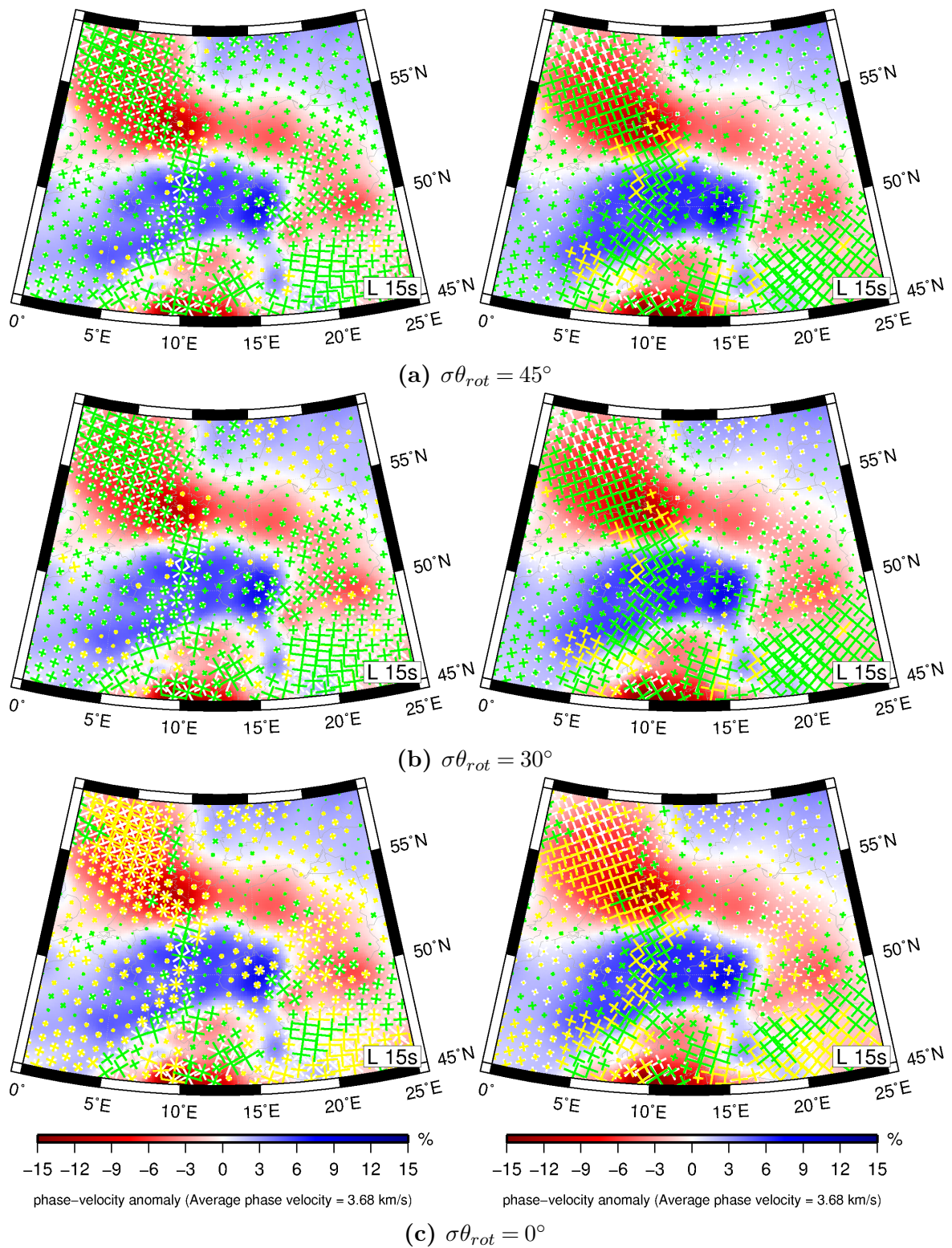


Fig. 5.16: Same as figure 5.14 for Love waves.

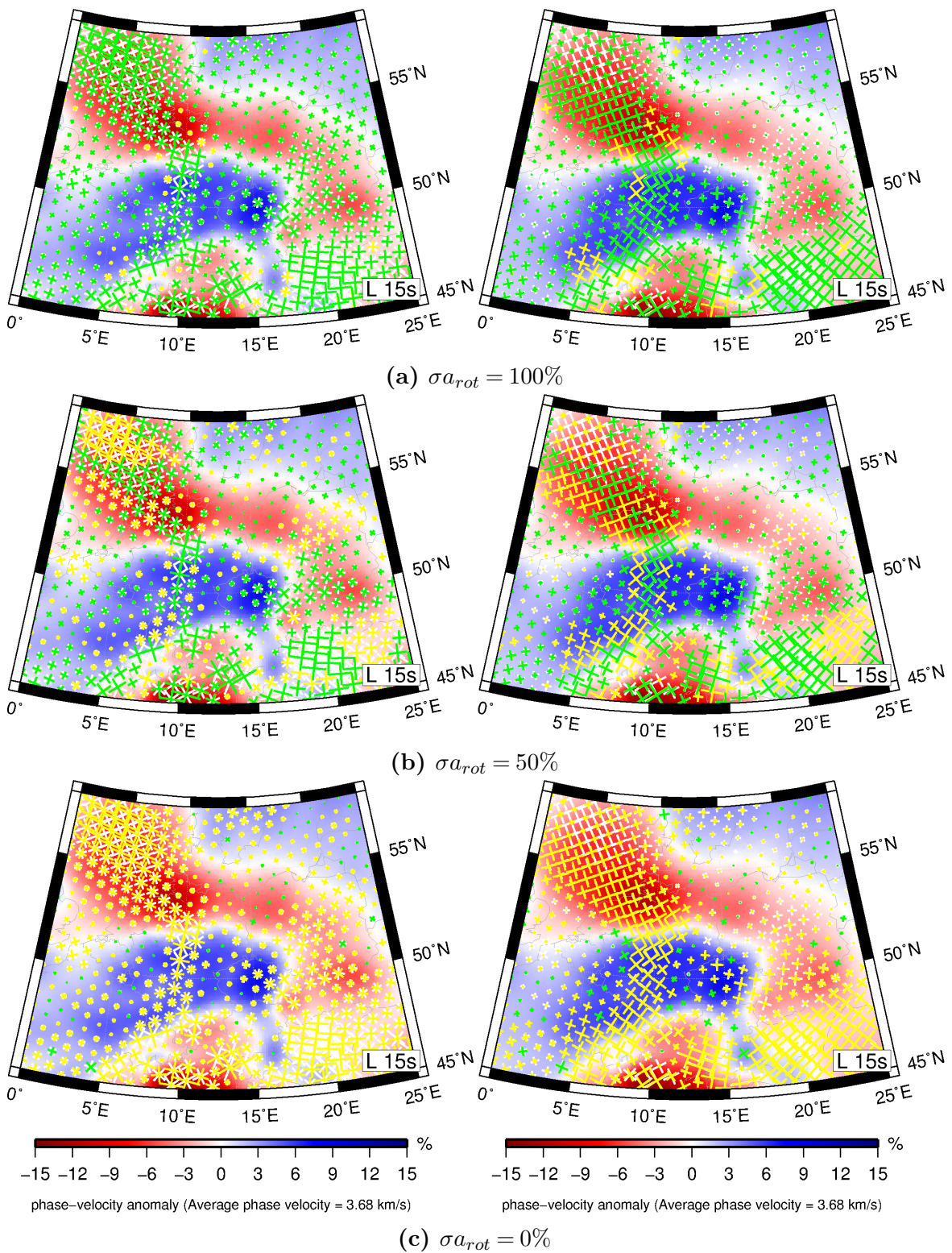


Fig. 5.17: Effect of changing anisotropic amplitude threshold for Love waves.

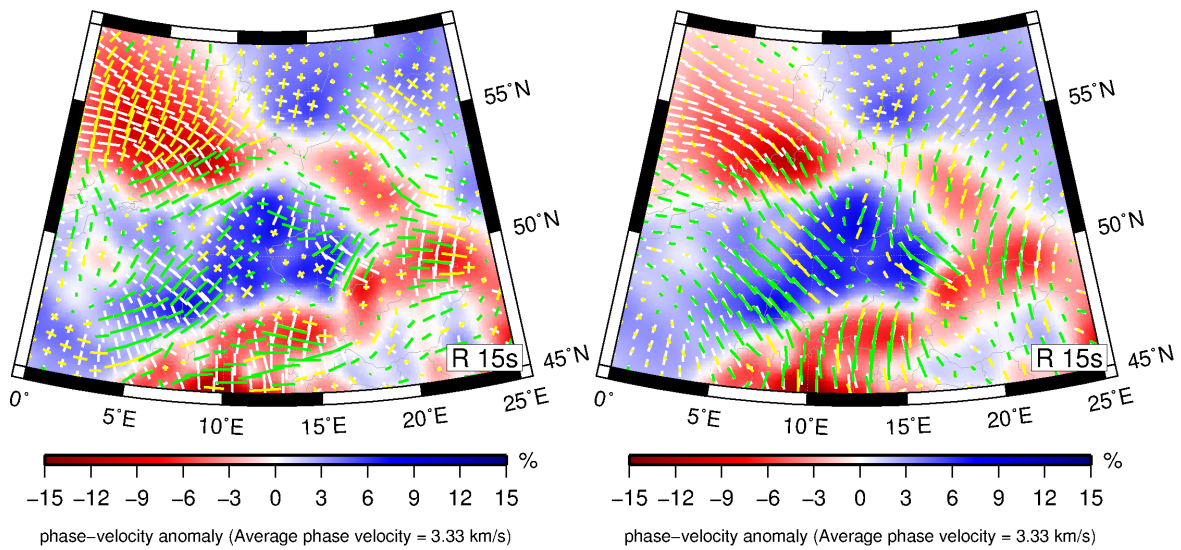


Fig. 5.18: The resulting Rayleigh wave phase velocity maps after finalizing the threshold parameter for anisotropic amplitude and direction (parameters used $\sigma_{\theta_{rot}} = 50^\circ$, $\sigma_{a_{rot}} = 50\%$). On left column the inversion result is plotted in yellow and the shifted result is plotted in white and the nodes where the anisotropy is resolved is plotted in green color. On the right column the result of the resolution test is plotted. Here yellow colored bars are input to resolution test, and output of the resolution test is plotted in white. The green colored nodes are accepted nodes after applying the amplitude and direction criteria.

nodes, where amplitude recovery is less than 50%. The 50% amplitude recovery is adequate enough as our main criterion is anisotropic direction threshold.

Fig. 5.18 is plotted after finalizing the amplitude and direction threshold for Rayleigh wave phase velocity maps. In figure (see fig. 5.18 left) the yellow bars are the tomographic inversion result (defined as 'M'), white bars are the 90° rotated anisotropy (defined as 'M90') and green colored nodes are the accepted nodes.

In figure (see fig. 5.18 right) the yellow bars are synthetics (defined as 'M90'), white bars are output of the resolution test (defined as 'M90_{rot}'), and green colored bars are the accepted nodes. The change in the amplitude and fast direction may indicate spurious anisotropy or leakage with other components (isotropic and 4Ψ). Therefore, this test is very useful, in order to know the areas where anisotropy in terms of amplitude and direction is well recovered and vice versa.

It can be observed that most of anisotropy is recovered except certain parts e.g. north-west and south-west and some parts near the Pannonian basin. Overall the result of this test shows that anisotropy is recovered in the areas with good path coverage (e.g. central Europe).

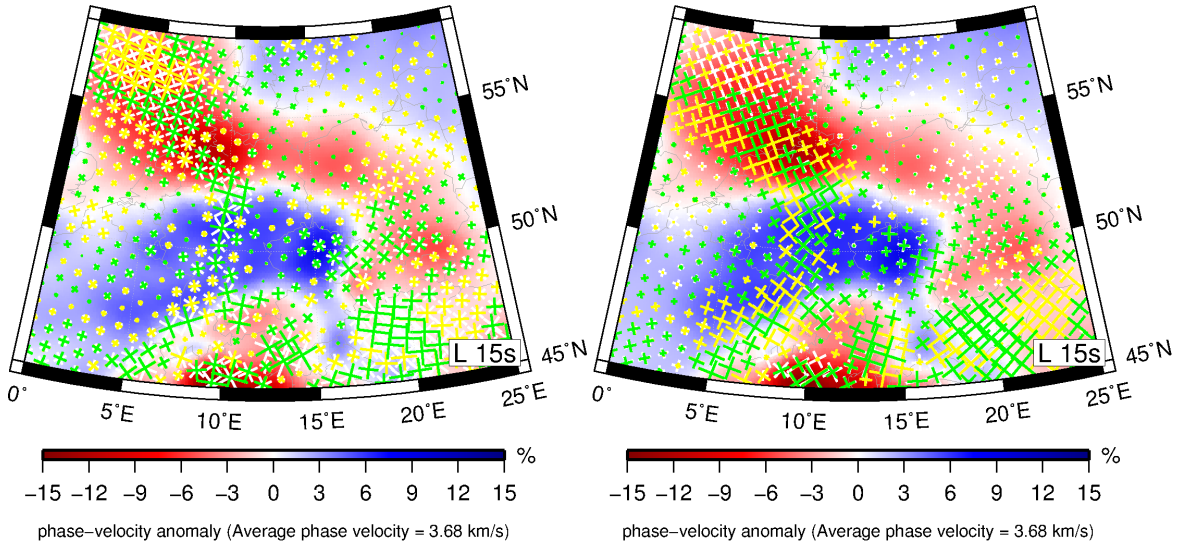


Fig. 5.19: same as figure 5.18, here plotted for Love wave.

5.4 Reliability test for Love wave 4Ψ Anisotropy

In order to test the reliability of the fast directions for Love waves which is $\pi/2$ periodic, we rotated the 4Ψ anisotropy by 45° and computed the synthetics. The synthetics is inverted and the inversion result ($M_{90_{rot}}$) is compared with the synthetics (M_{90}), to identify the unresolved nodes in terms of amplitude and direction of the anisotropy and later on remove these unresolved nodes automatically.

To accomplish this, we applied the similar procedure as for Rayleigh waves, with a difference in threshold limits of the fast direction. For Love waves the end members are 0° and 45° , where the threshold value of 0° is strict and 45° is loose one.

5.4.1 Removal of unresolved node

To find optimal amplitude and direction threshold limits for Love wave anisotropy, we fixed the direction of the anisotropic direction with the relaxed value of 45° and tested different amplitude threshold ranging from 0% to 100%. We concluded that 50% deviation in amplitude similar as Rayleigh waves is optimistic choice. Fig. 5.17 shows different amplitude thresholds for Love wave anisotropy.

To find optimal threshold parameter for anisotropic direction, we fixed amplitude to a relaxed value of 100% and varied the threshold values for anisotropic direction from 0° to 45° . We found 30° threshold as optimal choice for Love wave. The result of this test for anisotropic direction is shown in figure 5.16.

To explain the figure 5.16 first let us define some terms. The result of the inversion: M , 45° rotated (synthetic): M_{45} , 45° inversion result: $M_{45_{rot}}$. Similar as Rayleigh wave

(see fig. 5.18) we have plotted three thresholds, which are: $\sigma_{\theta_{rot}} = 45^\circ$ (see fig. 5.16 top), $\sigma_{\theta_{rot}} = 30^\circ$ (see fig. 5.16 middle), $\sigma_{\theta_{rot}} = 0^\circ$ (see fig. 5.16 bottom).

As green color is prevalent in fig. 5.16 (top), which shows that this threshold value is very loose, similarly in the fig. 5.16 (bottom) the yellow color is dominant; this shows that, this threshold value is very strict one. Therefore, we have to choose the threshold value in between these two end members.

In the figure 5.16 (middle) we have tested the deviation threshold of 30° . With this threshold value it can be observed that some parts in northern part of the map are not well resolved (yellow colored bars).

The nodes where the difference between synthetics ('M45') and rotated ('M45_{rot}') is larger than 30° will be removed automatically. The notable regions include the areas of less dense coverage e.g. north-east and north-west.

Fig. 5.19 is plotted after finalizing the amplitude and direction threshold for Love wave phase velocity maps.

In figure 5.19 (left) the yellow bars are the tomographic inversion result (defined as 'M'), white bars are the 45° rotated anisotropy (defined as 'M45') and green colored nodes are the accepted nodes.

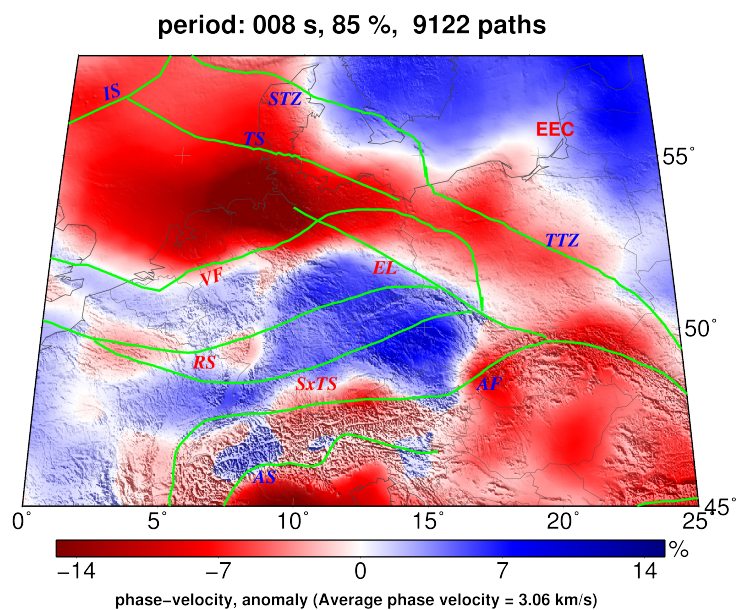
In figure 5.19 (right) the yellow bars are synthetics (defined as 'M45'), white bars are output of the resolution test (defined as 'M45_{rot}'), and green colored bars are the accepted nodes.

This test is very useful to identify the areas where the anisotropy in terms of amplitude and fast direction is not well resolved and vice versa.

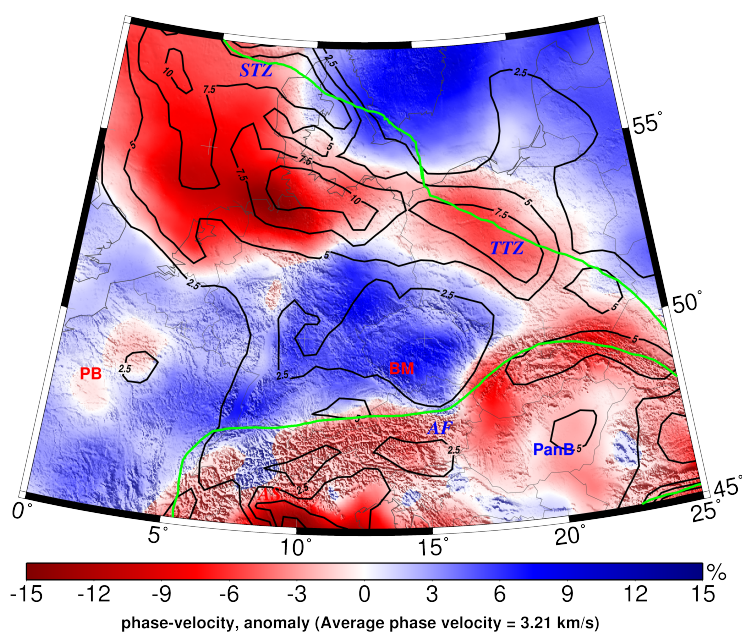
From the figure 5.19 it can be seen that the most of the nodes in terms of anisotropy and amplitude are well resolved (green colored nodes) except at some parts in e.g. southern Europe, north-eastern Europe.

5.5 Isotropic and azimuthally anisotropic Rayleigh and Love wave phase velocity maps for the central and northern Europe

The anisotropy is the directional or polarization dependence upon seismic wave-speed (Zhu & Tromp, 2013). Seismic anisotropy is helpful to constrain the deformation in the mantle lithosphere. Anisotropy can be LPO (lattice preferred orientation) or SPO (shape preferred orientation). LPO is also called CPO (crystallographic preferred orientation). In SPO the material aligns with distinct isotropic properties (heterogeneity) observable as for example cracks and melt pockets in the shallowest crust.

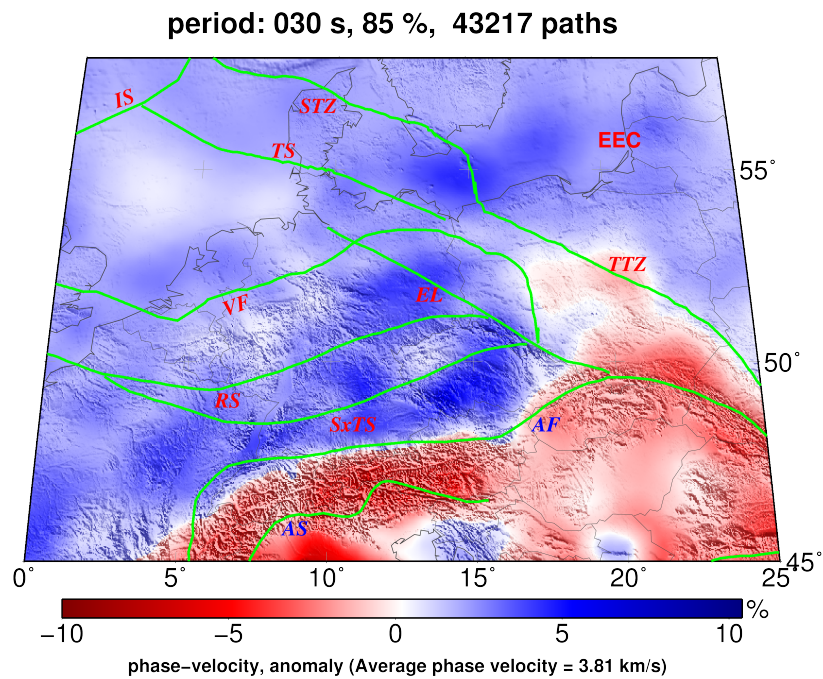


(a)

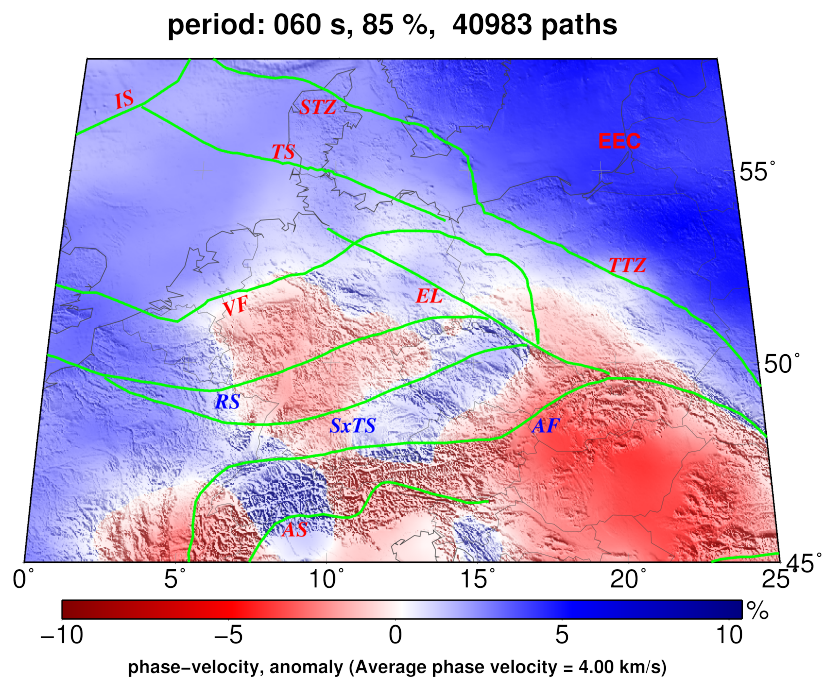


(b)

Fig. 5.20: 8 s (a) and 12 s (b) isotropic phase velocity maps. Low velocities in (a) and (b) match quite well with CEBS (central European basin system), outlines from EUCRUST07 Tesauro et al. (2008) are plotted on 12 s phase velocity map. Key to labels: IS, Iapetus suture; TS, Thor suture; STZ, Sorgenfrei–Tornquist Zone; TTZ, Tornquist–Teisseyre Zone; CDF, Caladonian deformation front; VF, Variscan front; EL, Elbe line; RS, Rheic suture; SxTS, Saxothuringian suture; AF, Alpine front; AS, Alpine suture; WECML, western European continental mantle lithosphere; PB, Paris basin; PanB, Pannonian basin; PB, Paris basin.

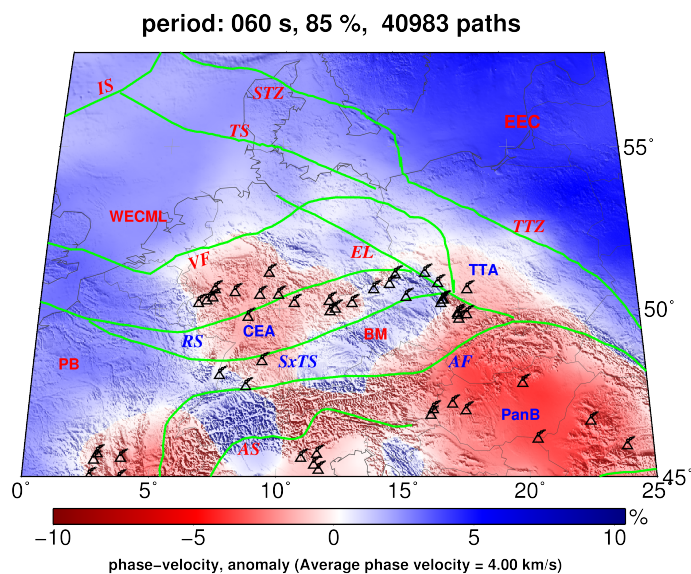


(a)

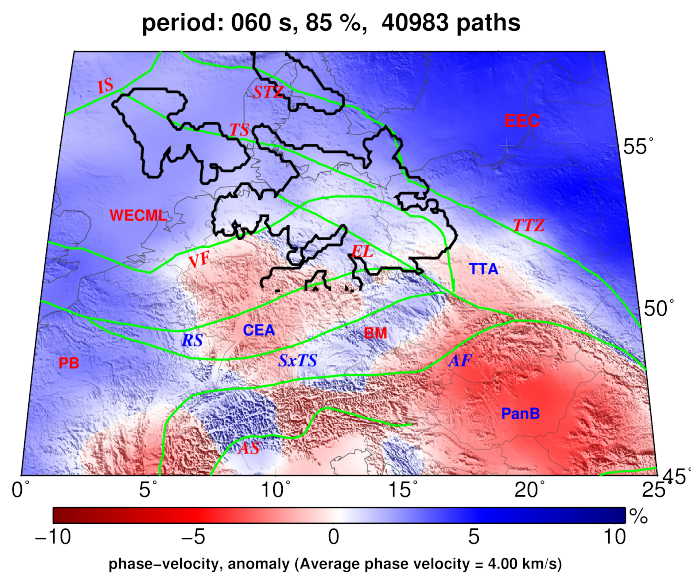


(b)

Fig. 5.21: 30 s (a) and 60 s (b) isotropic phase velocity maps. 30 s phase velocity maps are characterized by homogeneous mantle lithosphere in central Europe. In 60 s phase velocity maps central Europe is characterized by shallow asthenosphere. High velocities in north are due to thicker lithosphere. For labels see fig. 5.20)

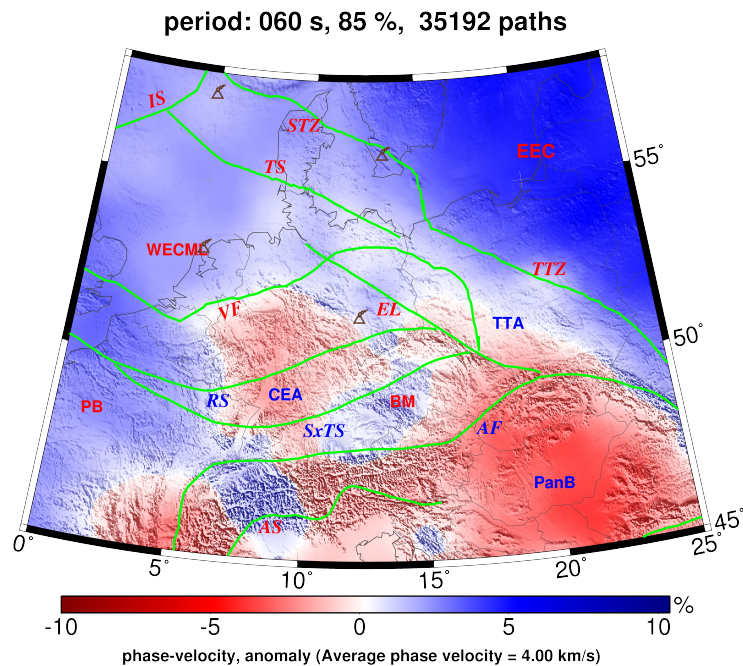


(a) 60 s phase velocity maps showing Cenozoic alkaline volcanism in central Europe. The areas with shallow mantle lithosphere matches quite well with volcanism.



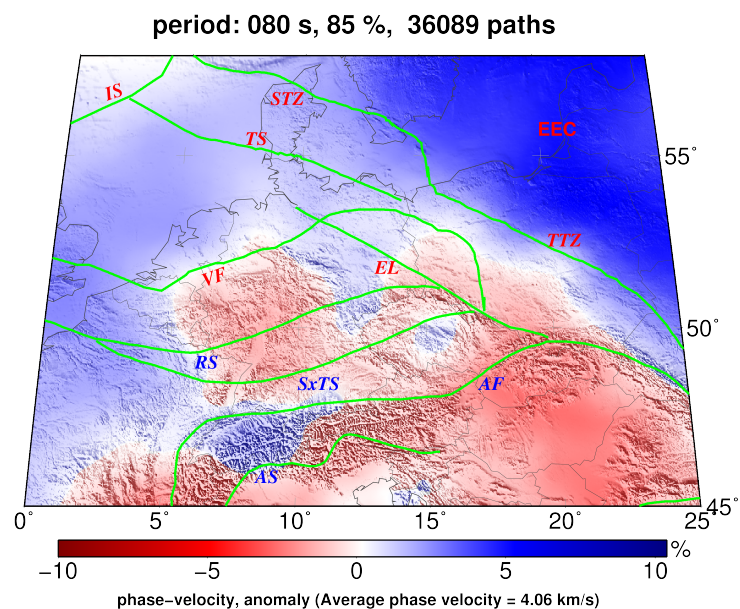
(b) 60 s phase velocity maps showing Rotliegend (Permian) volcanics of the age ca 290 Ma in the north-western Europe. The outlines are modified from Scheck-Wenderoth & Lamarche (2005b). High velocities match quite well with these volcanics and the region clearly differs from central Europe.

Fig. 5.22: Key to labels: IS, Iapetus suture; TS, Thor suture; STZ, Sorgenfrei–Tornquist Zone; TTZ, Tornquist–Teisseyre Zone; CDF, Caladonian deformation front; VF, Variscan front; EL, Elbe line; RS, Rheic suture; SxTS, Saxothuringian suture; AF, Alpine front; AS, Alpine suture; WECML, western European continental mantle lithosphere; PB, Paris basin; PanB, Pannonian basin; EEC, East European Craton; PB, Paris basin.



60 s phase velocity maps with Mesozoic volcanism, which coincides well in the region of high velocities.

(a)



80 s phase velocity map: High velocities (blue) in the north-west and north-east (EEC) are due to thick lithosphere, the red part shows shallow asthenosphere in central Europe, Pannonian basin, south-eastern France and north-western Italy, high velocities in Bohemian massif are due to thick lithosphere compared to neighboring areas. For labels see fig. 5.21.

(b)

Fig. 5.23

The fast direction of the anisotropy can give us the hints of deformation in LPO or CPO. With the change in stress regime, the fast direction changes and erases the information of the previous deformation. Therefore, the measured anisotropy in the lithosphere always shows last significant deformation or thermal event. After relaxation of the thermal event, the observed anisotropy may present in the form of frozen anisotropy (Wüstefeld et al., 2009). Due to tectonic activity the fast axis of these minerals align with the direction of flow, or principal extensions.

Therefore, flow pattern can be understood from the anisotropy and deformation caused in the preferred orientation of the anisotropic material. The anisotropy found in stable tectonic regimes caused by last tectonic activity may appear as frozen in anisotropy (Barruol et al., 1997, 1998; Heintz & Kennett, 2006; James & Assumpção, 1996; Vauchez & Nicolas, 1991). LPO is helpful to understand the process when rock is formed or deformed. Therefore, seismic anisotropy gives insight into dynamics of the earth.

The crust and upper mantle is composed of amphibole and olivine. The other constituent which contribute in anisotropy in the upper mantle is orthopyroxene. These materials are highly anisotropic because of CPO (Zhang & Karato, 1995). Olivine has a single-crystal shear wave anisotropy of $\sim 18\%$. In deep mantle in addition to olivine, other materials also contribute in anisotropy such as perovskite, post perovskite, and ferropericlasite.

Anisotropy in the asthenosphere is related to present day flow pattern (Debayle & Ricard, 2013) whereas the anisotropy in lithosphere is considered as frozen in anisotropy due to past deformation (Assumpção et al., 2001). Silver (1996); Silver & Chan (1991) argue that anisotropy in the lithosphere may be due to present or past deformation in mantle lithosphere.

Seismic anisotropy can be calculated using variety of methods. P-waves (e.g Babuska & Cara, 1991; Bear et al., 1999; Bokelmann, 1995, 2002; Schulte-Pelkum et al., 2001), receiver functions (Levin & Park, 1997), SKS splitting (Fukao, 1984; for reviews see Silver, 1996; Savage, 1999), and with surface waves (see chapter 2 for previous surface wave studies).

We performed the tomographic inversion on the phase velocity measurements obtained through the automated implementation of two-station method and obtained isotropic and azimuthally anisotropic phase velocity maps for Rayleigh and Love waves in broad period range (8–250 s). Although we have a path coverage in almost entire Europe, here we mainly focus on the distinct features in the central and northern Europe (see fig. 5.1).

The surface waves are sensitive to shear wave velocity but they are sensitive to density as well and there is a weak sensitivity to P-waves (Julia et al., 2000).

Here I discuss some main features of isotropic and azimuthally anisotropic phase velocity maps.

5.5.1 East European Craton

The north-eastern part in our phase velocity maps is characterized by higher phase velocities as compared to north-west and central Europe.

High shear wave velocities are reported by various global and regional body and surface wave tomographic studies (e.g. Amaru et al., 2008; Bijwaard & Spakman, 2000; Boschi et al., 2009; Grand, 2002; Káráson & Van Der Hilst, 2000; Koulakov et al., 2009; Kustowski et al., 2008; Lebedev & Van Der Hilst, 2008; Legendre et al., 2012; Lekic & Romanowicz, 2011; Lekic et al., 2011; Levshin et al., 2005; Masters et al., 2000; Mégnin & Romanowicz, 2000; Panning & Romanowicz, 2006; Peter et al., 2007; Pilidou et al., 2005; Priestley & McKenzie, 2006; Ritsema et al., 2004; Ritzwoller et al., 2002; Schaefer et al., 2011; Shapiro et al., 2005; Simmons et al., 2010; Woodhouse & Dziewonski, 1984; Zhang & Tanimoto, 1993; Zhou et al., 2006; Zhu et al., 2012).

The lower period (8–15 s) phase velocities are sensitive to middle to lower crust. High velocities in these lower period phase velocity maps are due to thick crust with little to no sedimentary cover in the Baltic shield, make the region distinct from the central European basin system (CEBS) and central Europe (see fig. 5.20 a). The little to no sedimentary cover in the region is evident in 12 s phase velocity map as well (see fig. 5.20 b).

The 60 s phase velocities (see fig. 5.21 b) are sensitive to mantle lithosphere. The lithosphere is very thick in this region with the thickness ranging from 160 to 350 km (Grad et al., 2015) and the Moho depth in this region is around 50 km (Grad & Tiira, 2009). High velocities in this region are also visible in Love wave phase velocity maps (see fig. 5.27).

The anisotropy at lower periods (8–15 s) (see fig. 5.24, top panel) is NW–SE, which is different from 60 s phase velocity maps (here it is NE–SW). The prevailing high velocities in north of TTZ may be due to thick continental old lithosphere (Precambrian) formed by consistent fabric (Babuška & Plomerová, 2006).

80 s phase velocities (see fig. 5.23b) are sensitive to the depth of around 100 to 120 km. High velocities at these periods in the north-eastern side (EEC) which is characterized by thick lithosphere. There are slight variations in anisotropic fast direction between 60 s and 80 s phase velocity maps. 80 s phase velocity maps sample deeper structure, here the anisotropic direction is changing from NE–SW to \sim N–S, this indicates a layering of anisotropy, lithospheric layering in anisotropy was also observed by Yuan & Romanowicz (2010) at north American Craton. As 60 s and 80 s phase velocity maps are roughly sensitive to 90 and 120 km depth, for an exact depth estimate a depth inversion is required, therefore, it is not clear from our phase velocity maps that the observed layering is within the lithosphere or within the lithosphere–asthenosphere system.

5.5.2 Central and north–western Europe

Low velocities at lower period (8–15 s) phase velocity maps in the north–western Europe (see fig. 5.20 a) are due to thick sedimentary cover, which represents the central European basin system (CEBS). This basin system extending from northwest in the north sea from Norwegian–Danish basin through North German basin extending to the south in Polish basin (Scheck-Wenderoth & Lamarche, 2005b). The lowest period (8 s) phase velocity map is characterized by very low velocities (see fig. 5.20 a) in the north sea. These low phase velocities in the north–west are consistent with the outlines of EUcrust07 (Tesauro et al., 2008) (see fig. 5.20 b), in this figure the areas with low velocities are matching quite well with thick sediment layer compared to the regions with little to no sediments (e.g. central Europe and EEC), and clearly show high resolution 3–D structure. The low velocities in north–western part are also imaged by Love wave phase velocity maps (see fig. 5.27, top panel).

Central Europe at lower period (8–15 s) phase velocity maps (see fig. 5.24, top panel) is characterized by higher phase velocities as compared to e.g. north–west – indicative of thick crust. The low velocities in Eifel area with thinner crust as compared to central Europe are clearly visible in our 8 s (see fig. 5.20 a) phase velocity maps.

A homogeneous mantle lithosphere (see fig. 5.21 a) at around 30 s period Rayleigh wave phase velocity maps is observed in central Europe as well as in Pannonian basin with higher velocities due to a thermal event in Permian (Wilson et al., 2004), the same is also imaged by 30 s Love wave phase velocity maps (see fig. 5.27, middle panel).

In 60 s phase velocity maps (see fig. 5.21 b) the velocity variations are different in the three north–western basin systems as compared to central Europe and Pannonian basin, the former is characterized by high velocities as compared to latter. This suggests a thick lithosphere in the north–western part and shallow asthenosphere in central Europe as well as in Pannonian basin. The northern Europe undergone widespread volcanism during Permian–Carboniferous times, which was accompanied by rifting process (Scheck-Wenderoth & Lamarche, 2005a). Due to this rifting process the asthenospheric upwelling might have occurred. The volcanic activity is abated at the end of early Permian. During Triassic time there was low volcanic activity and virtually no volcanic activity in early Jurassic might have resulted in thermal relaxation of the lithosphere with lithospheric cooling (Ziegler, 1992). Due to minor volcanic activity in the transition period from Jurassic to Cretaceous (see fig. 5.23a), might have resulted in asthenospheric upwelling. In this region there was no volcanic activity during upper Cretaceous–Cenozoic times resulted in lithospheric cooling (Ziegler, 1992). The outlines of the Rotliegend volcanics in Permian (ca 290 Ma) are shown in figure (5.22 b). These outlines match remarkably with these above mentioned three basin systems and make north–western Europe distinct from central Europe. The low velocities in central Europe including Eifel region are due to shallow asthenosphere (see fig. 5.21 b) with the lithospheric thickness around 80–100 km (Plomerová & Babuška, 2010). These

low velocities match quite well with Cenozoic volcanism (see fig. 5.22 a). The relation between low velocities and Cenozoic volcanism was already observed by (Hoernle et al., 1995). The low velocities along with volcanism in Eifel hotspot area are also observed (e.g. Kaiser et al., 2005; Mathar et al., 2006; Ritter et al., 2001). The lithosphere in the Bohemian massif is thicker than central Europe and Pannonian basin (see fig. 5.21 b).

60 s Love wave phase velocity maps (see fig. 5.27, middle panel) show high velocities in central Europe, as the depth sensitivity of Love waves is less focused as compared to Rayleigh waves. e.g. the 60 s Love wave carries the signal of crust as well as mantle lithosphere.

The north–western Europe in 80 s (see fig. 5.23b) isotropic phase velocity maps is characterized by thick lithosphere with thickness of around 100 to 120 km. The shallow asthenosphere in central Europe and in Pannonian basin is also visible in 80 s phase velocity maps.

Anisotropic fast directions at short periods (8–15 s) (see fig. 5.24, top panel) are NE–SW oriented in North Sea. At around 30 s (see fig. 5.24, middle panel) low values of the anisotropy are observed in the northwest with thin lithosphere. At 80 s (see fig. 5.24, bottom left) the anisotropic pattern completely changes to NW–SW following Thor suture.

The anisotropic trend in the central Europe at these lower periods (8–15 s) (see fig. 5.24, top panel) is following Variscan front with the fast direction of NE–SW. This trend abruptly changes to SE–NW near Elbe line. At central Europe the pattern of the anisotropy at around 60 s (see fig. 5.24, middle right) is similar to lower periods (see fig. 5.24, top panel) and follows Variscan front in central Europe and Elbe line near Bohemian massif, it follows Variscan Rheic suture in south of the central Europe. The pattern of the anisotropy at 80 s (see fig. 5.24, bottom left) period (sensitive to asthenosphere) in central Europe is following sutures in central Europe (e.g. Rheic suture, Saxothuringian suture), on the eastern side of central Europe the anisotropy is following Elbe line. These patterns are more visible in the zoomed in version of the 80 s phase velocity maps (see fig. 5.26). The anisotropic pattern at these periods is almost similar to the SKS splitting results of Vecsey et al., 2014.

5.5.3 Trans–European Suture Zone

The lower period (8–15 s) phase velocity maps in this region show lower velocities as compared to northern and central Europe. On south–eastern part of the Trans–European Suture Zone (TESZ), these low velocities correlate well with thick sediments of the polish basin which are outlined in the EUCRUST07 (Tesauro et al., 2008) (see fig. 5.20 b).

30 s phase velocity maps (see fig. 5.21 a) also show low phase velocities along TTTZ, which are due to thicker crust as compared to central and north–western part. The

thickness of the crust is around 40 to 45 km (Knapmeyer-Endrun et al., 2014) on TTZ part whereas it is less thick on the north–western part of TESZ i.e. STZ, its thickness is around 20 to 25 km (Grad & Tiira, 2009).

The 60 s phase velocity maps (see fig. 5.21 b) show remarkably a sharp and distinct boundary between complex and younger Phanerozoic Europe with that of cold and old Precambrian EEC, the boundary along north–western side is not as sharp as it is on south–eastern side rather a gradual transition in lithospheric thickness across STZ.

The 200 s phase velocity maps (see fig. 5.24, bottom right) around TESZ show deeper structure, with no evidence of suture, this shows that it is lithospheric feature.

Anisotropy at lower periods (8–15 s) (see fig. 5.24, top panel) at south–east of TESZ is in the direction of NW–SE. It is slightly northward along STZ. The anisotropic pattern at south–east of TESZ coincides well with TESZ at this region. At 30 s the similar pattern of anisotropy is observed along TTZ. Anisotropy is weak along north–western part of TESZ (STZ). The low values of the anisotropy in the west of TESZ (STZ) are also observed in SKS splitting studies by (e.g. Sroda et al., 2014; Vecsey et al., 2014; Wüstefeld et al., 2010).

The similar pattern of anisotropy at 60 s phase velocity maps (see fig. 5.24, middle right) is observed along TTZ and this pattern abruptly changes from NW–SE to E–W at the region of STZ. Overall the anisotropic direction along south–eastern part of TTZ remains similar.

5.5.4 Alps and Carpathians

The lower period (8–15 s) phase velocity maps (see fig. 5.24, top panel) at this region show lower velocities as compared to the central Europe. Low velocities in south–west make them distinct from the central Europe, which is characterized by high velocities. The low velocities in south–west confirm the deeper structure in the region.

30 s phase velocity maps (see fig. 5.21 a) also show low velocities on the south–western side due to thick crust. The low velocities in the Carpathian and Pannonion basin are due to thin lithosphere, here the Moho is around 25 km deep (Knapmeyer-Endrun et al., 2014).

A remarkable feature in our phase velocity maps is that European slab has started to become visible on south–western side at periods starting from 60 s (see fig. 5.21 b).

In southern Europe the E–W trend of anisotropy following Alpine suture. In Carpathian and Pannonion basin the anisotropy is following the Alpine and Carpathian arc. The low value of anisotropy in the Pannonian basin may be due to the different composition as compared to Alpine region. This anisotropic trend prevails up to 80 sec.

In the south of the Alpine front (Po basin), there is a clear difference in the pattern of the anisotropy in the middle (~ 15 s) and the lower crust (~ 30 s). At 15 sec the anisotropic direction is E–W, whereas at 30 sec, it is changing to SE–NW. This difference in the direction of the anisotropy is due to layering of the anisotropy, as different processes and origins affect the anisotropy within each layer. This parallel trend of the anisotropy may be the result of the frozen-in anisotropy due to pre-Alpine orogenic events (Fry et al., 2010). The layering in the anisotropy is also discussed by Fry et al., 2010.

Fry et al. (2010) observed a change in fast direction from parallel to transverse in Alpine orogeny at the periods starting from 24 s. We zoomed in our phase velocity maps (see fig. 5.25) to make the region similar to Fry et al., 2010, but we are unable to observe the change in the direction of anisotropy at 30–40 s (see fig. 5.25 bottom panel for comparison of our phase velocity maps with Fry et al. (2010)). There are similarities in fast direction at lower periods (<15 s) with Fry et al. (2010) (see fig. 5.25, top panel for comparison of our phase velocity maps with Fry et al. (2010) at 8 sec). Fry et al. (2010) used noise data of 36 stations and phase velocity measurements between 185 and 332, whereas we have more than 40000 inter-station paths at 40 s (see histogram in figure 5.2).

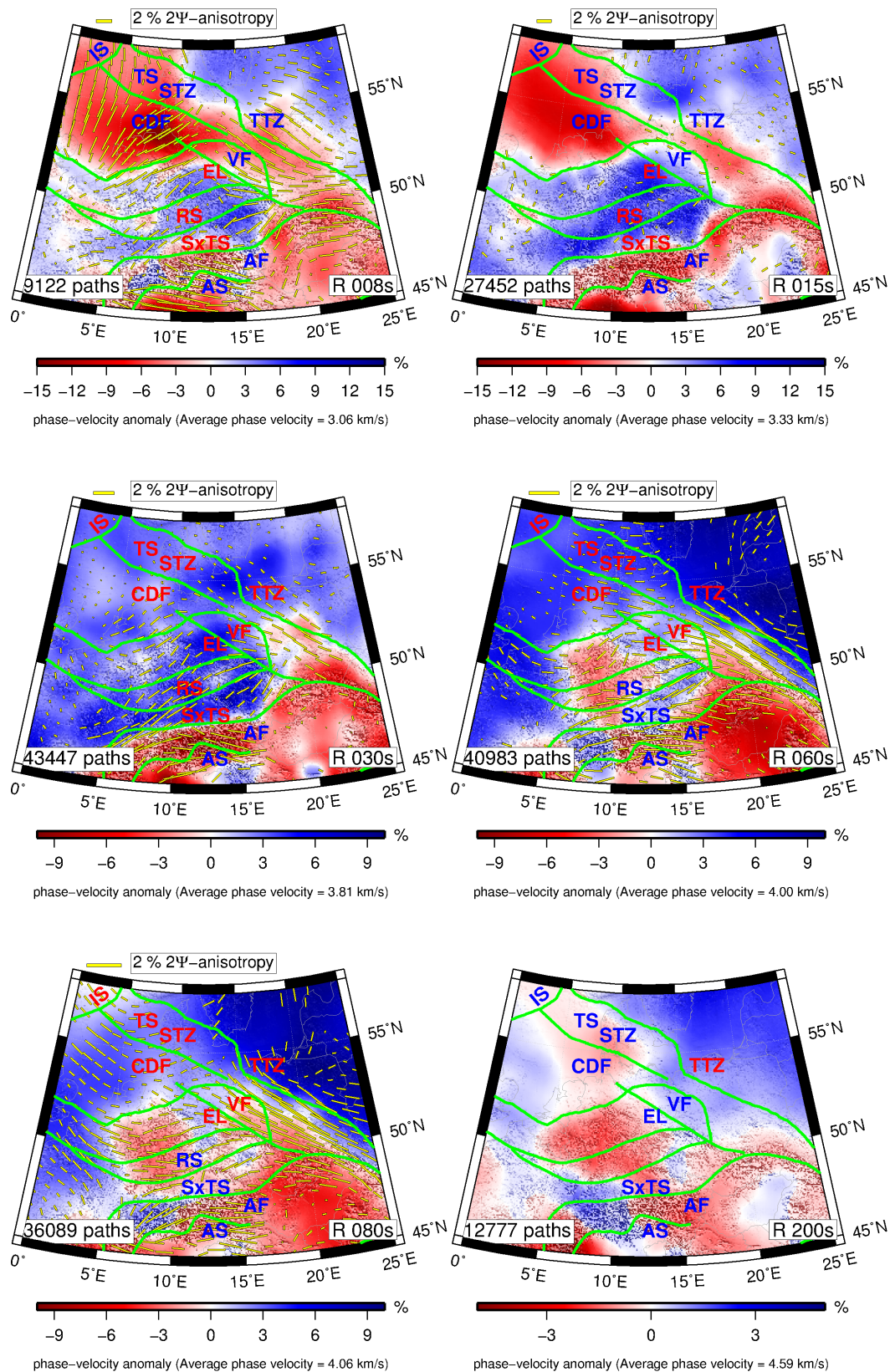


Fig. 5.24: Rayleigh wave phase velocity maps after applying quality control criteria (200 s phase velocity map is isotropic only). Key to labels: IS, Iapetus suture; TS, Thor suture; STZ, Sorgenfrei–Tornquist Zone; TTZ, Tornquist–Teisseyre Zone; CDF, Caladonian deformation front; VF, Variscan front; EL, Elbe line; RS, Rheic suture; SxTS, Saxothuringian suture; AF, Alpine front; AS, Alpine suture.

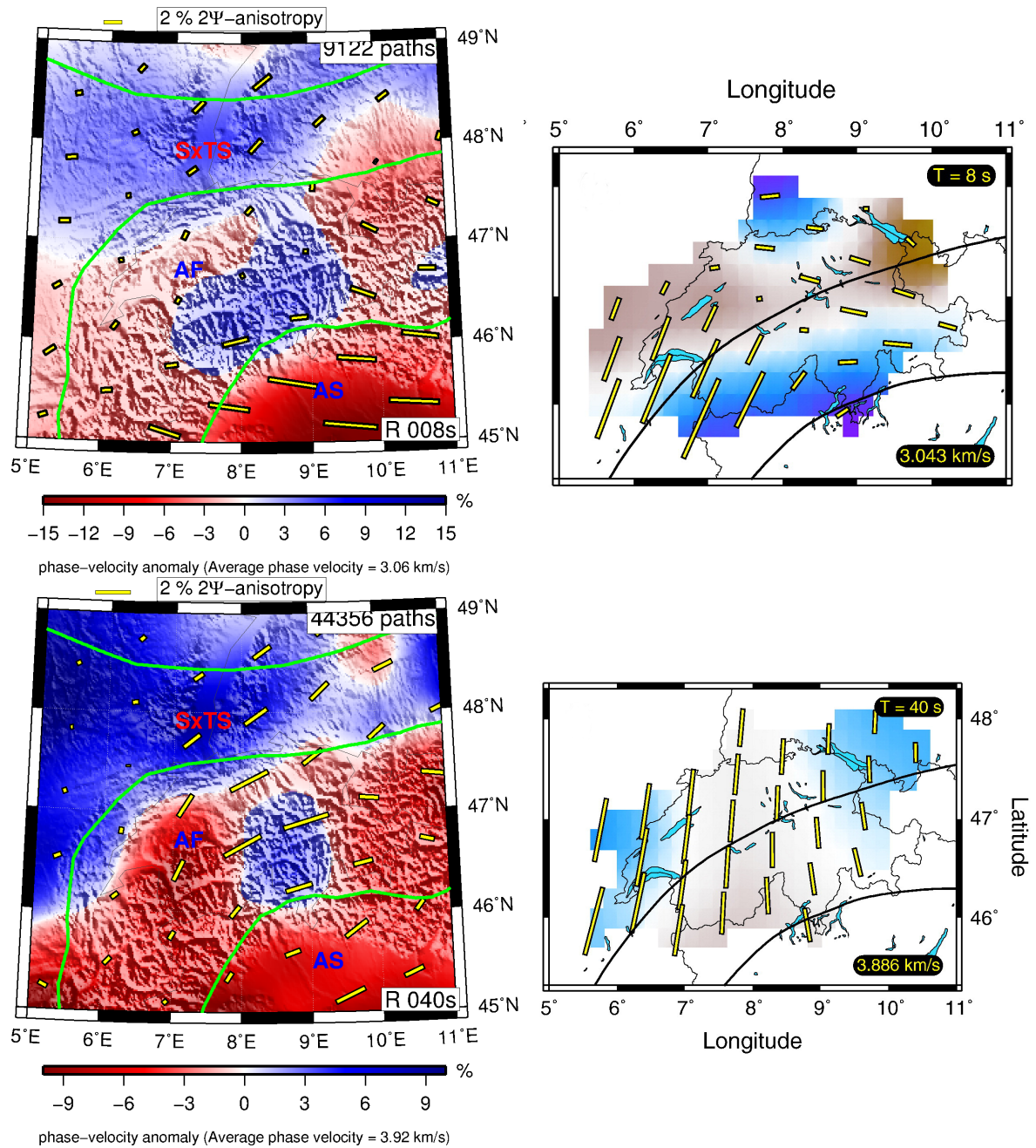


Fig. 5.25: Comparison of the Rayleigh wave phase velocity maps with Fry et al. (2010). 08 s and 40 s phase velocity map are plotted on top and bottom panels respectively. Key to labels: SxTS, Saxothuringian suture; AF, Alpine front; AS, Alpine suture.

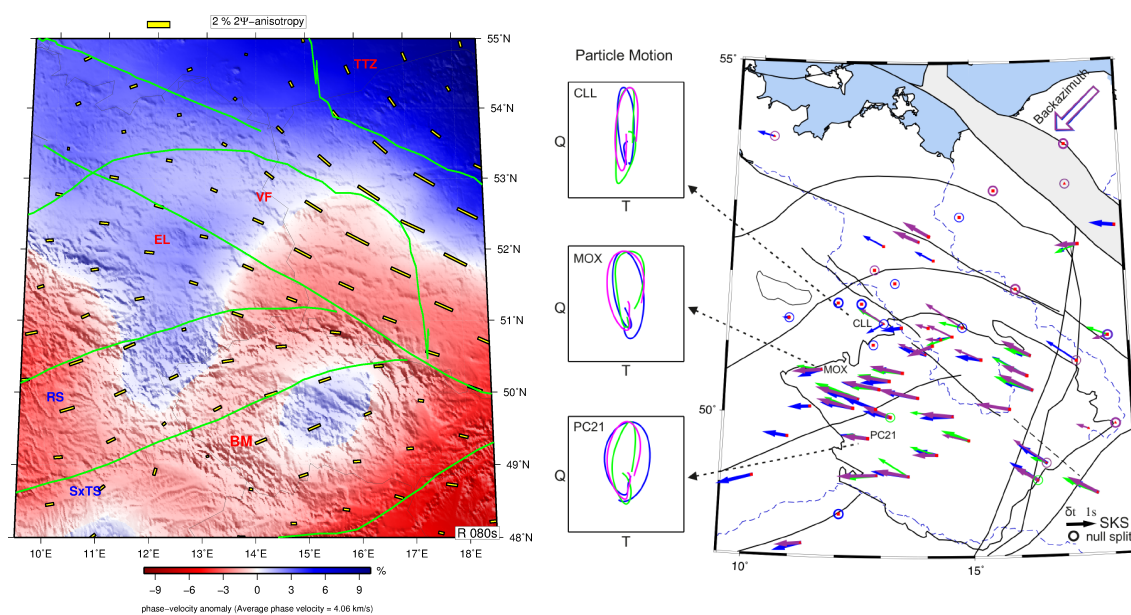


Fig. 5.26: Comparison of the result with SKS splitting result of Vecsey et al. (2014). Key to labels: TTZ, Tornquist–Teisseyre Zone; VF, Variscan front; EL, Elbe line; RS, Rheic suture; SxTS, Saxothuringian suture; BM, Bohemian massif.

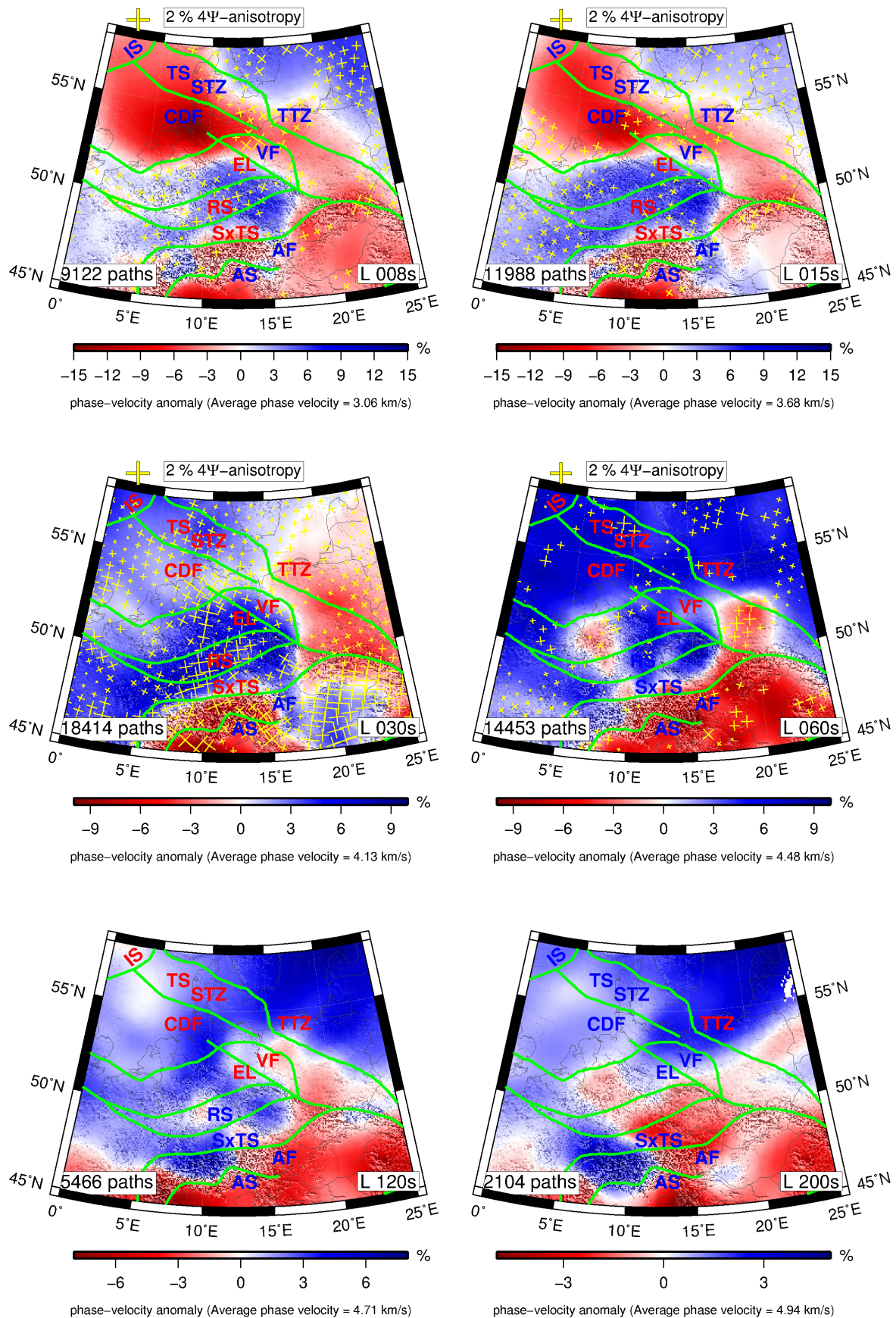


Fig. 5.27: Love wave isotropic and azimuthally anisotropic phase velocity maps with unresolved nodes removed. Key to labels: IS, Iapetus suture; TS, Thor suture; STZ, Sorgenfrei–Tornquist Zone; TTZ, Tornquist–Teisseyre Zone; CDF, Caladonian deformation front; VF, Variscan front; EL, Elbe line; RS, Rhenish suture; SxTS, Saxothuringian suture; AF, Alpine front; AS, Alpine suture.

Chapter 6

Conclusions and future outlook

6.1 Conclusions

An automated procedure for the determination of high quality very broad band phase velocity dispersion measurements for both Love and Rayleigh wave in period range from 8 s to more than 250 s is presented.

A cross correlation procedure is applied to the waveform data of the two single stations and frequency dependent windows are applied to the cross correlation function. All the smooth segments of the phase velocity dispersion curves for each inter-station path are selected based upon certain number of criteria which are frequency and distance dependent.

The averaging of all the smooth segments of the phase velocity dispersion curves and comparison of measurements in opposite propagation direction is useful check to overcome systematic deviations between two directions and reducing the errors due to off path propagation, polarity, timing errors, and instrument response issues.

We have rigorously tested the new implementation of the inter-station method to a huge data-set covering almost entire Europe where the easy access to the data through WebDC made it possible to test the method.

Our data set comprise more than 1000 permanent and temporary stations in the period range from January 1990 to October 2013 and around 1.38 million events from which we obtained 164231 inter-station paths and performed 12 million cross-correlations. This resulted in 63000 and 27500 smooth average dispersion curves in a broad period range between 8 s to more than 250 s for Rayleigh and Love waves, respectively. The statistical analysis on the data set show that the overall standard deviation and standard error is less than 1.5 % and 0.5 %, respectively. With the help of automated procedure large data volumes can be processed easily and repeated measurements with different parameters is helpful in order to obtain consistent phase velocity measurements.

The method is suitable to permanent as well as temporary networks where small amount of the data may require varying the criteria as it may be difficult to obtain observations in both propagation directions. Stations with erroneous response and timing can be detected with this method.

We have obtained phase velocity maps for both Rayleigh and Love waves in the broad period range from 8-200 s for Rayleigh waves and Love waves, respectively.

The checker board tests suggest the lateral resolution constrained by our data set varies between 100 km to 150 km in central Europe, it is around 100 km in the areas with dense path coverage e.g. central Europe and 150 km elsewhere. This shows that we are able to obtain a new level of resolution as compared to previous available tomographic studies for study of lithospheric structure in central Europe.

Low velocities in the northern Europe coincide well with Central European basin system (CEBS) extending from north German basin in north towards Polish basin in south. These low velocities are delineated with the outlines of EUCRUST07 (Tesauro et al., 2008). The azimuthal anisotropy in the north is NE oriented. In the south the low velocities are attributed to Alpine and Carpathian region. Central Europe is characterized by a homogeneous mantle lithosphere with high velocities due to a thermal event in Permian, and there is no imprint of Variscan suture at Moho level.

A remarkable feature of our phase velocity maps is that the boundary between Precambrian EEC and Phanerozoic central Europe is well pronounced across southern part of TESZ (Trans-European suture zone) i.e. Tornquist-Teisseyre Zone. The TESZ has strong lateral contrast across the Tornquist-Teisseyre Zone (TTZ) and a gradual transition across the Sorgenfrei-Tornquist Zone (STZ). The anisotropy is NW oriented at south of TTZ. Another remarkable feature of our phase velocity maps is that the European slab is clearly visible beneath western Alps at periods between 60 s and 120 s.

The 60 s phase velocity maps show high velocities in the north which characterize thick lithosphere. The thick lithosphere in north west matches well with Rotliegend volcanics of Permian (ca 290 Ma), here the lithosphere is around 100 to 120 km thick. Wide spread volcanism accompanied by rifting might have resulted in asthenospheric upwelling during Permian, lithospheric cooling in early Jurassic followed by some volcanic activity during the transition period of late Jurassic and upper Cretaceous might have resulted in asthenospheric upwelling. The low velocities in central Europe as well as in Pannonian basin are due to shallow asthenosphere. The Cenozoic inter-plate volcanism occurs in the region of thin lithosphere.

These observations are valid for Love wave phase velocity maps as well. Though the depth sensitivity of Love waves is less focused as compared to Rayleigh waves, some distinct features well resolved in Rayleigh wave phase velocity maps are present in Love wave phase velocity maps as well e.g. low velocities in CEBS and Alpine Carpathian region and a homogeneous mantle lithosphere.

6.2 Future outlook

The next step after obtaining isotropic and azimuthally anisotropic phase velocity maps is to invert them for 1-D shear wave velocity structure as well as 3-D shear wave velocity structure. As we have obtained high resolution phase velocity maps for both Rayleigh and Love waves, therefore we wish to use these both data sets to compute isotropic shear wave velocity model with the use of $\delta v_S = (\delta v_{SH} + \delta v_{SV})/2$ and radially anisotropic variations in shear wave velocity with the use of $\delta a_S = (\delta v_{SH} - \delta v_{SV})$ equations.

With the 3-D shear wave velocity model, we can obtain horizontal as well as vertical slices, which will help in obtaining shear velocity variations at particular depths as well as particular geographic location.

We also wish to use our large amount of data in ambient noise tomography and want to compare phase velocity dispersion measurements obtained through earthquake based inter-station method with that of noise based method, and want to combine both data sets in order to obtain even higher resolution image of the crust and mantle lithosphere.

Due to automated procedure the method can be utilized to other regions in the world as well e.g. Japan, north America – where dense station coverage may be helpful in obtaining high resolution image of the middle to lower crust as well as lithosphere-asthenosphere system. In addition to that I wish to utilize the method to Pakistan where the crust as well as lithosphere - asthenosphere is not well studied, therefore, I wish to use the method in this region, which will be helpful in providing new insights of the region under study.

The receiver functions are sensitive to shear wave velocity structure beneath the receivers, the surface waves are sensitive to both horizontally and vertically polarized shear wave velocity structure beneath the source receiver, with the joint inversion of both data-sets may provide better constraints on the lithospheric structure. Therefore, I wish to perform a joint inversion of the receiver functions and surface wave data-set.

References

- Adam, J. M.-C. & Lebedev, S., 2012. Azimuthal anisotropy beneath southern Africa from very broad-band surface-wave dispersion measurements, *Geophysical Journal International*, **191**(1), 155–174.
- Agius, M. R. & Lebedev, S., 2013. Tibetan and Indian lithospheres in the upper mantle beneath Tibet: Evidence from broadband surface-wave dispersion, *Geochemistry, Geophysics, Geosystems*, **14**(10), 4260–4281.
- Ahern, T., Casey, R., Barnes, D., Benson, R., & Knight, T., 2012. *SEED Reference Manual - Standard for the Exchange of Earthquake Data*, International Federation of Digital Seismograph Networks Incorporated Research Institutions for Seismology United States Geological Survey, version 2.4 edn.
- Aki, K. & Richards, P., 1980. *Quantitative Seismology*, W.H. Freeman and Company, San Francisco, U.S.
- Al-Lazki, A. I., Sandvol, E., Seber, D., Barazangi, M., Turkelli, N., & Mohamad, R., 2004. Pn tomographic imaging of mantle lid velocity and anisotropy at the junction of the Arabian, Eurasian and African plates, *Geophysical Journal International*, **158**(3), 1024–1040.
- Allen, R. V., 1978. Automatic earthquake recognition and timing from single traces, *Bulletin of the Seismological Society of America*, **68**(5), 1521–1532.
- Alterman, Z., Jarosch, H., & Pekeris, C. L., 1961. Propagation of Rayleigh Waves in the Earth, *Geophysical Journal of the Royal Astronomical Society*, **4**, 219–241.
- Amaru, M. L., Spakman, W., Villaseñor, A., Sandoval, S., & Kissling, E., 2008. A new absolute arrival time data set for Europe, *Geophys. J. Int.*, **173**(2), 465–472.
- Arrowsmith, S. J., Kendall, M., White, N., VanDecar, J. C., & Booth, D. C., 2005. Seismic imaging of a hot upwelling beneath the British Isles, *Geology*, **33**(5), 345–348.
- Artemieva, I. M. & Thybo, H., 2013. EUNaseis: A seismic model for Moho and crustal structure in Europe, Greenland, and the North Atlantic region, *Tectonophysics*, **609**, 97–153.
- Assumpção, M., Heintz, M., Vauchez, A., Silva, M. E., Barbosa, J. R., & Benevides, T., 2001. Upper mantle anisotropy in SE and Central Brazil from SKS splitting, in *7th International Congress of the Brazilian Geophysical Society*.

- Ates, a., Ates, a., Kearey, P., Kearey, P., Tufan, S., & Tufan, S., 1999. New gravity and magnetic anomaly maps of, *Turkey, Geophys. J. In*, **t136**, 499–502.
- Babuska, V. & Cara, M., 1991. *Seismic anisotropy in the Earth*, Kluwer Academic Publishers, Boston.
- Babuška, V. & Plomerová, J., 2001. Subcrustal lithosphere around the Saxothuringian–Moldanubian Suture Zone—a model derived from anisotropy of seismic wave velocities, *Tectonophysics*, **332**(1), 185–199.
- Babuška, V. & Plomerová, J., 2006. European mantle lithosphere assembled from rigid microplates with inherited seismic anisotropy, *Physics of the Earth and Planetary Interiors*, **158**, 264–280.
- Baer, M. & Kradolfer, U., 1987. An automatic phase picker for local and teleseismic events, *Bulletin of the Seismological Society of America*, **77**(4), 1437–1445.
- Baer, M., Zweifel, P., & Giardini, D., 2000. The Swiss digital seismic network (SDSNet), *Orfeus Newsl*, **2**(2), 1–5.
- Bakırcı, T., Yoshizawa, K., & Özer, M. F., 2012. Three-dimensional S-wave structure of the upper mantle beneath Turkey from surface wave tomography, *Geophysical Journal International*, **190**(2), 1058–1076.
- Banka, D., Pharaoh, T., Williamson, J., & Group, T. P. P. F. C., 2002. Potential field imaging of Palaeozoic orogenic structure in northern and central Europe, *Tectonophysics*, **360**(1), 23–45.
- Barazangi, M., Sandvol, E., & Seber, D., 2006. Structure and tectonic evolution of the Anatolian plateau in eastern Turkey, *Geological Society of America Special Papers*, **409**, 463–473.
- Barruol, G., Silver, P. G., & Vauchez, A., 1997. Seismic anisotropy in the eastern United States: Deep structure of a complex continental plate, *Journal of Geophysical Research*, **102**, 8329.
- Barruol, G., Souriau, A., Vauchez, A., Diaz, J., Gallart, J., Tubia, J., & Cuevas, J., 1998. Lithospheric anisotropy beneath the Pyrenees from shear wave splitting, *Journal of Geophysical Research*, **103**(98), 30039.
- Bartol, J. & Govers, R., 2014. A single cause for uplift of the Central and Eastern Anatolian plateau?, *Tectonophysics*, **637**, 116–136.
- Bartzsch, S., Lebedev, S., & Meier, T., 2011. Resolving the lithosphere-asthenosphere boundary with seismic Rayleigh waves, *Geophysical Journal International*, **186**(3), 1152–1164.
- Bassin, C., Laske, G., & Masters, G., 2000. The Current Limits of Resolution for Surface Wave Tomography in North America, in *EOS Trans AGU*, vol. 81 (48), p. F897.

- Bear, L. K., Pavlis, G. L., & Bokelmann, G. H. R., 1999. Multi-wavelet analysis of three-component seismic arrays: Application to measure effective anisotropy at Pinon Flats, California, *Bulletin of the Seismological Society of America*, **89**, 693–705.
- Becker, T. W. & Boschi, L., 2002. A comparison of tomographic and geodynamic mantle models, *Geochemistry, Geophysics, Geosystems*, **3**(1).
- Becker, T. W., Kustowski, B., & Ekström, G., 2008. Radial seismic anisotropy as a constraint for upper mantle rheology, *Earth and Planetary Science Letters*, **267**(1), 213–227.
- Beghein, C., Snoke, J. A., & Fouch, M. J., 2010. Depth constraints on azimuthal anisotropy in the Great Basin from Rayleigh-wave phase velocity maps, *Earth and Planetary Science Letters*, **289**(3–4), 467 – 478.
- Ben-Menahem, A. & Singh, A., 1981. *Seismic Waves and Sources*, Springer, New York.
- Beyreuther, M., Barsch, R., Krischer, L., Megies, T., Behr, Y., & Wassermann, J., 2010. ObsPy: A Python Toolbox for Seismology, *Seismological Research Letters*, **81**(3), 530–533.
- Bijwaard, H. & Spakman, W., 2000. Non-linear global P-wave tomography by iterated linearized inversion, *Geophysical Journal International*, **141**(1), 71–82.
- Blundell, D. J., Freeman, R., & Mueller, S., 1992. *A Continent Revealed: The European Geotraverse, Structure and Dynamic Evolution*, Cambridge University Press.
- Bodin, T. & Maupin, V., 2008. Resolution potential of surface wave phase velocity measurements at small arrays, *Geophys. J. Int.*, **172**(2), 698–706.
- Bodin, T., Capdeville, Y., Romanowicz, B., & Montagner, J.-P., 2015. Interpreting radial anisotropy in global and regional tomographic models, in *The Earth's Heterogeneous Mantle*, pp. 105–144, Springer.
- Bogdanova, S., Bingen, B., Gorbatshev, R., Kheraskova, T., Kozlov, V., Puchkov, V., & Volozh, Y. A., 2008. The East European Craton (Baltica) before and during the assembly of Rodinia, *Precambrian Research*, **160**(1), 23–45.
- Bokelmann, G. H. R., 1995. P-wave array polarization analysis and effective anisotropy of the brittle crust, *Geophysical Journal International*, **120**, 145 – 162.
- Bokelmann, G. H. R., 2002. Convection-driven motion of the North American craton: Evidence from P-wave anisotropy, *Geophysical Journal International*, **148**, 278–287.
- Boschi, L., Fry, B., Ekström, G., & Giardini, D., 2009. The European Upper Mantle as Seen by Surface Waves, *Surveys in Geophysics*, **30**(4-5), 463–501.
- Bouchon, M. & Sanchez-Sesma, F. J., 2007. Boundary integral equations and boundary elements methods in elastodynamics, in *Advances in Geophysics, Vol 48*, vol. 48 of **Advances in Geophysics**, pp. 157–189+.
- Brilliant, R. & Ewing, M., 1954. Dispersion of Rayleigh waves across the U.S., *Bulletin of the Seismological Society of America*, **44**, 149–158.

- Brune, J. & Dorman, J., 1963. Seismic waves and earth structure in the Canadian shield, *Bulletin of the Seismological Society of America*, **53**(1), 167–209.
- Brune, J. N., Nafe, J. E., & Alsop, L. E., 1961. The polar phase shift of surface waves on a sphere, *Bulletin of the Seismological Society of America*, **51**(2), 247–257.
- Byerly, P., 1930. The Dispersion of Seismic Waves of the Love Type and the Thickness of the Surface Layer of the Earth under the Pacific, *Gerlands Beitr. z. Geophysik*, **26**, 27–33.
- Calcagnile, G. & Panza, G., 1978. Crust and upper mantle structure under the Baltic shield and Barents Sea from the dispersion of Rayleigh waves, *Tectonophysics*, **47**(1), 59–71.
- Calcagnile, G. & Panza, G., 1979. CRUSTAL AND UPPER MANTLE STRUCTURE BENEATH THE APENNINES REGION AS INFERRED FROM THE STUDY OF RAYLEIGH-WAVES, *JOURNAL OF GEOPHYSICS-ZEITSCHRIFT FUR GEOPHYSIK*, **45**(3), 319–327.
- Calcagnile, G. & Panza, G., 1980. The main characteristics of the lithosphere-asthenosphere system in Italy and surrounding regions, *Pure and Applied Geophysics*, **119**(4), 865–879.
- Calcagnile, G. & Panza, G., 1990. Crustal and upper mantle structure of the Mediterranean area derived from surface-wave data, *Physics of the Earth and Planetary Interiors*, **60**(1), 163–168.
- Calcagnile, G., Mascia, U., del Gaudio, V., & Panza, G., 1985. Deep structure of southeastern Europe from the dispersion of Rayleigh Waves, *Tectonophysics*, **110**, 93–111.
- Campillo, M. & Paul, A., 2003. Long-range correlations in the diffuse seismic coda., *Science (New York, N.Y.)*, **299**, 547–549.
- Capon, J., 1970. Analysis of Rayleigh-wave multipath propagation at LASA, *Bulletin of the Seismological Society of America*, **60**(5), 1701–1731.
- Cara, M. & Lévêque, J. J., 1987. Waveform inversion using secondary observables, *Geophysical Research Letters*, **14**(10), 1046–1049.
- Carcione, J. M., 1994. The wave equation in generalized coordinates, *Geophysics*, **59**(12), 1911–1919.
- Chaljub, E. & Tarantola, A., 1997. Sensitivity of SS precursors to topography on the upper-mantle 660-km discontinuity, *Geophysical Research Letters*, **24**(21), 2613–2616.
- Chang, S.-J., van der Lee, S., Flanagan, M. P., Bedle, H., Marone, F., Matzel, E. M., Pasyanos, M. E., Rodgers, A. J., Romanowicz, B., & Schmid, C., 2010. Joint inversion for three-dimensional S velocity mantle structure along the Tethyan margin, *Journal of Geophysical Research: Solid Earth (1978–2012)*, **115**(B8).

- Chevrot, S. & Zhao, L., 2007. Multiscale finite-frequency Rayleigh wave tomography of the Kaapvaal craton, *Geophys. J. Int.*, **169**(1), 201–215.
- Claerbout, J. F., 1968. Synthesis of a layered medium from its acoustic transmission response, *Geophysics*, **33**(2), 264–269.
- Cotte, N., Pedersen, H. A., Campillo, M., Farra, V., & Cansi, Y., 2000. Off-great-circle propagation of intermediate-period surface waves observed on a dense array in the French Alps, *Geophysical Journal International*, **142**(3), 825–840.
- Crotwell, H. P. & Owens, T. J., 2005. Automated Receiver Function Processing, *Seismological Research Letters*, **76**(6), 702–709.
- Czech Regional Seismic Network, 2013. website.
- Dadlez, R., Grad, M., & Guterch, A., 2005. Crustal structure below the Polish Basin: Is it composed of proximal terranes derived from Baltica?, *Tectonophysics*, **411**(1), 111–128.
- Dahlen, F. & Tromp, J., 1998. *Theoretical Global Seismology*, Princeton University Press, Princeton, NJ.
- Dando, B. D. E., Stuart, G. W., Houseman, G. A., Hegedüs, E., Brückl, E., & Radovanović, S., 2011. Teleseismic tomography of the mantle in the Carpathian–Pannonian region of central Europe, *Geophysical Journal International*, **186**(1), 11–31.
- Darbyshire, F. a. & Lebedev, S., 2009. Rayleigh wave phase-velocity heterogeneity and multilayered azimuthal anisotropy of the Superior Craton, Ontario, *Geophysical Journal International*, **176**, 215–234.
- De Vos, D., Paulssen, H., & Fichtner, A., 2013. Finite-frequency sensitivity kernels for two-station surface wave measurements, *Geophysical Journal International*, **194**(2), 1042–1049.
- Debayle, E., 1999. SV-wave azimuthal anisotropy in the Australian upper mantle: preliminary results from automated Rayleigh waveform inversion, *Geophysical Journal International*, **137**(3), 747–754.
- Debayle, E. & Ricard, Y., 2012. A global shear velocity model of the upper mantle from fundamental and higher Rayleigh mode measurements, *Journal of Geophysical Research: Solid Earth*, **117**(B10), n/a–n/a.
- Debayle, E. & Ricard, Y., 2013. Seismic observations of large-scale deformation at the bottom of fast-moving plates, *Earth and Planetary Science Letters*, **376**(0), 165–177.
- Debayle, E. & Sambridge, M., 2004. Inversion of massive surface wave data sets: Model construction and resolution assessment, *J. Geophys. Res.*, **109**(B2), B02316–.
- Derode, A., Larose, E., Tanter, M., de Rosny, J., Tourin, A., Campillo, M., & Fink, M., 2003. Recovering the Green’s function from field-field correlations in an open scattering medium.

- Deschamps, F., Lebedev, S., Meier, T., & Trampert, J., 2008. Azimuthal anisotropy of Rayleigh-wave phase velocities in the east-central United States, *Geophysical Journal International*, **173**(3), 827–843.
- Dost, B., 1990. Upper mantle structure under western Europe from fundamental and higher mode surface waves using the NARS array, *Geophysical Journal International*, **100**(1), 131–151.
- Dziewonski, A. & Anderson, D., 1981. Preliminary reference earth model, *Physics of the Earth and Planetary Interiors*, **25**, 297–356.
- Dziewonski, A., Bloch, S., & Landisman, M., 1969. A Technique For The Analysis Of Transient Seismic Signals, *Bulletin Of The Seismological Society Of America*, **59**(1), 427–444.
- Dziewonski, A. M., 2005. The robust aspects of global seismic tomography, *Geological Society of America Special Papers*, **388**, 147–154.
- Dziewonski, A. M., Hager, B. H., & O’Connell, R. J., 1977. Large-scale heterogeneities in the lower mantle, *Journal of Geophysical Research*, **82**(2), 239–255.
- Ekström, G., Tromp, J., & Larson, E. W. F., 1997. Measurements and global models of surface wave propagation, *Journal of Geophysical Research: Solid Earth*, **102**(B4), 8137–8157.
- Ekström, G., 2011. A global model of Love and Rayleigh surface wave dispersion and anisotropy, 25–250s, *Geophysical Journal International*, **187**(3), 1668–1686.
- Endrun, B., Meier, T., Bischoff, M., & Harjes, H.-P., 2004. Lithospheric structure in the area of Crete constrained by receiver functions and dispersion analysis of Rayleigh phase velocities, *Geophysical Journal International*, **158**(2), 592–608.
- Endrun, B., Meier, T., Lebedev, S., Bohnhoff, M., Stavrakakis, G., & Harjes, H.-P., 2008. S velocity structure and radial anisotropy in the Aegean region from surface wave dispersion, *Geophysical Journal International*, **174**(2), 593–616.
- Endrun, B., Lebedev, S., Meier, T., Tirel, C., & Friederich, W., 2011. Complex layered deformation within the Aegean crust and mantle revealed by seismic anisotropy, *Nature Geosci*, **4**(3), 203–207.
- Engdahl, E., van der Hilst, R., & Buland, R., 1998. Global Teleseismic Earthquake Relocation with Improved Travel Times and Procedures for Depth Determination, *Bulletin Of The Seismological Society Of America*, **88**, 722–743.
- Evans, M. S., Kendall, J.-M., & Willemann, R. J., 2006. Automated SKS splitting and upper-mantle anisotropy beneath Canadian seismic stations, *Geophysical Journal International*, **165**(3), 931–942.
- Ewing, M. & Press, F., 1950. Crustal structure and surface-wave dispersion, *Bulletin of the Seismological Society of America*, **40**(4), 271–280.

- Fichtner, A., Kennett, B. L. N., Igel, H., & Bunge, H.-P., 2009. Full seismic waveform tomography for upper-mantle structure in the Australasian region using adjoint methods, *Geophysical Journal International*, **179**(3), 1703–1725.
- Fichtner, A., Kennett, B. L., Igel, H., & Bunge, H.-P., 2010. Full waveform tomography for radially anisotropic structure: New insights into present and past states of the Australasian upper mantle, *Earth and Planetary Science Letters*, **290**(3-4), 270–280.
- Forsyth, D. W. & Li, A., 2005. Array-analysis of two-dimensional variations in surface wave phase velocity and azimuthal anisotropy in the presence of multi-pathing interference, in *Seismic Earth: Array Analysis of Broadband Seismograms*, vol. 157, pp. 81–98, eds Levander, A. & Nolet, G., Geophysical Monograph Series, AGU Washington D.C., ISBN 0-87590-422-X.
- Foster, A., Ekström, G., & Nettles, M., 2014. Surface wave phase velocities of the Western United States from a two-station method, *Geophysical Journal International*, **196**(2), 1189–1206.
- French, S. W. & Romanowicz, B. A., 2014. Whole-mantle radially anisotropic shear velocity structure from spectral-element waveform tomography, *Geophysical Journal International*, **199**(3), 1303–1327.
- Friederich, W., Wielandt, E., & Stange, S., 1994. Non-Plane Geometries of Seismic Surface Wavefields and Their Implications For Regional Surface-Wave Tomography, *Geophys. J. Int.*, **119**(3), 931–948.
- Friederich, W., Hunzinger, S., & Wielandt, E., 2000. A note on the interpretation of seismic surface waves over three-dimensional structures, *Geophys. J. Int.*, **143**(2), 335–339.
- Fry, B., Stehly, L., Campillo, M., Boschi, L., & Giardini, D., 2005. Surface wave tomography of the central alps: merging traditional source and non-traditional noise dispersion measurements, in *AGU Fall Meeting Abstracts*, vol. 1, p. 0284.
- Fry, B., Boschi, L., Ekstrom, G., & Giardini, D., 2008. Europe-Mediterranean tomography: High correlation between new seismic data and independent geophysical observables, *Geophysical Research Letters*, **35**, L04301.
- Fry, B., Deschamps, F., Kissling, E., Stehly, L., & Giardini, D., 2010. Layered azimuthal anisotropy of Rayleigh wave phase velocities in the European Alpine lithosphere inferred from ambient noise, *Earth and Planetary Science Letters*, **297**(1-2), 95–102.
- Fukao, Y., 1984. Evidence from core-reflected shear waves for anisotropy in the Earth's mantle, *Nature*, **309**(5970), 695–698.
- Gee, L. S. & Jordan, T. H., 1992. Generalized seismological data functionals, *Geophysical Journal International*, **111**(2), 363–390.
- Giacomuzzi, G., Civalleri, M., De Gori, P., & Chiarabba, C., 2012. A 3D Vs model of the upper mantle beneath Italy: Insight on the geodynamics of central Mediterranean, *Earth and Planetary Science Letters*, **335-336**, 105–120.

- Gibbons, S. J., 2006. On the Identification and Documentation of Timing Errors: An Example at the KBS Station, Spitsbergen, *Seismological Research Letters*, **77**(5), 559–571.
- Gök, R., 2003. Sn attenuation in the Anatolian and Iranian plateau and surrounding regions, *Geophysical Research Letters*, **30**(24), 1–13.
- Golitzin, B., 1912. On dispersion and attenuation of surface seismic waves, *Izv. Russ. Acad. Sci*, **2**.
- Grad, M. & Tiira, T., 2009. The Moho depth map of the European Plate, *Geophysical Journal International*, **176**(1), 279–292.
- Grad, M., Polkowski, M., Wilde-Piórko, M., Suchcicki, J., & Arant, T., 2015. Passive Seismic Experiment “13 BB Star” in the Margin of the East European Craton, Northern Poland, *Acta Geophysica*, **63**(2), 352–373.
- Grand, S. P., 2002. Mantle shear-wave tomography and the fate of subducted slabs, *Philosophical Transactions of the Royal Society of London A: Mathematical, Physical and Engineering Sciences*, **360**(1800), 2475–2491.
- Greve, S., Paulssen, H., Goes, S., & van Bergen, M., 2014. Shear-velocity structure of the Tyrrhenian Sea: Tectonics, volcanism and mantle (de) hydration of a back-arc basin, *Earth and Planetary Science Letters*, **400**, 45–53.
- Gutenberg, B., 1924. Dispersion und Extinktion von seismischen Oberflächenwellen und der Aufbau der obersten Erdschichten, *Physikalische Zeitschrift*, **XXV**, 377–381.
- Gutenberg, B., 1926. Untersuchungen zur Frage, bis zu welcher Tiefe die Erde kristallin ist, *Z. Geophys*, **2**, 24–29.
- Gutenberg, B. & Richter, C. F., 1936. Materials for the study of deep-focus earthquakes, *Bulletin of the Seismological Society of America*, **26**(4), 341–390.
- Güralp, 2013. website.
- Hanka, W., Saul, J., Weber, B., Becker, J., Harjadi, P., Fauzi, & Group, G. S., 2010. Real-time earthquake monitoring for tsunami warning in the Indian Ocean and beyond, *Natural Hazards and Earth System Science*, **10**(12), 2611–2622.
- Heintz, M. & Kennett, B. L. N., 2006. The apparently isotropic Australian upper mantle, *Geophysical Research Letters*, **33**(August), 1–5.
- Helmberger, D. V., Wen, L., & Ding, X., 1998. Seismic evidence that the source of the Iceland hotspot lies at the core-mantle boundary, *Nature*, **396**(November), 251–255.
- Henger, M., Berckhemer, H., & Seidl, D., 2002. The history of the development of the German Regional Seismic Network, *Ten years of German Regional Seismic Network (GRSN). Report*, **25**, 1–8.
- Hoernle, K., Zhang, Y.-S., & Graham, D., 1995. Seismic and geochemical evidence for large-scale mantle upwelling beneath the eastern Atlantic and western and central Europe.

- Horváth, F., 1993. Towards a mechanical model for the formation of the Pannonian basin, *Tectonophysics*, **226**, 333–357.
- Horváth, F., Bada, G., Szafián, P., Tari, G., Ádám, A., & Cloetingh, S., 2006. Formation and deformation of the Pannonian Basin: constraints from observational data, *Geological Society, London, Memoirs*, **32**(1), 191–206.
- Houser, C., Masters, G., Shearer, P., & Laske, G., 2008. Shear and compressional velocity models of the mantle from cluster analysis of long-period waveforms, *Geophysical Journal International*, **174**(1), 195–212.
- Igel, H. & Weber, M., 1995. SH-wave propagation in the whole mantle using high-order finite differences, *Geophys. Res. Lett.*, **22**(6), 731–734.
- Igel, H. & Weber, M., 1996. P-SV wave propagation in the Earth's mantle using finite differences: Application to heterogeneous lowermost mantle structure, *Geophys. Res. Lett.*, **23**, 415–418.
- James, D. & Assumpção, M., 1996. Tectonic implications of S-wave anisotropy beneath SE Brazil, *Geophysical Journal International*, pp. 1–10.
- Janutyte, I., Majdanski, M., Voss, P., Kozlovskaya, E., Group, P. W., et al., 2014. Upper mantle structure around the Trans-European Suture Zone obtained by teleseismic tomography, *Solid Earth Discussions*, **6**, 1723–1763.
- Jeffreys, H., 1928. Some cases of instability in fluid motion, *Proceedings of the Royal Society of London. Series A, Containing Papers of a Mathematical and Physical Character*, pp. 195–208.
- Jeffreys, H., 1935. The Surface Waves of Earthquakes., *Geophysical Journal International*, **3**(7), 253–261.
- Julia, J., Ammon, C. J., Herrmann, R. B., & Correig, A. M., 2000. Joint inversion of receiver function and surface wave dispersion observations, *Geophys. J. Int.*, **143**(1), 99–112.
- Kaiser, A., Reicherter, K., Hübscher, C., & Gajewski, D., 2005. Variation of the present-day stress field within the North German Basin—insights from thin shell FE modeling based on residual GPS velocities, *Tectonophysics*, **397**(1), 55–72.
- Kárason, H. & Van Der Hilst, R. D., 2000. Constraints on mantle convection from seismic tomography, *The history and dynamics of global plate motions*, pp. 277–288.
- Knapmeyer-Endrun, B., Krüger, F., Legendre, C., & Geissler, W., 2013a. Tracing the influence of the Trans-European Suture Zone into the mantle transition zone, *Earth and Planetary Science Letters*, **363**(0), 73–87.
- Knapmeyer-Endrun, B., Krüger, F., Legendre, C., & Geissler, W., 2013b. Tracing the influence of the Trans-European Suture Zone into the mantle transition zone, *Earth and Planetary Science Letters*, **363**(0), 73–87.

- Knapmeyer-Endrun, B., Krüger, F., Legendre, C. P., Geissler, W. H., Wilde-Piórko, M., Plomerová, J., Grad, M., Babska, V., Bruckl, E., Cyziene, J., Czuba, W., England, R., Gaczyński, E., Gazdova, R., Gregersen, S., Guterch, a., Hanka, W., Hegedus, E., Heuer, B., Jedlička, P., Lazauskiene, J., Keller, G. R., Kind, R., Klinge, K., Kolinsky, P., Komminaho, K., Kozlovskaya, E., Kruger, F., Larsen, T., Majdański, M., Malek, J., Motuza, G., Novotný, O., Pietrasiak, R., Plenefisch, T., Ružek, B., Sliupa, S., Środa, P., Świeczak, M., Tiira, T., Voss, P., & Wiejacz, P., 2013c. Tracing the influence of the Trans-European Suture Zone into the mantle transition zone, *Earth and Planetary Science Letters*, **363**, 73–87.
- Knapmeyer-Endrun, B., Krüger, F., & Group, t. P. W., 2014. Moho depth across the Trans-European Suture Zone from P- and S-receiver functions, *Geophysical Journal International*, **197**(2), 1048–1075.
- Knopoff, L., Mueller, S., & Pilant, W., 1966. Structure of the crust and upper mantle in the Alps from the phase velocity of Rayleigh waves, *Bulletin of the Seismological Society of America*, **56**(5), 1009–1044.
- Köhler, A., Weidle, C., & Maupin, V., 2012. Crustal and uppermost mantle structure of southern Norway: results from surface wave analysis of ambient seismic noise and earthquake data, *Geophysical Journal International*, **191**(3), 1441–1456.
- Komatitsch, D. & Tromp, J., 2002. Propagación de ondas sísmicas en modelos de tierra global 3-D usando elementos espectrales, pp. 676–686.
- Koulakov, I., Kaban, M. K., Tesauro, M., & Cloetingh, S., 2009. P- and S -velocity anomalies in the upper mantle beneath Europe from tomographic inversion of ISC data, *Geophysical Journal International*, **179**(1), 345–366.
- Koulakov, I., El Khrepy, S., Al-Arifi, N., Kuznetsov, P., & Kasatkina, E., 2015. Structural cause of a missed eruption in the Harrat Lunayyir basaltic field (Saudi Arabia) in 2009, *Geology*, **43**(5), 1–5.
- Kulesh, M., Diallo, M., & Holschneider, M., 2005. Wavelet analysis of ellipticity, dispersion, and dissipation properties of Rayleigh waves, *Acoustical Physics*, **51**(4), 425–434.
- Küperkoch, L., Meier, T., Lee, J., Friederich, W., & Working Group, E., 2010. Automated determination of P-phase arrival times at regional and local distances using higher order statistics, *Geophysical Journal International*, **181**(2), 1159–1170.
- Kustowski, B., Ekstrom, G., & Dziewonski, A., 2008. Anisotropic shear-wave velocity structure of the Earth's mantle: A global model, *J. Geophys. Res.*, **113**, B06306.
- Landisman, M., Dziewonski, A., & Sato, Y., 1969. Recent Improvements in the Analysis of Surface Wave Observations, *Geophysical Journal of the Royal Astronomical Society*, **17**(4), 369–403.
- Larose, E., Derode, A., Clorennec, D., Margerin, L., & Campillo, M., 2005. Passive retrieval of Rayleigh waves in disordered elastic media, *Physical Review E - Statistical, Nonlinear, and Soft Matter Physics*, **72**.

- Laske, G. & Masters, G., 1996. Constraints on global phase velocity maps from long-period polarization data, *J. Geophys. Res.*, **101**(B7), 16059–16075.
- Laske, G., Markee, A., Orcutt, J. A., Wolfe, C. J., Collins, J. A., Solomon, S. C., Detrick, R. S., Bercovici, D., & Hauri, E. H., 2011. Asymmetric shallow mantle structure beneath the Hawaiian Swell—evidence from Rayleigh waves recorded by the PLUME network, *Geophysical Journal International*, **187**(3), 1725–1742.
- Lay, T. & Wallace, T. C., 1995a. *Modern global seismology*, vol. 58, Academic press.
- Lay, T. & Wallace, T. C., 1995b. *Modern Global Seismology*, vol. 58 of **International Geophysics**, Academic Press, 1st edn.
- Lebedev, S. & Van Der Hilst, R. D., 2008. Global upper-mantle tomography with the automated multimode inversion of surface and S-wave forms, *Geophysical Journal International*, **173**, 505–518.
- Lebedev, S., Nolet, G., Meier, T., & van der Hilst, R., 2005. Automated multimode inversion of surface and S waveforms, *Geophys. J. Int.*, **162**(3), 951–964.
- Lebedev, S., Meier, T., & van der Hilst, R. D., 2006. Asthenospheric flow and origin of volcanism in the Baikal Rift area, *Earth and Planetary Science Letters*, **249**(3&4), 415 – 424.
- Lebedev, S., Boonen, J., & Trampert, J., 2009. Seismic structure of Precambrian lithosphere: New constraints from broad-band surface-wave dispersion, *Lithos*, **109**(1-2), 96–111.
- Lebedev, S., Adam, J. M.-C., & Meier, T., 2013. Mapping the Moho with seismic surface waves: A review, resolution analysis, and recommended inversion strategies, *Tectonophysics*, **609**, 377–394.
- Lee, E.-J. & Chen, P., 2013. Automating seismic waveform analysis for full 3-D waveform inversions, *Geophysical Journal International*.
- Legendre, C. P., Meier, T., Lebedev, S., Friederich, W., & Viereck-Götte, L., 2012. A shear wave velocity model of the European upper mantle from automated inversion of seismic shear and surface waveforms, *Geophysical Journal International*, **191**, 282–304.
- Lekic, V. & Romanowicz, B., 2011. Inferring upper-mantle structure by full waveform tomography with the spectral element method, *Geophysical Journal International*, **185**(2), 799–831.
- Lekic, V., French, S. W., & Fischer, K. M., 2011. Lithospheric Thinning Beneath Rifted Regions of Southern California, *Science*, **334**(6057), 783–787.
- Levin, V. & Park, J., 1997. P-SH conversions in a flat-layered medium with anisotropy of arbitrary orientation, *Geophysical Journal International*, **131**, 253–266.
- Levshin, A., Yanovskaya, T., Lander, A., Bukchin, B., Barmin, M., Ratnikova, L., & Its, E., 1989. *Seismic Surface Waves in a Laterally Inhomogeneous Earth*, Kluwer Academic Publishers, Dordrecht Netherlands.

- Levshin, A., Barmin, M., Ritzwoller, M., & Trampert, J., 2005. Minor-arc and major-arc global surface wave diffraction tomography, *Phys. Earth Plan. Int.*, **149**(3-4), 205–223.
- Levshin, A. L., Ritzwoller, M. H., & Resovsky, J. S., 1999. Source effects on surface wave group travel times and group velocity maps, *Phys. Earth Plan. Int.*, **115**(3-4), 293–312.
- Li, X.-D. & Romanowicz, B., 1996. Global mantle shear velocity model developed using nonlinear asymptotic coupling theory, *Journal of Geophysical Research: Solid Earth (1978–2012)*, **101**(B10), 22245–22272.
- Liu, X. & Dziewonski, A., 1994. Lowermost mantle shear wave velocity structure, *EOS, Trans. Am. geophys. Un.*, **78**, 663.
- Liu, X.-F. & Dziewonski, A. M., 1998. *Global Analysis of Shear Wave Velocity Anomalies in the Lower-Most Mantle*, pp. 21–36, American Geophysical Union.
- Lomax, A. & Snieder, R., 1995. The contrast in upper mantle shear-wave velocity between the east european platform and tectonic Europe obtained with genetic algorithm inversion of rayleigh-wave group dispersion, *Geophys. J. Int.*, **123**(1), 169–182.
- Love, A. E. H., 1911. *Some Problems of Geodynamics: Being an Essay to which the Adams Prize in the University of Cambridge was Adjudged in 1911*, Cambridge.
- Maggi, A. & Priestley, K., 2005. Surface waveform tomography of the Turkish-Iranian plateau, *Geophysical Journal International*, **160**(3), 1068–1080.
- Maggi, A., Tape, C., Chen, M., Chao, D., & Tromp, J., 2009. An automated time-window selection algorithm for seismic tomography, *Geophysical Journal International*, **178**(1), 257–281.
- Mantovani, E., Nolet, G., & Panza, G., 1985. Lateral heterogeneity in the crust of the Italian region from regionalized Rayleigh-wave group velocities, in *Annales geophysicae*, vol. 3, pp. 519–529, Gauthier-Villars.
- Masters, G., Jordan, T. H., Silver, P. G., & Gilbert, F., 1982. Aspherical Earth structure from fundamental spheroidal-mode data, *Nature*, **298**(5875), 609–613.
- Masters, G., Johnson, S., Laske, G., Bolton, H., & Davies, J., 1996. A shear-velocity model of the mantle [and discussion], *Philosophical Transactions of the Royal Society of London. Series A: Mathematical, Physical and Engineering Sciences*, **354**(1711), 1385–1411.
- Masters, G., Laske, G., Bolton, H., & Dziewonski, A., 2000. The relative behavior of shear velocity, bulk sound speed, and compressional velocity in the mantle: implications for chemical and thermal structure, *Earth's deep interior: mineral physics and tomography from the atomic to the global scale*, pp. 63–87.
- Mathar, J. P., Ritter, J. R. R., & Friederich, W., 2006. Surface waves image the top of the Eifel plume, *Geophys. J. Int.*, **164**(2), 377–382.

- Maupin, V., 2011. Upper-mantle structure in southern Norway from beamforming of Rayleigh wave data presenting multipathing, *Geophysical Journal International*, **185**(2), 985–1002.
- McEvelly, T. V., 1964. Central U.S. Crust-Upper mantle structure from Love and Rayleigh wave phase velocity inversion, *Bulletin of the Seismological Society of America*, **54**(6A), 1997–2015.
- Mégnin, C. & Romanowicz, B., 2000. The three-dimensional shear velocity structure of the mantle from the inversion of body, surface and higher-mode waveforms, *Geophysical Journal International*, **143**(3), 709–728.
- Meier, T., Dietrich, K., Stöckhert, B., & Harjes, H.-P., 2004. One-dimensional models of shear wave velocity for the eastern Mediterranean obtained from the inversion of Rayleigh wave phase velocities and tectonic implications, *Geophysical Journal International*, **156**(1), 45–58.
- Meschede, M. & Romanowicz, B., 2015. Lateral heterogeneity scales in regional and global upper mantle shear velocity models, *Geophysical Journal International*, **200**(2), 1078–1095.
- Mindevalli, O. Y. & Mitchell, B. J., 1989. Crustal structure and possible anisotropy in Turkey from seismic surface wave dispersion, *Geophysical Journal International*, **98**(1), 93–106.
- Mocquet, A., Romanowicz, B., & Montagner, J., 1989. Three-dimensional structure of the upper mantle beneath the Atlantic Ocean inferred from long-period Rayleigh waves: 1. Group and phase velocity distributions, *Journal of Geophysical Research: Solid Earth (1978–2012)*, **94**(B6), 7449–7468.
- Mueller, S. & Sprecher, C., 1978. Upper mantle structure along a profile through the eastern Alps from Rayleigh wave dispersion, *Alps, Apennines, Hellenides*, **38**, 40–44.
- Muyzert, E. & Snieder, R., 1996. The Influence of Errors in the Source Parameters on Phase Velocity Measurements of Surface Waves, *Bull. Seismol. Soc. Am.*, **86**, 1863–1872.
- Nataf, H.-C., Nakanishi, I., & Anderson, D. L., 1986. Measurements of mantle wave velocities and inversion for lateral heterogeneities and anisotropy: 3. Inversion, *Journal of Geophysical Research: Solid Earth (1978–2012)*, **91**(B7), 7261–7307.
- Nicolson, H., Curtis, A., Baptie, B., & Galetti, E., 2012. Seismic interferometry and ambient noise tomography in the British Isles, *Proceedings of the Geologists' Association*, **123**(1), 74–86.
- Nolet, G., 1990. Partitioned waveform inversion and two-dimensional structure under the network of autonomously recording seismographs, *Journal of Geophysical Research: Solid Earth*, **95**(B6), 8499–8512.
- Nolet, G. & Zielhuis, A., 1994. Low S velocities under the Tornquist-Teisseyre zone: Evidence for water injection into the transition zone by subduction, *Journal of Geophysical Research: Solid Earth (1978–2012)*, **99**(B8), 15813–15820.

- Olivieri, M. & Clinton, J., 2012. An Almost Fair Comparison Between Earthworm and SeisComp3, *Seismological Research Letters*, **83**(5), 833.
- Pallister, J. S., McCausland, W. a., Jónsson, S., Lu, Z., Zahran, H. M., Hadidy, S. E., Aburukbah, A., Stewart, I. C. F., Lundgren, P. R., White, R. a., & Moufti, M. R. H., 2010. Broad accommodation of rift-related extension recorded by dyke intrusion in Saudi Arabia, *Nature Geoscience*, **3**(10), 705–712.
- Palomeras, I., Thurner, S., Levander, A., Liu, K., Villasenor, A., Carbonell, R., & Harnafi, M., 2014. Finite-frequency Rayleigh wave tomography of the western Mediterranean: Mapping its lithospheric structure, *Geochemistry, Geophysics, Geosystems*, **15**(1), 140–160.
- Panning, M. & Romanowicz, B., 2006. A three-dimensional radially anisotropic model of shear velocity in the whole mantle, *Geophysical Journal International*, **167**(1), 361–379.
- Passier, M. L. & Snieder, R. K., 1995. Using differential waveform data to retrieve local S velocity structure or path-averaged S velocity gradients, *Journal of Geophysical Research: Solid Earth*, **100**(B12), 24061–24078.
- Paul, A., Campillo, M., Margerin, L., Larose, E., & Derode, A., 2005. Empirical synthesis of time-asymmetrical Green functions from the correlation of coda waves, *Journal of Geophysical Research B: Solid Earth*, **110**, 1–13.
- Pedersen, H., Campillo, M., & Balling, N., 1994. Changes in the lithospheric structure across the Sorgenfrei-Tornquist Zone inferred from dispersion of Rayleigh waves, *Earth and Planetary Science Letters*, **128**(1), 37–46.
- Pedersen, H., Debayle, E., & Maupin, V., 2013. Strong lateral variations of lithospheric mantle beneath cratons – Example from the Baltic Shield, *Earth and Planetary Science Letters*, **383**(0), 164 – 172.
- Pedersen, H. A., Bruneton, M., & Maupin, V., 2006. Lithospheric and sublithospheric anisotropy beneath the Baltic shield from surface-wave array analysis, *Earth Plan. Sc. Let.*, **244**(3-4), 590–605.
- Peter, D., Tape, C., Boschi, L., & Woodhouse, J. H., 2007. Surface wave tomography: Global membrane waves and adjoint methods, *Geophysical Journal International*, **171**, 1098–1117.
- Pharaoh, T. C., 1999. Palaeozoic terranes and their lithospheric boundaries within the Trans-European Suture Zone (TESZ): a review, *Tectonophysics*, **314**(1-3), 17–41.
- Pilidou, S., Priestley, K., Gudmundsson, O., & Debayle, E., 2004. Upper mantle S-wave speed heterogeneity and anisotropy beneath the North Atlantic from regional surface wave tomography: The Iceland and Azores plumes, *Geophysical Journal International*, **159**, 1057–1076.
- Pilidou, S., Priestley, K., Debayle, E., & Gudmundsson, O., 2005. Rayleigh wave tomography in the North Atlantic: high resolution images of the Iceland, Azores and Eifel mantle plumes, *Lithos*, **79**(3-4), 453–474.

- Piromallo, C., 2003. wave tomography of the mantle under the Alpine-Mediterranean area, *Journal of Geophysical Research*, **108**(B2), 1–23.
- Plomerová, J. & Babuška, V., 2010. Long memory of mantle lithosphere fabric—European LAB constrained from seismic anisotropy, *Lithos*, **120**(1), 131–143.
- Polat, G., Lebedev, S., Readman, P. W., O’Reilly, B. M., & Hauser, F., 2012. Anisotropic Rayleigh-wave tomography of Ireland’s crust: Implications for crustal accretion and evolution within the Caledonian Orogen, *Geophysical Research Letters*, **39**(4).
- Press, F., 1956. Determination Of Crustal Structure From Phase Velocity Of Rayleigh Waves Part I: Southern California, *Geological Society of America Bulletin*, **67**(12), 1647–1658.
- Priestley, K. & McKenzie, D., 2006. The thermal structure of the lithosphere from shear wave velocities, *Earth and Planetary Science Letters*, **244**(1-2), 285–301.
- Prindle, K. & Tanimoto, T., 2006. Teleseismic surface wave study for S-wave velocity structure under an array: Southern California, *Geophysical Journal International*, **166**(2), 601–621.
- Rickers, F., Fichtner, A., & Trampert, J., 2013. The Iceland-Jan Mayen plume system and its impact on mantle dynamics in the North Atlantic region: Evidence from full-waveform inversion, *Earth and Planetary Science Letters*, **367**(0), 39 – 51.
- Ritsema, J., van Heijst, H. J., & Woodhouse, J. H., 2004. Global transition zone tomography, *Journal of Geophysical Research: Solid Earth (1978–2012)*, **109**(B2).
- Ritsema, J., Deuss, A., van Heijst, H. J., & Woodhouse, J. H., 2011. S40RTS: a degree-40 shear-velocity model for the mantle from new Rayleigh wave dispersion, teleseismic traveltime and normal-mode splitting function measurements, *Geophysical Journal International*, **184**(3), 1223–1236.
- Ritter, J. R. R., Jordan, M., Christensen, U. R., & Achauer, U., 2001. A mantle plume below the Eifel volcanic fields, Germany, *Earth Plan. Sc. Let.*, **186**(1), 7–14.
- Ritzwoller, M., Levshin, A., Smith, S., & Lee, C., 1995. Making accurate continental broadband surface wave measurements, Tech. rep., DTIC Document.
- Ritzwoller, M. H. & Levshin, A. L., 1998. Eurasian surface wave tomography: Group velocities, *J. Geophys. Res.*, **103**(B3), 4839–4878.
- Ritzwoller, M. H., Shapiro, N. M., Barmin, M. P., & Levshin, A. L., 2002. Global surface wave diffraction tomography, *Journal of Geophysical Research: Solid Earth (1978–2012)*, **107**(B12), ESE–4.
- Rost, S. & Weber, M., 2002. The upper mantle transition zone discontinuities in the Pacific as determined by short-period array data, *Earth Plan. Sc. Let.*, **204**(3-4), 347–361.

- Roux, E., Moorkamp, M., Jones, A. G., Bischoff, M., Endrun, B., Lebedev, S., & Meier, T., 2011. Joint inversion of long-period magnetotelluric data and surface-wave dispersion curves for anisotropic structure: Application to data from Central Germany, *Geophysical Research Letters*, **38**(5).
- Roux, P., Sabra, K. G., Kuperman, W. A., & Roux, A., 2005. Ambient noise cross correlation in free space: Theoretical approach, *The Journal of the Acoustical Society of America*, **117**(1), 79–84.
- Sabra, K. G., Gerstoft, P., Roux, P., Kuperman, W. A., & Fehler, M. C., 2005. Surface wave tomography from microseisms in Southern California, *Geophysical Research Letters*, **32**, 1–4.
- Sandoval, S., Kissling, E., Ansgor, J., & the SVEKALAPKO Seismic Tomography Working Group, 2004. High-resolution body wave tomography beneath the SVEKALAPKO array – II. Anomalous upper mantle beneath the central Baltic Shield, *Geophys. J. Int.*, **157**, 200–214.
- Savage, M. K., 1999. Seismic anisotropy and mantle deformation: What have we learned from shear wave splitting?, *Reviews of Geophysics*, **37**(1), 65–106.
- Schaefer, J. F., Boschi, L., & Kissling, E., 2011. Adaptively parametrized surface wave tomography: methodology and a new model of the European upper mantle, *Geophysical Journal International*, **186**(3), 1431–1453.
- Schaeffer, A. & Lebedev, S., 2013. Global shear-speed structure of the upper mantle and transition zone, *Geophys. J. Int.*, **194**(1), 417–449.
- Scheck-Wenderoth, M. & Lamarche, J., 2005a. Crustal memory and basin evolution in the Central European Basin System - new insights from a 3D structural model, *Tectonophysics*, **397**(1-2), 143 – 165, Integration of Geophysical and Geological Data and Numerical Models in Basins.
- Scheck-Wenderoth, M. & Lamarche, J., 2005b. Crustal memory and basin evolution in the Central European Basin System—new insights from a 3D structural model, *Tectonophysics*, **397**(1), 143–165.
- Schivardi, R. & Morelli, A., 2009. Surface wave tomography in the European and Mediterranean region, *Geophysical Journal International*, **177**(3), 1050–1066.
- Schulte-Pelkum, V., Masters, G., & Shearer, P. M., 2001. Upper mantle anisotropy from long-period P polarization, *Journal of Geophysical Research-Solid Earth*, **106**, 21917–21934.
- Shapiro, N. & Campillo, M., 2004. Emergence of broadband Rayleigh waves from correlations of the ambient seismic noise, *J. Geophys. Res.*, **31**, L07614.
- Shapiro, N. M., Campillo, M., Stehly, L., & Ritzwoller, M. H., 2005. High-resolution surface-wave tomography from ambient seismic noise., *Science (New York, N.Y.)*, **307**, 1615–1618.
- Shearer, P. M., 2009. *Introduction to seismology*, Cambridge University Press.

- Shen, Y., Solomon, S. C., Bjarnason, I. T., & Purdy, G., 1996. Hot mantle transition zone beneath Iceland and the adjacent Mid-Atlantic Ridge inferred from P-to-S conversions at the 410-and 660-km discontinuities, *Geophysical research letters*, **23**(24), 3527–3530.
- Shen, Y., Solomon, S. C., Th, I., Nolet, G., Morgan, W. J., Allen, R. M., Vogfjo, K., Stefa, R., Julian, B. R., & Foulger, G. R., 2002. Seismic evidence for a tilted mantle plume and north ^ south mantle £ ow beneath Iceland, **197**.
- Silveira, G. & Stutzmann, E., 2002. Anisotropic tomography of the Atlantic Ocean, *Physics of the Earth and Planetary Interiors*, **132**(4), 237–248.
- Silver, P. G., 1996. SEISMIC ANISOTROPY BENEATH THE CONTINENTS: Probing the Depths of Geology, *Annual Review of Earth and Planetary Sciences*, **24**(1), 385–432.
- Silver, P. G. & Chan, W. W., 1991. Shear wave splitting and subcontinental mantle deformation, *J. geophys. Res*, **96**(16), 429–16.
- Simmons, N. A., Forte, A. M., & Grand, S. P., 2006. Constraining mantle flow with seismic and geodynamic data: A joint approach, *Earth and Planetary Science Letters*, **246**(1–2), 109 – 124.
- Simmons, N. A., Forte, A. M., Boschi, L., & Grand, S. P., 2010. GyPSuM: A joint tomographic model of mantle density and seismic wave speeds, *Journal of Geophysical Research: Solid Earth*, **115**(B12), n/a–n/a.
- Snieder, R., 1988. The Optical Theorem For Surface-Waves And The Relation With Surface-Wave Attenuation, *Geophysical Journal-Oxford*, **95**(2), 293–302.
- Snieder, R., 2004. Extracting the Green’s function from the correlation of coda waves: a derivation based on stationary phase., *Physical review. E, Statistical, nonlinear, and soft matter physics*, **69**, 046610.
- Soomro, R., Weidle, C., Cristiano, L., Lebedev, S., M. T., & Group, P. W., 2015. Phase velocities of Rayleigh and Love waves in central and northern Europe from automated, broadband, inter-station measurements, *submitted to GJI*.
- Souriau, A., Chevrot, S., & Olivera, C., 2008. A new tomographic image of the Pyrenean lithosphere from teleseismic data, *Tectonophysics*, **460**(1-4), 206–214.
- Sroda, P., the POLCRUST, & Groups, P. W., 2014. Seismic anisotropy and deformations of the TESZ lithosphere near the East European Craton margin in SE Poland at various scales and depths, in *EGU General Assembly 2014, Geophysical Research Abstracts, 16, EGU2014-6463-1, 2014*.
- Stange, S. & Friederich, W., 1993. Surface-Wave Dispersion And Upper-Mantle Structure Beneath Southern Germany From Joint Inversion Of Network Recorded Teleseismic Events, *Geophysical Research Letters*, **20**(21), 2375–2378.
- Stoneley, R., 1926. The Effect of the Ocean on Rayleigh Waves., *Geophysical Journal International*, **1**(s7), 349–356.

- Stoneley, R., 1928. The dispersion of waves in a double superficial layer, *Geophysical Journal International*, **1**(s10), 527–532.
- Su, W.-j., Woodward, R. L., & Dziewonski, A. M., 1994. Degree 12 model of shear velocity heterogeneity in the mantle, *Journal of Geophysical Research: Solid Earth (1978–2012)*, **99**(B4), 6945–6980.
- Sun, D. & Helmberger, D., 2011. Upper-mantle structures beneath USArray derived from waveform complexity, *Geophysical Journal International*, **184**(1), 416–438.
- Tanimoto, T. & Prindle, K., 2007. Surface wave analysis with beamforming, *Earth, Planets and Space*, **59**(5), 453–458.
- Tape, C., Liu, Q., Maggi, A., & Tromp, J., 2010. Seismic tomography of the southern California crust based on spectral-element and adjoint methods, *Geophysical Journal International*, **180**(1), 433–462.
- Tari, G., Dövényi, P., Dunkl, I., Horváth, F., Lenkey, L., Stefanescu, M., Szafián, P., & Tóth, T., 1999. Lithospheric structure of the Pannonian basin derived from seismic, gravity and geothermal data, *Geological Society, London, Special Publications*, **156**(1), 215–250.
- Tesauro, M., Kaban, M. K., & Cloetingh, S. a. P. L., 2008. EuCRUST-07: A new reference model for the European crust, *Geophysical Research Letters*, **35**(December 2007), 3–7.
- Thybo, H., 2000. Crustal structure and tectonic evolution of the Tornquist Fan region as revealed by geophysical methods, *Bulletin of the Geological Society of Denmark*, **46**, 145–160.
- Toksöz, M. N. & Ben-Menahem, A., 1963. Velocities of mantle Love and Rayleigh waves over multiple paths, *Bulletin of the Seismological Society of America*, **53**(4), 741–764.
- Totaro, C., Koulakov, I., Orecchio, B., & Presti, D., 2014. Detailed crustal structure in the area of the southern Apennines–Calabrian Arc border from local earthquake tomography, *Journal of Geodynamics*, **82**, 87–97.
- Trampert, J. & Woodhouse, J. H., 2003. Global anisotropic phase velocity maps for fundamental mode surface waves between 40 and 150 s, *Geophys. J. Int.*, **154**(1), 154–165.
- Vaccari, F. & Panza, G., 1993. VPVS estimation in southwestern Europe from P-wave and surface-wave tomography analysis, *Physics of the earth and planetary interiors*, **78**(3), 229–237.
- van der Lee, S., Marone, F., van der Meijde, M., Giardini, D., Deschamps, A., Margheriti, L., Burkett, P., Solomon, S. C., Alves, P. M., Chouliaras, M., et al., 2001. Eurasia-Africa plate boundary region yields new seismographic data, *EOS Transactions*, **82**, 637–646.

- Vauchez, A. & Nicolas, A., 1991. Mountain building: strike-parallel motion and mantle anisotropy.
- Vdovin, O., Rial, J. A., Levshin, A. L., & Ritzwoller, M. H., 1999. Group-velocity tomography of South America and the surrounding oceans, *Geophysical Journal International*, **136**(2), 324–340.
- Vecsey, L., Plomerová, J., & Babuška, V., 2014. Mantle lithosphere transition from the East European Craton to the Variscan Bohemian Massif imaged by shear-wave splitting, *Solid Earth*, **5**, 779–792.
- Walther, M., Plenefisch, T., & Rumpker, G., 2014. Automated analysis of SKS splitting to infer upper mantle anisotropy beneath Germany using more than 20 yr of GRSN and GRF data, *Geophysical Journal International*, **196**(2), 1207–1236.
- Wang, Z. & Dahlen, F. A., 1995. Validity of surface-wave ray theory on a laterally heterogeneous earth, *Geophysical Journal International*, **123**(3), 757–773.
- Wapenaar, K., 2004. Retrieving the elastodynamic Green's function of an arbitrary inhomogeneous medium by cross correlation, *Physical Review Letters*, **93**.
- Weaver, R. L. & Lobkis, O. I., 2001. Ultrasonics without a source: thermal fluctuation correlations at MHz frequencies., *Physical review letters*, **87**, 134301.
- Weaver, R. L. & Lobkis, O. I., 2004. Diffuse fields in open systems and the emergence of the Green's function (L).
- Weidle, C., Maupin, V., Ritter, J., Kvaerna, T., Schweitzer, J., Balling, N., Thybo, H., Faleide, J. I., & Wenzel, F., 2010. MAGNUS – A Seismological Broadband Experiment to Resolve Crustal and Upper Mantle Structure beneath the Southern Scandes Mountains in Norway, *Seism. Res. Let.*, **81**(1), 76–84.
- Weidle, C., Soomro, R., Cristiano, L., & Meier, T., 2013. Identification of response and timing issues at permanent European broadband stations from automated data analysis, *Advances in Geosciences*, **36**, 21–25.
- Wessel, P. & Smith, W. H., 1998. New, improved version of the Generic Mapping Tools released, *EOS Trans. AGU*, **79**, 579.
- Wielandt, E., 1993. Propagation and Structural Interpretation of Non-Plane Waves, *Geophys. J. Int.*, **113**(1), 45–53.
- Wielandt, E., Sigg, A., Plešinger, A., Horálek, J., & Pěč, K., 1987. Deep structure of the bohemian massif from phase velocities of Rayleigh and Love waves, *Studia Geophysica et Geodaetica*, **31**(1), 1–7.
- Wilde-Piórko, M., Geissler, W., Plomerová, J., Grad, M., Babuška, V., Brückl, E., Cyziene, J., Czuba, W., England, R., Gaczyński, E., et al., 2008. PASSEQ 2006–2008: passive seismic experiment in Trans-European Suture Zone, *Studia geophysica et geodaetica*, **52**(3), 439–448.

- Wilde-Piórko, M., Geissler, W., Plomerová, J., Grad, M., Babuška, V., Brückl, E., Cyziene, J., Czuba, W., England, R., Gaczyński, E., Gazdova, R., Gregersen, S., Guterch, A., Hanka, W., Hegedűs, E., Heuer, B., Jedlička, P., Lazauskiene, J., Keller, G., Kind, R., Klinge, K., Kolinsky, P., Komminaho, K., Kozlovskaya, E., Krüger, F., Larsen, T., Majdański, M., Málek, J., Motuza, G., Novotný, O., Pietrasiak, R., Plenefisch, T., Ržek, B., Sliupa, S., Środa, P., Świeczak, M., Tiira, T., Voss, P., & Wiejacz, P., 2008. PASSEQ 2006 – 2008: Passive seismic experiment in Trans-European Suture Zone, *Studia Geophysica et Geodaetica*, **52**(3), 439–448.
- Wilde-Piórko, M., Świeczak, M., Grad, M., & Majdański, M., 2010. Integrated seismic model of the crust and upper mantle of the Trans-European Suture zone between the Precambrian craton and Phanerozoic terranes in Central Europe, *Tectonophysics*, **481**(1), 108–115.
- Wilson, M., Neumann, E.-R., Davies, G. R., Timmerman, M., Heeremans, M., & Larsen, B. T., 2004. Permo-Carboniferous magmatism and rifting in Europe: introduction, *Geological Society, London, Special Publications*, **223**(1), 1–10.
- Winchester, J. A., 2002. Palaeozoic amalgamation of Central Europe: new results from recent geological and geophysical investigations, *Tectonophysics*, **360**(1-4), 5–21.
- Withers, M. M., 1999. An automated local and regional seismic event detection and location system using waveform correlation, *Bull. Seism. Soc. Am*, pp. 657–669.
- Woodhouse, J. H. & Dziewonski, A. M., 1984. Mapping the upper mantle: Three-dimensional modeling of Earth structure by inversion of seismic waveforms, *Journal of Geophysical Research: Solid Earth (1978–2012)*, **89**(B7), 5953–5986.
- Wortel, M. J. & Spakman, W., 2000. Subduction and slab detachment in the Mediterranean-Carpathian region., *Science (New York, N.Y.)*, **290**(5498), 1910–1917.
- Wüstefeld, A., Bokelmann, G., Barruol, G., & Montagner, J. P., 2009. Identifying global seismic anisotropy patterns by correlating shear-wave splitting and surface-wave data, *Physics of the Earth and Planetary Interiors*, **176**, 198–212.
- Wüstefeld, A., Bokelmann, G., & Barruol, G., 2010. Evidence for ancient lithospheric deformation in the East European Craton based on mantle seismic anisotropy and crustal magnetics, *Tectonophysics*, **481**(1-4), 16–28.
- Yang, Y., Ritzwoller, M. H., Levshin, A. L., & Shapiro, N. M., 2007. Ambient noise Rayleigh wave tomography across Europe, *Geophysical Journal International*, **168**, 259–274.
- Yang, Y., Ritzwoller, M. H., Lin, F.-C., Moschetti, M. P., & Shapiro, N. M., 2008. Structure of the crust and uppermost mantle beneath the western United States revealed by ambient noise and earthquake tomography, *J. Geophys. Res.*, **113**(B12), B12310.
- Yanovskaya, T. & Ditmar, P., 1990. Smoothness criteria in surface wave tomography, *Geophysical Journal International*, **102**(1), 63–72.

- Yao, H., van der Hilst, R. D., & de Hoop, M. V., 2006. Surface-wave array tomography in SE Tibet from ambient seismic noise and two-station analysis- I. Phase velocity maps, *Geophysical Journal International*, **166**(2), 732–744.
- Yoshizawa, K. & Ekström, G., 2010. Automated multimode phase speed measurements for high-resolution regional-scale tomography: application to North America, *Geophysical Journal International*, **183**(3), 1538–1558.
- Yuan, H. & Romanowicz, B., 2010. Lithospheric layering in the North American craton, *Nature*, **466**(7310), 1063–1068.
- Zhang, S. & Karato, S.-i., 1995. Lattice preferred orientation of olivine aggregates deformed in simple shear.
- Zhang, X., Paulssen, H., Lebedev, S., & Meier, T., 2007. Surface wave tomography of the Gulf of California, *Geophys. Res. Lett.*, **34**(15), L15305–.
- Zhang, Y.-S. & Tanimoto, T., 1993. High-resolution global upper mantle structure and plate tectonics, *Journal of Geophysical Research: Solid Earth (1978–2012)*, **98**(B6), 9793–9823.
- Zhou, Y., Nolet, G., Dahlen, F. A., & Laske, G., 2006. Global upper-mantle structure from finite-frequency surface-wave tomography, *J. Geophys. Res.*, **111**(B04304), B04304.
- Zhou, Y., Liu, Q., & Tromp, J., 2011. Surface wave sensitivity: mode summation versus adjoint SEM, *Geophysical Journal International*, **187**(3), 1560–1576.
- Zhu, H. & Tromp, J., 2013. Mapping tectonic deformation in the crust and upper mantle beneath Europe and the North Atlantic Ocean., *Science (New York, N.Y.)*, **341**(2013), 871–5.
- Zhu, H., Bozdağ, E., Peter, D., & Tromp, J., 2012. Structure of the European upper mantle revealed by adjoint tomography, *Nature Geoscience*, **5**(June), 493–498.
- Ziegler, P., 1992. North Sea rift system, *Tectonophysics*, **208**(1), 55–75.
- Zingg, D. W., 2000. Comparison of High-Accuracy Finite-Difference Methods for Linear Wave Propagation, *SIAM Journal on Scientific Computing*, **22**(2), 476–502.
- Zingg, D. W., Lomax, H., & Jurgens, H., 1996. High-Accuracy Finite-Difference Schemes for Linear Wave Propagation, *SIAM Journal on Scientific Computing*, **17**(2), 328–346.
- Zor, E., 2003. The crustal structure of the East Anatolian plateau (Turkey) from receiver functions, *Geophysical Research Letters*, **30**(24), 2–5.
- Zor, E., 2008. Tomographic evidence of slab detachment beneath eastern Turkey and the Caucasus, *Geophysical Journal International*, **175**(3), 1273–1282.

CURRICULUM VITAE

Riaz Ahmed Soomro

soomro@geophysik.uni-kiel.de

PERSONEL

Nationality: Pakistani
Home town: Shikarpur, Pakistan

EDUCATION

- M.S. Seismology** September 2009
International institute of seismology and earthquake engineering, Tsukuba, Japan
- PGD Computer Software and Hardware** 1998
Computer Training Center, UGC campus, Islamabad, Pakistan
- B.E. Electronic Engineering** 1997
Mehran University of Engineering and technology, Jamshoro, Pakistan

CAREER HISTORY

- PhD student**, *Christian-Albrechts University Kiel, 24118 Kiel, Germany* January 2011 - Present
- The title of my PhD thesis is "Automated surface wave dispersion measurements and surface wave tomography of central and northern Europe Research assistant.
- Senior engineer**, *Micro Seismic Studies Program, Islamabad, Pakistan* 1998-2008

PUBLICATIONS

- Soomro, R.A., C. Weidle, S. Lebedev, L. Cristiano, T. Meier. "**Phase velocities of Rayleigh and Love waves in central and northern Europe from automated, broadband, inter-station measurements**," Submitted to *GeoPhysical Journal International*, 2015
- Weidle, C., Soomro, R., Cristiano, L. & Meier, T. "**Identification of response and timing issues at permanent European broadband stations from automated data analysis**," *Advances in Geosciences*, 36, pp. 21-25, 2013.
- Soomro, R. A. master thesis report
<http://iisee.kenken.go.jp/syndb/?action=abstr&id=MEE08161&est=S&year=2009> titled "**RECEIVER FUNCTION ANALYSIS FOR CRUSTAL STRUCTURE BENEATH PAKISTAN**," 2009

CONFERENCE PUBLICATIONS

- Soomro, R.A., C. Weidle, S. Lebedev, L. Cristiano, J. Behrmann, and T. Meier,, "**Anisotropic Love and Rayleigh wave phase velocity maps for central to northern Europe**", American Geophysical Union Fall Meeting, San Francisco, December 15-19, 2014.
- Viereck, L., Michael Abratis, Riaz Soomro, Christian Weidle, Luigia Cristiano, S. Lebedev, Thomas Meier, "**Compositional variations of magmas in volcanic fields of the Central European Cenozoic Igneous Province reflect the shape of its asthenospheric reservoir**", *GeoFrankfurt 2014, Dynamik des Systems Erde / Earth System Dynamics, Goethe Universitt Frankfurt a.M.*, 21-24 September 2014.
- Soomro, R.A., Christian Weidle, S. Lebedev, Luigia Cristiano, Jan Behrmann, and Thomas Meier, "**Surface wave tomography of central and northern Europe from automated inter-station dispersion measurements**", Poster, Second European Conference on Earthquake Engineering and Seismology (2ECEES), Istanbul, 24-29 August 2014.
- Soomro, R.A., C. Weidle, S. Lebedev, L. Cristiano, J. Behrmann, T. Meier, "**Surface wave tomography of central and northern Europe from automated inter-station dispersion measurements**", Talk (12 March), *Deutschen Geophysikalischen Gesellschaft (DGG)*, Karlsruhe, 10-13 March, 2014.
- Soomro, R. A.; Weidle, C.; Lebedev, S.; Cristiano, L.; Meier, T. , "**Surface wave tomography of central and northern Europe from automated inter-station dispersion measurements**", American Geophysical Union, Fall Meeting 2013, abstract No. S33A-2392, San Francisco, December 09-13, 2013.

- Soomro, R.A., C. Weidle, S. Lebedev, L. Cristiano, T. Meier, “**Automated Inter-station Measurements of Fundamental Mode Phase Velocities, and Tomographic Inversion of Surface Waves for Central to Northern Europe**“, (Talk, 7 March), Deutschen Geophysikalischen Gesellschaft, Leipzig, 4 - 7 March 2013.
- Soomro, R.A., C. Weidle, S. Lebedev, L. Cristiano, T. Meier. “**Automated inter-station measurements of fundamental mode phase velocities, and tomographic inversion for Central and Northern Europe, EGU General Assembly**,” Vienna, Austria, April 2013.
- C. Weidle, Soomro, R.A., L. Cristiano, T. Meier. “**Identification of response and timing issues at permanent European broadband stations from automated data analysis, EGU General Assembly**”, Vienna, Austria, April 2013.
- Soomro, R.A., C. Weidle, S. Lebedev, L. Cristiano, T. Meier. “**Surface wave tomography of central to northern Europe First tests using automated inter-station dispersion measurements (ES4: P086, Poster)**”, European Seismological Commission 33rd General Assembly, 19 - 24 August, Moscow, Russia.
- Soomro, R.A., C. Weidle, S. Lebedev, T. Meier. “**Automated Inter-Station Measurements of Fundamental Mode Phase Velocities Examples and Tests (ES1: O17, Talk)**”, European Seismological Commission 33rd General Assembly, 19 - 24 August, Moscow, Russia.
- Soomro, R.A., C. Weidle, S. Lebedev and T. Meier. “**Automated inter station measurements of fundamental mode phase velocities first tests 4th PASSEQ Workshop**”, Jachranka, 14-17 March 2012. Soomro, R.A., C. Weidle, S. Lebedev and T. Meier. “**Automated inter station measurements of fundamental mode phase velocities first tests (SO-P.008, Poster)**”. Deutschen Geophysikalischen Gesellschaft (DGG), 5 - 8 March.

SKILLS

Programming: C/C++, Shell scripting, JavaScript, L^AT_EX, Python, Visual Basic, SQL, GMT Seismic analysis software (ObsPy, Seismic Handler, SAC)

Operating Systems: Windows, Linux, UNIX

AWARDS AND HONORS

First position, Secondary School Certificate Examination, BISE, Sukkur, pakistan

1987-1888